AN ABSTRACT OF THE DISSERTATION OF

Wade R. Marcum for the degree of Doctor of Philosophy in Nuclear Engineering presented on December 3, 2010.

Title: Predicting Mechanical Instability of a Cylindrical Plate under Axial Flow Conditions

Abstract approved: _____

Brian G. Woods

Five U.S. high performance research reactors (HPRRs) are currently part of an international non-proliferation program with the objective of ultimately converting their highly enriched uranium (HEU) fuel to a new high density, low enriched uranium (LEU) fuel while still maintaining their reactor kinetic and thermal hydraulic performance. A uranium-molybdenum (U-Mo) alloy is under development as the proposed LEU fuel. This prototypic fuel must be qualified through the relevant regulator (either the Department of Energy (DoE) or Nuclear Regulatory Commission (NRC)) prior to its implementation in the HPRRs. One particular aspect of this qualification being investigated is the hydro-mechanical integrity of the fuel elements during typical operation conditions; with emphasis on coolant-clad reactions. Due to the highly turbulent flow conditions which produce extreme viscous forces over the plate type fuel elements found in the HPRRs, interfacial reactions regarding the prototypic fuel are of concern for the fuel's qualification. One issue associated with coolant-clad interactions is the onset mechanical fuel plate instability induced by the flow field. This phenomenon has the potential to induce sufficient plate membrane stresses to challenge the hydro- and thermo-mechanical integrity of the elements. In this study, a flow induced vibration model is developed to characterize elastic plate motion of a single HPRR fuel plate in an attempt to address plate instability concerns associated with HPRR elements.

Predicting Mechanical Instability of a Cylindrical Plate under Axial Flow Conditions

by

Wade R. Marcum

A DISSERTATION

submitted to

Oregon State University

in partial fulfillment of

the requirements for the

degree of

Doctor of Philosophy

Presented December 3, 2010

Commencement June 2011

Doctor of Philosophy dissertation of Wade R. Marcum presented on December 3, 2010.

APPROVED:

Major Professor, representing Nuclear Engineering

Head of the Department of Nuclear Engineering and Radiation Health Physics

Dean of the Graduate School

I understand that my dissertation will become part of the permanent collection of Oregon State University libraries. My signature below authorizes release of my dissertation to any reader upon request.

Wade R. Marcum, Author

ACKNOWLEDGEMENTS

I would like to take this opportunity and thank those who have significantly influenced my collegiate experience during the duration of time in which I have progressed through the doctoral program. Although there are numerous individuals who have impacted my life over the past several years, I accredit my successful completion to a select few.

My deepest gratitude to my advisor, Dr. Brian Woods. I have been very fortunate to have an advisor who gave me the freedom to explore on my own while also providing me with direction and support when needed and for that I am grateful.

I appreciate the time that my committee members; Dr. Roy Haggerty, Dr. Jim Liburdy, Dr. Steve Reese, Dr. Daniel Wachs, and Dr. Qiao Wu have allocated out of their busy schedules to supervise the progression of my degree.

It is with sincere thanks that I acknowledge Dr. Mark Galvin, Brian Jackson, and Seth Cadell for the collective feedback that they have given me, whether it was over a tedious task or significant topical issue they were there when I needed them most.

My family's continual support has guided me to finish even during times of self doubt and frustration.

Lastly I would like to recognize my wife for the sacrifice she has made by allowing me to continue through my collegiate tenure and recognize a career goal that I have had. Thank you Molly.

TABLE OF CONTENTS

TABLE OF CONTENTS (CONTINUED)

TABLE OF CONTENTS (CONTINUED)

TABLE OF CONTENTS (CONTINUED)

LIST OF FIGURES

LIST OF FIGURES (CONTINUED)

Figure Page

LIST OF FIGURES (CONTINUED)

Figure Page

LIST OF FIGURES (CONTINUED)

LIST OF TABLES

Predicting Mechanical Instability of a Cylindrical Plate under Axial Flow Conditions

1 INTRODUCTION

The Global Threat Reduction Initiative (GTRI), previously known as the Reduced Enrichment for Research and Test Reactors (RERTR) program, was established in 1978 by the Department of Energy (DoE). One of the primary missions of this program has been to develop a substitute fuel of higher-density, low enriched uranium (LEU), which is not suitable for weapon use [1]. As of August 2009, approximately 48 research reactors have been converted from highly enriched uranium (HEU) to LEU fuel of the 129 that the GTRI has set out to convert by 2018 [2]. Among the remaining reactors awaiting conversion are numerous facilities that currently employ fuels which contain uranium loadings much larger than that currently available in LEU form [3]. Reactors which fall in this category are considered high performance research reactors (HPRRs).

The Convert Branch of the National Nuclear Security Administration (NNSA) GTRI is currently working to develop very-high uranium density fuels for research reactors which currently do not have economically feasible LEU fuel available for their conversion (the HPRRs) [3]. There are five U.S. Reactors that fall under the HPRR category including the Massachusetts Institute of Technology Reactor (MITR), the National Bureau of Standards Reactor (NBSR) at the National Institute of Standards and Technology, the Missouri University Research Reactor (MURR) at the University of Missouri-Columbia, the Advanced Test Reactor (ATR) at the Idaho National Laboratory (INL), and the High Flux Isotope Reactor (HFIR) at Oak Ridge National Laboratory (ORNL).

The development of prototypic research reactor fuel has been centered around two objectives including (1) the continued reactor performance characteristics currently held by each facility while, (2) meeting all reactor specific safety requirements [4]. To meet these objectives two uranium-molybdenum (U-Mo) alloy fuel designs are being investigated, a dispersion design and a monolithic design [5].

The fuel meat in current dispersion fuel elements consists of a fuel powder dispersed in a matrix material [4]. The uranium loading of this fuel type is limited by the amount of material that can be packed into the fuel meat region and by the uranium density of the fuel phase. Research reactor fuel comprised of uranium-silicide (U_3Si_2) in an aluminum matrix has been licensed by the Nuclear Regulatory Commission (NRC) at a uranium loading of 4.8 gU/cm^3, providing the highest uranium density currently available for research reactor applications [4]. Attempts to raise the fuel loading of dispersion fuel have focused on increasing the fraction of fuel phase in the fuel meat region and on changing the fuel phase to an alloy which contains a higher uranium density [4]. Increased loadings for U_3Si_2 have resulted in experimentally demonstrated loadings of 6 gU/cm^3. Using a U-Mo alloy powder in a high-volume fraction dispersion fuel plate has yielded uranium loadings of up to 8.5 gU/cm^3, both of which are still too low to produce fission rate densities sufficient to meet the fuel development program's reactor performance objective. However, the monolithic fuel form has been identified as a promising very-high density fuel type that is appropriate for research reactor applications producing fuel loading up to 15.3 gU/cm^3 [4]. This fuel design consists of a monolithic U-Mo alloy foil as shown in Figure 1-1.

(a) (b)

Figure 1-1: Comparison of dispersion and monolithic fuel types
(a) dispersion cross sectional view and (b) monolithic cross sectional view

The five U.S. HPRRs are entirely unique in their designs, from their integral system components to fuel element (Figure 1-2) and plate geometry. Figure 1-3 presents a generalized representation of each unique fuel plate geometry type found in the U.S. HPRRs. Each of these geometric forms presents its own unique set of challenges from fuel fabrication processes, to safety analyses, and operations. Although the GTRI program and its goals address all five U.S. HPRRs, this study will use the ATR as a reference case, as its fuel plate geometry is that of a cylindrical plate.

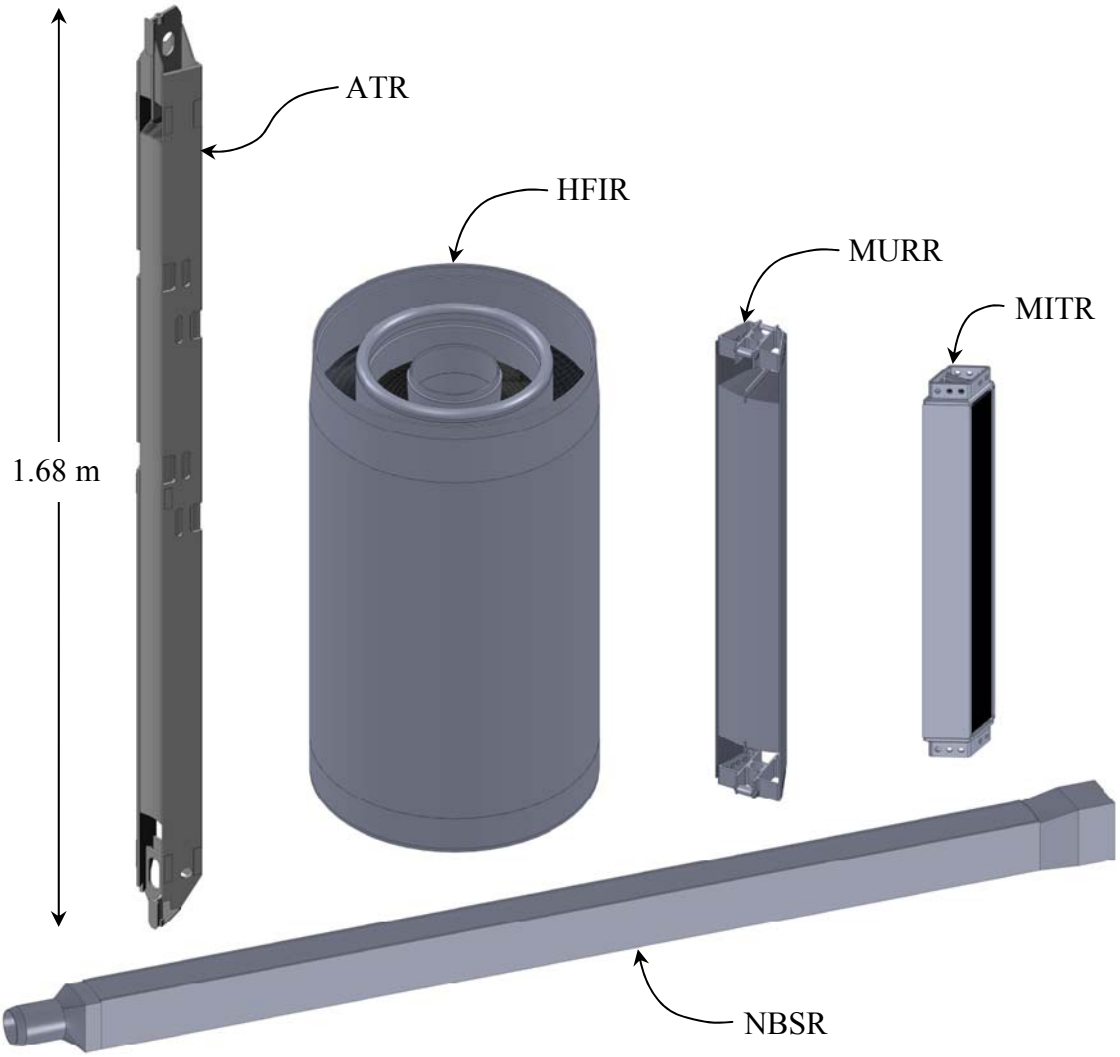

Figure 1-2: Comparison the five U.S. HPRR elements

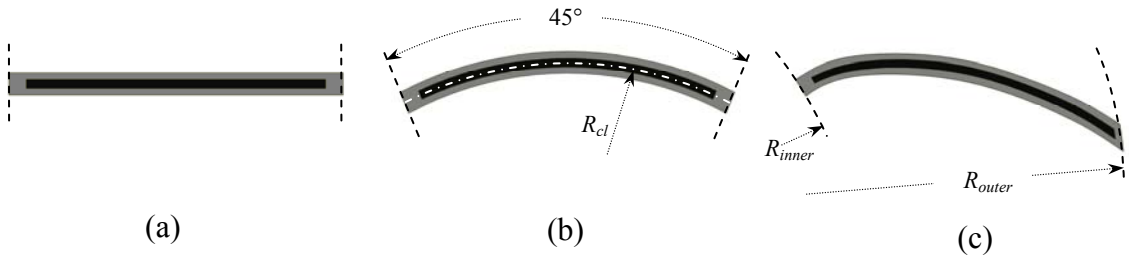

Figure 1-3: Cross sectional view of U.S. HPRR fuel plate geometry types
(a) MITR, (b) ATR, MURR, NBSR, (c) HFIR

1.1 Motivation

Significant progress has been made recently regarding the micro-structural performance of very-high density U-Mo alloy fuel [6-14]. However, additional study of the macroscopic behavior of these elements must be examined before the fuel can be fully implemented [15]. One critical area of study is the behavior of reactor specific fuel elements under prototypic thermal hydraulic conditions [15, 16]. The prototypic conditions under discussion include all current operational safety limit bounds of the HPRRs. The critical areas of focus associated with fuel-specific mechanical integrity under thermal hydraulic conditions based on the methods used to qualify the HEU fuel currently employed in the ATR include:

- Pressure deflection tests [17]:
  - Static single plate testing to confirm the effect of membrane forces on the laminate fuel plate.
  - Static fuel element side plate spring rate[i] testing to evaluate membrane force of the side plates.
  - Static full element tests to confirm analytical procedures as well as to evaluate mechanical performance.
  - Dynamic hydraulic pressure deflection testing to evaluate hydraulic weakening.

- Thermal distortion tests [18]:
  - Single plate testing to examine the extent of thermally induced fuel plate rippling and plastic deformation.
  - Fuel element testing to identity mechanical stability of fuel element under thermal loading.
- Hydraulic buckling tests [17, 19]:
  - Hydraulic buckling testing to incrementally measure fuel plate and element plastic deformation caused by extreme axial pressure gradients.

[i] Spring rate: Force required to compress a linear spring (side plate in this instance) one inch.

  - Channel blockage testing to create temporal artificial channel blockages causing extreme axial pressure drops.
  - Vibration and fatigue testing in order to identify key harmonics associated with the fuel against provided flow rates.

- Burnout tests [20-22]:
  - Single plate tests under iso-thermal and iso-flux conditions to determine a characteristic critical heat flux correlation.

- Heat transfer tests [23]:
  - Single subchannel tests under iso-thermal and iso-flux conditions to determine a characteristic heat transfer coefficient correlation.
  - Single plate tests under iso-thermal and iso-flux conditions at various gage pressures and aluminum alloys to determine oxide layer growth rate correlations.

- Flow instability studies [24-28]:
  - Lumped parameter subchannel studies to determine onset of flow instability during steady state mixed convection and accident scenario conditions.

Although these critical areas of focus rigorously characterize the macroscopic behavior of fuel plates and elements under thermal, hydraulic, static, and dynamic loads, previous fuel qualification studies have not directly addressed fuel surface roughness effects on the hydro- and thermo-mechanical integrity of the fuel elements. Surface roughness variability was eliminated from previous HPRR fuel qualification programs by strict fuel fabrication criteria and acceptance requirements set forth by the facilities' quality assurance programs (QAPs) [21].

As a requirement of the ATR's QAP, all elements received from the fuel fabricator must pass receipt inspection to verify critical tolerances (including surface roughness

specifications) prior to insertion into the core. However, post-cycle visual examination of numerous elements has revealed several cases outside these tolerances although no abnormal observations were made during the cycle operation. On a few occasions, failure has occurred. A statement from the ATR Upgraded Final Safety Analysis Report (UFSAR), acknowledges this claim [20] pp. 4-30:

> *"A limited number of fuel plate failures (i.e., breach of the fuel plate cladding leading to fission product release) have been encountered over the years of operation, and the failure trends in recent years have been favorable. . ."* continuing, *"From reactor start-up in December 1969 through November 1974, a total of 55 fuel elements exhibited evidence of cladding failures as determined by post-cycle visual examination. Most of the defects were described as 'pimples,' which occurred in areas of thin cladding, and were caused by breaches of the cladding, allowing stagnant water to become entrapped next to the fuel. The cause of the breaches may have been micro-cracks in the thin cladding."* Furthermore; *"Five confirmed leaky fuel elements have been destructively examined to determine the cause of the failures. In each case, the leaks were believed to have been caused by pinhole failures, which resulted from pitting corrosion."*

Although the above statement postulates one likely cause of these fuel element failures, there is no definitive evidence that shows *pitting corrosion* was the only direct parent phenomenon producing *pinhole failures*, or micro-cracks, in the fuel element cladding. There are numerous mechanisms which are plausible for the ignition of a single micro-crack, including cyclic material fatigue. One of these plausible mechanisms is that of flow induced vibration (FIV) [29]. FIV has not explicitly been determined an irrelevant issue in previous analyses regarding the ATR fuel element, although it has been shown through demonstration in both experimental studies that an ATR element is mechanically stable under hydraulic loads which significantly exceed that observed during normal operations [20].

FIV is caused by fluid instability due to the reaction of a rigid body against a hydraulic load and can occur over a wide spectrum of frequencies depending on geometric and hydraulic conditions of a prescribed system. Therefore, if FIV spurs the birth and propagation of a single micro-crack on a fuel plate, the crack growth rate and lifecycle becomes highly nonlinearly (stiffly) coupled with the plate vibration onset by the fluid flow. Coupling this phenomenon to other phenomenon typical of aluminum clad fuel plates including fuel clad oxidization and pitting corrosion makes identification of a single mechanism of failure nearly impossible to determine for fuel clad breach.

Much investigation has been directed toward pitting corrosion and clad oxidization, while little attention has been given to FIV. This phenomenon has been regarded as inherently insignificant due to the structural design (cylindrical plate) of the (ATR) element assuming the most likely cause of failure is plastic deflection of the fuel plates caused by the coolant at a critical flow velocity [29]. Previous studies of flat plate fuel elements have shown that FIV can occur at flow velocities approximately half that of the critical flow velocity prediction [30], thus producing unexplored regions in fuel element structural stability which may be of importance to the safety of these high performance reactors.

1.2 Objectives

The objective of the work presented in this document is to create a semi-numerical model to assess FIV of cylindrical plates. The purpose of this study is to further the understanding of FIV of shells (cylindrical plates) in fluid media and assess how hydraulic loads created by the flow field relate to the mechanical stability of plate type fuel elements when compared to currently used static equilibrium models for the prediction of mechanical instability. This work is performed in the following four steps:

1. Compare plastic plate deformation prediction methods of cylindrical plate type geometry (of ATR element geometry) using current safety analysis methods.

2. Develop a three dimensional FIV model for axial flow over a cylindrical plate based on ATR type fuel element geometry.

3. Employ the developed vibration model and compare the criticality of plastic plate deflection safety criteria used in current safety analyses to the fatigue of a cylindrical fuel plate over a fuel element life cycle. This fatigue information will be explicitly calculated using the natural frequencies (eigenvalues) and modal shapes (eigenfunctions) produced from the FIV model.

4. Assess the pressure fields which are most likely to cause FIV in geometry representative of an ATR element and provide a relation between plate dimensional characteristics and the onset of mechanical instability for range of pressure values along the axial and radial direction of the plate.

1.3 Document Overview

This document is organized as follows:

Chapter 1: **Introduction –** Introduction to the topic and motivation for the work presented on behalf of the study under discussion.

Chapter 2: **Survey of Literature –** Background information, a survey of available literature on plate vibration models and flow fields that onset mechanical instability.

Chapter 3: **Advanced Test Reactor Overview –** High level overview of the ATR and its relation to the significance of predicting mechanical instability of cylindrical plates under axial flow conditions.

Chapter 4: **Analysis of Static Plate Divergence –** Overview of Miller's method for prediction of critical velocity, extending his methods to additional boundary condition cases, and lastly comparing Miller's critical velocity

against that developed by Smith for various geometries and boundary conditions.

Chapter 5: **Model and Methodology –** Comprehensive description of plate dynamic module, flow module, and methods used to couple these models to produce a FIV model for axial flow over a cylindrical plate.

Chapter 6: **Results and Discussion –** Presentation of system model results and discussion of the phenomena that are captured as a part of this study's work which have been neglected in previous studies by direct comparison.

Chapter 7: **Conclusions –** Concluding remarks and observations relative to this dissertation work and of future work areas to improve the simulation tool and extend its applicability to other reactor fuel element geometry types.

This document concludes with lists of referenced works, nomenclature and symbols, and appendices with additional details not contained within the chapters.

2 SURVEY OF LITERATURE

Stability of plates under axial flow conditions has been examined by many investigators under both hydro-elastic[ii] and -plastic[iii] conditions [30]. Plate stability has been recognized as an issue of significant importance since the earliest research reactor designs; it was qualitatively postulated that there was a direct relation between flow and fuel plate vibration as pertaining to reactor element geometry during the design process of the High Flux Reactor (HFR) [31].

2.1 Flow Induced Vibration of Flat Plate-Type Geometry

Flat plate-type geometry has been studied more than any other geometric form regarding its susceptibility to failure caused by hydraulic instability [29]. This geometry has been the focus of research due to its relatively weak structural capabilities with respect to other geometric shapes including that of a cylindrical plate or pipe.

One of the first formally published reports regarding FIV and its pertinence to the research reactor discipline was produced in 1948 by Stromquist and Sisman [31]. The purpose of their study was to determine whether the frequency of the fuel plate vibrations would be of significant importance to the mechanical strength of a fuel assembly or the operating characteristics of the reactor. At the conclusion of the study Stromquist and Sisman determined that (1) the examined fuel assembly was able to withstand all vibrational stresses as well as fatigue requirements within the experimental ranges considered and (2) the buckling[iv] of plates occurred under very unusual conditions (e.g. improper plate spacing, insufficient restraint of plate ends, and brazing defects). It is noteworthy that the experimental investigation fell short in extending its flow rates to produce sufficient hydraulic forces necessary to buckle the plates using a simple static force balance.

[ii] Hydro-elastic: Elastic deformation of a component caused by hydraulic loading.
[iii] Hydro-plastic: Plastic deformation of a component caused by hydraulic loading.
[iv] Buckling: Bending of a sheet, plate, or column supporting a compressive load.

In 1958, during the fuel element design, development, and construction for integration into the Engineering Test Reactor (ETR), Ronald Doan qualitatively discussed a critical flow field associated with the onset of plastic plate deflection [32]. His hypothesis was soon followed by Daniel Miller who developed a method for the prediction of a critical flow velocity[v] (V_{cr}) by equating the pressure differences between coolant channels to the elastic restoring force of a single fuel plate [33]. This force balance theory is more commonly referred to as 'neutral equilibrium'. In order to acquire this hydraulic force Miller related the change in local pressure in a flow channel resulting from a slight perturbation in the flow channel's wall. Considering a plate centered around two adjacent flow channels, the net pressure applied to the plate for a small differential change in cross sectional flow area is

$$P = \frac{\rho}{2}\left[\left(\frac{U}{1-\frac{\Delta S}{S}}\right)^2 - \left(\frac{U}{1+\frac{\Delta S}{S}}\right)^2\right] \tag{2-1}$$

where S is the flow channel original cross sectional area and ΔS is the change in cross sectional area. For small changes in cross sectional area, that is for $\Delta S/S < 0.2$, (2-1) may be linearized to

$$P = 2\rho U^2 \frac{\Delta S}{S} \tag{2-2}$$

The relation (2-2) was employed by Miller to predict the critical velocity required to induced plate deformation. As the change in area approaches zero, Equation (2-3) is Miller's model representing a flat plate with fixed (clamped) edges under axial flow conditions,

$$V_{cr} = \left[\frac{15Ea^3h}{\rho b^4\left(1-\upsilon^2\right)}\right]^{\frac{1}{2}} \tag{2-3}$$

where E and υ are the plate averaged modulus of elasticity and Poisson's ratio; ρ is the fluid density; a and b are the plate thickness and width; and lastly h is the subchannel height.

Miller's model is based on the following assumptions [33]:

---

[v] Critical velocity: Flow velocity past a rigid body producing enough hydraulic load to buckle the body.

- The plate is homogeneous, isotropic, elastic, and initially flat or uniformly curved, uniform in spacing and dimensions are free of unidentified sources of deformation.
- The coolant is incompressible, all channels have the same mass flow, at any cross section normal to the longitudinal axis the flow within any channel is uniform, and leakage between channels is suppressed.
- The plates are broad enough (in comparison with their thickness) so that shear deformation is negligible, and are long enough (in comparison with their breadth) so that they can deflect locally without significant redistribution of flow among the coolant channels.
- The side plates or supports are rigid.

These assumptions, although quite limiting on the physics of the system, were novel for the time period. Davis and Kim experimentally verified that Miller's model predicts a critical velocity of approximately twice that required to plastically deform ETR type fuel plates [34]. However, there were several limitations to Miller's model. By assuming the plate takes the form of a wide beam (using wide beam theory), the model neglects to consider any local effects occurring in the vicinity of the upstream and or downstream edges of the plate. At the upstream and downstream edges, the plate is no longer, in effect, a wide beam, and the deflection at these edges will be greater than that calculated in the analysis.

Within the same year of Miller's hypothesis, Zabriskie [35, 36] experimentally evaluated both critical flow values and length-to-width geometry effects of the onset of plastic deformation. His experimental studies concluded that (1) Miller's model gave a good approximation for that flow rate which induces a plate to undergo large deflections; (2) the plates do not suddenly collapse at Miller's predicted velocity but rather deflect at lower velocities while the amount of deflection increases as the flow increases until very large deflections occur in the vicinity of Miller's predicted flow rate; and (3) the inlet region of the plates is the most susceptible plate region flow induced deflections occur, primarily because this section of the plate is less rigid than sections further downstream.

Johansson [37] improved Miller's work in 1960 and was able to produce a flat plate model which included the effects of fluid friction and flow redistribution within the flow channel, the second term of (2-4). However, Johansson too had several assumptions that limited the physics found in his model:

- The pressure drop through all channels is equal.
- The static pressure distribution across the span of a plate is uniform at each axial location.
- Small deflection elastic theory holds for the plates (membrane stresses are negligible).
- The water is incompressible and no voids or bubbles exist.

Incorporating the above assumptions and using clamped edge boundary conditions Johansson produced the following relation:

$$V_{cr} = \left[\frac{15Ea^3h}{\rho b^4\left(1-\upsilon^2\right)}\right]^{\frac{1}{2}}\left\{\left(1+\Phi\right)\left[1+\frac{3}{8}\frac{\varpi\ell_2}{2h}-\frac{3\ell_2}{4l\left(1+G\right)}\left(1+k_i+\frac{\varpi\ell_1+\frac{\varpi\ell_2}{2}}{2h}\right)\right]^{-\frac{1}{2}}\right\} \tag{2-4}$$

where

$$G = \frac{\left(\frac{\varpi l}{2h}\right)}{k_i + k_e} \tag{2-5}$$

and ϖ is the friction factor, k_i and k_e are the inlet and exit channel form major loss coefficients, l is the effective plate length, Φ is a corrective parameter for axial bending stiffness, and ℓ_1 and ℓ_2 are the axial distance from the inlet to the start of the deflected plate region and axial length of deflected plate region. Based on the required inputs for Johansson's correlation (k_i, k_e, ℓ_1, ℓ, and Φ) to predict critical velocity the result is highly subjective based on the flexibility of a user's inputs and therefore it has not been historically adopted for research reactor safety analyses.

In 1962 Rosenberg and Youngdahl [38] formulated a dynamical model and obtained the same critical velocity as Miller's prediction when incorporating a two-dimensional mode. They did this by linearizing the pressure drop expression using only a first order

approximation. The linearization was accomplished by assuming the change in flow channel area after a plate has deflected is much smaller than that of the total unperturbed flow channel area. This model assumes plate divergence (buckling of the first mode) in both the span-wise and axial direction.

Then in 1963, Kane [39] investigated spacing deviations of subchannels for plate type fuel elements based on Miller's model while applying a modified continuity equation such that a spacing deviation in subchannels adjacent to a single plate may create a Bernoulli effect. At the completion of his study Kane determined that (1) for flow rates in excess of Miller's prediction, plate deflections become quite large with small deviations in subchannel geometry, and (2) under certain geometric conditions for lower flow rates deflections occur which may be significant. A similar study by Groninger and Kane [40] was conducted during the same year which focused on flow-induced deflections of individual plates for three parallel plate assemblies. Their model showed that (1) adjacent plates always move in opposite directions at high flow rates, causing alternate opening and closing of the channel, and (2) they detected a violent dynamic instability at approximately 1.9 times that of Miller's collapse velocity (similar to that observed by Davis and Kim [34]).

Earl Dowell [41, 42] conducted one of the first in-depth studies on dynamic instabilities of rectangular plates in 1967 pertaining to flutter[vi] under axial flow conditions. Air was used as the fluid medium flowing over a flat panel in his study. Dowell focused his attention on three types of plate oscillations: A coupled-mode oscillation[vii], single-mode oscillation[viii], and single mode-zero frequency oscillation (buckling). He investigated each physical type of hydro-mechanical instability and its relevance to the Mach (M) number of the medium surrounding the plate. A few of the most significant conclusions drawn from Dowell's study include (1) the coupled-mode oscillations occur at $M >> 1$, single-mode oscillations occur at $M \approx 1$, and single mode-zero frequency oscillations

[vi] Flutter: The oscillatory loss of stability of a panel in the form of a flat plate or shallow shell

[vii] Coupled-mode oscillation: Multiple modes of flutter constructively and destructively interacting in one lineal direction

[viii] Single-mode oscillation: Single mode of flutter observed in one lineal direction.

occur at $M<1$, and (2) that the analysis of the nonlinear oscillations of a fluttering plate using the full linearized aerodynamic theory can be carried through in essentially the same manner as when quasi-steady (neutral equilibrium) aerodynamics are employed.

Expanding on all prior studies, Scavuzzo [43] and Wambsganss [44] made further improvements to Miller's model by considering the nonlinearity caused by large deflections. They did this by retaining the second-order bending terms for a wide beam in an attempt to assess their influence on stability. The second-order terms generate an additional stability criterion in the form of an upper bound on the amplitude of quasi-static deflections for stable oscillations. Wambsganss [44] derived a new expression for critical velocity as presented below:

$$V_{cr}=\left[\frac{15Ea^3h}{\rho b^4\left(1-\upsilon^2\right)}\right]^{\frac{1}{2}}\left\{\left[1+\left(\frac{\delta_{CR}}{\theta h}\right)^2\right]\left(\frac{15}{\phi}\right)\right\}^{-\frac{1}{2}} \tag{2-6}$$

where θ and ϕ are mode dependent constants, and δ_{CR} is the critical plate deflection. Similar to Johansson's correlation, the first term of (2-6) is the same as Miller's model, while the additional parameters presented in the second term capture the second order accurate physics of the model. However, due to the inherent boundedness of the second order model, numerous boundary conditions are required which are application specific and subjective. Wambsganss presents one of these terms as the design constant (δ_{CR}/h) which allows a user to artificially determine a critical deflection of the plates within the model prior to determining a required critical velocity. Similarly, θ and ϕ are defined as mode dependent constants in Wambsganss' model and were determined by using first order approximations to the bending stiffness of the plate under various boundary conditions. Due to the complex methodology used to develop the model along with the number of subjective model 'tuning' parameters, the use of Wambsganss' model was never widely employed in application.

Following previous work which had primarily focused on static deformation or 'neutral equilibrium' theory, Smissaert [45, 46] performed analytical and experimental investigations on a Materials Test Reactor (MTR) type flat plate fuel element. The

experimental results [45] showed that (1) for low velocities the plates deform as a result of static pressure differences in the channels between these plates, and (2) at high fluid velocities a high amplitude flutter vibration is observed. This flutter does not appear below a minimum average water velocity referred to as the flutter velocity, which is approximately equal to two times the Miller velocity (or 1.9 times that of the Miller velocity as determined by Groninger and Kane [40]). In the analytical study, Smissaert [46] indicated that a plate assembly is characterized by two velocities; Miller's velocity and a flutter velocity. His explanation of the dynamic instability (flutter) was that the excitation frequency of the fully-developed turbulent flow approaches the in-fluid natural frequency (NF) of the plate. Under this condition the resonance amplitude of the plate vibration becomes large.

In 1968 a National Aeronautics and Space Administration (NASA) study led by Roger Smith [47] expanded on Miller's model once again. Smith did this by incorporating neutral equilibrium theory into a semi-empirical correlation for flat plate-type geometry. His correlation was presented in a representation of critical dynamic pressure (P_{cr});

$$P_{cr} = \left(\frac{15E}{1-\upsilon^2}\right)\left(\frac{a^3 h}{b^4}\right)\left[\left(1+\frac{4\pi\upsilon l h}{b^2}\right)\left(1+\frac{4\upsilon l^2}{3b^2}\right)\right]^{-1}. \tag{2-7}$$

Recalling (2-2), (2-7) may be reformulated into a critical velocity. This is done such that the limit of the change in cross sectional area goes to zero in order to determine the onset of instability itself. Smith's correlation may be reformulated in terms of critical velocity by inserting (2-7) into (2-2) for comparison against Miller's model.

$$V_{cr} = \left[\frac{15Ea^3 h}{\rho b^4\left(1-\upsilon^2\right)}\right]^{\frac{1}{2}}\left[\frac{1}{2}\left(1+\frac{4\pi\upsilon l h}{b^2}\right)\left(1+\frac{4\upsilon l^2}{3b^2}\right)\right]^{-\frac{1}{2}} \tag{2-8}$$

Notice that the first term in (2-8) is the same as Miller's model, while the second term is added to incorporate dynamic pressure drop variations along the axial length of the plate. Smith's correlation accounts for the effect of fluid redistribution as well as some form loss effect at the inlet of the subchannel due to a sudden contraction in cross sectional flow area. Although Smith's correlation incorporates more physics than Miller's model, it has not been employed in application due to the similar critical velocity value that it

produces relative to Miller's predicted velocity, while Miller's model had already been used widely in industry for more than ten years prior to the release of Smith's correlation.

Weaver and Unny [48] studied the dynamic behavior of a single flat plate, one side of which was exposed to high flow rates of a heavy fluid. They examined the variation of natural frequencies according to the rate of flow. They concluded that for a given mass relationship, the neutral zone of stability is followed by a zone of static instability. After this stage the plate quickly returns to neutral stability, which continues until the occurrence of dynamic stability (occurring at approximately twice that of Miller's critical velocity).

Leissa [49] conducted a lengthy theoretical study on free vibration[ix] of rectangular plates, and acquired a relative error for the general frequency parameter (λ_m) used when conducting dynamic analyses through implementation of the classic plate equations. Leissa presented the value of λ_m and its corresponding error using his method for all twenty six potential boundary condition combinations (simply supported, clamped, and free edges) for a four sided plate given an option of five different plate aspect ratios and one Poisson's ratio value ($\upsilon = 0.3$). The work presented in Leissa's paper is often used to assess the accuracy and credibility of eigenvalue solutions produced when a part of mechanical instability studies as applied to wide beams and plates.

Kornecki et al. [50] considered a flat panel of infinite width and finite length embedded in an infinite rigid plane with uniform compressible potential flow over its upper surface. The studied plate was constrained (considering both clamped and simply supported cases) along their leading and trailing edges. The case of a panel clamped at its leading edge and free at its trailing edge was investigated both theoretically and experimentally. The obtained results demonstrated that a panel fixed at its leading and trailing edges loses its stability by divergence (static instability), while the cantilevered panel loses its stability by flutter (dynamic instability).

[ix] Free vibration: Dynamic response of a rigid body subject to no externally applied load.

In 1977 Holmes [51] took Leissa's [49] work one step further and conducted a stability analysis on a fluttering panel caused by flow, focusing his work on bifurcations[x] to divergence and flutter in flow induced oscillations. Holmes used Galerkin's method and modal truncation, in the form of an ordinary differential equation to recast the nonlinear terms of a fluid loaded panel under motion. Holmes concluded his study by acknowledging that however rigorous his derivation to analyze bifurcation of a simple panel was, it left many unanswered questions, and was unable to completely identify all regions of stability.

In the 1980s when computational resources became more readily available, much work shifted from theoretical modeling of plate vibration into the application of finite element models, and the advancement of finite element analysis (FEA) using both low and high resolution schemes [52-55].

In 1991 Davis and Kim [34] developed a single plate semi-numerical model with unequal subchannel coolant velocities perturbing the stability of the plate. They looked at both simply supported and clamped edges in order to compare the relative difference in stability of the plate under different boundary conditions. Their results were different from that produced in previous dynamic stability studies. Davis and Kim found that the flutter velocity was approximately 2.5 times larger than that of Miller's velocity for a simply supported plate and 2.2 times larger for a clamped plate. It was acknowledged in their model that by including only a single plate, there was a possibility of reducing the damping factor of the system and therefore inducing instability at lower velocities than may physically occur.

In 1993 Guo et al. [56] developed a dynamic semi-numerical model for flat parallel plate assemblies. Their limiting assumption was that regardless of the deformation a plate takes, all subchannels have uniform spacing. Employing this multi-plate model, Guo et

[x] Bifurcation: To divide into two parts, or branch.

al. produced predicted flutter velocities that were significantly larger than that of Davis and Kim [34]. They attributed their large difference to the additional damping caused by surrounding plates.

Then in 1995, Kim and Davis [30] published a second semi-numerical study which was very thorough in its derivation of the model and results presented. In this study, Kim and Davis considered five separate cases: a one, two, three, four, and five plate model. Their primary objective was to answer the question raised by Guo et al. [56] in a previous study as to the affect of damping due to the addition of plates in a dynamic model. At the conclusion of their study, when comparing the calculated plate NF versus plate stiffness for all five cases, they found that the NF was reduced significantly with the addition of a single plate (two plate model), while results don't start to asymptotically collapse until the addition of the fifth plate. Therefore, it was concluded necessary to incorporate five plates in a dynamic flat plate model in order to identify the NF of an individual plate.

These early studies spurred a number of other investigations which focused on hydrodynamic instabilities associated with flat plate type solid-fluid interfaces [57] while many other studies focused on modeling plate mechanics using free vibration analysis [58-60], a transformation method (also known as spectral characterization) [61-63], and perturbation theory [64-67]. In 1997 Yang and Zhang [68] developed a multi-span elastic beam model to imitate a typical substructure of a parallel-plate structure. In their analytical model, there exists a narrow channel between the lower surface of a wide beam and the upper surface of the bottom plate of a water trough. By using the added water mass and damping coefficients, the free vibrational frequencies of the system were analyzed. Yang and Zhang [69] further investigated a parallel flat plate-type structure in a rigid water trough and rigid rectangular tube to expand their comprehensive formulation.

Guo and Paidoussis [70] theoretically studied the stability of rectangular plates with free side-edges in inviscid channel flow. They treated the plate as one dimensional and the channel flow as two-dimensional. The Galerkin method was utilized to solve the plate equation, while the Fourier transform technique was employed to obtain the perturbation

pressure from the potential flow equations. They investigated seven combination of classical supports at the leading and trailing edges of the plates. They concluded that divergence and coupled mode flutter may occur for plates with any type of end supports, while single mode flutter only arises for non-symmetrically supported plates.

More recently, Guo and Paidoussis [71] developed a more accurate and general theoretical analysis for parallel-plate assembly system. In their analysis, the plates were treated to be two-dimensional, with a finite length, and the flow field was taken to be inviscid. Advanced Strength and Applied Elasticity [72] presents the equation of motion of an elastic plate using *Classic Plate Theory*[xi]

$$m\frac{\partial^2 W}{\partial t^2}+\mathcal{L}[W]+P=0 \qquad (2\text{-}9)$$

$W(x,y,z,t)$ is the lateral displacement; x, y, z are the spatial coordinates; $P(x,y,z,t)$ is the pressure on the exposed surface; and t is time. $m(x,y,z,t)$ is the mass per unit area, and $\mathcal{L}$ is the linear operator representing the load-deflection relationship of the panel. In Guo and Paidoussis' study of flow over a flat plate, $\mathcal{L}[W]$ is

$$\mathcal{L}[W]=K\left(\frac{\partial^4 W}{\partial x^4}+2\frac{\partial^4 W}{\partial x^2\partial y^2}+\frac{\partial^4 W}{\partial y^4}\right), \qquad (2\text{-}10)$$

and

$$K=\frac{Ea^3}{12(1-\upsilon)}, \qquad (2\text{-}11)$$

where K is the flexural rigidity.

Employing (2-9) with its corresponding plate type geometry conditions, Guo and Paidoussis drew several important conclusions: (1) single-mode divergence, mostly in the first mode and coupled-mode flutter involving adjacent modes were found; (2) the frequencies at a given flow velocity and the critical velocities increase as the aspect ratio decreases; (3) in the case of large aspect ratios and small channel-height-to-plate-width ratios, the plates lose stability by first-mode divergence, however, very short plates

[xi] The development and a supplement explanation of the classical plate equation can be found in Appendix A.

usually lose stability by coupled-model flutter in the first and second modes; (4) critical velocities for both divergence and flutter are insensitive to changes in damping coefficients [72].

Within the past decade a number of studies have been conducted, both experimentally and theoretically including that of Ho et al. [73] who experimentally examined two parallel plates and investigated the relevance of including combs (plate spacers) between the fuel plates to reduce the dynamic instability and increase the critical velocity. They concluded that although the combs produced a larger required critical velocity, the resultant redistribution of flow between subchannel must be considered before application in high flux reactors.

Recently a study was conducted by Shufrin et al. [74] with the focus on a semi-analytical approach for the prediction of plate instability. This approach was termed as the multi-term extended Kantorovich method (MTEKM). The Kantorovich reduction method has been paramount to the development of newly modified and extended techniques for the study of plate instability due to its ability in reducing nonlinear differential equations in a single dimensional direction such that all other directions may be solved for.

Further development of FIV models applied to flat plate type geometry have since been expanded upon, however, because of the general foundation for which Gui and Paidoussis' model was based around, none have produced such significant conclusions [71].

There are a number of commonly referred book references regarding FIV to be of help including Blevins [75] which includes a thorough set of beam integrals and frequency parameters; Yu [76] containing a wide variety of methods for evaluating both static and dynamic elastic deflection of plates; Qatu [77] evaluates techniques unique to laminated plates, starting with basics and expanding on some of the most advanced theoretical methods currently available. Blevins, Naudascher, and Kaneko [78-80] wrote several books which provide unique perspective on the issue of FIV from the perspective of a

lifelong career in the field, each book gives both simple back-of-the-envelope methods for solving rigid and free body vibrating system as well as complex approaches which address issues in the area of FIV that have not been resolved yet.

2.2 Flow Induced Vibration of Curved Plate-Type Geometry

Although hydro-elastic instability pertaining to flat plate-type geometry has been a more popular subject of study within the field of hydro-mechanical instability, cylindrical plate-type geometry is no less significant of an issue. Numerous high flux reactors around the world currently employ cylindrical plate-type geometry including three of the five U.S. HPRRs (ATR, MURR, and NBSR).

In the same study which produced a model for critical velocity prediction using flat plate geometry, Daniel Miller [33] similarly developed a model for a cylindrical plate geometry using 'neutral equilibrium' theory. Miller achieved his formulation by simply transforming the flat plate geometry into an approximated cylindrical coordinate system. Miller's critical velocity prediction for cylindrical plate-type geometry is

$$V_{cr} = \left[\frac{2Ea^3 h\beta \sin^5(\theta/2)}{3\rho b^4 (1-\upsilon^2)\left(\frac{1}{6} - \frac{\sin(\theta)}{4\theta} + \frac{\cos(\theta)}{12}\right)} \right]^{\frac{1}{2}} \tag{2-12}$$

where

$$\beta = \left(\frac{1}{2\sin^2(\theta/2)}\right)\left(\frac{\theta}{4} + \frac{\sin(\theta)}{4}\right)\left(\frac{\tilde{A}R_{cl}^2}{I}\right)\left(1 - \frac{1}{\theta} + \frac{I}{\tilde{A}R_{cl}^2}\right), \tag{2-13}$$

and R_{cl}, $\tilde{A}$, θ, and I are the mean radius of plate curvature, plate cross sectional area per unit width, curved-plate arc between two supports, and area moment of inertia of plate.

Soon after Miller's work, in 1959 Lyell Sanders [81] conducted a study at the NASA. His study led to a newly developed set of differential equations for mapping surface moments and resultants in shells. The differential equations produced as a result of his study are commonly referred to as the 'simple set' of differential equations for plate dynamics.

In 1963 Ferris and Moyers [82] conducted a rigorous experimental investigation pertaining to ATR type fuel elements and their subsequent cylindrical shape. The objective of their study was to identify flaws in the various fuel element designs based on extreme hydraulic loads. The experimental investigation included six alternative ATR element designs which incorporated subtle variations in subchannel width, plate thickness, side plates, and end fittings. Steady state hydraulic tests of each fuel element were conducted at a system pressure of 600 psig while the coolant temperature and flow rate was varied between 150 – 420 °F and 40 – 1100 gpm. At the conclusion of their study they found that (1) four of the six element designs tested plastically buckled and completely collapsed the flow channel; (2) of the two designs that did not show signs of extreme buckling, one had a fuel plate deflection of approximately 0.058 inches relative to its centerline which is a 74.3% reduction in flow channel spacing; lastly they acknowledged that (3) under realistic mass flux ranges that the elements would be exposed to under operational conditions one element design had less than a 0.012 inch lateral plastic deflection in a single fuel plate, which was assumed to be within fuel element design limits.

Ferris and Jahren [17] conducted a second study in the same year considering static buckling and deflection criteria of individual cylindrical type fuel plates along with fabricated elements as well. They compared experimental deflection tests against a theoretical model employing static equilibrium and wide beam theory. Their theoretical results compared well to the experimental deflection values under small deflection cases, however, the results diverged when the nonlinear effects became large during the experiment under large deflection situations.

A study was conducted by Sewall et al. [83] in 1964 from NASA pertaining to vibration analysis of ring stiffened cylindrical structures for theoretical applications associated with fuel tanks in space flight. A Rayleigh type vibration analysis was performed and compared against experimental data collected for a similar geometry. The authors found that the experimental data and analytical analysis compared quite well with regard to such a complex system. They accounted this good agreement for the careful handling of

area moment of inertia calculations associated with the geometry of the system that were performed to produce the analytical results. This study paved the road for a number of studies that followed with respect to vibration of curved plate type geometries by providing a set of fundamental tools and reasoning to relate the theory of mechanical plate instability to a physical system.

Sewall [84] then conducted a second study in 1967 pertaining to vibration analysis of curved panels expanding his original study to a more broad set of conditions with the intent of employing these theoretical results as a part of the design process for a new fuel tank applied to space travel. The study employed the Rayleigh-Ritz method from a theoretical perspective for both clamped and simply supported curved panels and compared these results to experimentally obtained data.

Most methods studied to date focused primarily on solving differential equations of motion that hold for shallow plates only [84]. In 1969 a study by Petyt and Deb Nath [85] was conducted to investigate possible methods of solving a set of differential equations which hold for non-shallow-[xii] as well as shallow-plates[xiii]. Several techniques were compared [86] for solving free vibration of a rectangular curved plate. At the conclusion of the report a single method was endorsed by the authors; the Kantorovich reduction method for reducing the differential equations into eight order differential equations and then applying a modified matrix progression (MMP) technique for solving them. The MMP described in the study was a modified version of the matrix progression technique first presented by Tottenham [87]. Petyt and Deb Nath were able to produce eigenvalues for various edge boundary conditions, but did not evaluate the edge boundary conditions which are under discussion in this study. At the conclusion of their study, they found that all instabilities can exponentially collapse upon a ‘frequency parameter’ which is a function of material properties and geometry. The basis for choosing Petyt and Deb Nath’s work as a basis for this study is presented in Chapter 4.

[xii] Non-shallow-plate: A curved plate who’s radius of curvature is of a small enough value such that the area moment of inertia is located outside the plate’s cross section.

[xiii] Shallow-plate: A curved plate who’s radius of curvature is of a large enough such that the area moment of inertia is located inside the plate’s cross section.

Outside of reactor applications, several investigations were conducted in the 1980's pertaining to structural design of bridges under high wind loads, nearly all these studies apply previously developed finite element methods and are very specific in the geometry that they are investigating [52-55].

In the early 1990's the Advanced Neutron Source (ANS) research reactor (similar to the HFIR design) was under development at ORNL. During this period of time, many experimental and theoretical studies were undertaken to support the design of this reactor. These studies focused on both flow and mechanical instability of the plates under static and dynamic conditions. Focus was directed at the fuel element geometry itself to identify weaknesses in its hydraulic loading capabilities. Although this reactor was never constructed, much was learned as a result of the preliminary design studies. In 1990, a newly developed method (similar to that of Miller's neutral equilibrium theory) was established by Swinson and Yahr [88] for calculating plastic deflection of ANS type fuel plates. This method assumes that the primary mechanism for plate deflection is the dynamic pressure onset by the extreme kinetic energy of the coolant. At the conclusion of their study they compared their math model to experimental data collected by Smissaert [45] for flat and cylindrical plates and showed that for small deflection cases their model produced results that were quite accurate. At deflection values which became large enough that the nonlinearity in the classic plate equations is no longer negligible, their model began to diverge from the experimental data.

Then in 1993 Swinson et al. [89] conducted an experimental follow up study on stability of ANS type fuel plates. Their thorough investigation only included flow velocities up to approximately 12 m/s, which is much lower than Miller's critical velocity. The deflections that were observed, however, are not consistent with that produced in similar previous experiments [89]. The following observations are acknowledged in their concluding remarks: (1) It was determined in the experiment that the entrance conditions were sensitive variables in determining the plate's response to flow (it was recommended that the flow be as smooth entering the plates as possible), (2) the experimental results

and analytical models do not correlate on several points, (3) the data did not show a sudden or rapid increase in the entrance deflection as predicted by analytical models, (4) the most critical deflection region of the plate does not always occur at the entrance as predicted by theory, and lastly (5) the maximum deflection of the plate as determined by experiment was bounded by the dynamic pressure being applied as a load to the plate, whereas the collapse theory predicts unbounded deflections.

Sartory [90] supported the study of Swinson et al. [89] by utilizing a structural finite element code. Particular attention was directed toward the effect of an imperfection in the fluid channels. At the conclusion of Sartory's study it was determined that a bifurcation point occurs at a coolant velocity of approximately 45 m/s when varying plate deflection as a function of coolant velocity. This predicted velocity is approximately 1.8 times larger than the operational velocity of the ANS and therefore was concluded to be of little relevance in the ANS safety regime.

The last published hydro-mechanical study conducted on the prototypic ANS and its fuel plates was reported in 1995 by Luttrell [91]. Luttrell continued the work done by Sartory, investigating three particular thermal hydraulic conditions: (1) extremely high flow velocities and (2) under pressure due to a partial flow channel blockage. Luttrell began by assessing Miller's model as it applies to ANS type fuel plates. Table 2-1 lists the results of varying the edge conditions on an ANS fuel plate calculated by Luttrell [91]. Considering the three cases under investigation, Luttrell suggested a new core design of the ANS that included larger subchannels to reduce the flow velocity from approximately 25 m/s to 20 m/s. He concluded that a combination of thermal stresses in the fuel plate along with extreme hydraulic loading have potential to cause fuel plate failure at nominal operating conditions in the ANS.

Table 2-1: Critical velocity from fixity studies

Boundary Conditions	Critical Velocity [m/s]
100% Fixed edges	46.03
50% Simply supported edges	40.56
75% Simply supported edges	36.52
100% Simply supported edges	3.99

The studies described in this chapter have added contributions to the fields of mechanical stability and hydro-elastic instability from both theoretical and experimental perspectives. These studies have touched on all known significant topics with these fields. However, many more questions have been raised as a result of these works as well. A summary of the literature surveyed as a part of this study is outlined in Table 2-2. It includes major authors contributing to the work of mechanical stability of flat- and cylindrical-plates and their specific addition to the field. This studies work will add to the knowledge of: (1) dynamic instability, and (2) static instability as it applies to cylindrical-plate type geometry.

Table 2-2: Summary of literature survey

Author(s) [reference(s)]	Phenomena Investigated							
	Flat Plate Type Geometry				Cylindrical Plate Type Geometry			
	Dynamic Instability (Flutter)	Static Instability (Buckling)	Predicting Critical Velocity	Experimental Work	Dynamic Instability (Flutter)	Static Instability (Buckling)	Predicting Critical Velocity	Experimental Work
Stromquist & Sisman [31]	X	X						
Doan [32]			X				X	
Miller [33]		X	X			X	X	
Zabriskie [35, 36]			X	X				X
Johansson [37]			X					
Rosenberg & Youngdahl [38]	X							
Kane [39]		X						
Groninger & Kane [40]		X	X	X				
Dowell [41, 42]	X							
Scavuzzo [43]		X						
Wambsganss [44]			X					
Smissaert [45, 46]	X	X		X	X	X		X
Smith [47]		X	X					
Weaver & Unny [48]	X							
Leissa [49]	X							
Kornecki et al. [50]	X							
Holmes [51]	X							
Davis & Kim [34]	X							
Guo et al. [56]	X	X						
Kim & Davis [30]	X							
Yang & Zhang [68, 69]	X							
Guo & Paidoussis [70, 71]	X							
Ho et al. [73]	X		X	X				
Sanders [81]					X	X		
Ferris & Moyers [82]					X	X	X	X
Sewall et al. [83, 84]					X			X
Ferris & Jahren [17]						X		
Petyt & Deb Nath [85, 86]					X			
Swinson & Yahr [88]						X	X	
Swinson et al. [89]					X	X		X
Sartory [90]						X	X	
Luttrell [91]					X	X	X	

3 ADVANCED TEST REACTOR OVERVIEW

3.1 Overview

The ATR is an experimental irradiation facility and provides the capability to insert experiments into its core. The ATR, located at Idaho National Laboratory (INL), is a 250 MW_{th} high flux test reactor designed to study the effects of radiation on samples of reactor structural materials, fuels, and poisons. The ATR is the highest licensed thermal power research reactor in the world. Construction of the reactor began in November of 1961 and completed in 1965. Fuel loading commenced in 1967 and core testing was completed in 1969. Full power operation began in August 1969 and the first experiment operating cycle began in December 1969 [20].

3.2 Element Description

The current ATR core contains forty fuel elements arranged in a serpentine pattern to form nine flux trap regions. Each fuel element forms a 45-degree sector of a right circular cylinder and consists of nineteen fuel plates with coolant channels on both sides of each plate. The fuel plates are 1.2573 meters in length with an active fuel length of 1.2192 meters loaded with highly enriched uranium-aluminum matrix (UAl_x) in an aluminum sandwich plate cladding. B_4C is impregnated into specific plates as a burnable poison to minimize radial power peaking and extend the cycle life of the fuel elements. The ATR operates continuously, with the exception of ‘outages’ (fuel change-outs), equipment maintenance, and emergency shutdowns. ATR outages occur approximately every four months, during which time one third of the fuel elements are removed and replaced with fresh elements while the remaining are manipulated within the core to extend their core life as long as possible. A graphical rendering of a typical ATR fuel element is presented in Figure 3-1.

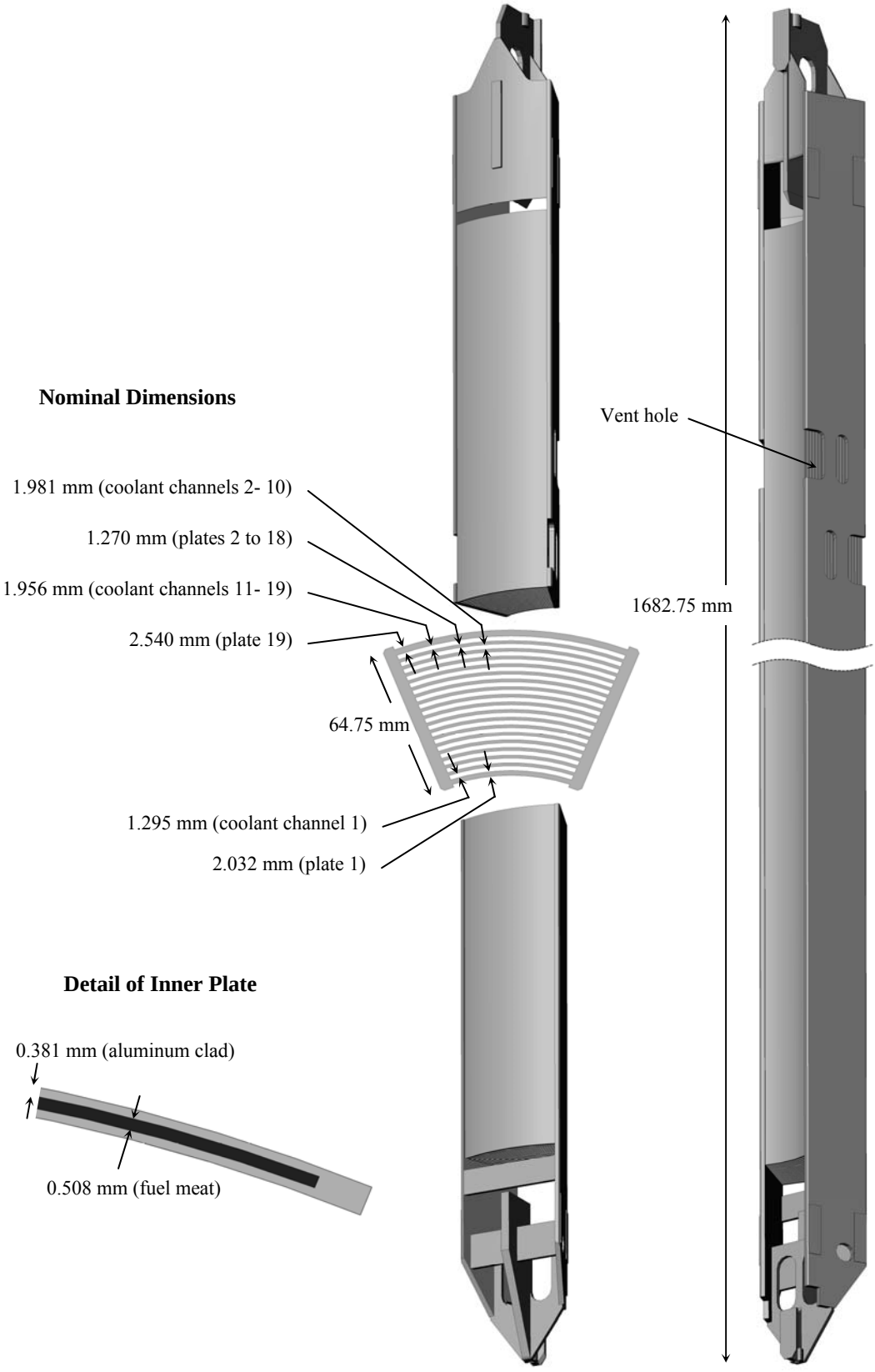

Figure 3-1: Pictorial view of ATR fuel element

Figure 3-1 presents the nominal dimensions associated with plate and element geometry. The inherently compact geometric configuration that this element is based around, along with the relative dimensional size of each plate and subchannel thickness sets up for the possibility of significant percent changes in fabrication dimensions relative to that of the nominal drawing dimensions below due to tolerances. Consider a single ATR interior fuel plate with nominal thickness 1.27 mm; fabrication tolerances allow this plate to have a minimum thickness of 1.219 mm. Now consider an interior subchannel adjacent to this plate. The nominal thickness of this subchannel is 1.981 mm; while the minimum and maximum flow channel dimensions are 1.803 and 2.159 mm, respectively. This combination of dimensional tolerances sets up the possibility for difference of ~18% in subchannel thickness in adjacent channels creating an opportunity for significant flow biasing in one flow channel versus its neighbor which may result in a pressure difference and produce a net pressure acting on the 1.219 mm plate centered around these two subchannels. Although this combination of geometric parameters is extreme relative to that of the nominal plate geometry, it is a valid combination of *stack-up imperfections* as a result of the fabrication drawing tolerances for each element.

3.3 Facility Operations

The ATR has four primary coolant pumps (PCPs) available for use. Three of the four pumps are required for operational use leaving the fourth as an installed spare component. It is left to the reactor operating staff's discretion to employ the required number of pumps needed to adequately remove the heat load of the core, generally operating within a thermal load range which requires two or three pumps at full capacity. The reactor vessel is pressurized with a core inlet of approximately 2.48 MPa gage and a core outlet of approximately 1.79 MPa gage during three PCP operation at a nominal primary coolant system (PCS) operating pressure of 2.56 MPa gage. The same PCS and core inlet pressure are maintained for two PCP operation resulting in a core outlet pressure of approximately 1.95 MPa gage. Nominal core inlet and outlet coolant temperatures are 51.67 °C and 76.67 °C respectively during all operational conditions, sufficiently low to prevent nucleate boiling. A portion of the primary coolant flow is directed through the fuel elements and the remainder through the reactor internals. The

PCS flow rate with three PCPs is nominally 3.1545 m^3/s resulting in a flow rate of 1.7633 m^3/s through the fuel elements or 0.04408 m^3/s per fuel-element with a nominal channel coolant superficial velocity of 14.295 m/s. With two PCPs operating, the PCS flow rate is nominally 2.7442 m^3/s resulting in a flow rate of 1.5344 m^3/s through the fuel elements or 0.03836 m^3/s per fuel-element and a nominal coolant superficial velocity of 12.466 m/s.

The ATR's design incorporates several unique features. The primary coolant system flows downward through the core as opposed to the upward flow found in a typical light water reactor (LWR). The core kinetics are manipulated by control drums at the core periphery which rotate about a central axis vice control rods inserted into the active fuel region. Approximately 60 azimuthal degrees of the control drum contains neutron absorber material while the remaining portion contains the control drum drive components and filler material. By rotating these control drums about their central axis, the reactor operator is able to increase or decrease the solid angle potential of neutron absorber material to fuel element surface area and therefore control the neutron population without impacting the axial flux profile. The serpentine core configuration along with control drum drive system allows for reactor power to be offset in any number of the five core lobes (center, northwest, northeast, southwest, southeast) at any given time. ATR technical specifications limit the power offset across the core to remain less than 80% to 20% power contribution at all times. A cross sectional rendering of the ATR is presented in Figure 3-2.

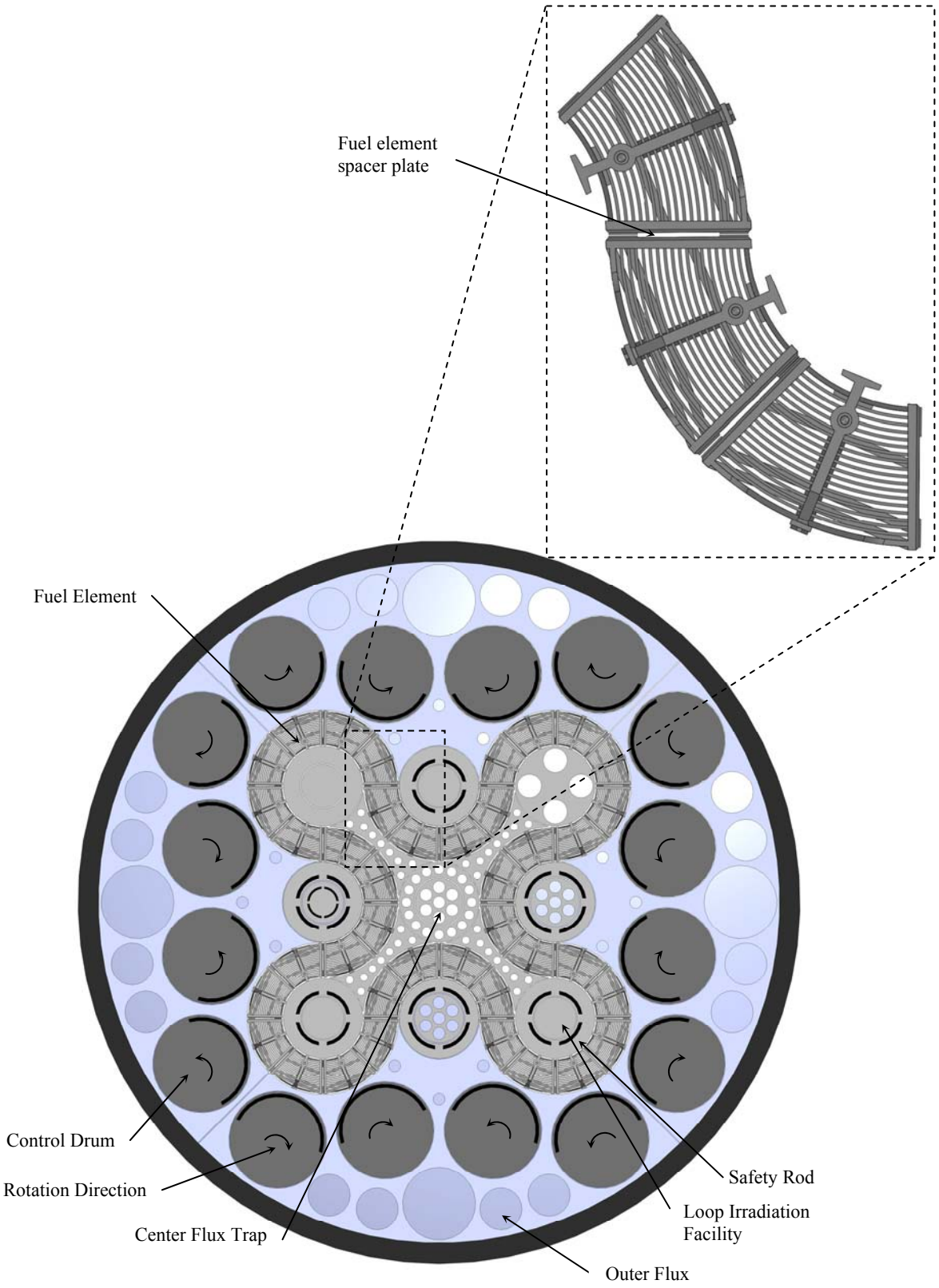

Figure 3-2: Advanced Test Reactor core cross section

3.4 The ATR & Flow Induced Vibration

Based on the wide range of operational core conditions the thermal and hydraulic loads induced on the fuel elements and plates over a fuel cycle may vary significantly, potentially resulting in fuel plate fatigue. A qualitative discussion can be made in order to determine the relevance of FIV associated with the ATR safety analysis. Considering the geometry of the outer most radial fuel plate in an ATR fuel element, a critical flow velocity of 36.167 m/s is calculated using Miller's model [33]. This predicted critical velocity is approximately 2.98 and 2.60 times larger, respectively, than the two and three PCP velocities. However, it has been shown that the use of Miller's relations on ETR fuel plates predicts critical velocities twice as large as they occur experimentally [35]. The ETR's fuel element geometry is similar to that of the ATR (cylindrical fuel plates), therefore, if Miller's model is adjusted to the ATR, the critical velocity ratio drops to 1.49 and 1.30 respectively. Similarly, it has been stated that although plastic deflection of ETR type fuel plates occurs at approximately twice the critical velocity, large plate vibrations have been reported at coolant velocities "much less than the experimental critical velocities" [36].

Several design features incorporated into the ATR element promote sustained flow and reduce the significance of FIV caused by large pressure drops across the length of the element which Miller's model predicts. These features include (1) four vent holes located on each side plate of an element (Figure 3-1) that span across several subchannels allowing for pressure re-equilibrium at these axial locations along the length of the fuel element and (2) fuel element spacer plates which allows for a small percentage of the integral core flow to pass through the outside of the fuel plates and provides for a volume of fluid which can be exchanged with subchannel coolant caused by mixing at each vent hole location.

4 ANALISYS OF STATIC PLATE DIVERGENCE

This section describes methods used to develop two widely recognized unique models for the prediction of mechanical instability through divergence of plates under static loading. A set of results are presented for generic geometric boundary conditions to provide a qualitative demonstration of the relationship between the load necessary for a plate failure. Lastly, critical flow velocity values which are approximately representative of those comprising an ATR fuel plate are presented.

4.1 Miller's Method

As discussed previously, Miller [33] produced the first widely recognized relationship between the hydraulic loading force imposed by a flow field on the plate's primary surface and the mechanical rigidity of a plate (flat and cylindrical) exposed to that load. Miller's equation for critical velocity was developed using neutral equilibrium theory as it applies to a wide beam. A flat "wide beam" (plate) under growing deformation with a uniformly applied pressure (P) and having clamped boundary conditions (C-F-C-F) at both span-wise ends has a deformation shape of

$$w = \frac{P\left(1-\upsilon^2\right)}{24EI}\left(y^4 - 2by^3 + b^2y^2\right); \tag{4-1}$$

note that (4-1) holds true for the coordinate system defined in Figure A-1. Integrating w along y from 0 to b, multiplying by two to include the total reduction in cross sectional area of the flow channel due to the adjacent plate collapsing inward, and dividing by bh (subchannel original cross sectional area) yields the percent change in cross sectional area that is produced due to a uniformly applied pressure, or

$$\frac{\Delta S}{S_0} = \frac{Pb^4\left(1-\upsilon^2\right)}{360EIh}. \tag{4-2}$$

If the area moment of inertia, I, of the plate is defined as $a^3/12$, then (4-2) becomes

$$\frac{\Delta S}{S_0} = \frac{Pb^4\left(1-\upsilon^2\right)}{30Ea^3h}. \tag{4-3}$$

Recall that the pressure differential developed across the plate away from the upstream and downstream ends of the deformed regions is

$$P_{cr} = 2\rho V_{cr}^2 \frac{\Delta S}{S_0}. \tag{2-2}$$

Inserting (4-3) into (2-2) yields the equation developed by Miller for prediction of critical velocity of a flat plate with C-F-C-F edge boundaries;

$$V_{cr} = \left[\frac{15Ea^3h}{\rho b^4 \left(1-\upsilon^2\right)} \right]^{\frac{1}{2}}. \tag{2-3}$$

The same methodology may be used to calculate a modified version of Miller's critical velocity for a flat plate with one edge clamped and the other edge simply supported (C-F-SS-F). The deflection profile of a wide beam with these prescribed boundary conditions and a uniformly applied pressure has been defined as [92];

$$w = \frac{P\left(1-\upsilon^2\right)}{48EI}\left(2y^4 - 5by^3 + 3b^2y^2\right). \tag{4-4}$$

Integrating from 0 to b, multiplying by two and dividing by bh results in the percent change in, or

$$\frac{\Delta S}{S_0} = \frac{3b^4\left(1-\upsilon^2\right)}{40Ea^3h}. \tag{4-5}$$

Substituting (4-5) into (2-2) produces the critical velocity for a flat plate with C-F-SS-F edge boundaries,

$$V_{cr} = \left[\frac{40Ea^3h}{3\rho b^4 \left(1-\upsilon^2\right)} \right]^{\frac{1}{2}}. \tag{4-6}$$

Note that the only difference between (4-6) and (2-3) may be found with the multiplier coefficients where (2-3) has a value of 15 and (4-6) has a value of 40/3. The ratio of these two quantities provides a qualitative basis to claim that a flat plate with C-F-C-F edge boundaries is 1.125 times more mechanically stable than that of a plate with C-F-SS-F edge boundaries. As a part of that Miller's original study he also developed a prediction for mechanical instability of a flat plate with both edges simply supported (SS-F-SS-F)

$$V_{cr} = \left[\frac{5Ea^3h}{2\rho b^4 \left(1-\upsilon^2\right)} \right]^{\frac{1}{2}}. \tag{4-7}$$

Recall that for a cylindrical plate with C-F-C-F edge boundaries, the critical velocity is

$$V_{cr}=\left[\frac{2Ea^3h\beta\sin^5(\theta/2)}{3\rho b^4\left(1-\upsilon^2\right)\left(\frac{1}{6}-\frac{\sin(\theta)}{4\theta}+\frac{\cos(\theta)}{12}\right)}\right]^{\frac{1}{2}}. \tag{2-12}$$

Equation (2-12) may be rearranged to the following form

$$V_{cr}=\left[\frac{15Ea^3h}{\rho b^4\left(1-\upsilon^2\right)}\right]^{\frac{1}{2}}\left[\frac{2\beta\sin^5(\theta/2)}{45\left(\frac{1}{6}-\frac{\sin(\theta)}{4\theta}+\frac{\cos(\theta)}{12}\right)}\right]^{\frac{1}{2}}. \tag{4-8}$$

Through the examination of the first term in (4-8) shows that it is identical to Miller's formulation for critical velocity of a flat plate with clamped boundary condition seen in (2-3), leaving the second term as the *transformation relation* between and flat and cylindrical plate with clamped edges. Miller derived the displacement relation for clamped edges in the radial direction corresponding to the critical velocity presented in (4-8), as

$$w=\frac{6PR_{cl}^4\left(1-\upsilon^2\right)}{\beta Ea^3}\left(\frac{2\phi\sin(\phi)}{\theta}+\frac{2\cos(\phi)}{\theta}-\frac{\sin^2(\phi)}{2\sin(\theta/2)}-\frac{\sin(\theta/2)}{2}-\frac{\sin(\theta/2)}{(\theta/2)}\right), \tag{4-9}$$

on the interval of $\phi\in[0,\theta/2]$ where the displacement profile holds true for the coordinate system in Figure 5-1. Miller determined that the percent change in cross sectional area due to membrane pressure on the plate may be obtained by integrating (4-8) from as follows

$$\frac{\Delta S}{S_0}=\frac{s}{bh}\int_0^{\theta/2}w\,d\phi, \tag{4-10}$$

where b may be approximated as $R_{cl}\theta$, the coefficient s for this case is equal to integer 4 and is included to account for the displacement of the adjacent plate and symmetry to account for $\phi\in[\theta/2,\theta]$ of the plate during the integral. Miller similarly developed a displacement relation for a cylindrical plate with simply supported boundaries as seen here,

$$w=\frac{PR_{cl}^4\left(1-\upsilon^2\right)C}{2EI\Upsilon\sin(\theta/2)}, \tag{4-11}$$

where

$$\Upsilon = \frac{\tilde{A}R_{cl}^2}{I}\frac{1}{2\sin^2(\theta/2)}\left(\frac{\theta}{2}-\frac{3\sin(\theta)}{4}+\frac{\theta\cos(\theta)}{4}\right)+\frac{1}{2\sin^2(\theta/2)}\left(\frac{\theta}{4}+\frac{\sin(\theta)}{4}\right), \tag{4-12}$$

and

$$C = -\frac{2}{3}+\sin(\theta)\left(\frac{3}{4}\cot(\theta/2)-\frac{\theta}{2}\right)-\frac{4}{3}\cos(\theta)+\frac{\theta\cot(\theta/2)}{2}\left(1-\frac{\cos(\theta)}{2}\right). \tag{4-13}$$

Integrating (4-11) by use of (4-10), the solution yields the percent change in cross sectional area of the subchannel for a plate with simply supported boundary conditions on both edges (SS-F-SS-F).

It is desired to estimate the critical velocity for a cylindrical plate with one edge clamped and the other edge simply supported using Miller's methods. This may be done by modifying (4-10) such that *s* is equal to the integer 2, integrating (4-9) and (4-11) using (4-10) and summing them to produce the total percent area change in the subchannel for a cylindrical plate with one edge clamped and the other edge simply supported (C-F-SS-F), the result is as follows;

$$\frac{\Delta S}{S_0} = \frac{3Pb^4\left(1-\upsilon^2\right)}{16Ea^3h}\left(\frac{\csc^5(\theta/2)C}{\Upsilon}+\frac{2\left(\frac{1}{6}-\frac{\sin(\theta)}{4\theta}+\frac{\cos(\theta)}{12}\right)}{\beta\sin^5(\theta/2)}\right). \tag{4-14}$$

By inserting (4-14) into (2-2), one may obtain a modified version of Miller's critical velocity for a cylindrical plate with C-F-SS-F edge boundaries;

$$V_{cr} = \left[\frac{15Ea^3h}{\rho b^4\left(1-\upsilon^2\right)}\right]^{\frac{1}{2}}\left[\frac{8}{45\left(\frac{\csc^5(\theta/2)C}{\Upsilon}+\frac{2\left(\frac{1}{6}-\frac{\sin(\theta)}{4\theta}+\frac{\cos(\theta)}{12}\right)}{\beta\sin^5(\theta/2)}\right)}\right]^{\frac{1}{2}}. \tag{4-15}$$

A qualitative comparison of the mechanical rigidity for a cylindrical plate with both edges clamped, to that of a plate with one edge clamped and one edge simply supported may be made by taking the ratio of critical velocity (VR_1) in (4-8) to that of (4-15).

$$VR_1 = \left[\frac{2\beta\sin^5(\theta/2)}{45\left(\frac{1}{6}-\frac{\sin(\theta)}{4\theta}+\frac{\cos(\theta)}{12}\right)}\right]^{\frac{1}{2}}\left[\frac{8}{45\left(\frac{\csc^5(\theta/2)C}{\Upsilon}+\frac{2\left(\frac{1}{6}-\frac{\sin(\theta)}{4\theta}+\frac{\cos(\theta)}{12}\right)}{\beta\sin^5(\theta/2)}\right)}\right]^{-\frac{1}{2}} \tag{4-16}$$

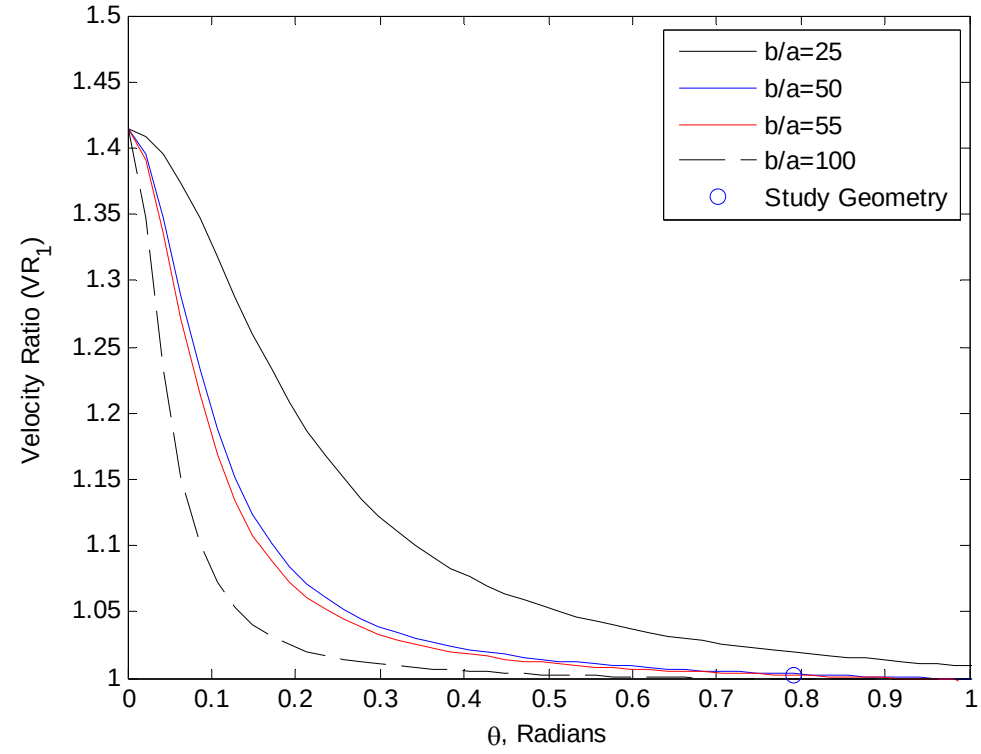

(a)

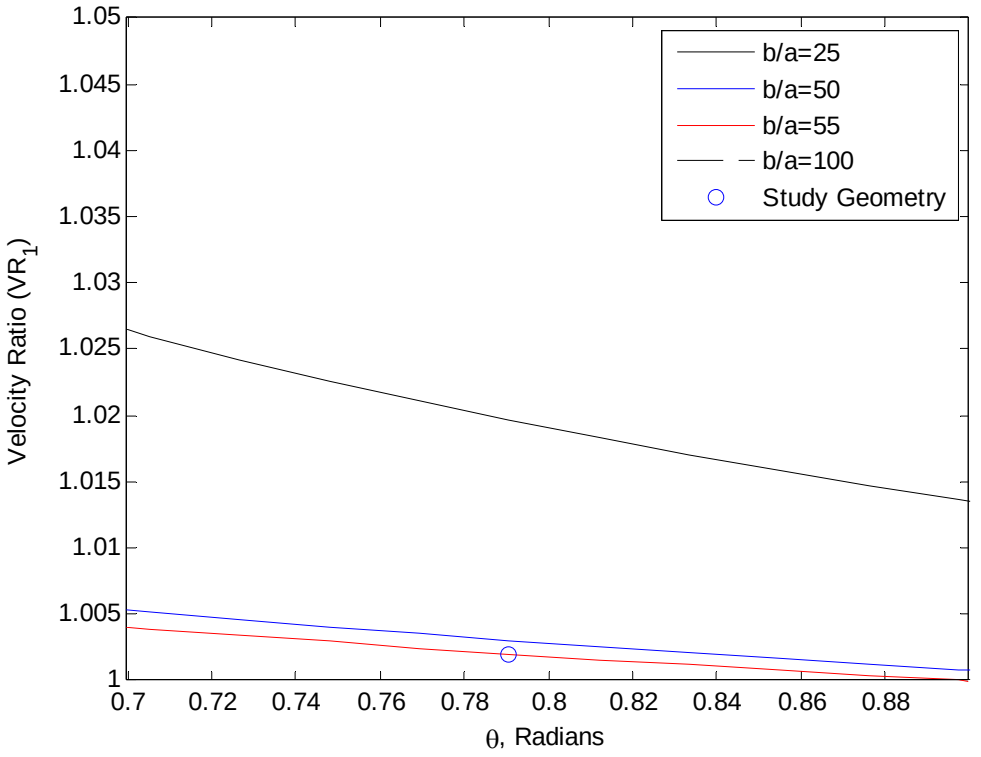

(b)

Figure 4-1: Critical velocity ratio (VR_1) dependant on edge boundary angle (a) for θ ranging from 0 to 1 and (b) for θ ranging from 0.7 to 0.9

The velocity ratio VR_1 is presented in Figure 4-1 for various plate aspect ratios (b/a) as a function of edge boundary angle. For all aspect ratios in Figure 4-1 as θ approaches zero the cylindrical plate with C-F-C-F edges becomes 1.415 times more mechanically stable than the plate with C-F-SS-F edges. However, as θ increases, the trend approaches unity for all aspect ratios until the relationship between boundary conditions C-F-C-F and C-F-SS-F becomes analogous. Figure 4-1 presents a single value for a cylindrical plate with similar boundary conditions to that of an ATR fuel plate $(b/a \approx 55 \text{ and } \theta = \pi/4)$; note that the ATR fuel plate falls within the analogous region for C-F-C-F and C-F-SS-F boundary conditions using Miller's methodology.

Employing the same methodology as previously described while applying SS-F-SS-F edge boundaries, Miller created a critical velocity prediction for a cylindrical plate with SS-F-SS-F edge boundaries;

$$V_{cr} = \left[\frac{5Eha^3}{2\rho b^4\left(1-\upsilon^2\right)}\right]^{\frac{1}{2}}\left[\frac{4\beta\sin^5\left(\theta/2\right)}{15\left(\frac{1}{6}-\frac{\sin(\theta)}{4\theta}+\frac{\cos(\theta)}{12}\right)}\right]^{\frac{1}{2}}. \tag{4-17}$$

This may be verified by visual comparison of the velocity ratio (VR_2) derived by Miller to create a relationship between a cylindrical plate with boundary conditions C-F-C-F and SS-F-SS-F;

$$VR_2 = \left[\frac{6\left(\frac{2b^2\left(\theta/2\right)^2}{15a^2}\left(1-\frac{5\left(\theta/2\right)^2}{42}\right)+1-\frac{9\left(\theta/2\right)^2}{14}\right)}{\frac{2b^2\left(\theta/2\right)^2}{5a^2}\left(1-\frac{\left(\theta/2\right)^2}{21}\right)+1-\frac{11\left(\theta/2\right)^2}{21}}\right]^{\frac{1}{2}}. \tag{4-18}$$

Plotting (4-18) as a function of edge boundary angle for various plate aspect ratios produces Figure 4-2. For all aspect ratios in Figure 4-2, as θ approaches zero the cylindrical plate with C-F-C-F edges becomes 2.450 times more mechanically stable than the plate with SS-F-SS-F edges. While within typical ATR fuel plate geometry, the boundary conditions are nearly analogous, as was observed with VR_1.

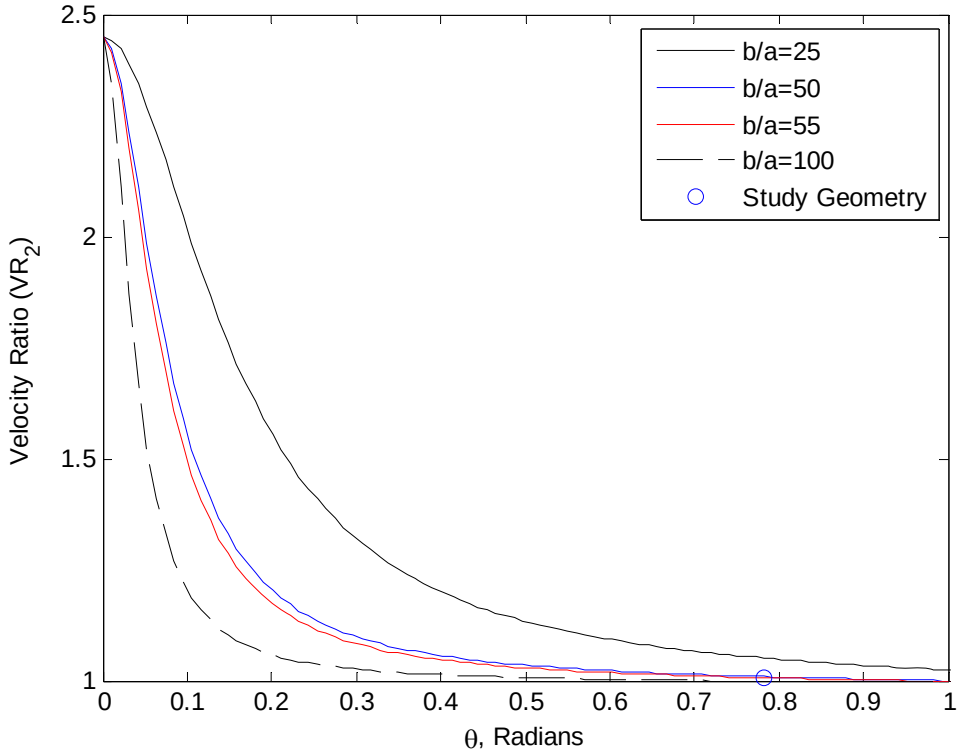

(a)

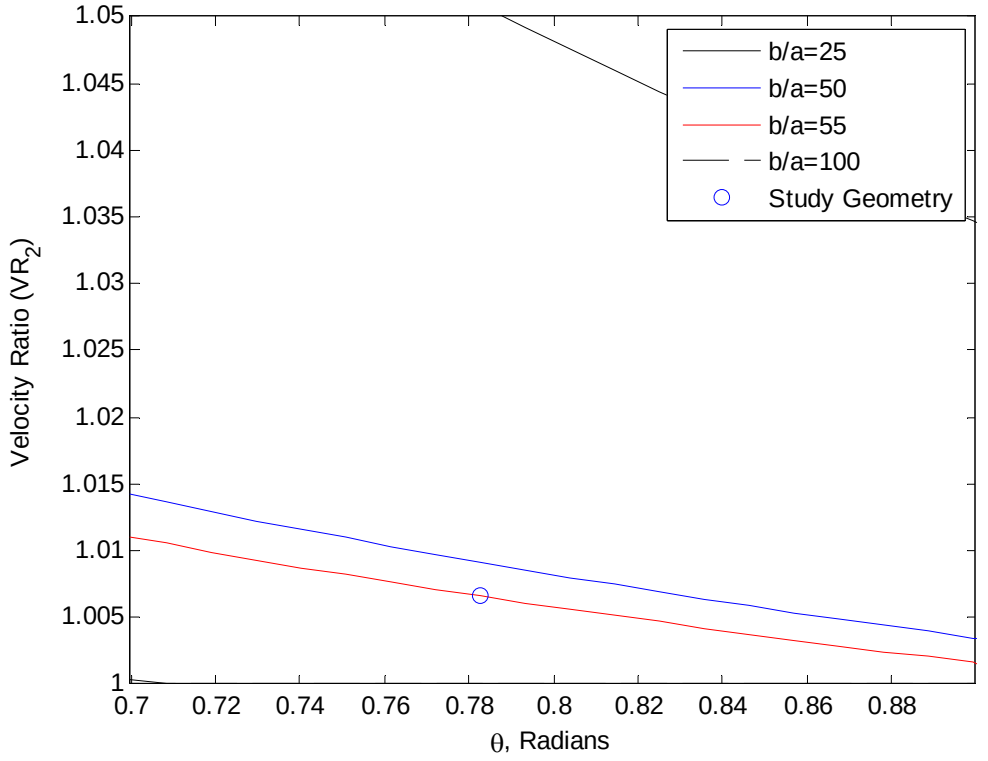

(b)

Figure 4-2: Critical velocity ratio (VR_2) dependant on edge boundary angle (a) for θ ranging from 0 to 1 and (b) for θ ranging from 0.7 to 0.9

By taking the ratio of the critical velocity derived for cylindrical plates for a given boundary condition type, to that of a flat plate with congruent boundary conditions a number of qualitative observations may be deduced. Miller considered this ratio relationship for the case of a plate with C-F-C-F edge boundaries as seen in (4-19):

$$VR_3 = \left[\frac{48\beta \sin^5(\theta/2)}{45\left(4 - 6\frac{\sin(\theta)}{\theta} + 2\cos(\theta)\right)} \right]^{\frac{1}{2}}. \tag{4-19}$$

Figure 4-3 presents the relative increase in mechanical stability of a cylindrical plate to that of a flat plate with C-F-C-F edge boundaries for various plate aspect ratios. Given, representative geometry of a typical ATR fuel plate; a cylindrical plate with C-F-C-F boundaries is approximated to be 5.451 times more mechanical stable than that of a flat plate with similar edge boundaries.

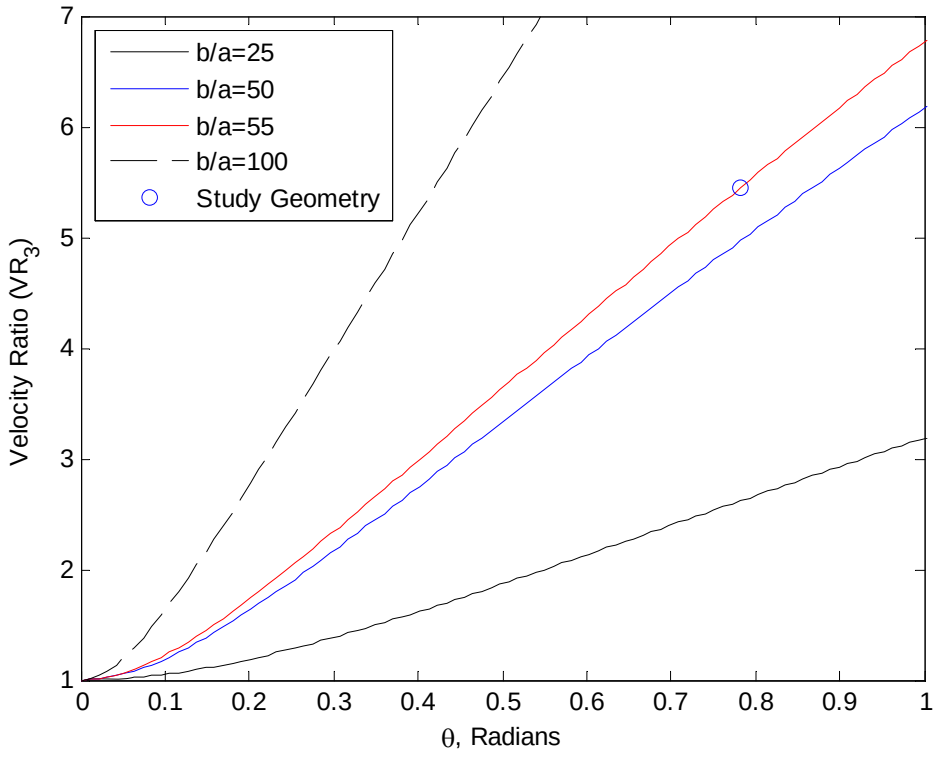

Figure 4-3: Critical velocity ratio (VR_3) dependant on edge boundary angle

A similar velocity relation (VR_4) may be produced by taking the ratio of (4-15) to (4-6) which yields

$$VR_4 = \left[\frac{64}{405\left(\frac{\csc^5(\theta/2)C}{\Upsilon} + \frac{2\left(\frac{1}{6} - \frac{\sin(\theta)}{4\theta} + \frac{\cos(\theta)}{12} \right)}{\beta \sin^5(\theta/2)} \right)} \right]^{\frac{1}{2}}. \tag{4-20}$$

Inserting geometric conditions representative of an ATR fuel plate, demonstrates an increase in mechanical stability of approximately 5.457 times that observed for a cylindrical plate with C-F-SS-F edge boundaries than that of a flat plate with similar edge boundaries. A demonstration of the relationship between azimuthal angle and VR_4 for various plate aspect ratios may be seen in Figure 4-4.

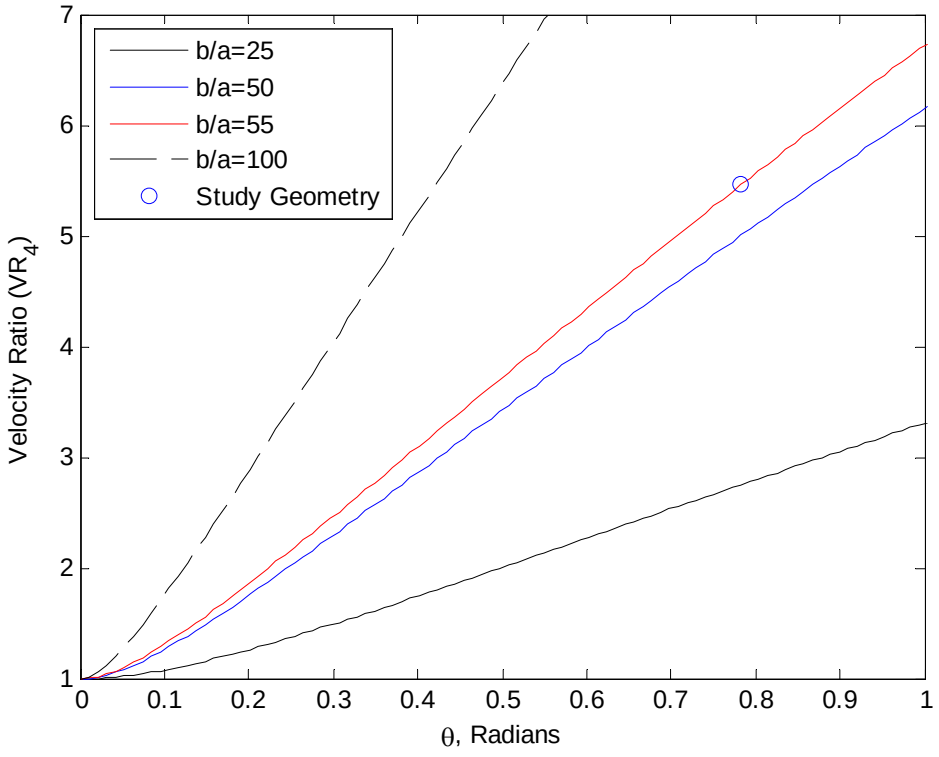

Figure 4-4: Critical velocity ratio (VR_4) dependant on edge boundary angle

4.2 Smith's Method

As previously discussed, Roger Smith [47] expanded on Miller's critical velocity prediction by including longitudinal plate deformation effects through empirically collected data. Recall that Smith's relation is

$$V_{cr} = \left[\frac{15Ea^3h}{\rho b^4\left(1-\upsilon^2\right)}\right]^{\frac{1}{2}}\left[\frac{1}{2}\left(1+\frac{4\pi\upsilon lh}{b^2}\right)\left(1+\frac{4\upsilon l^2}{3b^2}\right)\right]^{-\frac{1}{2}}. \tag{2-8}$$

However a limitation to Smith's analysis requires the effective length, l, to be approximated equal to b for all plate lengths greater than b, therefore if it is assumed that $l > b$, (2-8) becomes

$$V_{cr} = \left[\frac{15Ea^3h}{\rho b^4\left(1-\upsilon^2\right)}\right]^{\frac{1}{2}}\left[\frac{1}{2}\left(1+\frac{4\pi\upsilon h}{b}\right)\left(1+\frac{4\upsilon}{3}\right)\right]^{-\frac{1}{2}}. \tag{4-21}$$

A qualitative comparison of Smith's relation may be derived by taking the ratio (VR_5) of (4-21) to Miller's formula for a flat plate with C-F-C-F edge boundaries, or

$$VR_5 = \left[\frac{1}{2}\left(1+\frac{4\pi\upsilon h}{b}\right)\left(1+\frac{4\upsilon}{3}\right)\right]^{-\frac{1}{2}}. \tag{4-22}$$

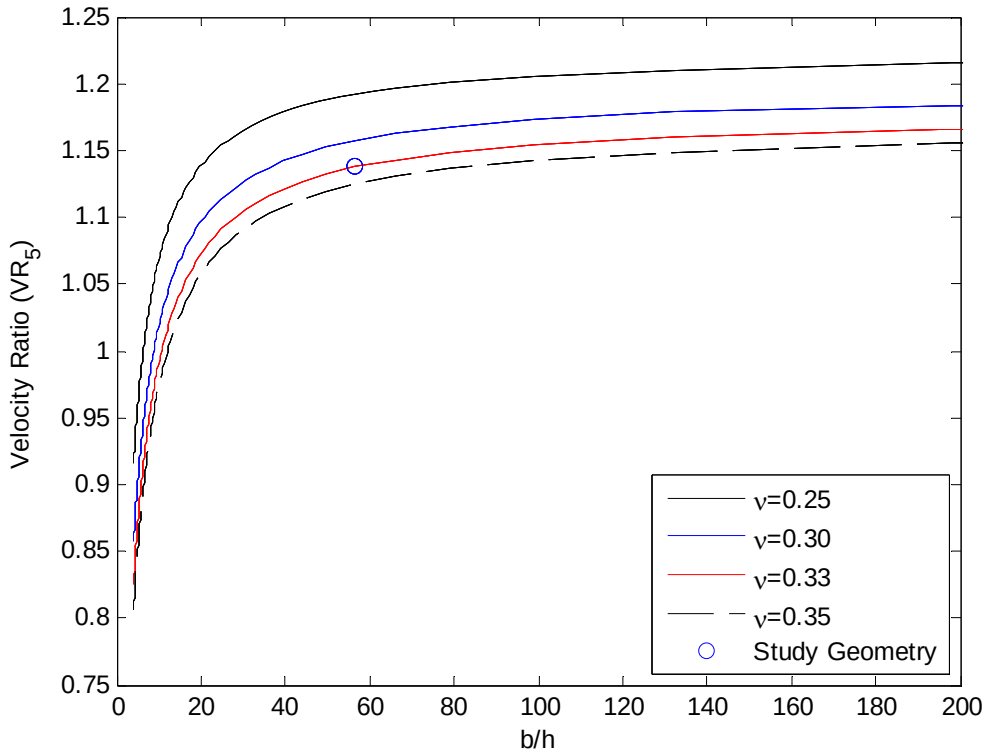

Figure 4-5: Critical velocity ratio (VR_5) dependant on edge boundary angle

Notice that in Figure 4-5 the critical velocity ratio asymptotically approaches a plateau value at a *b/h* of approximately 200 regardless of the Poisson's ratio. For geometry representative for this study, the critical velocity predicted by Smith's correlation is approximately 1.138 times higher than that predicted using Miller's model. Furthermore, for any *b/h* value greater than approximately 20 and all Poisson's ratio values considered, Smith's correlation produces higher critical velocities than that of Miller's model.

4.3 Closing

A set of common boundary conditions that will be used through the duration of this study are presented in Table 4-1. The material properties in the table are representative of Aluminum 6061-T0 and the plate geometric values are characteristic of plate 18 of the 19 fuel plate ATR element. Plate 18 is the second largest radius plate and has historically been analysed in safety analyses as the mechanically weakest plate in the ATR element geometry due to its combination of large radius and relatively small thickness [17].

Table 4-1: Cylindrical plate input parameters

Geometric Description	Value
Element entry length prior to plate, ℓ_i [m] (in)	0.1524 (6)
Element outlet length after plate, ℓ_o [m] (in)	0.1524 (6)
Plate axial length, L [m] (in)	1.2573 (49.5)
Subchannel height, h [m] (in)	0.00198 (0.078)
Plate thickness, a [m] (in)	0.00127 (0.05)
Plate Radius, R_{cl} [m] (in)	0.13324 (5.246)
Angle between edge boundaries, θ [radians] (degrees)	0.78539 (45)
Plate arc length, b	θR_{cl}
Plate area moment of inertia, I	$a^3/12$
Plate modulus of elasticity, E [MPa] (psi)	68947.57 (10×10^6)
Plate Poisson's ratio, υ	0.33
Plate density, ρ [Pa] (psi)	2700 (0.098)

Table 4-2 presents the predicted critical velocity and provides a demonstration for the large variation of predicted hydraulic characteristics necessary to buckling a plate under various boundary conditions. As expected from the previous discussion, the adapted Smith relation applied to a cylindrical plate with C-F-C-F edge boundaries produces the largest predicted critical velocity of 180.886 m/s while Miller's method for a flat plate with SS-F-SS-F edge boundaries results in the lowest predicted critical velocity at 8.011 m/s.

Table 4-2: Buckling results comparison against various boundary conditions

Plate Geometry	Boundary Condition	Critical Velocity Relationship	Value [m/s]
Flat Plate	C-F-C-F	Miller, Eq. (2-3)	19.623
		Smith, Eq. (4-21)	22.269
	C-F-SS-F	Adapted Miller, Eq. (4-6)	18.501
		Adapted Smith, Eq. (4-6)×(4-22)	20.996
	SS-F-SS-F	Miller Eq. (4-7)	8.011
		Adapted Smith, Eq. (4-7)×(4-22)	9.091
Cylindrical Plate	C-F-C-F	Miller Eq. (4-8)	159.395
		Adapted Smith, Eq. (4-8)×(4-22)	180.886
	C-F-SS-F	Adapted Miller, Eq. (4-15)	158.997
		Adapted Smith, Eq. (4-15)×(4-22)	180.435
	SS-F-SS-F	Miller, Eq. (4-17)	158.2083
		Adapted Smith, Eq. (4-17)×(4-22)	179.5396

5 MODEL AND METHODOLOGY

This chapter comprehensively describes the analytical derivation and numerical discritization developed from first principles and used to predict the mechanical stability of a single cylindrical plate under hydraulic loading. This is accomplished by coupling a plate stability module and flow module to simulate the dynamic response of a plate to representative reactor flow conditions. This chapter concludes with a discussion as to how these modules are coupled together such that they combine to produce a three dimensional FIV model of a single plate which is representative of ATR type fuel element geometry.

5.1 Plate Stability Module

As a corollary to the extensive quantity of literature available regarding flat plate type geometry and a contrary lack of cylindrical plate type geometry literature, the added complexities required for solving the vibration of a cylindrical-plate are often avoided if feasible. Appendix A presents a summary of the general semi-numerical method used to solve flat-plate stability problems which are simplified dramatically relative to the work presented in this chapter. In contrast to that of a flat plate or ‘wide beam’, determining (or predicting) the mode shapes and frequencies at which mechanical instability occurs is a very complicated process for a cylindrical plate. It has been hypothesized [93] that one never observes a single mode instability in a beam with both flat edges clamped, thus a curved plate only undergoes multi-mode vibration, however, this premise has yet to be studied rigorously.

5.1.1 Introduction

The coordinate system employed during this study is that of the cylindrical type. Figure 5-1 displays the geometry of the cylindrical plate under discussion along with its corresponding coordinate system. Any set of edge boundary conditions may be applied to this geometry using the semi-numerical method outlined in this study if done so in the appropriate manner.

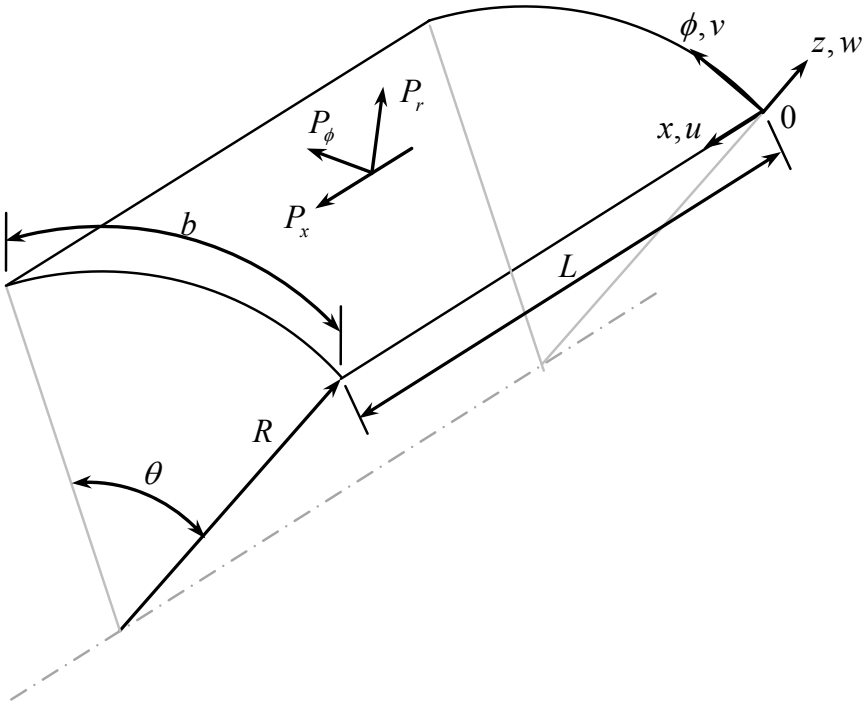

Figure 5-1: Geometry of a singly curved rectangular plate

The externally applied membrane pressures $(P_x,\ P_r,\ \text{and}\ P_\phi)$ shown in Figure 5-1 are scalars that are applied normal to the primary surface exposed in their coordinate direction. In other words, P_x is the pressure applied to the leading edge of the plate and is positive along the *x*+ coordinate direction, P_r is applied to the interior radial surface of the plate and is positive in the outward radial direction, P_ϕ is applied to the fixed edges. During this study these membrane pressures will be explicitly inserted into the equations of motion based on the hydraulic loads produced for a given flow condition. Throughout this study the fixed edges do not experience any hydraulic load as the surface normal to P_ϕ is not exposed to the flow field and is therefore set to zero for all cases considered, herein. However, all analytical derivation includes P_ϕ such that it may be utilized for future studies.

Figure 5-2 displays the shell element of differential length $\partial\phi$ along the azimuthal direction and $(1/R)\partial x$ along the axial direction based on the coordinate system of choice

presented in Figure 5-1. Figure 5-2(a) contains all external and internal forces acting on the element and Figure 5-2(b) contains the moments. Under equilibrium the forces and moments may be simply equated to each other such that they balance in each direction, however, in order to evaluate this elemental shell under non-equilibrium conditions (buckling or vibration) the coordinate system must be subject to a small displacement, only then may the forces and moments be balanced correctly. In order to define the relations for all stress resultants and moments two assumptions must be made: (1) all points aligned normal to the middle surface before deformation, remain congruent to the middle surface afterwards; and (2) for all kinematic relations the distance z of a point from the middle surface may be considered as unaffected by the deformation of the shell. The first assumption provides a mechanism for the exclusion of Q_x and Q_ϕ in Figure 5-2(a), as they are insignificant to the outcome of the solution. The second assumption states that the z direction is negligible to the outcomes of stress and strain in the plate during this study; that is, deformation in the z direction is considered, but the extensional stresses in x and ϕ dominate the z, therefore the z directional stresses are neglected.

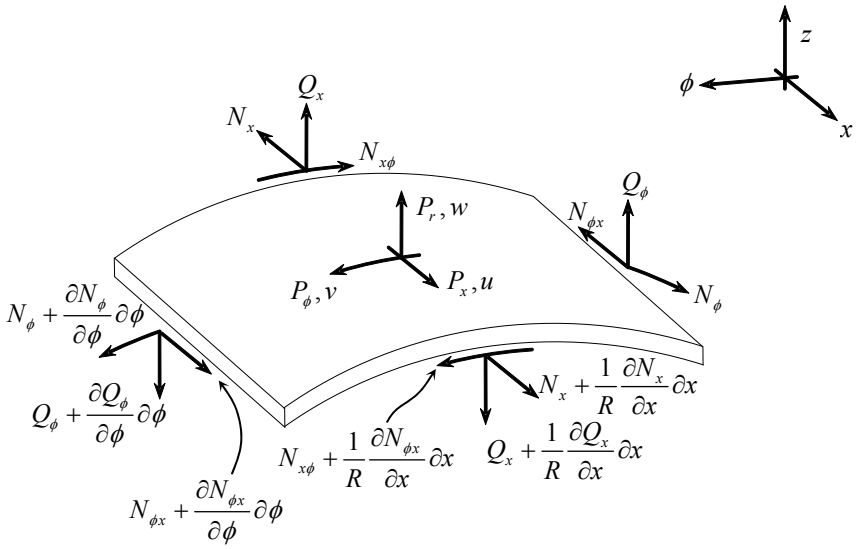

(a)

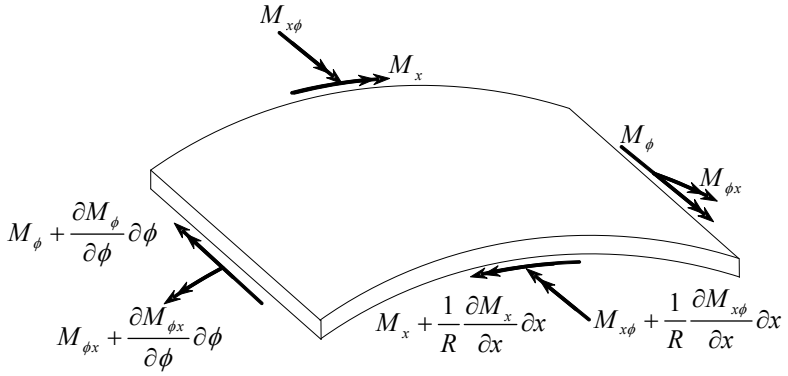

(b)

Figure 5-2: An element of cylindrical shell geometry (a) forces and (b) moments

Employing the methods presented in Flügge (Ref [94], Eq's 5.3a – 5.6a) the resultants and moments may be defined as follows:

$$N_x = \int_{-a/2}^{a/2} \sigma_x \left(1 + \frac{z}{R}\right) dz \,, \tag{5-1}$$

$$N_\phi = \int_{-a/2}^{a/2} \sigma_\phi dz \,, \tag{5-2}$$

$$N_{x\phi} = \int_{-a/2}^{a/2} \tau_{x\phi} \left(1 + \frac{z}{R}\right) dz \,, \tag{5-3}$$

$$N_{\phi x} = \int_{-a/2}^{a/2} \tau_{\phi x} dz \,, \tag{5-4}$$

$$M_x = -\int_{-a/2}^{a/2} \sigma_x \left(1 + \frac{z}{R}\right) z dz \,, \tag{5-5}$$

$$M_\phi = -\int_{-a/2}^{a/2} \sigma_\phi z dz \,, \tag{5-6}$$

$$M_{x\phi} = -\int_{-a/2}^{a/2} \tau_{x\phi} \left(1 + \frac{z}{R}\right) z dz \,, \tag{5-7}$$

and

$$M_{\phi x} = -\int_{-a/2}^{a/2} \tau_{\phi x} z dz \,, \tag{5-8}$$

where σ and τ are normal and shear stresses in their prescribed directions, respectively, and may be directly related to their partner strain as (refer to Appendix A for a discussion of these stress strain relations)

$$\sigma_x = \frac{E}{1-\upsilon^2}\left(\varepsilon_x + \upsilon\varepsilon_\phi\right), \tag{5-9}$$

$$\sigma_\phi = \frac{E}{1-\upsilon^2}\left(\varepsilon_\phi + \upsilon\varepsilon_x\right), \tag{5-10}$$

and

$$\tau_{x\phi} = \frac{E}{2(1+\upsilon)}\gamma_{x\phi}. \tag{5-11}$$

Note that ε_x, ε_ϕ, and $\gamma_{x\phi}$ are normal strain in *x* and ϕ, and shear strain crossed by *x* and ϕ. These strains are defined by Flügge [94] in the form of displacements and there derivatives for a cylindrical coordinate system as

$$\varepsilon_x = \frac{1}{R}\frac{\partial u}{\partial x} - \frac{z}{R^2}\frac{\partial^2 w}{\partial x^2}, \tag{5-12}$$

$$\varepsilon_\phi = \frac{1}{R}\frac{\partial v}{\partial \phi} - \frac{z}{R(R+z)}\frac{\partial^2 w}{\partial \phi^2} + \frac{z}{R+z}w, \tag{5-13}$$

and

$$\gamma_{x\phi} = \frac{1}{R+z}\frac{\partial u}{\partial \phi} + \frac{R+z}{R^2}\frac{\partial v}{\partial x} - \frac{1}{R}\left(\frac{z}{R} + \frac{z}{R+z}\right)\frac{\partial w}{\partial x}\frac{\partial w}{\partial \phi}. \tag{5-14}$$

When the stresses from (5-9) through (5-11) expressed by the strains in (5-12) through (5-14) are combined into (5-1) through (5-8) the integrations with respect to *z* may be completed appropriately for the case of plate deformation. Completing these integrations in their proper manner yields the following set of relations. These stress resultants may be formulated in terms of the displacements and their derivatives, in the form of the forces and their derivatives, or in a mixed way. During this study they are always formulated in terms of the displacements and their derivatives, as these parameters are more physically interpretable.

Direct stress resultants:

$$\begin{aligned} N_\phi &= \frac{D}{R}\left(\frac{\partial v}{\partial \phi}+w+\upsilon\frac{\partial u}{\partial x}\right)+\frac{K}{R^3}\left(w+\frac{\partial^2 w}{\partial \phi^2}\right) \\ &= \left(\frac{D\upsilon}{R}\right)\frac{\partial u}{\partial x}+\left(\frac{D}{R}\right)\frac{\partial v}{\partial \phi}+\left(\frac{K}{R^3}+\frac{D}{R}\right)w+\left(\frac{K}{R^3}\right)\frac{\partial^2 w}{\partial \phi^2}, \end{aligned} \tag{5-15}$$

$$\begin{aligned} N_x &= \frac{D}{R}\left(\frac{\partial u}{\partial x}+\upsilon\frac{\partial v}{\partial \phi}+\upsilon w\right)-\frac{K}{R^3}\left(\frac{\partial^2 w}{\partial x^2}\right) \\ &= \left(\frac{D}{R}\right)\frac{\partial u}{\partial x}+\left(\frac{D\upsilon}{R}\right)\frac{\partial v}{\partial \phi}+\left(\frac{D\upsilon}{R}\right)w-\left(\frac{K}{R^3}\right)\frac{\partial^2 w}{\partial x^2}, \end{aligned} \tag{5-16}$$

where D is referred to as the extensional rigidity known as $D = Eh/\left(1-\upsilon^2\right)$, and recall that K refers to the flexural rigidity, or $K = EI/\left(1-\upsilon^2\right)$.

Inplane shear stress resultants:

$$\begin{aligned} N_{x\phi} &= \frac{D(1-\upsilon)}{2R}\left(\frac{\partial u}{\partial \phi}+\frac{\partial v}{\partial x}\right)+\frac{K(1-\upsilon)}{2R^3}\left(\frac{\partial v}{\partial x}-\frac{\partial w}{\partial x}\frac{\partial w}{\partial \phi}\right) \\ &= \left(\frac{D(1-\upsilon)}{2R}\right)\frac{\partial u}{\partial \phi}+\left(\frac{D(1-\upsilon)}{2R}\right)\frac{\partial v}{\partial x}+\left(\frac{K(1-\upsilon)}{2R^3}\right)\frac{\partial v}{\partial x}-\left(\frac{K(1-\upsilon)}{2R^3}\right)\frac{\partial w}{\partial x}\frac{\partial w}{\partial \phi}, \end{aligned} \tag{5-17}$$

$$\begin{aligned} N_{\phi x} &= \frac{D(1-\upsilon)}{R^2}\left(\frac{\partial u}{\partial \phi}+\frac{\partial v}{\partial x}\right)+\frac{K(1-\upsilon)}{2R^3}\left(\frac{\partial v}{\partial x}+\frac{\partial w}{\partial x}\frac{\partial w}{\partial \phi}\right) \\ &= \left(\frac{D(1-\upsilon)}{R^2}\right)\frac{\partial u}{\partial \phi}+\left(\frac{D(1-\upsilon)}{R^2}\right)\frac{\partial v}{\partial x}+\left(\frac{K(1-\upsilon)}{2R^3}\right)\frac{\partial v}{\partial x}+\left(\frac{K(1-\upsilon)}{2R^3}\right)\frac{\partial w}{\partial x}\frac{\partial w}{\partial \phi}, \end{aligned} \tag{5-18}$$

Bending stress resultants (Moments):

$$\begin{aligned} M_x &= \frac{K}{R^2}\left(\frac{\partial^2 w}{\partial x^2}+\upsilon\frac{\partial^2 w}{\partial \phi^2}-\frac{\partial u}{\partial x}-\upsilon\frac{\partial u}{\partial \phi}\right) \\ &= -\left(\frac{K}{R^2}\right)\frac{\partial u}{\partial x}-\left(\frac{K\upsilon}{R^2}\right)\frac{\partial u}{\partial \phi}+\left(\frac{K}{R^2}\right)\frac{\partial^2 w}{\partial x^2}+\left(\frac{K\upsilon}{R^2}\right)\frac{\partial^2 w}{\partial \phi^2}, \end{aligned} \tag{5-19}$$

$$\begin{aligned} M_\phi &= \frac{K}{R^2}\left(w+\frac{\partial^2 w}{\partial \phi^2}+\upsilon\frac{\partial^2 w}{\partial x^2}\right) \\ &= \left(\frac{K}{R^2}\right)w+\left(\frac{K}{R^2}\right)\frac{\partial^2 w}{\partial \phi^2}+\left(\frac{\upsilon K}{R^2}\right)\frac{\partial^2 w}{\partial x^2}, \end{aligned} \tag{5-20}$$

Twisting stress resultants (Moments):

$$M_{x\phi} = \frac{K(1-\upsilon)}{R^2}\left(\frac{\partial w}{\partial x}\frac{\partial w}{\partial \phi} - \frac{\partial v}{\partial x}\right) = -\left(\frac{K(1-\upsilon)}{R^2}\right)\frac{\partial v}{\partial x} + \left(\frac{K(1-\upsilon)}{R^2}\right)\frac{\partial w}{\partial x}\frac{\partial w}{\partial \phi}, \tag{5-21}$$

$$M_{\phi x} = \frac{K(1-\upsilon)}{R^2}\left(\frac{1}{2}\frac{\partial u}{\partial \phi} - \frac{1}{2}\frac{\partial v}{\partial x} + \frac{\partial w}{\partial x}\frac{\partial w}{\partial \phi}\right) = \left(\frac{K(1-\upsilon)}{2R^2}\right)\frac{\partial u}{\partial \phi} - \left(\frac{K(1-\upsilon)}{2R^2}\right)\frac{\partial v}{\partial x} + \left(\frac{K(1-\upsilon)}{R^2}\right)\frac{\partial w}{\partial x}\frac{\partial w}{\partial \phi}, \tag{5-22}$$

Note that relations (5-15) through (5-22) are first presented in their compact form and secondly in their expanded form such that each directional component is independent; as this is how they will be employed during this study. In an attempt to be thorough, if it were not assumed that Q_x and Q_ϕ were insignificant to the solution, they would relate the bending and twisting moments as follows, where

$$Q_\phi = \frac{1}{R}\frac{\partial M_\phi}{\partial \phi} + \frac{1}{R}\frac{\partial M_{x\phi}}{\partial x} \tag{5-23}$$

and

$$Q_x = \frac{1}{R}\frac{\partial M_x}{\partial x} + \frac{1}{R}\frac{\partial M_{\phi x}}{\partial \phi}. \tag{5-24}$$

These then can be expanded such that they represent the complete form of the transverse shear stress resultants:

$$Q_\phi = -\left(\frac{K(1-\upsilon)}{R^3}\right)\frac{\partial^2 v}{\partial x^2} + \left(\frac{K}{R^3}\right)\frac{\partial w}{\partial \phi} + \left(\frac{K}{R^3}\right)\frac{\partial^3 w}{\partial \phi^3} + \left(\frac{K}{R^3}\right)\frac{\partial^2 w}{\partial x^2}\frac{\partial w}{\partial \phi}, \tag{5-25}$$

$$Q_x = -\left(\frac{K}{R^3}\right)\frac{\partial^2 u}{\partial x^2} + \left(\frac{K(1-\upsilon)}{2R^3}\right)\frac{\partial^2 u}{\partial \phi^2} - \left(\frac{K(1-\upsilon)}{2R^3}\right)\frac{\partial v}{\partial x}\frac{\partial v}{\partial \phi} + \left(\frac{K}{R^3}\right)\frac{\partial^3 w}{\partial \phi^3} + \left(\frac{K}{R^3}\right)\frac{\partial w}{\partial x}\frac{\partial^2 w}{\partial \phi^2}. \tag{5-26}$$

Nonetheless, (5-25) and (5-26) are not considered herein. Once these physical relations for all resultants have been accounted for, it is now necessary to acquire an appropriate set of equations of motion. Most variations of the differential equations applicable to plate mechanics differ in their bending terms. This is due to the simplifying assumptions made in the derivation of the equations. The equations may be divided into two broad groups. One group is known as the “simple set” (mentioned in chapter 2, developed by Sanders [81]) and the other is known as the “exact set”, differing only in the small

bending terms. For the set of differential equations based on a cylindrical plate the simple set of equations is usually used by structural engineers due to its simplicity. However, the exact set of equations will be used in this study so that all nonlinearities that may result from large plate deflections will be accounted for.

It is worthwhile to examine briefly the merits of both sets of equations given by Flügge [94]. First, both sets are symmetrical in structure with respect to the partial differential operators. The main appeal of the simple set is not only the simplicity, but, in certain cases, it will lead to the same type of solutions as the exact set (most often when opposite edges are simply supported). For reference, both sets are presented in (5-27) through (5-35). The geometry of the plate is shown in Figure 5-1, while the forces are shown in Figure 5-2. The exact set of equations mapping the motion of a curved plate presented by Flügge [94] are as follows;

$$\left(\frac{R^2\rho a}{Dg}\right)\frac{\partial^2 u}{\partial t^2} = \begin{aligned}&(1+q_x)\frac{\partial^2 u}{\partial x^2}+\left(\frac{(1-\upsilon)(1+k)}{2}+q_\phi\right)\frac{\partial^2 u}{\partial \phi^2}+(\upsilon-q_\phi)\frac{\partial w}{\partial x}\\&-(k)\frac{\partial^3 w}{\partial x^3}+\left(\frac{k(1-\upsilon)}{2}\right)\frac{\partial w}{\partial x}\frac{\partial^2 w}{\partial \phi^2}+\left(\frac{1+\upsilon}{2}\right)\frac{\partial v}{\partial x}\frac{\partial v}{\partial \phi}-(2q_z)\frac{\partial u}{\partial x}\frac{\partial u}{\partial \phi}\end{aligned}, \tag{5-27}$$

$$\left(\frac{R^2\rho a}{Dg}\right)\frac{\partial^2 u}{\partial t^2} = \begin{aligned}&\left(\frac{1+\upsilon}{2}\right)\frac{\partial u}{\partial x}\frac{\partial u}{\partial \phi}+\left(\frac{1-\upsilon}{2}+\frac{3k(1-\upsilon)}{2}+q_x\right)\frac{\partial^2 v}{\partial x^2}-\left(\frac{k(3-\upsilon)}{2}\right)\frac{\partial^2 w}{\partial x^2}\frac{\partial w}{\partial \phi},\\&+(1+q_\phi)\frac{\partial^2 v}{\partial \phi^2}+(1+q_\phi)\frac{\partial w}{\partial \phi}+(2q_z)\frac{\partial v}{\partial x}\frac{\partial v}{\partial \phi}+(2q_z)\frac{\partial w}{\partial x}\end{aligned} \tag{5-28}$$

and

$$-\left(\frac{R^2\rho a}{Dg}\right)\frac{\partial^2 u}{\partial t^2} = \begin{aligned}&(\upsilon-q_\phi)\frac{\partial u}{\partial x}+\left(\frac{k(1-\upsilon)}{2}\right)\frac{\partial u}{\partial x}\frac{\partial^2 u}{\partial \phi^2}-(k)\frac{\partial^3 u}{\partial x^3}+(1+q_\phi)\frac{\partial v}{\partial \phi}\\&-\left(\frac{k(3-\upsilon)}{2}\right)\frac{\partial^2 v}{\partial x^2}\frac{\partial v}{\partial \phi}+(1+k)w+(k)\frac{\partial^4 w}{\partial x^4}+(2k)\frac{\partial^2 w}{\partial x^2}\frac{\partial^2 w}{\partial \phi^2}\\&+(k)\frac{\partial^4 w}{\partial \phi^4}+(2k-q_\phi)\frac{\partial^2 w}{\partial \phi^2}-(q_x)\frac{\partial^2 w}{\partial x^2}+(2q_z)\frac{\partial v}{\partial x}-(2q_z)\frac{\partial w}{\partial x}\frac{\partial w}{\partial \phi}\end{aligned}. \tag{5-29}$$

where k is a dimensionless quantity and is defined as $k = K/\left(DR^2\right)$. Three now terms are introduced into these equations and account for the externally applied forces acting in each of the three principle directions; these terms may be expanded as $q_\phi = P_r R/D$, $q_x = P_x/D$, and $q_z = N_{x\phi}/D$. All in-plane stresses included in (5-27) through (5-29) are of opposite sign relative to that presented by Flügge [94] in order to comply with the coordinate system presented in Figure 5-1 and directional forces seen in Figure 5-2. Recall that the out of plane (z) forces (q_z) are dominated by those in the x and ϕ direction and therefore are assumed to be negligible reducing (5-27) through (5-29) to

$$\left(\frac{R^2\rho a}{Dg}\right)\frac{\partial^2 u}{\partial t^2} = \left(1+q_x\right)\frac{\partial^2 u}{\partial x^2} + \left(\frac{(1-\upsilon)(1+k)}{2} + q_\phi\right)\frac{\partial^2 u}{\partial \phi^2} + \left(\upsilon - q_\phi\right)\frac{\partial w}{\partial x}, \qquad (5\text{-}30)$$
$$-\left(k\right)\frac{\partial^3 w}{\partial x^3} + \left(\frac{k(1-\upsilon)}{2}\right)\frac{\partial w}{\partial x}\frac{\partial^2 w}{\partial \phi^2} + \left(\frac{1+\upsilon}{2}\right)\frac{\partial v}{\partial x}\frac{\partial v}{\partial \phi}$$

$$\left(\frac{R^2\rho a}{Dg}\right)\frac{\partial^2 u}{\partial t^2} = \left(\frac{1+\upsilon}{2}\right)\frac{\partial u}{\partial x}\frac{\partial u}{\partial \phi} + \left(\frac{1-\upsilon}{2} + \frac{3k(1-\upsilon)}{2} + q_x\right)\frac{\partial^2 v}{\partial x^2}, \qquad (5\text{-}31)$$
$$-\left(\frac{k(3-\upsilon)}{2}\right)\frac{\partial^2 w}{\partial x^2}\frac{\partial w}{\partial \phi} + \left(1+q_\phi\right)\frac{\partial^2 v}{\partial \phi^2} + \left(1+q_\phi\right)\frac{\partial w}{\partial \phi}$$

and

$$-\left(\frac{R^2\rho a}{Dg}\right)\frac{\partial^2 u}{\partial t^2} = \left(\upsilon - q_\phi\right)\frac{\partial u}{\partial x} + \left(\frac{k(1-\upsilon)}{2}\right)\frac{\partial u}{\partial x}\frac{\partial^2 u}{\partial \phi^2} - \left(k\right)\frac{\partial^3 u}{\partial x^3} + \left(1+q_\phi\right)\frac{\partial v}{\partial \phi}$$
$$-\left(\frac{k(3-\upsilon)}{2}\right)\frac{\partial^2 v}{\partial x^2}\frac{\partial v}{\partial \phi} + \left(1+k\right)w + \left(k\right)\frac{\partial^4 w}{\partial x^4} + \left(2k\right)\frac{\partial^2 w}{\partial x^2}\frac{\partial^2 w}{\partial \phi^2} \qquad (5\text{-}32)$$
$$+\left(k\right)\frac{\partial^4 w}{\partial \phi^4} + \left(2k - q_\phi\right)\frac{\partial^2 w}{\partial \phi^2} - \left(q_x\right)\frac{\partial^2 w}{\partial x^2}$$

It is this set, (5-30) through (5-32), that will be employed during this study. Reducing the exact set of equations with the appropriate assumptions that the bending terms are negligible yields the simple set of equations to be

$$\left(\frac{R^2\rho a}{Dg}\right)\frac{\partial^2 u}{\partial t^2} = \left(1+q_x\right)\frac{\partial^2 u}{\partial x^2} + \left(\frac{1-\upsilon}{2} + q_\phi\right)\frac{\partial^2 u}{\partial \phi^2} + \left(\frac{1+\upsilon}{2}\right)\frac{\partial v}{\partial x}\frac{\partial v}{\partial \phi} + \left(\upsilon - q_\phi\right)\frac{\partial w}{\partial x}, \qquad (5\text{-}33)$$

$$\left(\frac{R^2\rho a}{Dg}\right)\frac{\partial^2 v}{\partial t^2}=\left(\frac{1+\upsilon}{2}\right)\frac{\partial u}{\partial x}\frac{\partial u}{\partial \phi}+\left(1+q_\phi\right)\frac{\partial^2 v}{\partial \phi^2}+\left(\frac{1-\upsilon}{2}+q_x\right)\frac{\partial^2 v}{\partial x^2}+\left(1+q_\phi\right)\frac{\partial w}{\partial \phi}, \tag{5-34}$$

and

$$\left(\frac{R^2\rho a}{Dg}\right)\frac{\partial^2 w}{\partial t^2}=-\left(\upsilon-q_\phi\right)\frac{\partial u}{\partial x}-\left(1+q_\phi\right)\frac{\partial v}{\partial \phi}-(1)w-(k)\frac{\partial^4 w}{\partial x^4}-(2k)\frac{\partial^2 w}{\partial x^2}\frac{\partial^2 w}{\partial \phi^2}-(k)\frac{\partial^4 w}{\partial \phi^4}. \tag{5-35}$$

The qualitative difference between the two sets of equations is only in the terms associated with *k*. Equations (5-33) and (5-34) are completely free of *k* terms. The contribution to the bending by *u* and *v* is eliminated in (5-35). In terms of the energy of the plate, both sets account correctly for the membrane part of the energy but the simple set of equations does not account for the bending part of the energy. Therefore, if the state of deformation is purely or nearly flexural (bending) then it is necessary of use the exact set. On the other hand, if the deformation is primarily of extensional (stretching) type, either set of equations may be used.

Complexities are added with both types of differential equations relative to the equations for solving a flat plate. The added effort in solving the differential equations for cylindrical plates primarily results from the asymmetry in plate deflection in the normal direction to the primary plate surface (referred to later as *in-plane-forces*), whereas it is assumed that flat plates are symmetric and typically free of all internal shearing stresses, therefore simplifying the displacement equations significantly.

5.1.2 Discussion of Available Boundary Conditions

For determination of the constant of integration, the number of prescribed boundary conditions is required to be equal to the order of the system of equations. The present problem may be treated as a combination of a pair of two point boundary value problems, one in the variable *x* and other in ϕ. For the solution of each of these two-point boundary value problems, the order of the system of differential equations in each of the variables must be even so that half of the conditions may be prescribed at each edge.

Both exact and simple set of equations are of the order eight with respect to ϕ. Therefore, four boundary conditions are required at each edge (ϕ=0 and $\phi=\theta$). Similarly the simple set of equations is also of order eight with respect to x so that four conditions are required at each of the edges (x=0 and x=L). However, due to the presence of the term $[k]\partial^3 u/\partial x^3$ in (5-29), the exact set of equations are of order nine with respect to x. Under this situation, it will not be possible to prescribe the boundary conditions correctly. This difficulty may be overcome by eliminating the displacement of the plate along the axial direction (u) from the governing equations. During this study u is eliminated, therefore, both the sets of equations are of order eight with respect to both ϕ and x.

The small term $[k]\partial^3 u/\partial x^3$ is contributed to the equilibrium equation by the transverse shear Q_x. Although Q_x is small in magnitude, it might contain large derivatives. If the apparently small term $[k]\partial^3 u/\partial x^3$ is neglected, then the system of equations will no longer be symmetrical. In order to preserve the symmetry of the system, $[k]\partial^3 w/\partial x^3$ in (5-29) will also have to be neglected if $[k]\partial^3 u/\partial x^3$ is neglected in (5-27). Henceforth, only the exact set of equations (5-27) through (5-29) will be considered.

The edge boundary conditions most commonly encountered in practice are: (a) clamped, (b) simply supported, and (c) free edge.

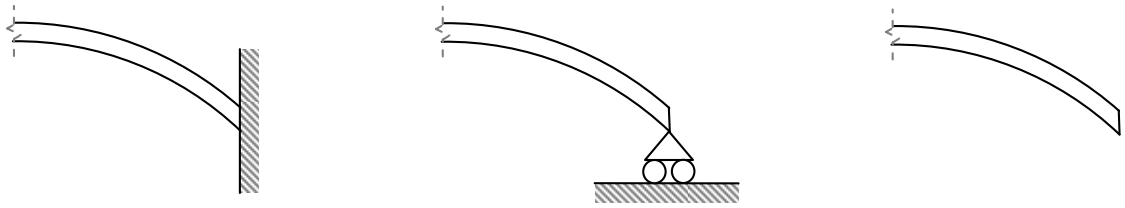

(a) (b) (c)

Figure 5-3: Example sketch of edge boundary condition types

Considering the geometry in Figure 5-3 along with the coordinate system and stress resultants presented in Figure 5-1 and Figure 5-2, respectively, the corresponding edge boundary conditions are as follows:

(a) Clamped:

$$u = v = w = \frac{\partial w}{\partial x} = 0, \qquad x = \text{constant} \tag{5-36}$$

$$u = v = w = \frac{\partial w}{\partial \phi} - v = 0, \qquad \phi = \text{constant} \tag{5-37}$$

(b) Simply Supported:

$$v = w = N_x = M_x = 0, \qquad x = \text{constant} \tag{5-38}$$

$$u = w = N_\phi = M_\phi = 0, \qquad \phi = \text{constant} \tag{5-39}$$

(c) Free Edge:

$$N_x = M_x = 0, \qquad x = \text{constant} \tag{5-40}$$

$$N_\phi = M_\phi = 0, \qquad \phi = \text{constant} \tag{5-41}$$

Similarly, other boundary equations, or a combination of those listed above may be formulated to reflect specific edge conditions desired [94]. Focus during this study will be directed toward boundary conditions (5-37), (5-39), and (5-40) as these pertain to cylindrical fuel plate-type geometric conditions. The focus of this study is aimed at two boundary value problems:

- Both straight edges Clamped and both curved edges Free
  (C-F-C-F)

  The C-F-C-F case assumes both straight edges are rigid and do not allow for flexure both in displacement and the first displacement derivative, this is the ideal mechanical case for an ATR fuel element.
- One straight edge Clamped, one straight Simply Supported, and both curved edges Free
  (C-F-SS-F)

  The C-F-SS-F case assumes that one straight edge is restricted in both displacement and the first displacement derivative, while the second straight

edge has the ability to flexure through the first displacement derivative. This allows for the simulation of torsion occurring in the element (the fuel element itself is not truly rigid) and is a more realistic case for an ATR fuel element.

5.1.3 Solution Method

In general, methods of solutions may be analytical, numerical, experimental or any combination thereof. The numerical methods such as the finite element technique or the experimental techniques are not considered in this chapter. Consideration will be given only to a semi-numerical method.

A purely analytical solution is obtainable only when all the four edges of the plate are simply supported. Exact solutions to the problem may be obtained only when any pair of opposite edges are simply supported. Otherwise, the solutions will always be approximate. The approximate methods for such solutions will be at best semi-numerical in character.

Such intermediate approximate analytical methods rest upon the works of notable mathematicians such as Ritz, Galerkin, Kantorovich, and Krylov. If the two dimensional problem were to be reduced to a one-dimensional problem it generally would become easier to solve. The method of Kantorovich's reduction may be used to reduce the partial differential equations to ordinary differential equations [95]. Then the ordinary differential equations may be solved by various methods, like the transfer matrices, matrix progression line solution, Ruge-Kutta, modified matrix progression, and others.

Kantrovich's method, or the method of reduction to ordinary equations, occupies a solution position between the exact solution of the problem (often unattainable) and the methods of Rayleigh-Ritz and Galerkin [86]. The method of Rayleigh-Ritz employs complete functions to use such that a beam or plate's eigenfunction is entirely assumed. These assumed functions are substituted into the expression for the Kinetic-Potential, Λ, which is a double integral commonly used in structures and plate theory. The problem then reduces to the determination of the undetermined constants in the assumed

functions, such that Λ is minimized. The minimum condition leads to the final set of algebraic equations. However, the solution obtained by assuming functions strongly depends upon the assumed functions themselves [95]. This inherently biases the results produced for a prescribed problem.

In the Kantorovich method the solution of the plate problem is assumed as the sum of products of functions in one direction and functions in the other direction. Then, assuming the functions in the one direction, the nonlinear partial differential equations of the plate problem are reduced to a system of nonlinear ordinary differential equations. The resulting one-dimensional solution serves as a starting point for an iterative procedure, in which the solution obtained in one direction is used as the assumed eigenfunctions in the second direction. Because the solution is inherently iterative it does not depend on the initial assumption (as long as that assumption is within the solution's radius of convergence), which may be poor or may not satisfy any of the boundary conditions.

5.1.4 Reduction of Equations (Kantorovich's Method)

If $F_m(x)$ is an assumed eigenfunction; after performing the integrations with respect to x the expression of an arbitrary convergence parameter (Λ) will contain undetermined functions of one variable which are $g_1(\phi)$, $g_2(\phi)$, and $g_3(\phi)$. The problem now reduces to finding these functions such that Λ is a minimum. The condition that Λ is minimum with respect to the undetermined functions yields a set of linear homogeneous ordinary differential equations.

This approach to Kantorovich's reduction is unnecessary in practice if the differential equations of motion are already available. If the equations of motion are known, Kantorovich has suggested a more convenient way of obtaining the ordinary differential equations [95]. Following the method of Kantorovich the exact set of equations (5-27) through (5-29) are reduced to a set of ordinary differential equations as follows. The equations of (5-27) through (5-29) may be written in operational form as:

$$\left(\frac{R^2\rho a}{Dg}\right)\frac{\partial^2 u}{\partial t^2} = L_1(u,v,w), \tag{5-42}$$

$$\left(\frac{R^2\rho a}{Dg}\right)\frac{\partial^2 v}{\partial t^2} = L_2(u,v,w), \tag{5-43}$$

and

$$-\left(\frac{R^2\rho a}{Dg}\right)\frac{\partial^2 w}{\partial t^2} = L_3(u,v,w), \tag{5-44}$$

where L_1, L_2, and L_3 are partial differential operators. If the boundary of the plate coincides with a rectangle (e.g. the edges of the geometry aligned with the coordinate system) the solutions for (5-42) through (5-44) may be written as follows

$$u = f_1(x)g_1(\phi)e^{i\omega t}, \tag{5-45}$$

$$v = f_2(x)g_2(\phi)e^{i\omega t}, \tag{5-46}$$

and

$$w = f_3(x)g_3(\phi)e^{i\omega t}, \tag{5-47}$$

where ω is the circular frequency of vibration and $g_1(\phi)$, $g_2(\phi)$, and $g_3(\phi)$ are functions to be determined. Recalling that f_1, f_2, and f_3 are assumed to be known, the reduction of (5-42) through (5-44) to ordinary differential equations is done in the following way. It is first assumed that $f_1 = (\bar{x}/\lambda_m)\partial F_m/\partial x$, $f_2 = F_m$, and $f_3 = F_m$ where F_m is the m^{th} eigenfunction of a straight beam, and $\bar{x}$ is a dimensionless plate length scale equivalent to L/R. Substituting *u*, *v*, and *w* from functions (5-45) through (5-47) into (5-42) through (5-44), multiplying each equation by $(\bar{x}/\lambda_m)\partial F_m/\partial x$, F_m, and F_m respectively, and integrating along the length of the plate yields

$$\int_{x=0}^{\bar{x}} \left[L_1(f_1g_1, f_2g_2, f_3g_3) + \Delta f_1 g_1\right] f_1 dx = 0, \tag{5-48}$$

$$\int_{x=0}^{\bar{x}} \left[L_2(f_1g_1, f_2g_2, f_3g_3) + \Delta f_2 g_2\right] f_2 dx = 0, \tag{5-49}$$

and

$$\int_{x=0}^{\bar{x}} \left[L_3(f_1g_1, f_2g_2, f_3g_3) - \Delta f_3 g_3\right] f_3 dx = 0, \tag{5-50}$$

where Δ is the frequency parameter and is defined as $\Delta = \left(R^2\omega^2\rho a/Dg\right)$.

This study assumes that $f_1(x)$, $f_2(x)$, and $f_3(x)$ are known. Note that the x direction is taken to have an assumed eigenfunction in this study for which the Rayleigh-Ritz method with characteristic beam vibration functions have produced acceptable results for flat plates suggesting that it yields a dependable solution if the x direction, this is why it is chosen for reduction. Furthermore, unless a transposition of the equations of motion is performed based on a reduction in the ϕ direction, the equations remain of order nine, preventing their solution in matrix form all together. After performing the term by term integrations and making necessary simplifications, (5-48) through (5-50) become [95]

$$L_{a1}\left(g_1,\, g_2,\, g_3\right)+\Delta g_1=0\,, \tag{5-51}$$

$$L_{a2}\left(g_1,\, g_2,\, g_3\right)+\Delta g_2=0\,, \tag{5-52}$$

and

$$L_{a3}\left(g_1,\, g_2,\, g_3\right)-\Delta g_3=0\,. \tag{5-53}$$

In these equations, L_{a1}, L_{a2}, and L_{a3}, are linear ordinary differential operators with constant coefficients. Thus the original partial differential equations are reduced to two sets of ordinary differential equations. The prescription of the required integrals and the reduced (5-51) through (5-53) must now be determined.

5.1.4.1 Prescribing Curved Edge Boundary Conditions (x = constant)

In the case where both axial ends ($x = 0$ and $x = L$) have free boundary conditions the formulation for the eigenfunction, $F_m(x)$ of a straight beam takes the form [75]:

$$F_m\left(x\right)=\left[\cosh\left(\frac{\lambda_m x}{\bar{x}}\right)+\cos\left(\frac{\lambda_m x}{\bar{x}}\right)\right]-\frac{\cosh\lambda_m-\cos\lambda_m}{\sinh\lambda_m-\sin\lambda_m}\left[\sinh\left(\frac{\lambda_m x}{\bar{x}}\right)+\sin\left(\frac{\lambda_m x}{\bar{x}}\right)\right] \tag{5-54}$$

where $\bar{x}$ is a dimensionless characteristic length of the plate defined as $\bar{x}=L/R$ and the transcendental equation for λ_m is

$$\cos\lambda_m\cosh\lambda_m=1\,. \tag{5-55}$$

Defining σ_m is defined as

$$\sigma_m=\frac{\cosh\lambda_m-\cos\lambda_m}{\sinh\lambda_m-\sin\lambda_m}\,, \tag{5-56}$$

simplifies (5-54) to

$$F_m(x) = \cosh\left(\frac{\lambda_m x}{\bar{x}}\right) + \cos\left(\frac{\lambda_m x}{\bar{x}}\right) - \sigma_m \sinh\left(\frac{\lambda_m x}{\bar{x}}\right) - \sigma_m \sin\left(\frac{\lambda_m x}{\bar{x}}\right). \quad (5\text{-}57)$$

The following expression will also be utilized in future application

$$I_m = \sigma_m^2 - \frac{2\sigma_m}{\lambda_m} \quad (5\text{-}58)$$

where I_m is the moment of inertia of a beam of unit width (wide beam). The values for λ_m may be obtained from Blevins [75]. From these tabulated values σ_m and I_m may then be calculated. These coefficients for the first 5 modes (m) are presented in Table 5-1.

Table 5-1: Single span beam modal coefficients

Mode (m)	λ_m	σ_m	I_m
1	04.73004074	0.982502215	0.54987984
2	07.85320462	1.000777312	0.74668416
3	10.99560790	0.999966450	0.81804820
4	14.13716550	1.000001450	0.85853162
5	17.27875970	0.999999937	0.88425083

A visual interpretation of the eigenfunction presented in (5-57) after applying the coefficients identified in Table 5-1 is provided in Figure 5-4. These displacement profiles are representative of the plate's assumed eigenfunction, or modal shape, in the axial direction (x), referring to Figure 5-1. The modal shape considered during this study is highly sensitive to both λ_m and σ_m in the higher modes. Chang and Craig [96] have shown that changes in σ_m as small as 10^{-6} can result in a significant change in the computed mode shape. It is for this reason that all digits available in the literature (and presented in Table 5-1) are employed during this study.

As can be seen from Figure 5-4 all even modal numbers are asymmetric about the beam centerline, while the odd modal numbers are symmetric; this observation will be elaborated upon in Chapter 6 when describing tendencies of the plate dynamic response over modal values.

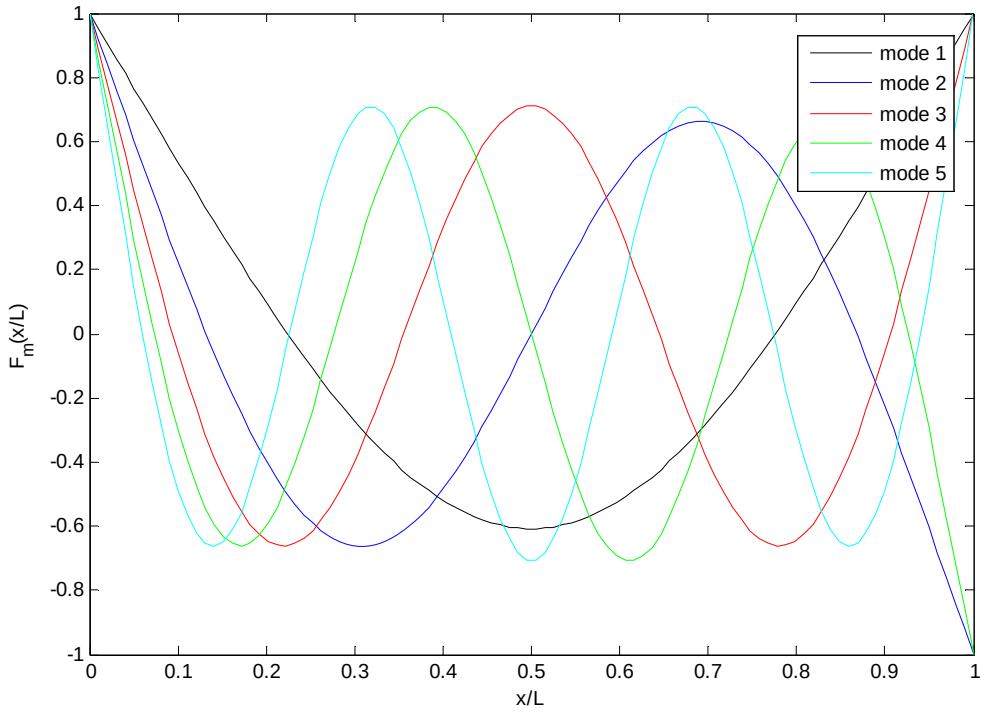

Figure 5-4: Normalized mode shapes of straight slender beams (both ends free)

Now that the appropriate eigenfunction has been acquired for this study, the x independent solution functions may be resolved; $f_1(x)$, $f_2(x)$, and $f_3(x)$ are written for each mode of vibration as

$$\begin{aligned} f_1 &= \frac{\bar{x}}{\lambda_m}\frac{\partial F_m}{\partial x} \\ &= \sinh\left(\frac{\lambda_m x}{\bar{x}}\right) - \sin\left(\frac{\lambda_m x}{\bar{x}}\right) - \sigma_m \cosh\left(\frac{\lambda_m x}{\bar{x}}\right) - \sigma_m \cos\left(\frac{\lambda_m x}{\bar{x}}\right), \end{aligned} \tag{5-59}$$

and

$$\begin{aligned} f_2 &= f_3 = F_m \\ &= \cosh\left(\frac{\lambda_m x}{\bar{x}}\right) + \cos\left(\frac{\lambda_m x}{\bar{x}}\right) - \sigma_m \sinh\left(\frac{\lambda_m x}{\bar{x}}\right) - \sigma_m \sin\left(\frac{\lambda_m x}{\bar{x}}\right). \end{aligned} \tag{5-60}$$

For explicitness the first four derivatives of $f_1(x)$, $f_2(x)$, and $f_3(x)$ with respect to x are presented below as they are necessary for performing the required integrals that follow. These first four derivatives are as follows:

$$\frac{\partial f_1}{\partial x} = \frac{\lambda_m}{\bar{x}}\left[\cosh\left(\frac{\lambda_m x}{\bar{x}}\right) - \cos\left(\frac{\lambda_m x}{\bar{x}}\right) - \sigma_m \sinh\left(\frac{\lambda_m x}{\bar{x}}\right) + \sigma_m \sin\left(\frac{\lambda_m x}{\bar{x}}\right)\right], \tag{5-61}$$

$$\frac{\partial^2 f_1}{\partial x^2} = \frac{\lambda_m^2}{\bar{x}^2}\left[\sinh\left(\frac{\lambda_m x}{\bar{x}}\right)+\sin\left(\frac{\lambda_m x}{\bar{x}}\right)-\sigma_m\cosh\left(\frac{\lambda_m x}{\bar{x}}\right)+\sigma_m\cos\left(\frac{\lambda_m x}{\bar{x}}\right)\right], \tag{5-62}$$

$$\frac{\partial^3 f_1}{\partial x^3} = \frac{\lambda_m^3}{\bar{x}^3}\left[\cosh\left(\frac{\lambda_m x}{\bar{x}}\right)+\cos\left(\frac{\lambda_m x}{\bar{x}}\right)-\sigma_m\sinh\left(\frac{\lambda_m x}{\bar{x}}\right)-\sigma_m\sin\left(\frac{\lambda_m x}{\bar{x}}\right)\right], \text{ and} \tag{5-63}$$

$$\frac{\partial^4 f_1}{\partial x^4} = \frac{\lambda_m^4}{\bar{x}^4}\left[\sinh\left(\frac{\lambda_m x}{\bar{x}}\right)-\sin\left(\frac{\lambda_m x}{\bar{x}}\right)-\sigma_m\cosh\left(\frac{\lambda_m x}{\bar{x}}\right)-\sigma_m\cos\left(\frac{\lambda_m x}{\bar{x}}\right)\right]; \tag{5-64}$$

and

$$\frac{\partial f_2}{\partial x} = \frac{\partial f_3}{\partial x} = \frac{\lambda_m}{\bar{x}}\left[\sinh\left(\frac{\lambda_m x}{\bar{x}}\right)-\sin\left(\frac{\lambda_m x}{\bar{x}}\right)-\sigma_m\cosh\left(\frac{\lambda_m x}{\bar{x}}\right)-\sigma_m\cos\left(\frac{\lambda_m x}{\bar{x}}\right)\right], \tag{5-65}$$

$$\frac{\partial^2 f_2}{\partial x^2} = \frac{\partial^2 f_3}{\partial x^2} = \frac{\lambda_m^2}{\bar{x}^2}\left[\cosh\left(\frac{\lambda_m x}{\bar{x}}\right)-\cos\left(\frac{\lambda_m x}{\bar{x}}\right)-\sigma_m\sinh\left(\frac{\lambda_m x}{\bar{x}}\right)+\sigma_m\sin\left(\frac{\lambda_m x}{\bar{x}}\right)\right], \tag{5-66}$$

$$\frac{\partial^3 f_2}{\partial x^3} = \frac{\partial^3 f_3}{\partial x^3} = \frac{\lambda_m^3}{\bar{x}^3}\left[\sinh\left(\frac{\lambda_m x}{\bar{x}}\right)+\sin\left(\frac{\lambda_m x}{\bar{x}}\right)-\sigma_m\cosh\left(\frac{\lambda_m x}{\bar{x}}\right)+\sigma_m\cos\left(\frac{\lambda_m x}{\bar{x}}\right)\right], \text{ and} \tag{5-67}$$

$$\frac{\partial^4 f_2}{\partial x^4} = \frac{\partial^4 f_3}{\partial x^4} = \frac{\lambda_m^4}{\bar{x}^4}\left[\cosh\left(\frac{\lambda_m x}{\bar{x}}\right)+\cos\left(\frac{\lambda_m x}{\bar{x}}\right)-\sigma_m\sinh\left(\frac{\lambda_m x}{\bar{x}}\right)-\sigma_m\sin\left(\frac{\lambda_m x}{\bar{x}}\right)\right]. \tag{5-68}$$

Appendix B presents the method and location in which the eigenfunction of choice and its derivatives are incorporated into the algorithm to produce a coupled eigenvalue in both the x and ϕ directions.

Now that the functions identifying variations in *u, v,* and *w* along the direction of x have been established the necessary integrations on (5-51) through (5-53) may be performed, producing the following set of ordinary differential equations (Appendix B presents all coefficients in integral form):

$$0 = \psi_{11}g_1 + \xi_{12}\frac{\partial^2 g_1}{\partial\phi^2} + \xi_{13}\frac{\partial g_2}{\partial\phi} + \psi_{12}g_3 + \xi_{16}\frac{\partial^2 g_3}{\partial\phi^2}, \tag{5-69}$$

$$0 = \xi_{21}\frac{\partial g_1}{\partial\phi} + \xi_{22}\frac{\partial^2 g_2}{\partial\phi^2} + \psi_{21}g_2 + \psi_{22}, \tag{5-70}$$

and

$$0 = \psi_{31}g_1 + \xi_{34}\frac{\partial^2 g_1}{\partial\phi^2} + \psi_{33}\frac{\partial g_2}{\partial\phi} + \psi_{32}g_3 + \psi_{34}\frac{\partial^2 g_3}{\partial\phi^2} + \xi_{39}\frac{\partial^4 g_3}{\partial\phi^4}. \tag{5-71}$$

It is possible to reduce (5-69) through (5-71) to a set of eight first-order ordinary differential equations [97]. This reduction requires the definitions of new parameters g_4 through g_8 as follows;

$$g_4 = \frac{\partial g_3}{\partial \phi}, \tag{5-72}$$

$$g_5 = \frac{\partial g_4}{\partial \phi} = \frac{\partial^2 g_3}{\partial \phi^2}, \tag{5-73}$$

$$g_6 = \frac{\partial g_5}{\partial \phi} = \frac{\partial^2 g_4}{\partial \phi^2} = \frac{\partial^3 g_3}{\partial \phi^3}, \tag{5-74}$$

$$g_7 = \frac{\partial g_1}{\partial \phi}, \tag{5-75}$$

and

$$g_8 = \frac{\partial g_2}{\partial \phi}. \tag{5-76}$$

From the newly defined parameters above, the following can then be assumed that

$$\frac{\partial g_6}{\partial \phi} = \frac{\partial^4 g_3}{\partial \phi^4}, \tag{5-77}$$

$$\frac{\partial g_7}{\partial \phi} = \frac{\partial^2 g_1}{\partial \phi^2}, \tag{5-78}$$

and

$$\frac{\partial g_8}{\partial \phi} = \frac{\partial^2 g_2}{\partial \phi^2}. \tag{5-79}$$

Using the newly defined parameters, from (5-69)

$$\begin{aligned} \frac{\partial g_7}{\partial \phi} = \frac{\partial^2 g_1}{\partial \phi^2} &= -\left[\frac{\psi_{11}}{\xi_{12}}\right] g_2 - \left[\frac{\psi_{12}}{\xi_{12}}\right] g_3 - \left[\frac{\xi_{16}}{\xi_{12}}\right] \frac{\partial^2 g_3}{\partial \phi^2} - \left[\frac{\xi_{13}}{\xi_{12}}\right] \frac{\partial g_2}{\partial \phi} \\ &= -\left[\frac{\psi_{11}}{a_{12}}\right] g_2 - \left[\frac{\psi_{12}}{a_{12}}\right] g_3 - \left[\frac{\xi_{16}}{\xi_{12}}\right] g_5 - \left[\frac{\xi_{13}}{\xi_{12}}\right] g_8 \end{aligned}; \tag{5-80}$$

from equation (5-70)

$$\begin{aligned} \frac{\partial g_8}{\partial \phi} = \frac{\partial^2 g_2}{\partial \phi^2} &= -\left[\frac{\psi_{21}}{\xi_{22}}\right] g_2 - \left[\frac{\psi_{22}}{\xi_{22}}\right] \frac{\partial g_3}{\partial \phi} - \left[\frac{\xi_{21}}{\xi_{22}}\right] \frac{\partial g_1}{\partial \phi} \\ &= -\left[\frac{\psi_{21}}{\xi_{22}}\right] g_2 - \left[\frac{\psi_{22}}{\xi_{22}}\right] g_4 - \left[\frac{\xi_{21}}{\xi_{22}}\right] g_7 \end{aligned}; \tag{5-81}$$

and from (5-71)

$$\frac{\partial g_6}{\partial \phi} = \frac{\partial^4 g_3}{\partial \phi^4} = -\left[\frac{\xi_{34}}{\xi_{39}}\right] \frac{\partial^2 g_1}{\partial \phi^2} - \left[\frac{\psi_{31}}{\xi_{39}}\right] g_1 - \left[\frac{\psi_{32}}{\xi_{39}}\right] g_3 - \left[\frac{\psi_{34}}{\xi_{39}}\right] \frac{\partial^2 g_3}{\partial \phi^2} - \left[\frac{\psi_{33}}{\xi_{39}}\right] \frac{\partial g_2}{\partial \phi}. \tag{5-82}$$

By applying the newly defined parameters and (5-80), this becomes

$$\frac{\partial g_6}{\partial \phi} = \chi_1 g_1 + \chi_3 g_3 + \chi_5 g_5 + \chi_8 g_8 \tag{5-83}$$

where

$$\chi_1 = \left[\frac{1}{\xi_{39}} \left(\psi_{11} \frac{\xi_{34}}{\xi_{12}} - \psi_{31} \right) \right] \tag{5-84}$$

$$\chi_3 = \left[\frac{1}{\xi_{39}} \left(\psi_{12} \frac{\xi_{34}}{\xi_{12}} - \psi_{32} \right) \right] \tag{5-85}$$

$$\chi_5 = \left[\frac{1}{\xi_{39}} \left(\xi_{16} \frac{\xi_{34}}{\xi_{12}} - \psi_{34} \right) \right] \tag{5-86}$$

$$\chi_8 = \left[\frac{1}{\xi_{39}} \left(\xi_{13} \frac{\xi_{34}}{\xi_{12}} - \psi_{33} \right) \right] \tag{5-87}$$

In matrix form the above system of equations, may now be written as

$$\frac{\partial \{\mathrm{G}\}}{\partial \phi} = [\mathrm{A}]\{\mathrm{G}\} \tag{5-88}$$

where $\{\mathrm{G}\} = [g_1, g_2, \ldots g_8]$ and A is expanded to become

$$\mathrm{A} = \begin{bmatrix} 0 & 0 & 0 & 0 & 0 & 0 & 1 & 0 \\ 0 & 0 & 0 & 0 & 0 & 0 & 0 & 1 \\ 0 & 0 & 0 & 1 & 0 & 0 & 0 & 0 \\ 0 & 0 & 0 & 0 & 1 & 0 & 0 & 0 \\ 0 & 0 & 0 & 0 & 0 & 1 & 0 & 0 \\ \chi_1 & 0 & \chi_3 & 0 & \chi_5 & 0 & 0 & \chi_8 \\ -\psi_{11}/\xi_{12} & 0 & -\psi_{12}/\xi_{12} & 0 & -\xi_{16}/\xi_{12} & 0 & 0 & -\xi_{13}/\xi_{12} \\ 0 & -\psi_{21}/\xi_{22} & 0 & -\psi_{22}/\xi_{22} & 0 & 0 & -\xi_{21}/\xi_{22} & 0 \end{bmatrix}. \tag{5-89}$$

5.1.5 Modified Matrix Progression (MMP)

Consider a discritized grid representative of that shown in Figure 5-5. Note that $\delta\theta$ is an interval spanning between nodes 1 and 2 where 1 is the origin node (j), then 2 must be $(j+1)$. This discritization scheme is employed when computing the frequency parameter and displacement vectors, described below;

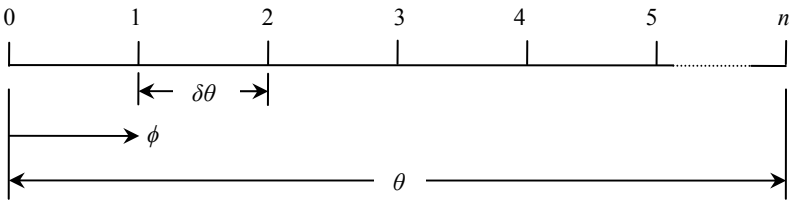

Figure 5-5: Discritization grid nomenclature in ϕ direction

A simplification of (5-88) can be conducted now that the coefficient matrix (Eq. (5-89)) has been evaluated. This simplification is dependent upon the application of boundary conditions applied. The matrix $\{G\}$ will be partitioned into two sub matrices where $\{G^*\}$ contains rows 1 through 4 of $\{G\}$ and $\{G^{**}\}$ occupies rows 5 through 8. Using this nomenclature, the generic boundary condition for (5-88) applied at $\phi = 0$ may be written as

$$\{G_0\} = \begin{Bmatrix} g_1 \\ g_2 \\ g_3 \\ g_4 \\ g_5 \\ g_6 \\ g_7 \\ g_8 \end{Bmatrix}_0 = [J_0(8\times 4)] \times \{G_0^{**}(4\times 1)\} \tag{5-90}$$

where the subscript 0 represents the boundary value at $\phi = 0$. J_0 in (5-90) is the coefficient matrix which includes all boundary values at the edge $\phi = 0$. The conditions at the other end, $\phi = \theta$, are expressed as

$$[K_\theta(4\times 8)] \times [G_\theta(8\times 1)] = \{0\} \tag{5-91}$$

where $[K_\theta]$ is the coefficient matrix in this case representing the boundary values present along the edge $\phi = \theta$. The solution of (5-88) is taken to be of the form

$$\{G_1\} = e^{[A]\phi}\{G_o\} = [H_1]\{G_o\} \tag{5-92}$$

where $[H_1] = e^{[A]\phi}$ is the exponentiation of $[A]\phi$. Introducing the boundary (5-90) gives the following solution at node *n* = 1 (Figure 5-5).

$$\{G_1\} = e^{[A]\phi}[J_0]\{G_0^{**}\} = [H_1][J_0]\{G_0^{**}\} = [F_1]\{G_0^{**}\} \tag{5-93}$$

where $[F_1]$ is the product of $[H_1]$ and $[J_0]$. At $\phi = \theta$

$$\begin{aligned}\{G_\phi\} &= e^{[A]\phi}[J_0]\{G_0^{**}\} \\ &= [H][J_0]\{G_0^{**}\}\end{aligned} \tag{5-94}$$

Pre-multiplying by $[K_\theta]$ and introducing the boundary equation, (5-91) yields

$$[K_\theta][H][J_0]\{G_0^{**}\} = 0 \tag{5-95}$$

This matrix equation represents four linear algebraic equations in the unknowns $\{G_0^{**}\}$, the matrix $[H]$ being a function of the frequency parameter Δ. For a non-trivial solution the determinant of coefficients should vanish [97], that is

$$\left|[K_\theta][H][J_0]\right| = 0 \tag{5-96}$$

which is the frequency determinant. Experience has shown that two of the off-diagonal elements of the matrix $[A]$ are very large in comparison with the other elements. This causes the determinant to increase monotonically with Δ, resulting in the disappearance of all the eigenvalues. This difficulty is overcome by dividing the interval $(0,\theta)$ into n_1 equal sub-intervals of size $\theta_1 = \theta/n_1$ and applying a modified matrix progression technique. At $\phi = \theta_1$

$$\{G_1\} = e^{[A]\phi_1}\{G_0\} = [H_1]\{G_0\} \tag{5-97}$$

Introducing the boundary equation (5-90) gives

$$\{G_1\} = [H_1][J_0]\{G_0^{**}\} = [F_1]\{G_0^{**}\} \tag{5-98}$$

Now partition this equation in the form

$$\begin{Bmatrix} G_1^{*}(4\times 1) \\ G_1^{**}(4\times 1) \end{Bmatrix} = \begin{bmatrix} F_1^{*}(4\times 4) \\ F_1^{**}(4\times 4) \end{bmatrix}\{G_0^{**}\} \tag{5-99}$$

where

$$\{G_1^{**}\} = [F_1^{**}]\{G_0^{**}\} \tag{5-100}$$

therefore

$$\{G_0^{**}\} = [F_1^{**}]^{-1}\{G_1^{**}\} \tag{5-101}$$

Substituting (5-101) into (5-99) gives

$$\{G_1\} = \left\{[F_1^{*}][F_1^{**}]^{-1}\right\}\{G_1^{**}\} = [J_1]\{G_1^{**}\} \tag{5-102}$$

I

where I is a (4x4) identity matrix. Similarly at $\phi = \theta_2$

$$\begin{aligned}\{G_2\} &= e^{[A]\phi_2}\{G_0\} \\ &= e^{[A]\phi_1}e^{[A]\phi_1}\{G_0\} \\ &= e^{[A]\phi_1}\{G_1\}\end{aligned} \tag{5-103}$$

The above procedure can now be repeated to give

$$\{G_2\} = [J_2]\{G_2^{**}\} \tag{5-104}$$

This process is repeated for all the sub-intervals. The final interval gives

$$\{G_{n_1}\} = [J_{n_1}]\{G_{n_1}^{**}\} = \{G_\theta\} \tag{5-105}$$

Pre-multiplying by $[K_\theta]$ and introducing the boundary equation (5-91) yields

$$[K_\theta][J_{n_1}]\{G_{n_1}^{**}\} = \{0\} \tag{5-106}$$

Since the matrix $[J_{n_1}]$ is a function of the frequency parameter Δ, the frequency determinant is

$$\left|[K_\theta][J_{n_1}]\right| = 0 \tag{5-107}$$

Recall from (5-96) that $\left|[K_\theta][H][J_0]\right| = 0$ then $[H][J_0] = [J_n]$; either relation (equation (5-96) or (5-107)) may be used to solve for the roots, that satisfy the eight equations of motion; (5-107) is employed here. This is due to the operation $[F_1^*][F_1^{**}]^{-1}$ which is performed at every step. No analytical solution to (5-107) has yet been successfully developed requiring the support of an iterative method. The numerical iterative technique adopted for this study is indicated in Figure 5-6. Each eigenvalue provides for a unique solution of (5-106) for $\{G_{n_1}^{**}\}$. This is used to determine the eigenvectors as follows. At the j^{th} step

$$\{G_j^{**}\} = [F_{j+1}^{**}]\{G_{j+1}^{**}\} \tag{5-108}$$

and

$$\{G_j\} = [J_j]\{G_j^{**}\} \tag{5-109}$$

Therefore a forward sweep of $\phi \in [0, \theta]$ is performed to determine the eigenvalues that satisfy the boundary conditions; once this is accomplished a backward sweep is

conducted using (5-108) and (5-109) to calculate the eigenvectors in each prescribed direction for a given eigenvalue solution.

5.1.5.1 Prescribing Straight Edge Boundary Conditions (ϕ = constant)

Recall from (5-36) through (5-41), the generic constraints for edge type boundary conditions are presented. Using these generic constraints and applying them to the two cases considered as a part of this study (C-F-SS-F and C-F-C-F) the following forcing function, is determined at prescribed ϕ values.

For the case of a clamped edge at $\phi = 0$, the conditions are $g_1 = g_2 = g_3 = g_4 = 0$; the forcing function then becomes

$$\mathrm{G}_0 = \begin{bmatrix} 0 & 0 & 0 & 0 \\ 0 & 0 & 0 & 0 \\ 0 & 0 & 0 & 0 \\ 0 & 0 & 0 & 0 \\ 1 & 0 & 0 & 0 \\ 0 & 1 & 0 & 0 \\ 0 & 0 & 1 & 0 \\ 0 & 0 & 0 & 1 \end{bmatrix}_o \times \begin{Bmatrix} g_5 \\ g_6 \\ g_7 \\ g_8 \end{Bmatrix}_o \tag{5-110}$$

Recall from (5-90) that the matrix notation for (5-110) is

$$\{\mathrm{G}_0\} = [\mathrm{J}_0]\{\mathrm{G}_0^{**}\}$$

Now considering the case of a clamped edge at $\phi = \theta$, the conditions are $g_1 = g_2 = g_3 = g_4 = 0$ and the forcing function becomes

$$\begin{bmatrix} 1 & 0 & 0 & 0 & 0 & 0 & 0 & 0 \\ 0 & 1 & 0 & 0 & 0 & 0 & 0 & 0 \\ 0 & 0 & 1 & 0 & 0 & 0 & 0 & 0 \\ 0 & 0 & 0 & 1 & 0 & 0 & 0 & 0 \end{bmatrix}_\phi \times \begin{bmatrix} g_1 \\ g_2 \\ g_3 \\ g_4 \\ g_5 \\ g_6 \\ g_7 \\ g_8 \end{bmatrix}_\phi = \begin{bmatrix} 0 \\ 0 \\ 0 \\ 0 \end{bmatrix}_\phi \tag{5-111}$$

Recall from (5-91), the matrix notation for (5-111) is

$$[\mathrm{K}_\theta]\{\mathrm{G}_\theta\} = 0$$

Considering the case where one straight edge is clamped and the other is simply supported recall (5-110) for the straight edge with $\phi = 0$. The appropriate boundary conditions for the simply supported edge at $\phi = \theta$ corresponds to conditions of

$g_1 = g_3 = \partial g_2 / \partial \phi = \partial^2 g_3 / \partial \phi^2 = 0$ and based on the relations previously presented reduces to $g_1 = g_3 = g_5 = g_8 = 0$, therefore the forcing function becomes

$$\begin{bmatrix} 1 & 0 & 0 & 0 & 0 & 0 & 0 & 0 \\ 0 & 0 & 1 & 0 & 0 & 0 & 0 & 0 \\ 0 & 0 & 0 & 0 & 1 & 0 & 0 & 0 \\ 0 & 0 & 0 & 0 & 0 & 0 & 0 & 1 \end{bmatrix}_{\phi} \times \begin{bmatrix} g_1 \\ g_2 \\ g_3 \\ g_4 \\ g_5 \\ g_6 \\ g_7 \\ g_8 \end{bmatrix}_{\phi} = \begin{bmatrix} 0 \\ 0 \\ 0 \\ 0 \end{bmatrix}_{\phi} \tag{5-112}$$

Utilizing the above technique along with a modified version of the algorithm for solving free vibration of a curved plate developed by Petyt [85] and expanding upon it to include body forces (P_r and P_x) one can create a relation between the axial forces imposed along the plate (P_x) as well as those applied in this radial direction (P_r) and their affect on the frequency parameter, or eigenvalue of the system.

Note that the results from a set of test cases are presented in Chapter 6 using the algorithm presented in Figure 5-6 and compared against results produced from other studies to verify that the plate stability model behaves as it should.

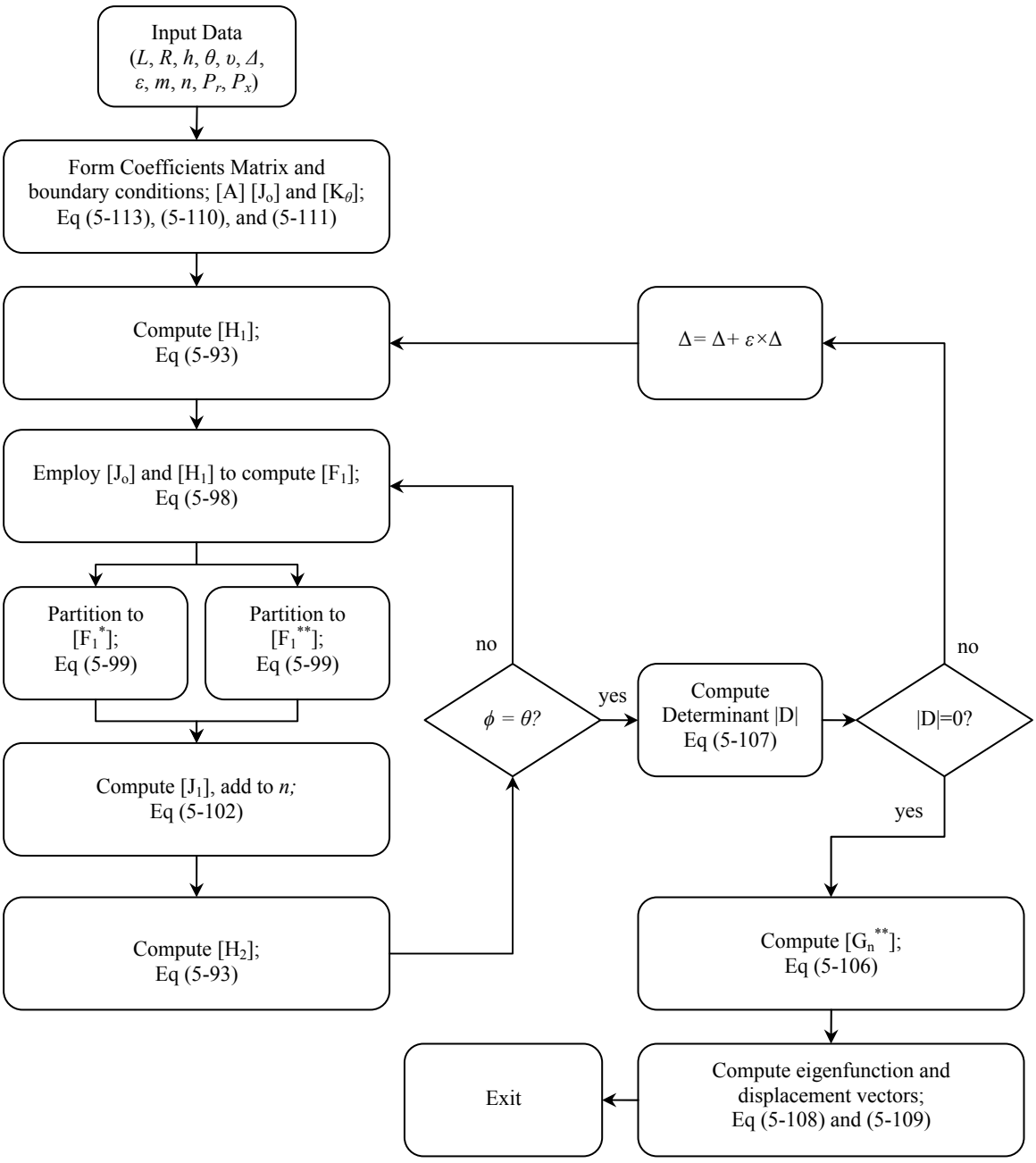

Figure 5-6: Flow diagram of modified matrix progression

5.2 Flow Module

The purpose of the flow module is to develop an estimate for the axial pressure (P_x) and radial pressure (P_r) imposed on the plate. These pressure values are onset from the flow field created by geometries similar to those of two adjacent subchannels in an ATR fuel element. Once acquired, these pressure values are inserted into the equations of motion in the plate stability module which is used to estimate modal stability of a cylindrical plate under axial flow conditions.

5.2.1 General Theory

The law of conservation of mass states that mass may neither be created nor destroyed. With respect to a control volume, the law of conservation of mass may be stated as

$$\left\{\begin{array}{c}\text{Rate of accumulation}\\ \text{of mass within}\\ \text{control volume}\end{array}\right\}+\left\{\begin{array}{c}\text{Rate of mass}\\ \text{efflux from}\\ \text{control volume}\end{array}\right\}-\left\{\begin{array}{c}\text{Rate of mass}\\ \text{flow into}\\ \text{control volume}\end{array}\right\}=0\,.$$

Mathematically, the integral expression for the mass balance over a general control volume then becomes

$$\frac{\partial}{\partial t}\iiint_{\text{c.v.}}\rho dV+\iint_{\text{c.s.}}\rho\left(\bar{\text{v}}\cdot\bar{\text{n}}\right)dS=0 \tag{5-114}$$

where $\bar{\text{v}}\cdot\bar{\text{n}}$ represents the fluid passing through the control surface; assuming steady flow conditions and integrating through the control surface from point *o* (outlet) to point *i* (inlet) such that all fluid passes through point *i* and exits at point *o*

$$\rho_o u_o S_o-\rho_i u_i S_i=0\,. \tag{5-115}$$

Assuming incompressible fluid state conditions, conservation of mass is extended to conservation of flow, or

$$u_o S_o-u_i S_i=0\,. \tag{5-116}$$

The first law of thermodynamics states that if a system is carried through a cycle, the total heat added to the system from its surroundings is proportional to the work done by the system on its surroundings, or

$$\left\{\begin{array}{c}\text{Rate of addition of}\\ \text{heat to control volume}\\ \text{from surroundings}\end{array}\right\}-\left\{\begin{array}{c}\text{Rate of work done}\\ \text{by control volume}\\ \text{on its surroundings}\end{array}\right\}$$

$$=\left\{\begin{array}{c}\text{Rate of accumulation}\\ \text{of energy within}\\ \text{control volume}\end{array}\right\}+\left\{\begin{array}{c}\text{Rate of energy efflux}\\ \text{from control volume}\\ \text{due to fluid flow}\end{array}\right\}-\left\{\begin{array}{c}\text{Rate of energy entering}\\ \text{control volume}\\ \text{due to fluid flow}\end{array}\right\}.$$

Mathematically, conservation of energy is

$$\frac{\delta Q}{\partial t}-\frac{\delta W}{\partial t}=\frac{\partial}{\partial t}\iiint_{\text{c.v.}}\vartheta\rho dV+\iint_{\text{c.s.}}\left(\vartheta+\frac{P}{\rho}\right)\rho\left(\bar{\text{v}}\cdot\bar{\text{n}}\right)dS\,, \tag{5-117}$$

where $\vartheta=\varsigma+\bar{u}^2/2+gz$ is the specific energy which includes the potential energy (gz) due to position of the fluid continuum in the gravitational field, the kinetic energy $\left(\bar{u}^2/2\right)$ of the fluid due to its velocity, and the internal energy (ς) of the fluid due to its thermal state; while P/ρ is termed the flow work, or the ratio of the thermodynamic pressure and fluid density. Note that flow work and fluid internal energy may be summed to equal fluid enthalpy $(h=\varsigma+P/\rho)$. Given the coordinate system of interest (i.e. vertical convective flow) the vector in-line with the gravitational field is congruent to the axial flow direction $(z=x)$. Integrating the energy equation similar to that done with the continuity equation, (5-114), assuming steady flow, no work is done, no heat is produced in the control volume, and the cross sectional flow area is constant along a straight length, then

$$\left(\frac{P}{\rho}+\frac{U^2}{2}+gx\right)_o-\left(\frac{P}{\rho}+\frac{U^2}{2}+gx\right)_i=0\,, \tag{5-118}$$

where U is the superficial fluid velocity. Equation (5-118) is most commonly referred to as Bernoulli's equation. Equation (5-118) may be reformulated to produce a differential pressure given as

$$\Delta P=P_o-P_i=\frac{\rho U_i^{\,2}}{2}\left(\varpi\frac{x_o-x_i}{D_h}+K\right)+\rho g\left(x_o-x_i\right). \tag{5-119}$$

The relations associated with kinetic energy of the fluid are referred to as non-recoverable pressure losses and are accounted for by form losses (K) and friction losses (ϖ).

5.2.2 *Development of Geometric Relations*

The flow system's cross sectional geometry is represented by Figure 5-7. The flow geometry assumes (1) 'perfect' cylindrical geometry, where the curvature for inner and outer radii of a single flow channel is uniform through the entire prescribed region, (2) uniform fuel plate thickness (a), and (3) the fuel plate considered during the study is uniform in both the azimuthal (ϕ) and axial (x) direction.

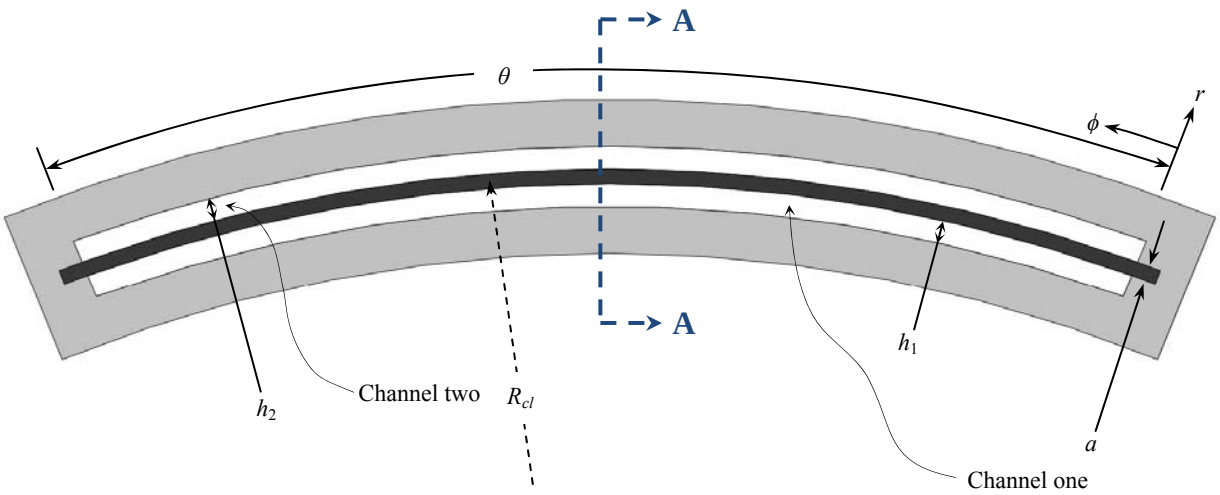

Figure 5-7: Top-down view of flow channel geometry

Considering the diagram above, the outer radius of channel two ($R_{2,o}$) may be defined as

$$R_{2,o} = R_{cl} + a/2 + h_2 \tag{5-120}$$

assuming a uniform plate thickness, a, and uniform flow channel height, h_2. Similarly, the inner radius of channel two ($R_{2,i}$) is then

$$R_{2,i} = R_{cl} + a/2\,. \tag{5-121}$$

The outer and inner radii for channel one may be defined using the same methodology as channel two, where

$$R_{1,o} = R_{cl} - a/2 \tag{5-122}$$

and

$$R_{1,i} = R_{cl} - a/2 - h_1\,. \tag{5-123}$$

Each flow channel's cross sectional area may then be assessed as

$$S_2 = \pi\left(R_{2,o}^2 - R_{2,i}^2\right)\left(\frac{\theta}{2\pi}\right) \tag{5-124}$$

and

$$S_1 = \pi\left(R_{1,o}^2 - R_{1,i}^2\right)\left(\frac{\theta}{2\pi}\right) \tag{5-125}$$

The hydraulic diameter is defined as $D_h = 4S/P_w$, where P_w is the wetted perimeter of a flow channel. Then the hydraulic diameter for flow channel two and one, respectively, may be described as

$$D_{h,2} = \frac{4S_2}{2h_2 + \left(R_{2,o} + R_{2,i}\right)\theta} \tag{5-126}$$

and

$$D_{h,1} = \frac{4S_1}{2h_1 + \left(R_{1,o} + R_{1,i}\right)\theta} \tag{5-127}$$

A vertical cross section of Figure 5-7 is given in Figure 5-8. From Figure 5-8, the inlet region of the fuel element is considered to have a common flow channel of length ℓ_i, and a common outlet of length ℓ_o. The hydraulic diameter of the inlet flow and outlet flow channel is then equivalent to

$$D_{h,i} = D_{h,o} = \frac{4S_i}{2h_1 + 2h_2 + 2a + \left(R_{2,o} + R_{1,i}\right)\theta}. \tag{5-128}$$

and the cross sectional area is

$$S_i = S_o = \pi\left(R_{2,o}^2 - R_{1,i}^2\right)\left(\frac{\theta}{2\pi}\right) \tag{5-129}$$

Given a prescribed inlet flow rate at $x = 0$ in Figure 5-8 the pressure field is uniform until it reaches the inlet of each subchannel. The flow field is forced to divide while passing through channel one and channel two and then remerges at $x = \ell_i + L$. Figure 5-9 presents a graphical sketch of the pressure profile along the axial length of the fuel element. Notice that at $x = \ell_i$ and $x = \ell_i + L$ the pressure associated with channel one and channel two is common. This is due to the unification of flow in the inlet and outlet regions of the fuel element.

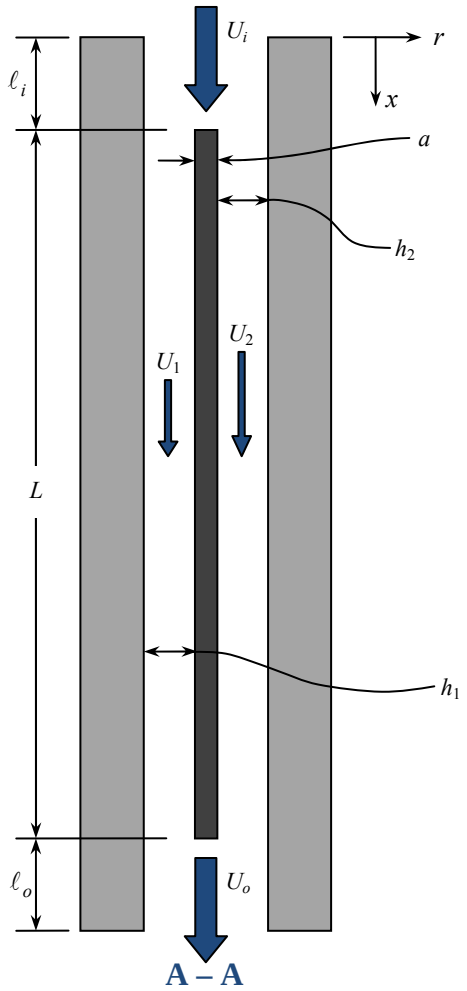

Figure 5-8: Vertical cross sectional view of flow channel geometry

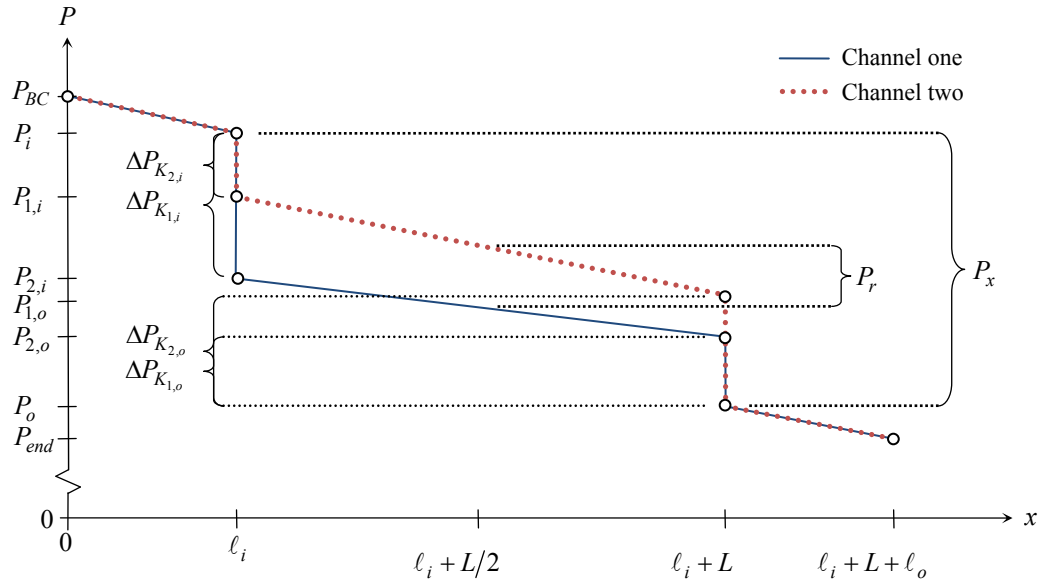

Figure 5-9: Pressure profile along flow direction

Recall from (5-119) that there are three components to pressure loss in Bernoulli's equation: (1) gravitation losses, (2) form losses, and (3) friction losses. The friction losses for pipe flow are addressed through the Fanning friction factor given for laminar flow is given as [98]

$$\varpi = 64\,\mathrm{Re}^{-1} \tag{5-130}$$

where Re is the Reynolds number and is defined as Re = $(\rho D_h U)/\mu$ and D_h is the hydraulic diameter. Onset of turbulent flow for this study is analogous of that considered for 'internal flows' and applies to Reynolds numbers in excess of 2300. The turbulent friction factored employed and developed specifically for the safety analysis of the ATR is [20]

$$\varpi = 0.0024 + 0.358\,\mathrm{Re}^{-0.437}\,. \tag{5-131}$$

Primary consideration will be given to (5-131), as the coolant velocities observed under normal operations in the ATR produce Re of the order 10^4 and larger.

Considering only friction losses through a given region of the fuel element while employing (5-119) results in the following general formulation of pressure loss equation:

$$\Delta P_f = \frac{\rho U^2}{2}\left(\varpi \frac{x_o - x_i}{D_h}\right). \tag{5-132}$$

The generalized equation above may be specified for four applicable locations within the fuel element including the (1) inlet region, (2) channel one, (3) channel two, and (4) outlet region:

$$\Delta P_{f,i} = \frac{\rho U_i^{\,2}}{2}\left(\varpi_i \frac{\ell_i}{D_{h,i}}\right), \tag{5-133}$$

$$\Delta P_{f,1} = \frac{\rho U_1^{\,2}}{2}\left(\varpi_1 \frac{L}{D_{h,1}}\right), \tag{5-134}$$

$$\Delta P_{f,2} = \frac{\rho U_2^{\,2}}{2}\left(\varpi_2 \frac{L}{D_{h,2}}\right), \tag{5-135}$$

and

$$\Delta P_{f,o} = \frac{\rho U_o^{\,2}}{2}\left(\varpi_o \frac{\ell_o}{D_{h,o}}\right). \tag{5-136}$$

The form losses in (5-119) are accounted for through the form loss coefficient (K). The form loss coefficient is a localized geometric parameter that quantifies fluid flow resistance due to a local change in geometry. The inlet and outlet form loss coefficients represent the form losses of the flow redistribution from a single bulk flow channel to individual flow channels surrounding each fuel plate. Form loss is a dimensionless parameter and is given as [98]

$$K = \frac{2\Delta P}{\rho \bar{u}^2}. \tag{5-137}$$

The general form loss relation presented above is not easily quantified, for this reason it is assumed that the form losses are comprised of either sudden expansions or sudden contractions (5-138) and (5-139) [99].

$$K_{SE} = \left(1 - \frac{D_{h,i}^2}{D_{h,o}^2}\right)^2 \tag{5-138}$$

and

$$K_{SC} \approx 0.42\left(1 - \frac{D_{h,o}^2}{D_{h,i}^2}\right) \tag{5-139}$$

Sudden expansion form losses typically result in a form loss less than a value of 1.0. For low flow, low pressure systems the resulting form loss is approximately 0.3. A visual of a sudden expansion and contraction is presented in Figure 5-10.

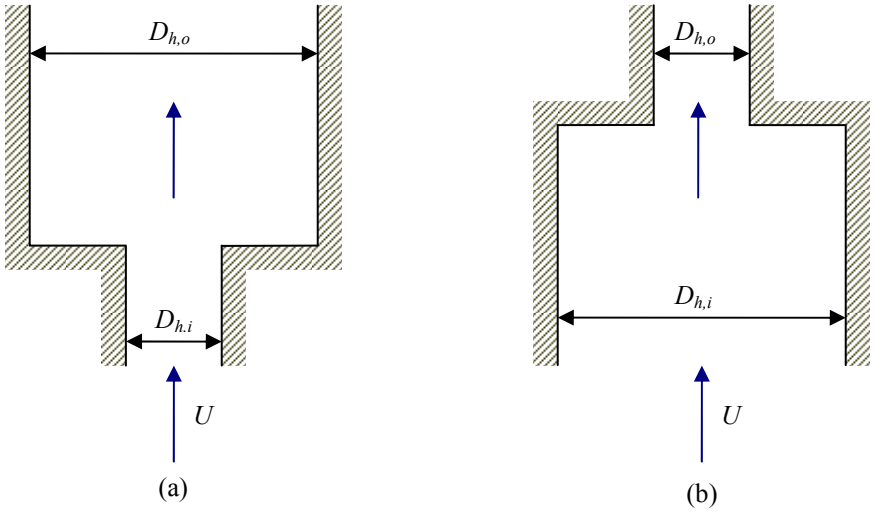

Figure 5-10: Geometry of (a) sudden expansion and (b) sudden contraction

The friction factor correlation chosen to use throughout this study was taken from the ATR UFSAR [20], and was experimentally acquired. Because this relation was acquired through experimental methods, there is an inherent characteristic uncertainty associated with it. A comparison of the friction factor used during this study is made against other widely used friction factor correlations including the Haaland correlation [100], Churchill correlation [101], Moody correlation [102], and McAdams correlation [103], all seen below

$$\frac{1}{\sqrt{f_{\text{Haaland}}}} = -1.8\log\left(\frac{6.9}{\text{Re}} + \left(\frac{\varepsilon/D_h}{3.7}\right)^{1.11}\right), \tag{5-140}$$

$$f_{\text{Churchill}} = 1.325\left(\ln\left(\frac{3.7D_h}{\varepsilon} + \frac{5.74}{\text{Re}^{0.9}}\right)\right)^{-2}, \tag{5-141}$$

$$f_{\text{Moody}} = 0.0055\left(1 + \left(2\times10^4\,\frac{\varepsilon}{D_h} + \frac{10^6}{\text{Re}}\right)^{0.333}\right), \tag{5-142}$$

and

$$f_{\text{McAdams}} = \frac{0.184}{\text{Re}^{0.2}}. \tag{5-143}$$

where ε in this case is the wall surface roughness and is assumed to be 0.11 micro-meters as this is the surface roughness employed throughout the ATR safety analysis [20]. Plotting the output friction factors for (5-131) and (5-140) through (5-143) over a spectrum of Re yields the distributions seen in Figure 5-11. Notice that all relations are quite similar in both trend and magnitude with exception of the Churchill correlation. Of the similar four correlations, the correlation created specifically for the ATR results in the smallest friction factor over the entire flow regime, if compared against the Haaland correlation, the friction factors deviate by approximately 13% at the lowest Reynolds number. This demonstrates that of the similar friction factor relations the influence on pressure drop due to frictional losses may deviate as much as approximately 13%, depending on the friction factor correlation used.

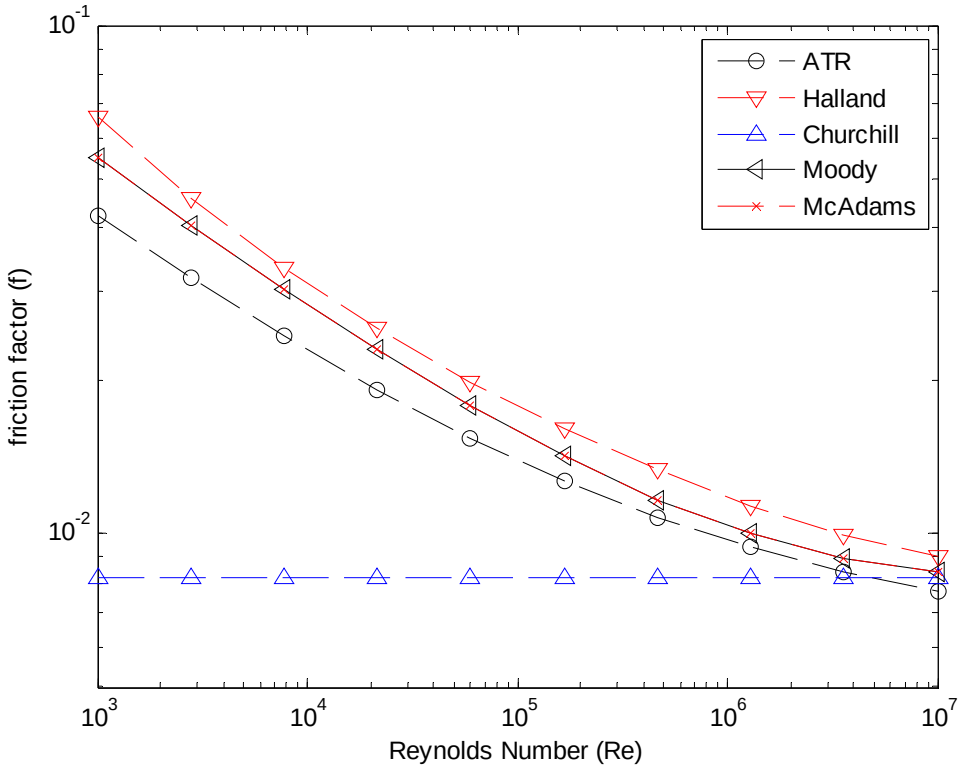

Figure 5-11: Comparison of friction factor coefficients against Reynolds Number

The pressure loss resulting from abrupt geometric changes may be evaluated differently depending on the empirical relation considered during the study. During this study (5-139) was used to estimate the non-recoverable pressure loss due to a sudden contraction in cross sectional and (5-138) was used to estimate the non-recoverable pressure loss caused by a sudden expansion in cross sectional flow area.

Two common explicit form loss values are generally employed when considering sudden contractions; 0.5 and 0.3 [104]. The values calculated for the geometry identified in Table 4-1 for a sudden expansion form loss for channel one was found to be 0.7189 and for two is 0.7187. The largest difference in form losses between that of channel one and the 0.3 form loss suggested by Abdelall et al. [104] resulting in a 81.0% difference in form loss values suggesting that the influence of pressure loss on that of the applied relation for a sudden expansion may be as large as approximately 81%.

Two common explicit form losses are generally utilized when accounting for sudden expansions including 0.4 [98] and 0.36 [104]. The values calculated for the geometry described in Table 4-1 for a sudden expansion form loss for channel one was found to be 0.3561 and for two is 0.3560. The values produced for this study relate well with those presents in other literature. A difference of approximately 11% is found between the form loss value suggested by White [98] and that calculated the sudden contraction of flow entering channel two.

Of the three non-recoverable pressure loss relations considered including friction losses, sudden contraction form losses, and sudden expansion form losses; it is found that the largest uncertainties when compared against other commonly used relations are found to be associated with the sudden contraction form losses while the other the relations correlate, in general, reasonably well with other published information.

Given an initial inlet superficial velocity of U_i from Figure 5-8, an estimate for individual flow channel velocities may be made by satisfying conservation of momentum and requiring the fluid pressure at the inlet of each flow channel (one and two) to be equal. This is done by assuming that the flow experiences a sudden contraction form loss at the inlet of flow channels one and two where the inlet hydraulic diameter in (5-139) is governed by (5-128) and the outlet hydraulic diameter is given by (5-126) or (5-127). The form loss coefficients associated with the sudden contraction of each flow channel are then defined as

$$K_{1,i} = 0.42\left(1-\frac{D_{h,1}^2}{D_{h,i}^2}\right) \tag{5-144}$$

and

$$K_{2,i} \approx 0.42\left(1-\frac{D_{h,2}^2}{D_{h,i}^2}\right). \tag{5-145}$$

Then employing (5-119), (5-144), and (5-145) for the inlet of each flow channel,

$$\Delta P_{K_{1,i}} = \frac{\rho_1 U_1^2}{2} K_{1,i} \tag{5-146}$$

and

$$\Delta P_{K_{2,i}} = \frac{\rho_2 U_2^2}{2} K_{2,i}\,, \tag{5-147}$$

which accounts for the non-recoverable losses associated with this geometric region. Applying (5-138) to the outlet region of each subchannel yields

$$K_{1,o} = \left(1 - \frac{D_{h,1}^2}{D_{h,o}^2}\right)^2 \tag{5-148}$$

and

$$K_{2,o} = \left(1 - \frac{D_{h,2}^2}{D_{h,o}^2}\right)^2 . \tag{5-149}$$

Similar to the methodology used to evaluate ΔP_{K_i}, the pressure drop as a result of each sudden expansion into the common flow channel must be evaluated; where

$$\Delta P_{K_{1,o}} = \frac{\rho U_1^2}{2} K_{1,o}\,, \tag{5-150}$$

and

$$\Delta P_{K_{2,o}} = \frac{\rho U_2^2}{2} K_{2,o}\,. \tag{5-151}$$

An assessment of the superficial velocities associated with each subchannel may be acquired by recalling that the pressure P_i and P_o in Figure 5-9 are common for both channel one and channel two pressure profiles. This observation forces the total pressure loss on the interval $x \in [\ell_i, \ell_i + L]$ for each flow channel to be equal in magnitude. Then the total pressure loss over this prescribed length within the fuel element associated with channel one may be described from the general pressure loss equation, (5-119)

$$\begin{aligned}
\Delta P_1 &= \Delta P_{K_{1,i}} + \Delta P_{f,1} + \Delta P_{K_{1,o}} \\
&= \frac{\rho_1 U_1^2}{2}\left(0.42\left(1 - \frac{D_{h,1}^2}{D_{h,i}^2}\right)\right) + \frac{\rho {U_1}^2}{2}\left(\varpi_1 \frac{L}{D_{h,1}}\right) + \frac{\rho U_1^2}{2}\left(1 - \frac{D_{h,1}^2}{D_{h,o}^2}\right)^2 \\
&= \frac{\rho_1 U_1^2}{2}\left[0.42\left(1 - \frac{D_{h,1}^2}{D_{h,i}^2}\right) + \left(\varpi_1 \frac{L}{D_{h,1}}\right) + \left(1 - \frac{D_{h,1}^2}{D_{h,o}^2}\right)^2\right].
\end{aligned} \tag{5-152}$$

Similarly, the pressure drop along channel two may be accounted for as

$$\begin{aligned}\Delta P_2 &= \Delta P_{K_{2i}} + \Delta P_{f,2} + \Delta P_{K_{2,o}} \\ &= \frac{\rho_2 U_2^2}{2}\left(0.42\left(1-\frac{D_{h,2}^2}{D_{h,i}^2}\right)\right)+\frac{\rho {U_2}^2}{2}\left(\varpi_2\frac{L}{D_{h,2}}\right)+\frac{\rho U_2^2}{2}\left(1-\frac{D_{h,2}^2}{D_{h,o}^2}\right)^2 \\ &= \frac{\rho_2 U_2^2}{2}\left[0.42\left(1-\frac{D_{h,2}^2}{D_{h,i}^2}\right)+\left(\varpi_2\frac{L}{D_{h,2}}\right)+\left(1-\frac{D_{h,2}^2}{D_{h,o}^2}\right)^2\right].\end{aligned} \tag{5-153}$$

By observation, ΔP_1 and ΔP_2 must be equal

$$\begin{aligned}&\frac{\rho_1 U_1^2}{2}\underbrace{\left[0.42\left(1-\frac{D_{h,1}^2}{D_{h,i}^2}\right)+\left(\varpi_1\frac{L}{D_{h,1}}\right)+\left(1-\frac{D_{h,1}^2}{D_{h,o}^2}\right)^2\right]}_{e_1} \\ &\quad = \frac{\rho_2 U_2^2}{2}\underbrace{\left[0.42\left(1-\frac{D_{h,2}^2}{D_{h,i}^2}\right)+\left(\varpi_2\frac{L}{D_{h,2}}\right)+\left(1-\frac{D_{h,2}^2}{D_{h,o}^2}\right)^2\right]}_{e_2}\end{aligned} \tag{5-154}$$

From conservation of flow in (5-116) the flow passing through each subchannel must sum to the total inlet flow,

$$U_i S_i = U_1 S_1 + U_2 S_2 . \tag{5-155}$$

Solving for U_2 in (5-155) yields

$$U_2 = \left(U_i S_i - U_1 S_1\right)\left(S_2\right)^{-1} . \tag{5-156}$$

The newly formulated relation for the superficial velocity in channel two from (5-156) may be inserted into (5-154)

$$U_1^2\frac{\rho_1 e_1}{2} = \left[\left(U_i S_i - U_1 S_1\right)\left(S_2\right)^{-1}\right]^2\frac{\rho_2 e_2}{2} \tag{5-157}$$

Simplifying (5-157) and removing common terms allows for the explicit solution of U_1

$$0 = U_1^2\left(\left(\frac{S_1}{S_2}\right)^2 e_2 - e_1\right) - U_1\left(\frac{U_i S_i S_1 e_2}{S_2^2}\right)+\left(\frac{U_i S_i}{S_2}\right)^2 e_2 \tag{5-158}$$

Notice the quadratic form of (5-158). The superficial velocity for subchannel one in (5-158) may now be solved for given an inlet flow rate and geometric boundary conditions. Recall that e_1 and e_2 in (5-158) contain Reynolds dependant friction factors, which must also be solved for simultaneously. Inserting in specific subchannel velocities into (5-131) yields

$$\varpi_1 = 0.0024 + 0.358\left(\frac{U_1\rho D_{h,1}}{\mu}\right)^{-0.437} \tag{5-159}$$

and

$$\varpi_2 = 0.0024 + 0.358\left(\frac{U_2 \rho D_{h,2}}{\mu}\right)^{-0.437} . \tag{5-160}$$

Recalling conservation of flow, (5-160) may be reformulated as

$$\varpi_2 = 0.0024 + 0.358\left(\frac{\left[\left(U_i S_i - U_1 S_1\right)\left(S_2\right)^{-1}\right]\rho D_{h,2}}{\mu}\right)^{-0.437} . \tag{5-161}$$

Formulations for the superficial velocity in channel one and the Fanning friction factor in channel one and two have now been acquired. Each of these variables may now be implicitly solved for.

Once U_1 has been obtained the superficial velocity in subchannel two can be tabulated by inserting the solution of (5-158) back into (5-155) yielding U_2.

5.2.3 Determination of Axial Membrane Pressure

Recall from section 5.1.4 that the eigenfunctions along the *x* (axial) direction have been assumed in the plate stability module. For this reason, only a single discrete value for P_x may be inserted in the equations of motion, therefore only an estimate for the average pressure induced by the fluid acting against the plate is needed for P_x.

The membrane pressure P_x acting along the axial direction may be acquired through (5-152) or (5-153), as these are both equal in valve in order to satisfy conservation of momentum.

5.2.4 Determination of Radial Membrane Pressure

The radial pressure (P_r) is equivalent to the net pressure acting on the primary surface of the plate due to a relative pressure difference in adjacent subchannels such that a P_r value is found to be in the outward radial direction or the pressure in channel one subtracted from the pressure in subchannel two. This net difference in pressure is acquired by evaluating the inlet pressure losses caused by sudden contraction in each flow channel, and then evaluating the pressure loss caused by viscous effects evaluated at half the

length of the plate as this is assumed to produce an appropriate value for the average pressure loss along the length of each flow channel,

$$\begin{aligned}\Delta\bar{P}_{L_1} &= \frac{1}{L}\int_0^L \frac{\rho U_1^2}{2}\left(\varpi_1 \frac{x}{D_{h,1}}\right)dx \\ &\cong \frac{\rho U_1^2}{2}\left(\varpi_1 \frac{L}{2D_{h,1}}\right),\end{aligned} \tag{5-162}$$

and

$$\begin{aligned}\Delta\bar{P}_{L_2} &= \frac{1}{L}\int_0^L \frac{\rho U_2^2}{2}\left(\varpi_2 \frac{x}{D_{h,2}}\right)dx \\ &\cong \frac{\rho U_2^2}{2}\left(\varpi_2 \frac{L}{2D_{h,2}}\right).\end{aligned} \tag{5-163}$$

Then the net pressure may be acquired as

$$P_r = \left(\Delta P_{K_{1,i}} + \Delta\bar{P}_{L_1}\right) - \left(\Delta P_{K_{2,i}} + \Delta\bar{P}_{L_2}\right). \tag{5-164}$$

5.3 Closing

Applying the plate dynamics equations using Kantorovich reduction along the axial length and solving them with the MMP technique allows for the closure of the plate dynamics equations. However, because this study's interest is focused on the onset of instability due to hydro-elastic forces, a modified version of Petyt's algorithm will be used to allow for an approach to incorporate hydro-dynamic forcing functions in the MMP model. Utilizing the values produced in (5-152) and (5-164) which result from the flow module and insertion into the plate stability module, an estimate for the modal stability of a cylindrical plate under axial flow conditions may be acquired. This alternative version of the MMP method is presented in Figure 5-12, while the added step for explicit calculation of the pressure field values is highlighted. A presentation and discussion of the flow induced vibration model developed under axial flow conditions follows. Matlab® was used exclusively to develop and couple the plate stability module and flow module as well as produce all results presented during this study.

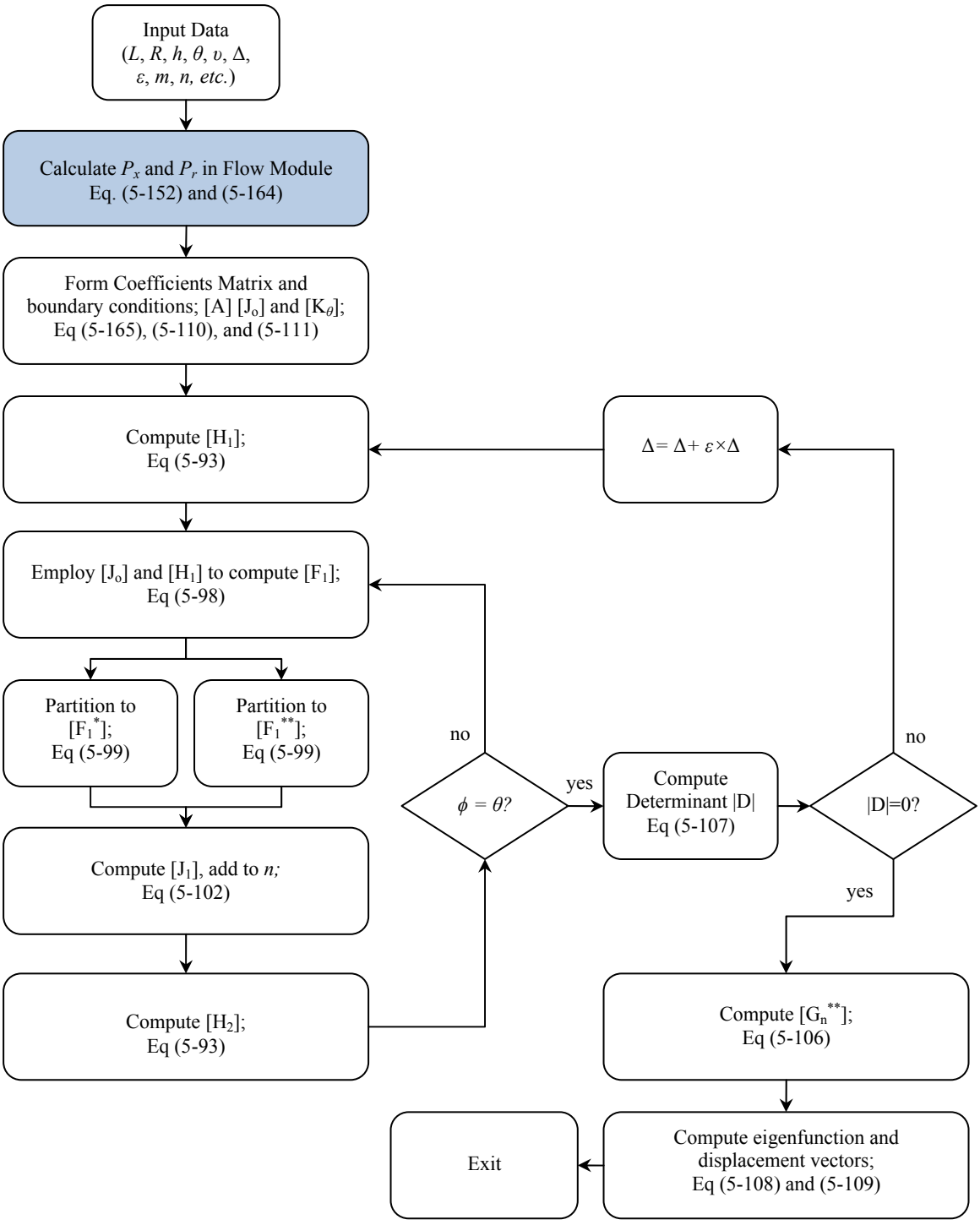

Figure 5-12: Flow diagram of flow induced vibration algorithm

6 RESULTS AND OBSERVATIONS

Results for the plate stability module, the flow module, and relationships created for flow induced vibration by coupling these modules are presented in this chapter. General observations are made between the methods used for predicting static instability of plates discussed in chapter 4 to that of FIV, by qualitatively defining conditions for an ATR type fuel plate that are more likely to statically fail or dynamically fail.

6.1 Plate Stability Module Results

Beyond the results and discussion presented in this section, a test case was run and compared against other theoretical methods and experimental data for similar boundary conditions to verify the plate stability module's capabilities of producing representative eigenvalue solutions. No known available literature was found to include NF values for a cylindrical plate with C-F-C-F or C-F-SS-F edge boundaries. However, a set of cases were published with natural frequencies including a Rayleigh, Rayleigh-Ritz and experimental result acquisition techniques for a square cylindrical plate with all four edges clamped. The results for this test case are presented in Appendix C and demonstrate that the plate stability module is capable of producing acceptable eigenvalue solutions under free vibration.

6.1.1 Grid Sensitivity

In order to verify that the correct frequency parameter is acquired for a given set of boundary conditions it is necessary to determine the grid independent solution, or grid resolution required to produce a representative frequency parameter. Figure 6-1 presents the solution determinant value calculated as a part of the flow induced vibration algorithm against the frequency parameter. Five mesh refinement cases were considered while varying the refinement only along the azimuthal direction, as this is the only direction which the solution iterates over. The geometric and material properties presented in Table 4-1 were used and applied to the C-F-C-F boundary values presented in section 5.1.5.1 with no applied membrane forces (i.e free vibration). Figure 6-1(a)

presents the determinant over the interval $\Delta \in [0, 0.5]$; at first glance all nodal refinement values considered produce similar roots, however, after closer examination from Figure 6-1(b) the roots are significantly different for the first eigenvalue solution. It was qualitatively determined by visual examination of Figure 6-1(b) that 500 nodes sweeping across the azimuthal direction is sufficient to produce a representative frequency parameter as the profile for 500 nodes is nearly analogous to that of 1000 nodes, therefore a grid resolution of 500 nodes along the azimuthal direction is employed throughout this study and all solutions presented during this study include 1000 nodes along the axial direction.

As previously discussed, when the determinant is equal to zero for the system of equations, the eigenvalue used to calculate the solution satisfies the equations of motion and therefore is representative of a given eigenvalue for prescribed boundary conditions. This may be graphically seen in Figure 6-2; each root represents a corresponding eigenvalue solution, the frequency parameter corresponding to the first root represents the frequency parameter for the n = 1 mode along the azimuthal direction. Continuing, the frequency parameter corresponding to the second root represents the n = 2 mode, and so on. Two eigenvalues from Figure 6-2 may be identified along the azimuthal direction (n), for a prescribed mode number of m = 1 along the axial direction.

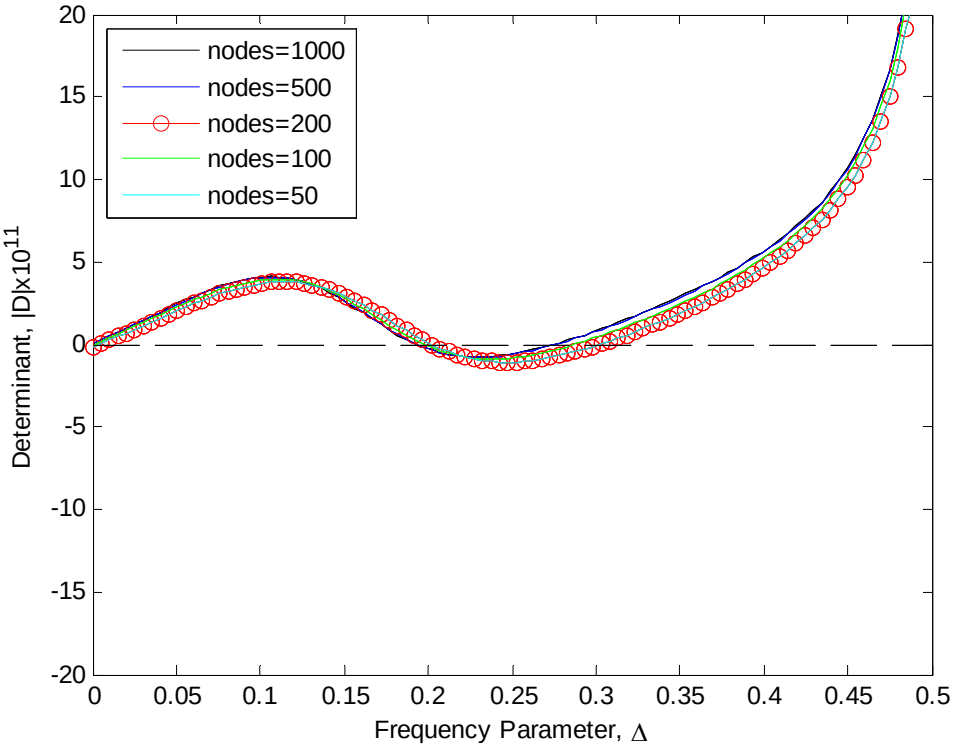

(a)

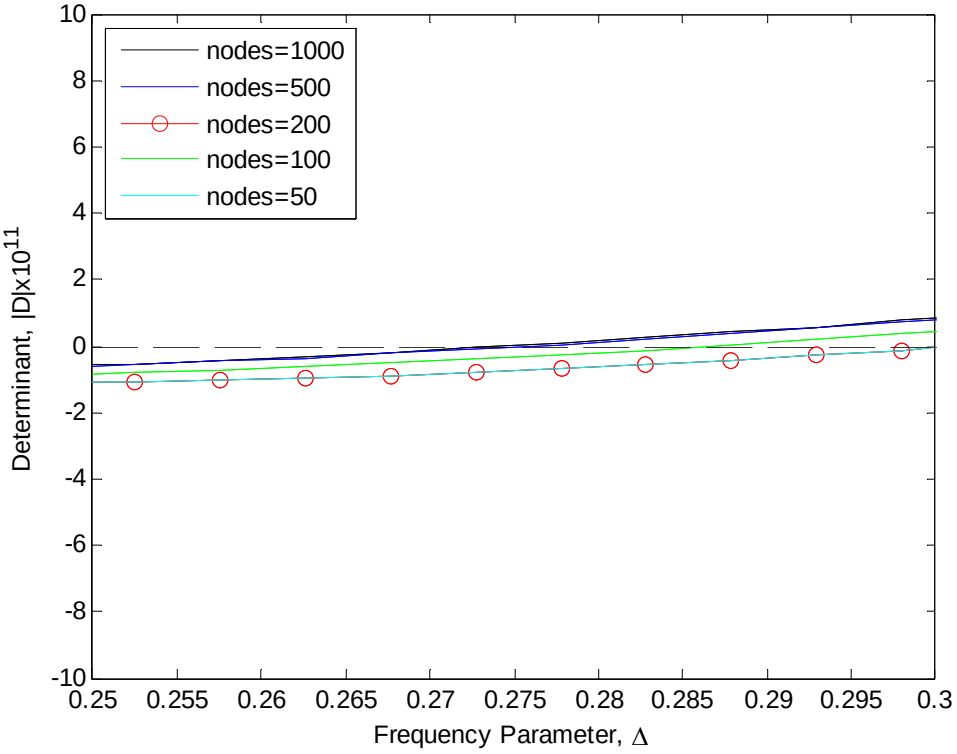

(b)

Figure 6-1: Solution determinant against frequency parameter (m = 1)

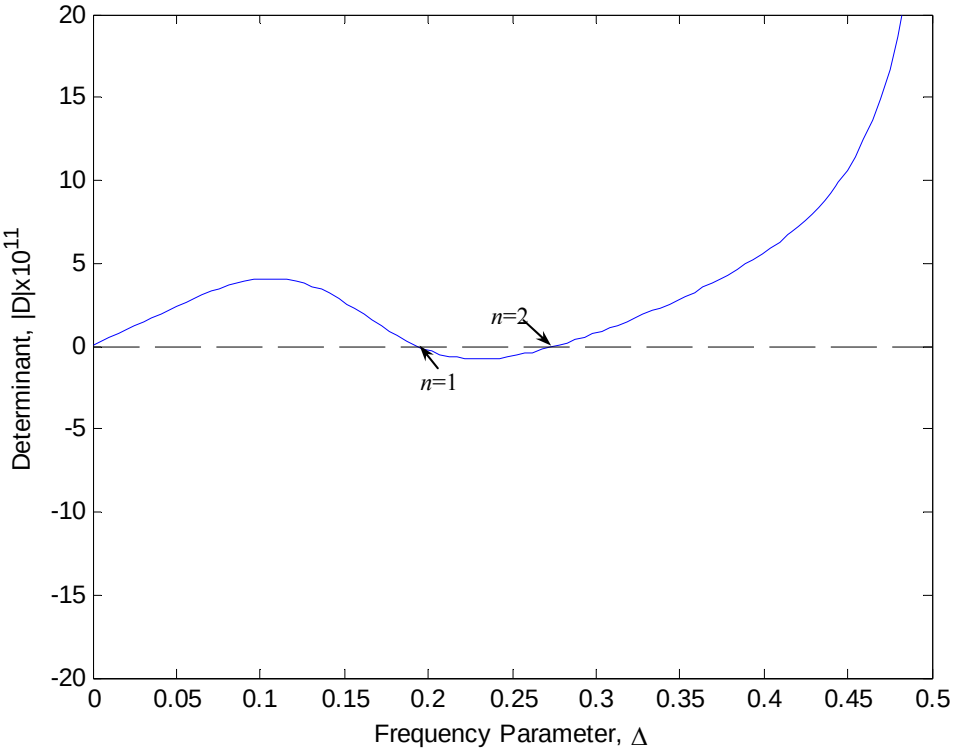

Figure 6-2: Solution determinant against frequency parameter (m = 1)

6.1.2 Frequency Results under Free Vibration

The determinant profile is inherently dependant on the buckling mode along the axial direction of the plate. Figure 6-3 presents the solution determinant profile for axial buckling modes m = 1, 2, and 3. The solution determinant is characteristically small in magnitude, as seen in Figure 6-3, it is for this reason that double precision was employed during all calculations numerically performed in Matlab® during this study.

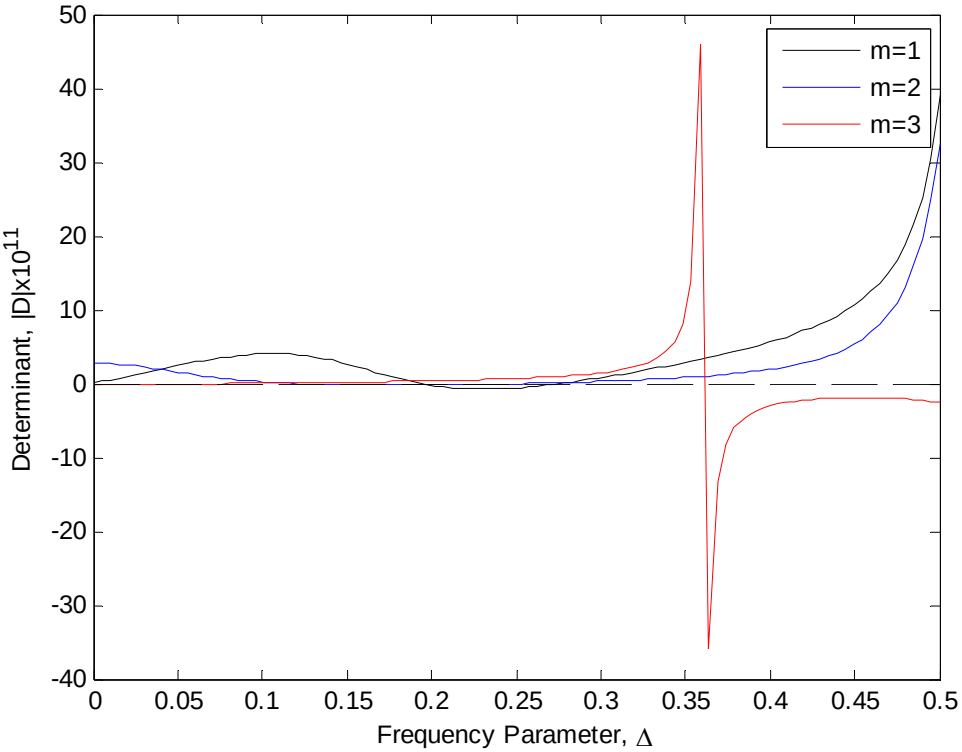

Figure 6-3: Solution determinant against frequency parameter for C-F-C-F edges

Although the solution determinant profile seen in Figure 6-3 is significantly different for each axial buckling mode, its roots are nearly analogous. Table 6-1 and Table 6-2 present the frequency parameter for various modal combinations given C-F-C-F and C-F-SS-F edge boundaries, respectively. It is observed that the axial mode of buckling does not impact the frequency parameter for both set edge boundaries. This is congruent with previous studies' observations which note that for *L/b* values which are much greater than 2, the mechanical stability along the azimuthal direction dominant the dependence on the frequency parameter [75].

Table 6-1: Frequency parameter for various modal combinations and C-F-C-F edges

	$n = 1$	$n = 2$	$n = 3$
$m = 1$	0.071	0.220	0.761
$m = 2$	0.071	0.220	0.761
$m = 3$	0.071	0.220	0.761

Table 6-2: Frequency parameter for various modal combinations and C-F-SS-F edges

	$n = 1$	$n = 2$	$n = 3$
$m = 1$	0.047	0.209	0.625
$m = 2$	0.047	0.209	0.625
$m = 3$	0.047	0.209	0.625

Taking these previous observations into consideration, a set of simulations were performed while varying the value of L/b where b was held fixed as $R_{cl}\theta$ and all other boundary conditions from Table 4-1 were held constant for the case of free vibration. The frequency parameter for azimuthal modal numbers n = 1, 2, and 3 were found while holding the axial modal number to 1 for both C-F-C-F and C-F-SS-F edge boundary cases. The results for these simulations are presented in Figure 6-4 and Figure 6-5.

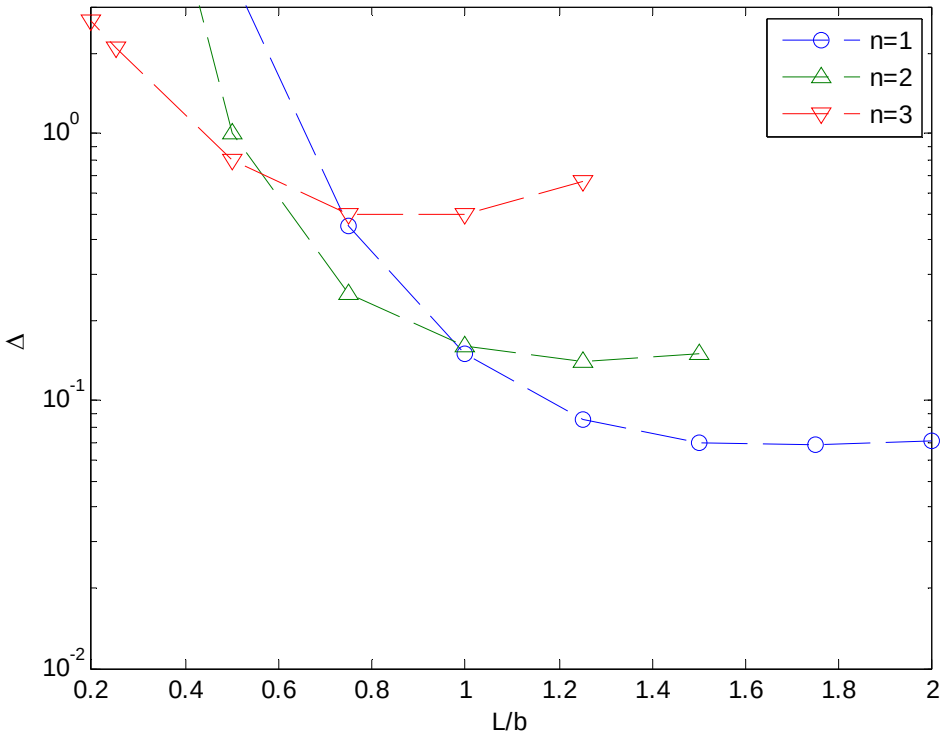

Figure 6-4: Frequency parameter against plate aspect ratio for m = 1 (C-F-C-F)

Notice for each of the two cases considered that the smallest magnitude frequency parameter is not necessarily applicable for the condition where n = 1. In fact each of the first three modal numbers along the azimuthal direction have a region in which they

produce the lowest frequency parameter for a prescribed set of *L/b* values. This indicates that the cylindrical plate will tend to dynamically fail under different modes of vibration depending on the plate's length to span width relation. As can be seen in both figures, the frequency parameter asymptotically flattens to a minimum value for $n = 1$ near an *L/b* of 2 where the frequency parameter for $n = 1$ is smallest in magnitude, indicating that for this study's geometric characteristics where $L/b = 7.4112$, the frequency parameter will be similar in magnitude to that of a plate with aspect ratio of $L/b = 2$. Similarly this observation reiterates the remark made regarding Table 6-1 and Table 6-2 which states that beyond a plate aspect ratio of approximately $L/b = 2$ the axial mode of buckling is insignificant to the dynamic characteristics of the plate which is dominated by the physics governed along the azimuthal direction.

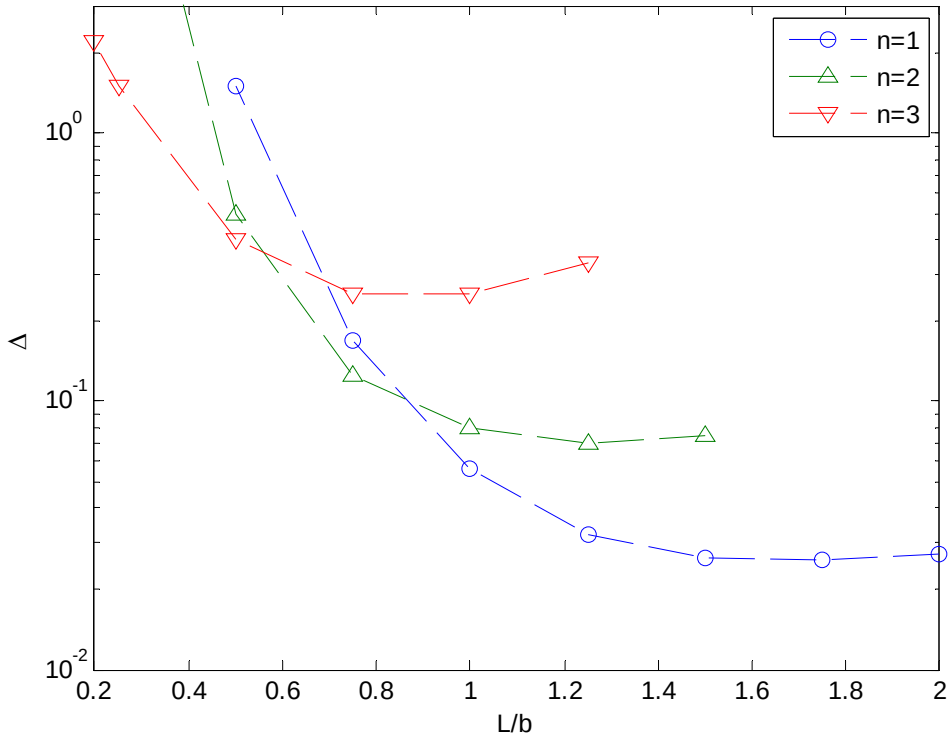

Figure 6-5: Frequency parameter against plate aspect ratio for $m = 1$ (C-F-SS-F)

Considering only the lowest magnitude frequency parameter acquired from Figure 6-4 and Figure 6-5, a comparison may be made regarding the dynamic mechanical stability of a plate under each edge boundary case considered. This comparison is presented in

Figure 6-6. The frequency parameter under all plate aspect ratios is lower for the C-F-SS-F edge boundary case. This is expected, as the frequency parameter is defined as $\Delta = R_{cl}^2 \rho \omega^2 (1-\upsilon^2)/Eg$, therefore the circular frequency (ω) for the plate with C-F-SS-F edge boundaries is lower, indicating that it is mechanically weaker than that of the plate with C-F-C-F edge boundaries. In this case a rigid body which is "mechanically weaker" suggests it will either buckle under smaller externally applied loads or dynamically respond to free vibration with a lower NF for a given modal number.

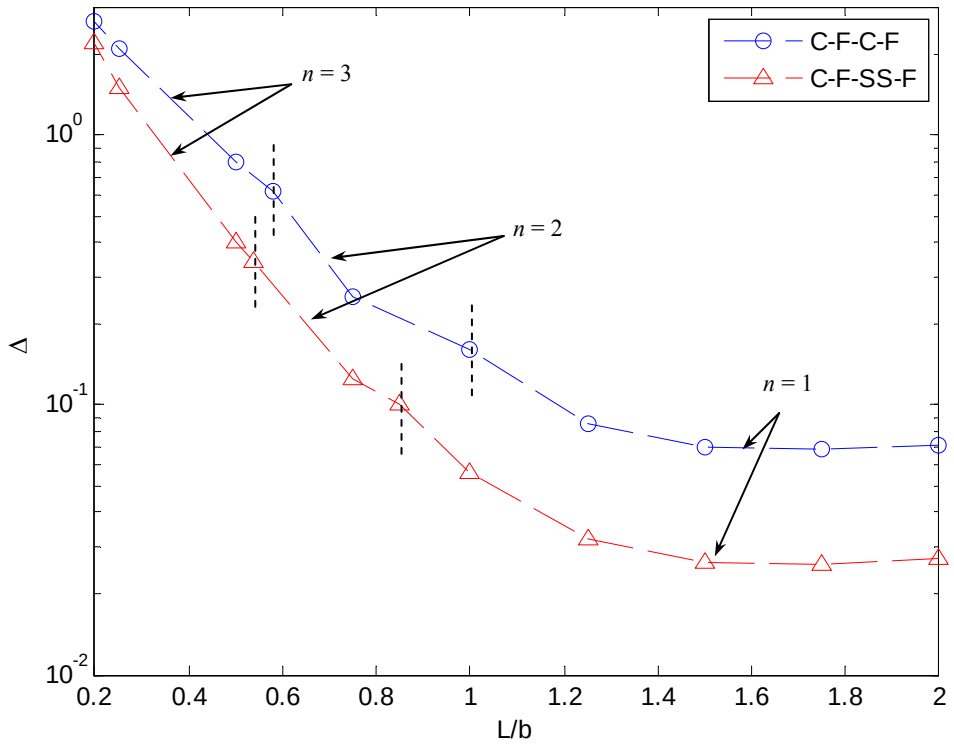

Figure 6-6: Lowest frequency parameter against plate aspect ratio for $m = 1$

For the case of C-F-C-F edge boundaries, if θ is increased to 360°, the solution domain is then representative of a cylinder. This is only true for even modal numbers in the azimuthal direction, as the position derivative at x = constant is forced to zero for the clamped edge boundary type and therefore the modal shape must be symmetric in order for each edge boundary to satisfy the cylindrical geometry. Figure 6-7 presents the frequency parameter for a C-F-C-F cylindrical plate where θ equals 360° as a function of dimensionless radius.

Blevins [75] presents the frequency parameter of a perfect cylinder of various modes using Flügge's equations of motion and applying them through the Rayleigh-Ritz method. Figure 6-7 displays the profiles given by Blevins along for various radius to plate thickness ratios. Notice that the trend seen in Figure 6-7 is similar to that seen in Figure 6-6 this can be seen through the relation of arc length where $b = R_{cl}\theta$, and for the case in Figure 6-7, θ is held constant. A number of observations may be made from Figure 6-7:

- The natural frequency is reduced with a reduction in dimensionless plate thickness (R_{cl}/a) for the trends presented in Blevins and those values calculated herein. This is due to a reduction in the mechanical rigidity found in the bending moment component of the plate (refer to Figure 5-2(a)).

- The frequency parameter calculated during this study becomes more representative of those presented by Blevins through use of the Rayleigh-Ritz method with a reduction in dimensionless plate thickness. This fundamental observation is caused by a mechanical weakening due to its reduction of the extensional rigidity.

- A region exists for all R_{cl}/a presents that the frequency parameter plateaus at the lowest possible modal number (n = 2). This is similar to that observed in Figure 6-6 and shows that the plate length becomes insignificant to the solution at this location.

- The calculated frequency parameter converges toward Blevins' results with an increase in L/R_{cl} ; it is hypothesized that this results from two primary factors:
    - The lowest frequency parameter may be seen through an increase in modal number (n) with a decrease in L/R_{cl} . As n increase, the modal shape along the azimuthal direction of the plate becomes primarily flexural. The clamped edge boundaries therefore become more influential to the

solution than that of lower modal numbers. These clamped edge boundaries are not truly representative of a cylindrical plate, but are rather engineering approximations to the physical response the cylindrical plate may undergo for prescribed eigenvalues.

- A decrease in L/R_{cl} results in a larger plate curvature, that is as L/R_{cl} approaches zero, R_{cl} must approach zero. Because of this, the bending stress terms included into the equations of motion for this study become more influential than that seen in the simplified Flügge equations. As a result of this increased influence on the bending stiffness terms, the frequency parameter increases slightly.

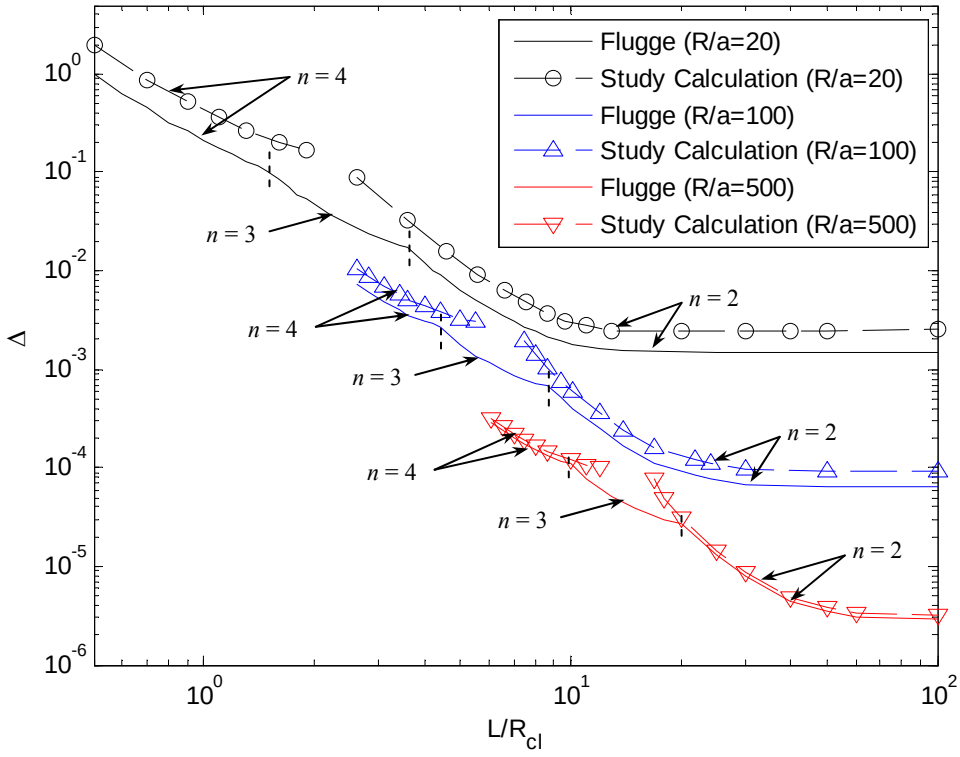

Figure 6-7: Lowest frequency parameter against radius for $m = 1$, θ=360° (C-F-SS-F)

Consider the case where R_{cl} approaches infinite, that is, that the cylindrical plate under discussion approaches that of a flat plate. In such a case, the flexural rigidity added by the curvature of the plate is diminished and the natural frequency or dynamic response of the

plate should be comparable to that of a flat plate. By definition $b \equiv R_{cl}\theta$. If θ is held constant, an objective comparison between the dynamic response of a flat plate relative to that of a cylindrical plate may be made as a function of arc length.

Blevins presents the frequency solution for a flat plate with C-F-C-F edge boundaries given as

$$f = \frac{\lambda_{m,n}^2}{2\pi b^2}\left[\frac{Ea^2}{12\rho(1-\upsilon^2)}\right]^{\frac{1}{2}}. \tag{6-1}$$

Through a reformulation (6-1) may be presented through the frequency parameter as:

$$\Delta_{\text{flat}} = \frac{a^2\lambda_{m,n}^4}{12gb^2\theta^2}, \tag{6-2}$$

where $\lambda_{m,n}$ is a two dimensional modal eigenvalue coefficient specific to the boundary conditions under consideration as opposed to the frequency parameter of a cylindrical plate

$$\Delta_{\text{cylindrical}} = \frac{b^2\rho\omega^2(1-\upsilon^2)}{\theta^2 Eg}. \tag{6-3}$$

A direct comparison against the frequency parameter of a cylindrical plate and that of a flat plate may be made by taking the ratio of (6-3) to that of (6-2). Figure 6-8 presents this ratio as a function of plate aspect ratio where θ has been held constant. A number of observation may be made from this figure:

- For small aspect ratios, that is, for arc lengths which are small relative to the thickness, the cylindrical plate is significantly more mechanically rigid to that of the flat plate. This is due to the large influence on radius of curvature associated with the cylindrical type geometry for small b values.

- At approximate $b/a \approx 8$ the cylindrical plate frequency parameter no longer converges toward the flat plate frequency parameter. At $b/a \approx 8$ the arc length b is significant enough that the influence of curvature no longer impacts the mechanical integrity of the plate.

- The frequency parameter for the cylindrical plate never becomes equal to that the flat plate, that is, $\Delta_{cylindrical}/\Delta_{flat}$ never reaches unity. A possible reason for this results from the original equations of motion, (5-27) through (5-29). In these equations, the coefficients in front of several terms include characteristic variables which inherently influence the dynamics of a cylindrical plate, but are not affected by the radial component these. By incorporating these components into the equations of motion, a fundamental bias in mechanical rigidity of a cylindrical plate is added relative to that of a flat plate as seen in Figure 6-8.

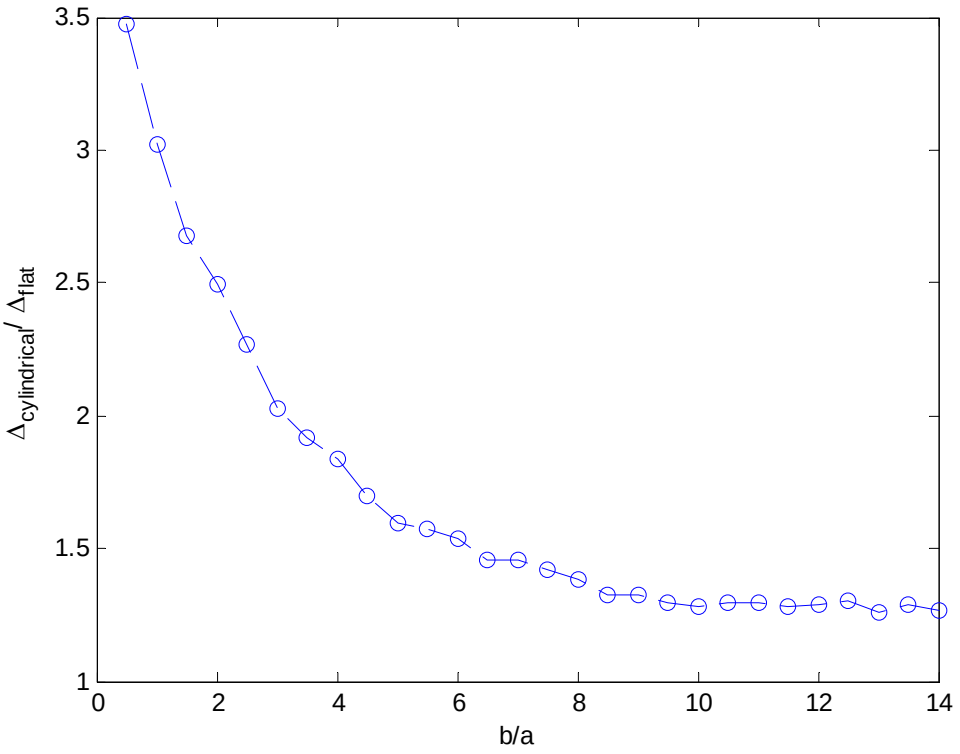

Figure 6-8: Cylindrical and flat plate frequency versus aspect ratio of C-F-C-F

6.1.3 Displacement Relations

The displacement of the plate is directly related to its internal stress resultants through the rate at which the plate's gradient changes. In contrast to the dynamic instability of a flat plate where the plate symmetrically displaces along both span-wise and axial planes, a cylindrical plate prefers to displace inward radially, that is, the maximum deflection

always occurs toward the radial center of the cylindrical plate rather than outward due to the bending terms in the equation of motion which are added for a cylindrical plate. This observation may be made from Figure 6-9. For the case of a plate with C-F-C-F edge boundaries, the maximum absolute value of displacement occurs at the azimuthal centerline of the plate and is directed inward. This is conveniently the same location where the change in displacement gradient is largest in absolute value. From Figure 6-9(b) one may collect that the location of maximum stress on the plate occurs at the azimuthal centerline and is equal at both the leading and trailing edges of the plate. Figure 6-9(b) presents the displacement profile at the leading edge of the plate. Notice that the gradient is 0 at each $\phi/\theta = 0$ and 1, which is inherent of clamped edge boundaries qualitatively verifying that the plate stability module accurately calculates the displacement profile of a plate for each eigenvalue solution.

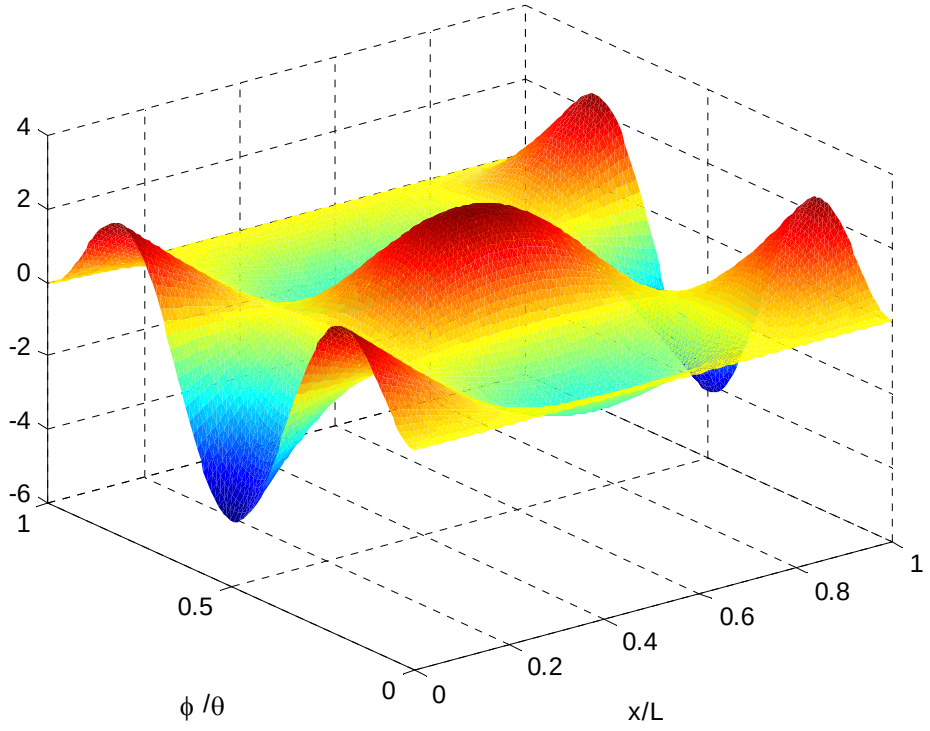

(a)

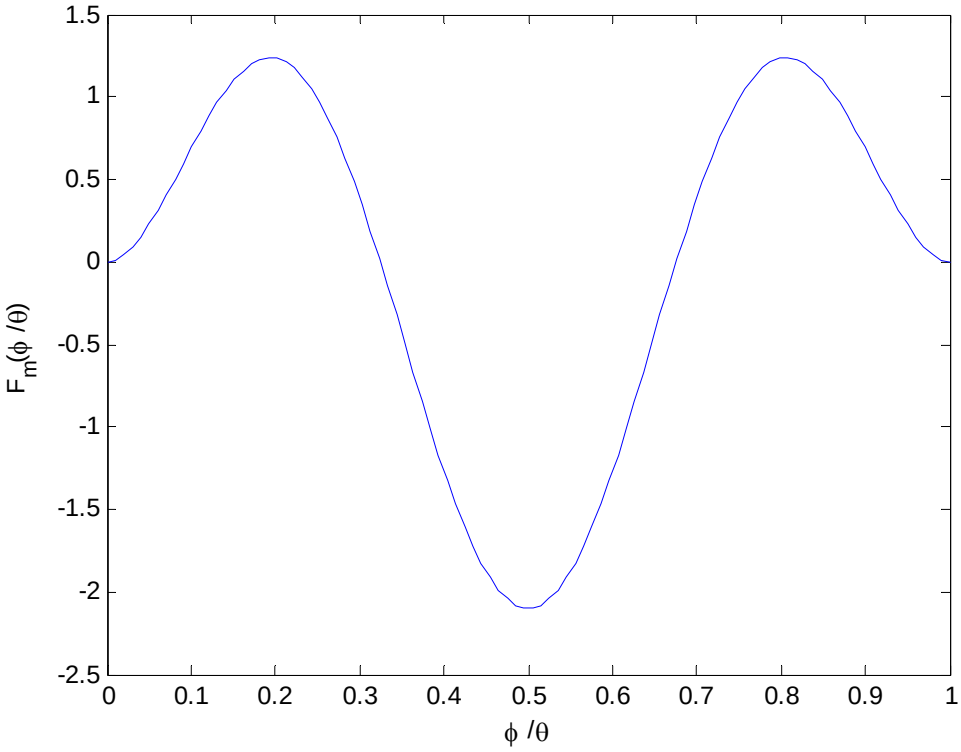

(b)

Figure 6-9: Normalized plate displacement in w of C-F-C-F (m = 1, n = 3)
(a) contour plot and (b) displacement profile

In contrast to the plate displacement profile in Figure 6-9(b), Figure 6-10(b) shows that the maximum displacement of the plate with C-F-SS-F edge boundaries, however directed inward radially is skewed toward one edge boundary, this is due to the asymmetry of applied boundary conditions. Notice that where $\phi/\theta = 0$ the displacement and displacement gradient are zero while at $\phi/\theta = 1$ only the displacement is zero. These characteristics are representative of the C edge boundary conditions being correctly applied to the $\phi/\theta = 0$ and SS edge boundary conditions at $\phi/\theta = 1$. It may also be seen from Figure 6-10(b) that the maximum outward displacement occurs toward the edge with the C edge demonstrating that the stresses are skewed in such a way that more stress occurs overall near the clamped edge side than the simply supported edge, this is congruent with literature regarding beam displacements with similar edge boundaries [92].

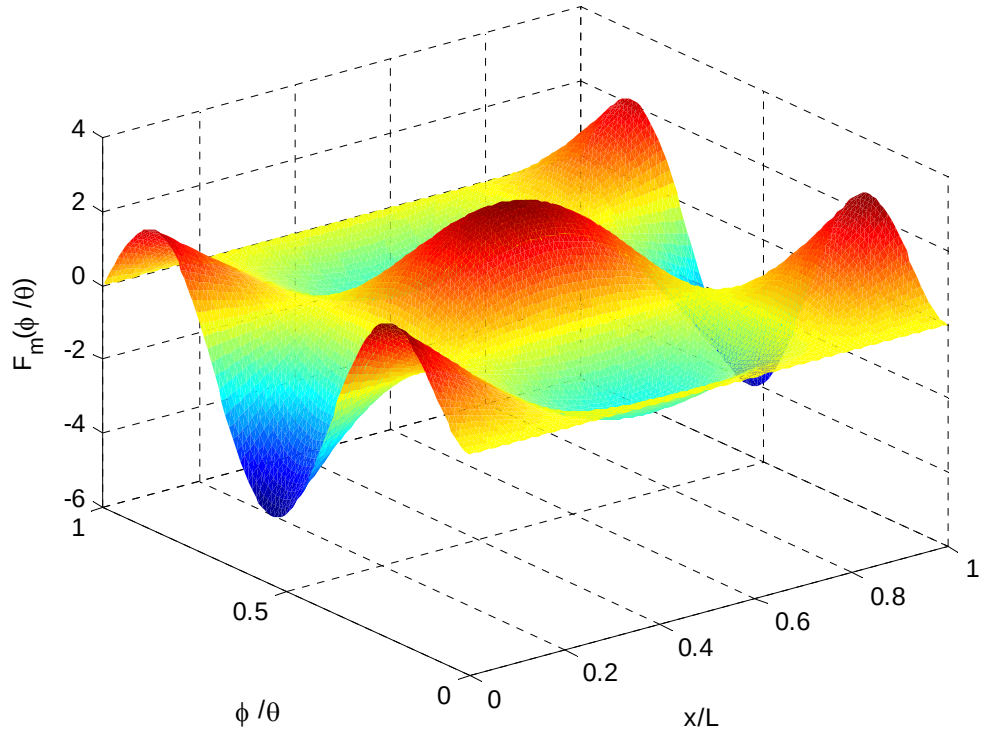

(a)

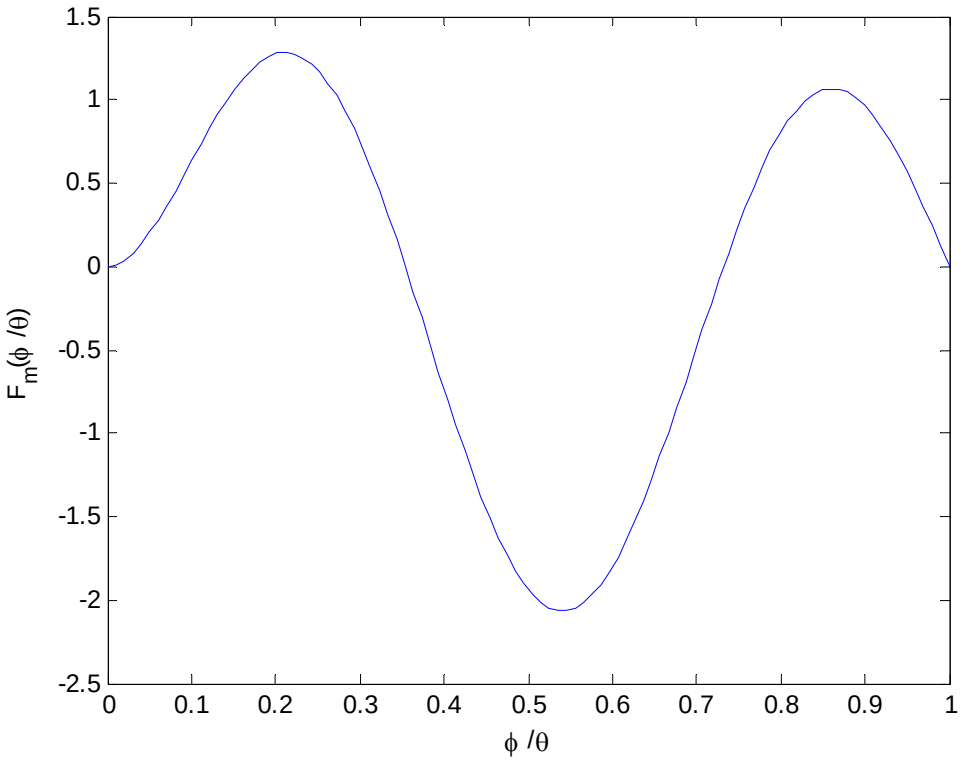

(b)

Figure 6-10: Normalized plate displacement in *w* of C-F-SS-F (*m* = 1, *n* = 3)
(a) contour plot and (b) displacement profile

Figure 5-4 in section 5.1.4.1 describes the eigenfunctions which have been employed throughout the duration of this study in the axial direction, recall that all odd numbered modal shapes in the axial direction (m) are of the symmetric type; conversely, the even modal numbers are anti-symmetric. Several developments results from the solution of the plate stability module these include two relations regarding the shapes of the displacement functions (1) when f_1 is symmetric in shape, f_2, and f_3 are inherently asymmetric, given by (5-59) and (5-60); and (2) f_2 is similar in shape to f_3 but differs in amplitudes based on the integration scheme developed in Appendix B when forming the coefficient matrix [A]. Similarly, f_1 is similar in shape with $\partial f_3/\partial x$ but differs in amplitude. These two relations attest to the relative shapes of the displacement functions, however, they do not define the shapes precisely. If f_3 is symmetric with one half wave, f_2 may be symmetric with either one or three half waves and f_1 may be asymmetric either with two or four half waves. This adds credibility to the hypothesis made by Jeong [105] stating that curved panels only see multiple modes of vibration; although this hypothesis is not completely true for this study in the sense that conditions may exist such that single modal response is dominant in the solution, it does verify that there exists the possibility that multiple modes of vibration occur concurrently.

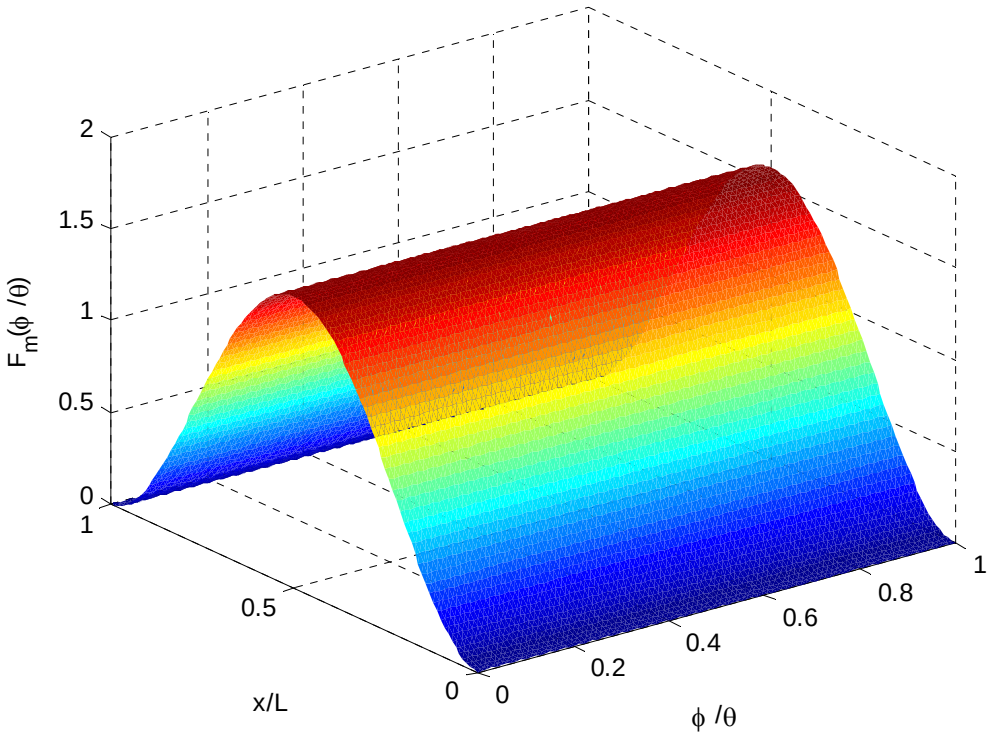

(a)

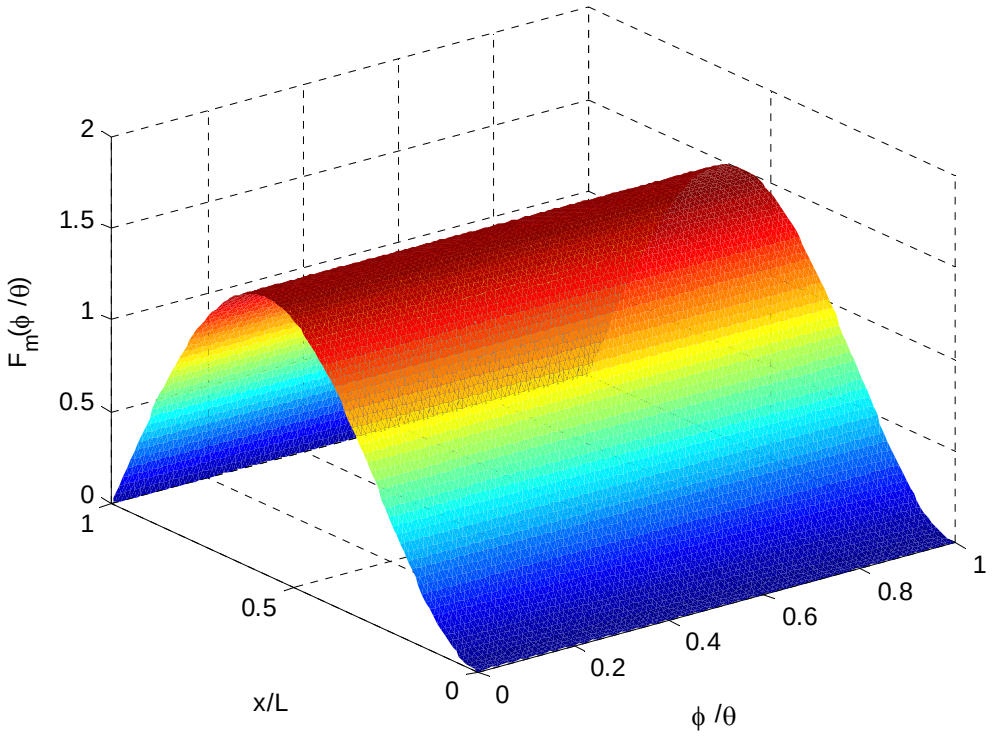

(b)

Figure 6-11: Contour plot of plate displacement in w ($m = 0$, $n = 1$)
(a) C-F-C-F and (b) C-F-SS-F boundary conditions

The displacement relations previously described may be visually interpreted from the line plots below and the view graphs in Appendix D. Recall from section 4.1.2 that two sets of boundary conditions are considered during this study (C-F-C-F, and C-F-SS-F). A contour plot of mode $m = 0$, $n = 1$ is presented below in Figure 6-12 for both cases. At first glance both displacement shapes along the azimuthal direction appear analogous to one another, however, if their profiles are overlaid (Figure 6-12) it becomes obvious that at either end ($\phi = 0$ and $\phi = \theta$), displacement and the first derivative of displacement are forced to zero for C-F-C-F solution. In contrast at $\phi = 0$ the displacement and the first derivative of displacement are forced to zero, while at $\phi = \theta$ the displacement and the moment are forced to zero for the C-F-SS-F solution.

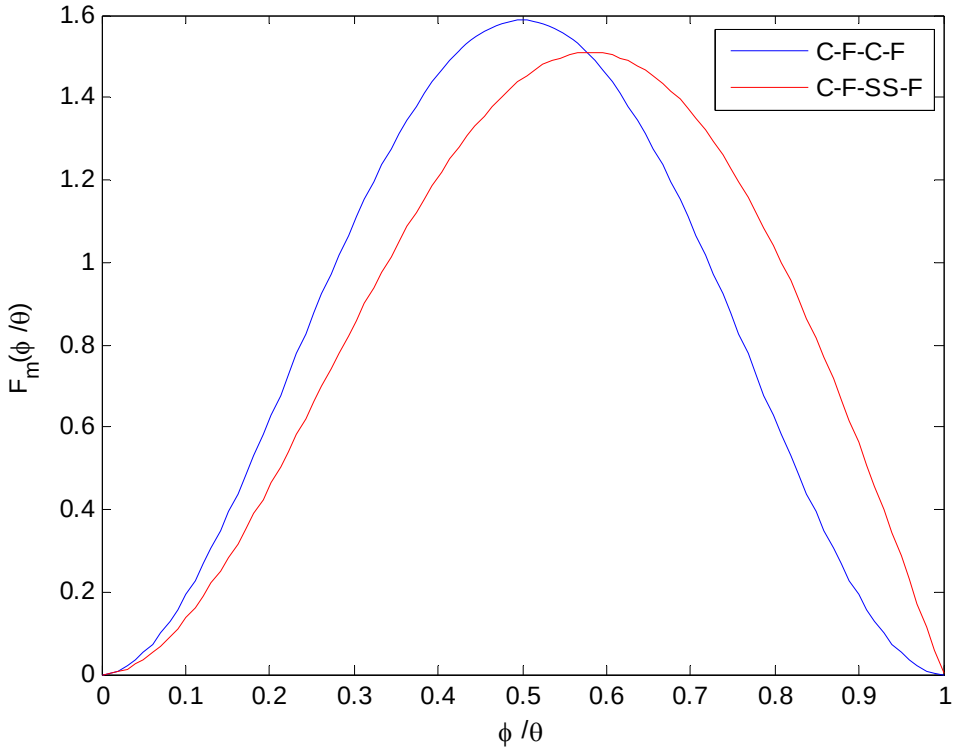

Figure 6-12: Displacement profile of C-F-C-F and C-F-SS-F along ϕ

The normalized eigenfunction along the azimuthal direction for modes 1 through 5 given C-F-C-F and C-F-SS-F are below in Figure 6-13(a) and Figure 6-13(b), respectively. It can be seen that the maximum deflection decrease with an increase in mode number for both sets of edge boundary cases, this is due to the conserved characteristic of the fixed

plate arc length. In Figure 6-13(a) all odd modes are symmetric about $\phi/\theta = 1/2$ while the even modes force anti-symmetric about the azimuthal centerline. In contrast all modal shapes are anti-symmetric about the azimuthal centerline in Figure 6-13(b) due to the mismatch in edge boundary conditions.

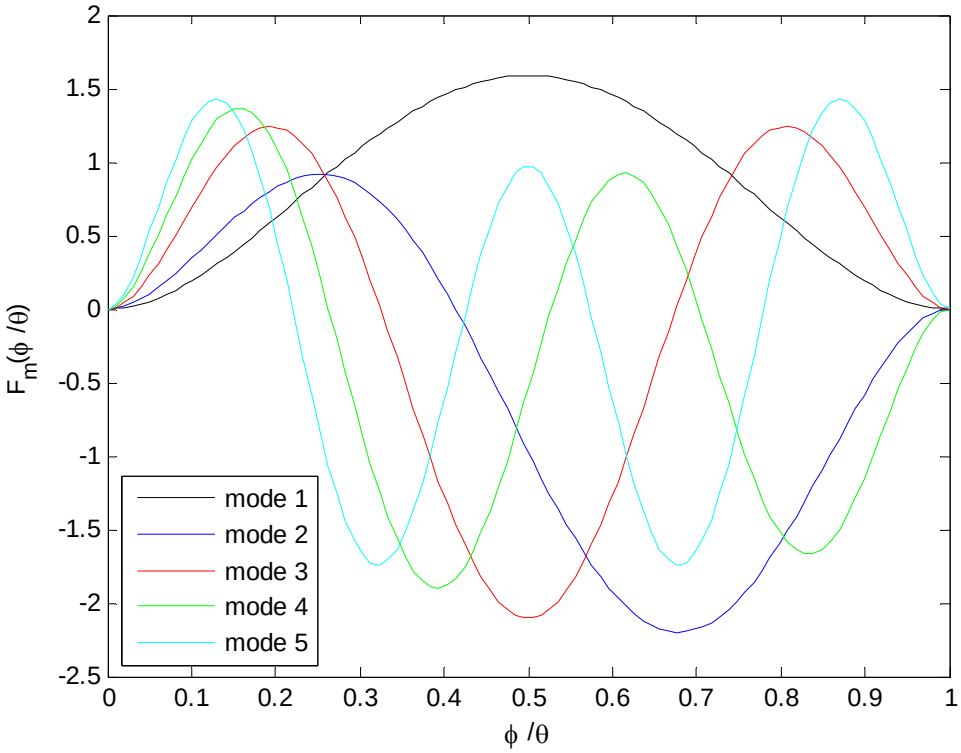

(a)

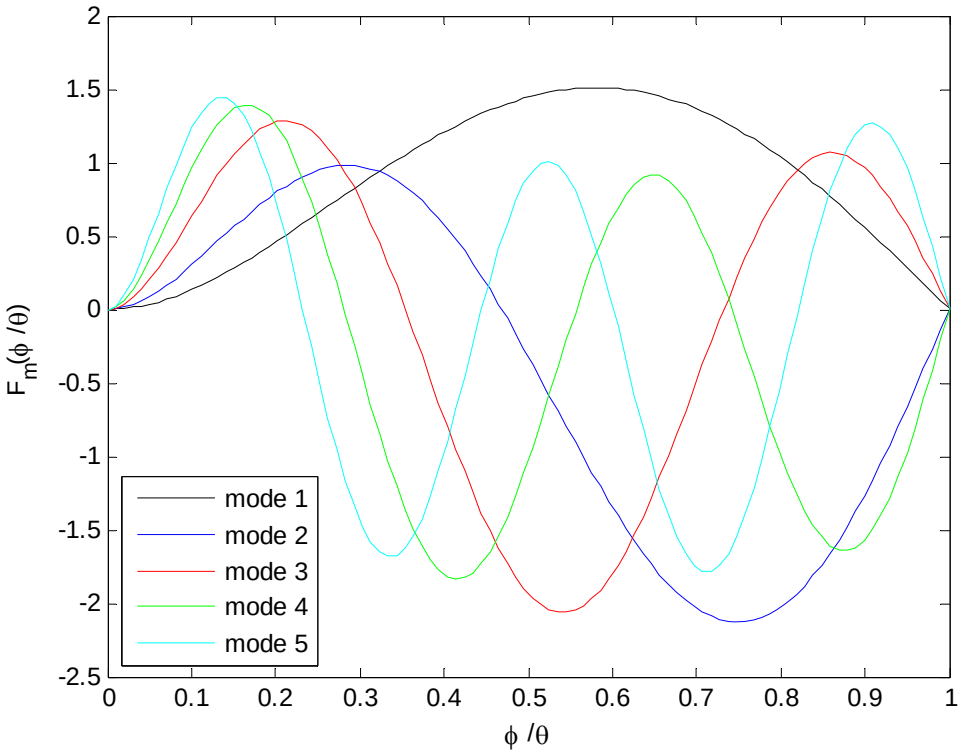

(b)

Figure 6-13: Normalized eigenfunctions along ϕ for various modes
(a) C-F-C-F and (b) C-F-SS-F edges

A complete set of displacement calculations were performed for all mode combinations given the available eigenfunction coefficients in the axial direction presented in Table 5-1 for each set of boundary conditions. These displacement contour plots are presented in Appendix D. As previously stated, the relations f_1, f_2, and f_3 describe the eigenfunction shape, and do not account for amplitude (true displacement), it is for this reason that the figures in Appendix D are presented in the form of normalized displacement such that the absolute maximum displacement coincides with an absolute amplitude of unity.

6.2 Flow Module Results

The objective of the flow module is to produce membrane forces on the plate of interest for a prescribed set of geometric and flow conditions. These flow results are representative of two subchannels on either side of plate 18 of a standard 19 plate ATR fuel element, the geometry and flow properties used to produce the flow module results were taken from Table 4-1 unless otherwise specified. Beyond the results presented in

this section, a test case was performed for the purpose of developing credibility on the flow module's capability in predicting flow and pressure values. The description and results for this test case are presented in Appendix E.

6.2.1 Flow versus Pressures

Figure 6-14 presents the evaluated pressure distribution along the length of the fuel element given an inlet superficial velocity of 10 and 20 m/s, respectively. The pressure profile in Figure 6-14 numerically demonstrates the "evaluated profile" presented in Figure 5-9 during the discussion of the flow module development. Note that a single inlet pressure boundary value of 4.1368 MPa was imposed on the solution for all results presented during this study. It may be qualitatively seen that the effect of pressure drop due to an increase in flow is correctly handled by an increase in local pressure drop at the inlet and outlet of the flow channels due to the form losses associated with the separation and recombining of the flow field.

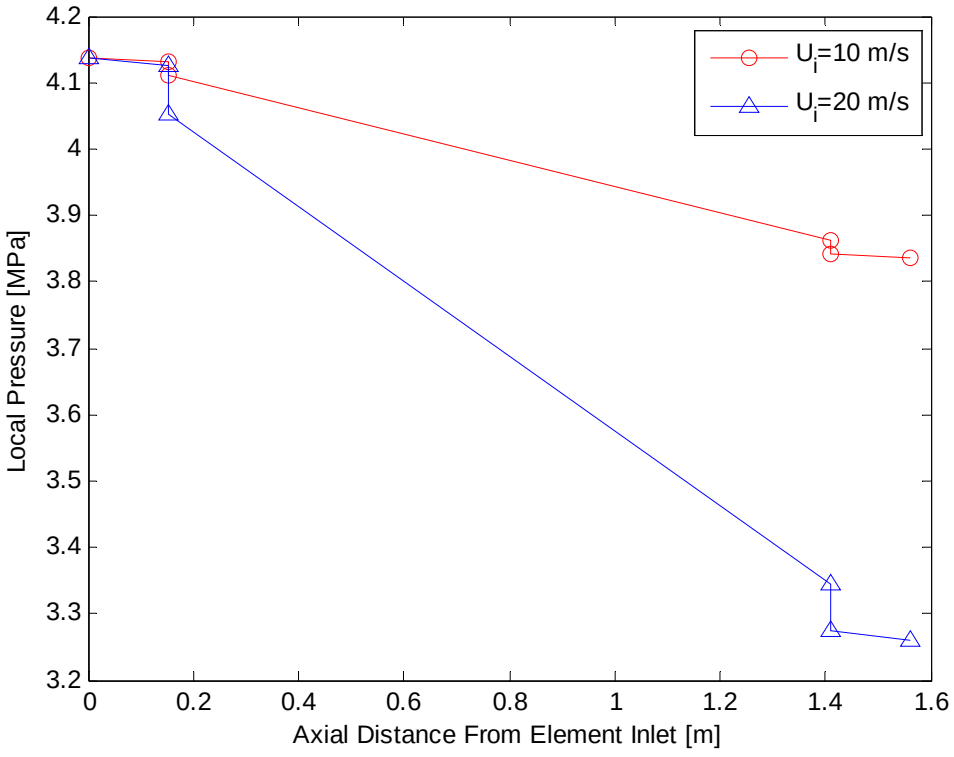

Figure 6-14: Local evaluated pressure distribution along fuel element length

Using the methodology presented in sections 5.2.3 and 5.2.4 the membrane pressure applied to the plate in both the x and r direction is presented over a range of flow rates as seen in Figure 6-15. The membrane pressures are presented against both inlet Reynolds number (Re_i) in Figure 6-15(a) and inlet superficial velocity (U_i) in Figure 6-15(b). Notice that for all flow rates the pressure acting along the x direction is greater than that in the r direction. This is expected as P_r is calculated by taking the net pressure difference between the adjacent flow channels while P_x accounts for the entire pressure drop across the element.

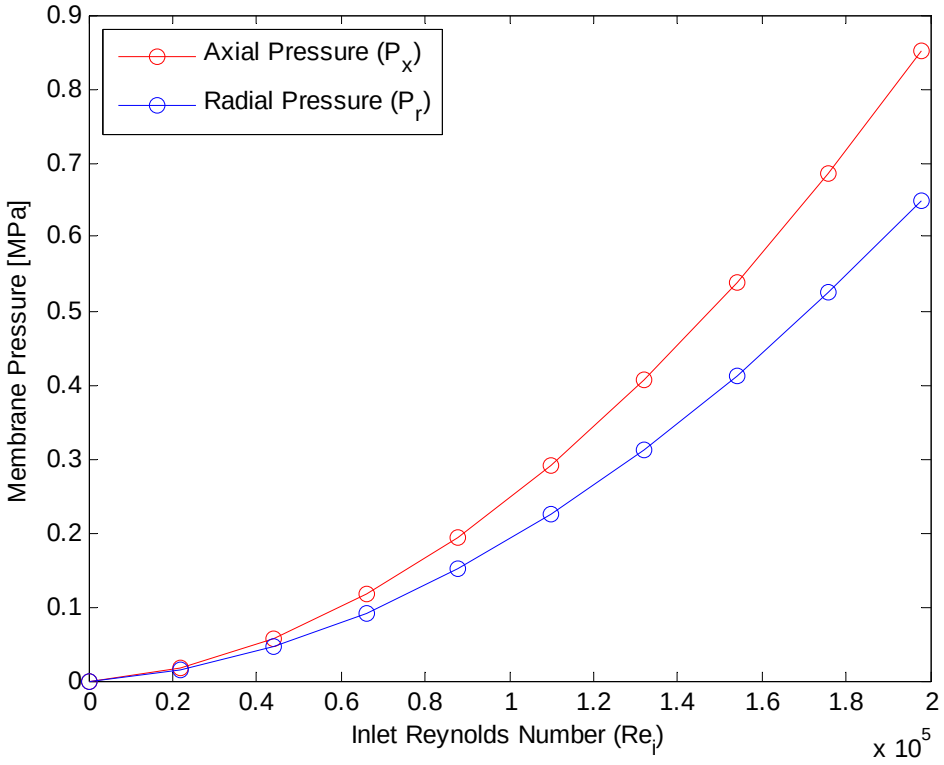

(a)

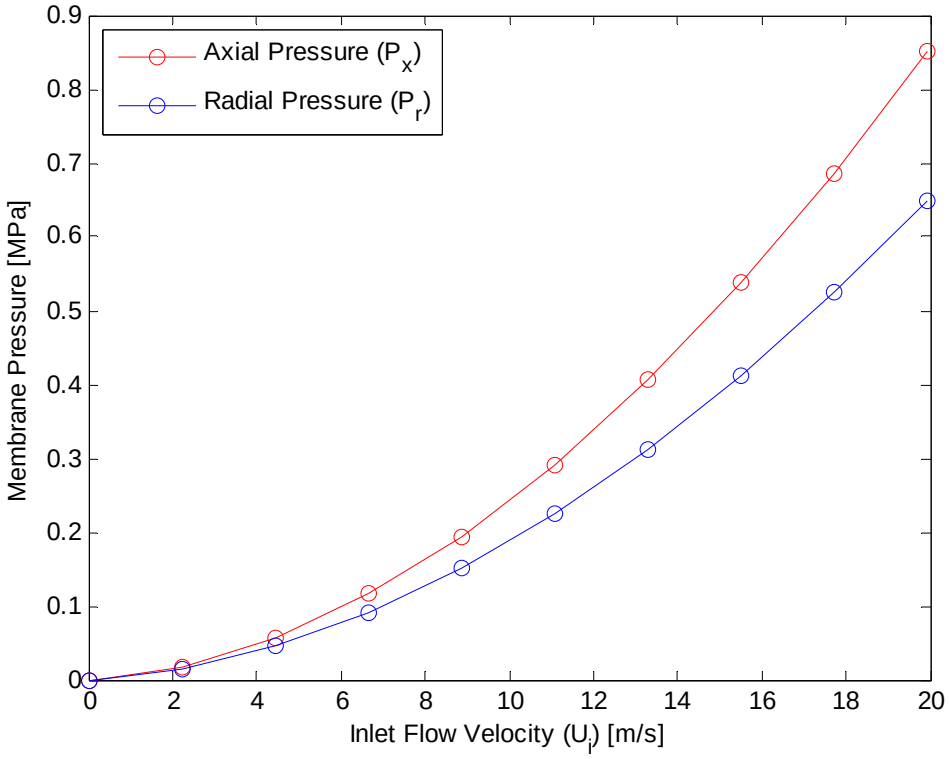

(b)

Figure 6-15: Plate membrane pressure(s) against flow rate
(a) flow rate = Re_i and (b) flow rate = U_i

6.2.2 Geometry Sensitivity

The membrane pressure values presented in Figure 6-15 are for the ideal geometry taken from the nominal dimensions off the ATR fuel element drawing and are representative of the dimensions presented in Table 4-1. The influence of machining tolerance of an element and the location of a given plate within that element may play a significant role in the pressures applied to the plate. Figure 6-16 presents the axial and radial pressure values applied to the plate of interest as a function of plate offset relative to its nominal position presented in Table 4-1. It is apparent that given coolant velocities which represent the upper envelope of operating conditions and the maximum offset of the plate in the outward radial direction (+0.5 mm) a significant increase in both pressure components results. The pressures increase by 178% for P_x and 169% for P_r in the most extreme case.

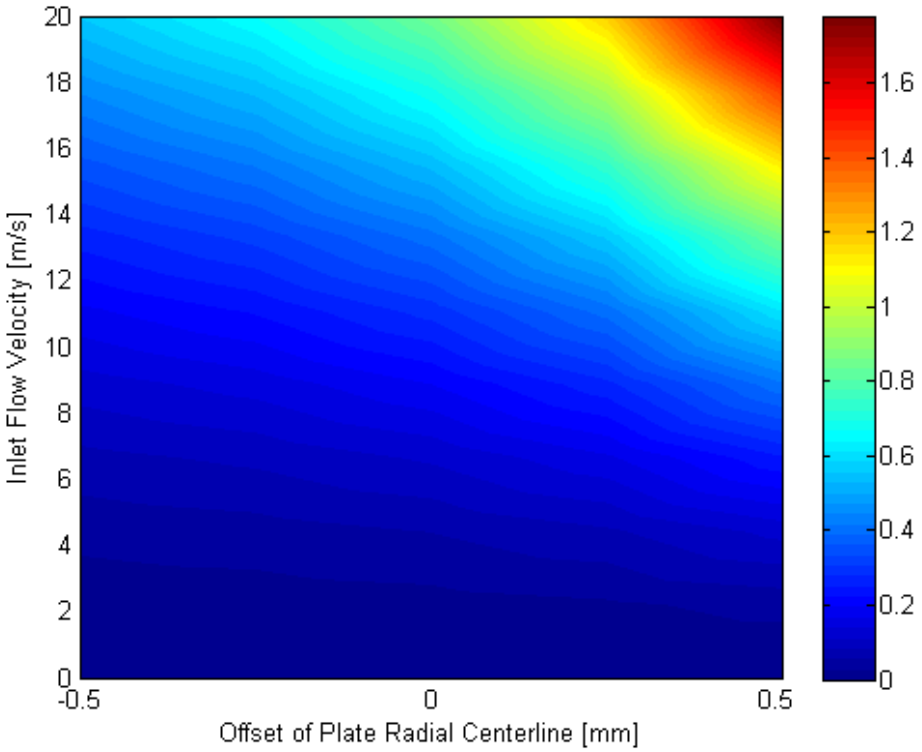

(a)

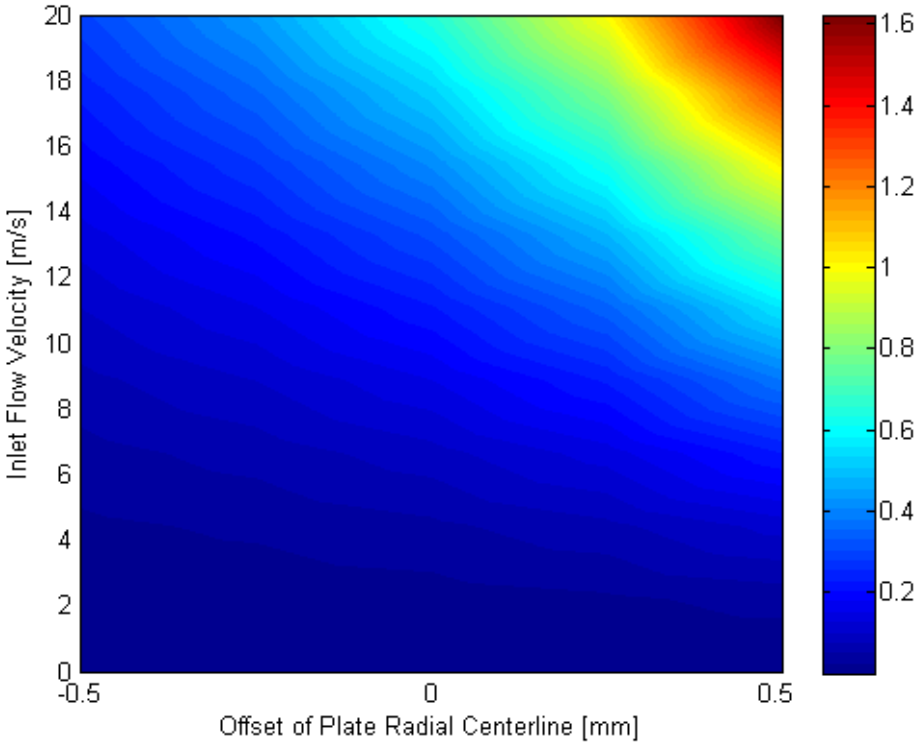

(b)

Figure 6-16: Plate membrane pressure versus flow rate and plate offset [MPa]
(a) P_x and (b) P_r

6.3 Flow Induced Vibration Results

An assessment of the dynamic instability of a plate under axial flow conditions is given here by applying a prescribed set of membrane pressure values to the plate and solving for the frequency parameter of that plate.

6.3.1 Membrane Pressure and Frequency Parameter

The frequency parameter solution for the first three buckling modes along the azimuthal direction given a combination of ten pressure loads are presented Table 6-3 and Table 6-4 for C-F-C-F and C-F-SS-F edge boundaries, respectively. The pressure loads were determined by collecting the corresponding pressure components for each of the ten equally spaced velocity intervals presented in Figure 6-15. Only the first axial modal number ($m = 1$) is considered here as the axial modal number was previously determined irrelevant to the value of the frequency parameter given an ATR fuel plate's aspect ratio (L/b).

Table 6-3: Frequency parameter against membrane pressure(s) for C-F-C-F edges

Imposed Membrane Pressure(s)		$m = 1$		
P_x [Pa]	P_r [Pa]	$n = 1$	$n = 2$	$n = 3$
0.00	0.00	0.071	0.220	0.761
16756.30	13523.85	0.072	0.222	0.770
56442.77	44777.34	0.075	0.228	0.774
116067.87	91126.35	0.079	0.239	0.785
194503.34	151577.43	0.086	0.248	0.799
291081.14	225542.32	0.094	0.261	0.816
405342.78	312617.36	0.103	0.277	0.837
536947.24	412502.23	0.113	0.296	0.860
685627.41	524961.76	0.125	0.316	0.887
851166.39	649804.97	0.138	0.339	0.916

Table 6-4: Frequency parameter against membrane pressure(s) for C-F-SS-F edges

Imposed Membrane Pressure(s)		$m = 1$		
P_x [Pa]	P_r [Pa]	$n = 1$	$n = 2$	$n = 3$
0.00	0.00	0.047	0.209	0.625
16756.30	13523.85	0.049	0.214	0.629
56442.77	44777.34	0.052	0.222	0.639
116067.87	91126.35	0.055	0.234	0.656
194503.34	151577.43	0.062	0.244	0.675

291081.14	225542.32	0.067	0.260	0.703
405342.78	312617.36	0.074	0.280	0.735
536947.24	412502.23	0.082	0.294	0.771
685627.41	524961.76	0.092	0.330	0.811
851166.39	649804.97	0.103	0.360	0.856

Plotting the frequency parameters presented in Table 6-3 and Table 6-4 against an inlet flow velocity produces Figure 6-17. A number of observations may be made from Figure 6-17. The first two modes tend to produce relatively similar frequency parameters while the frequency parameter for the third mode is approximately six to eight times larger than the first mode's frequency parameter. The second mode of buckling produces frequency parameter values which are nearly analogous for both the C-F-C-F and C-F-SS-F edge boundaries throughout the entire range of flow conditions considered. For the third mode

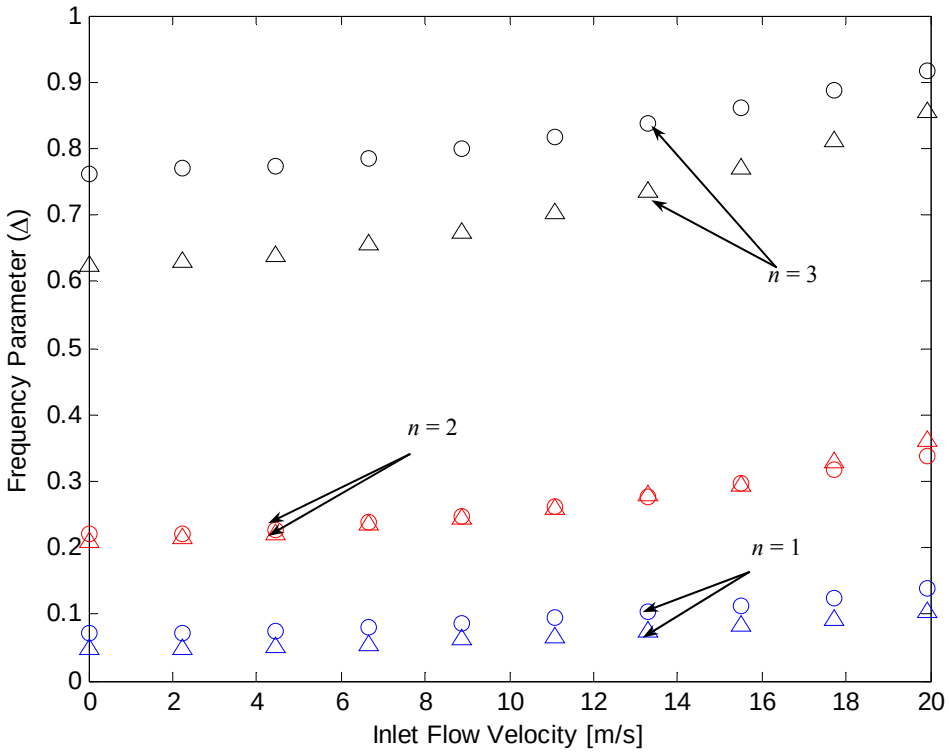

Figure 6-17: Frequency parameter for various *n* modes while *m* = 1 (O = C-F-C-F and Δ = C-F-SS-F)

the C-F-C-F edge boundary tends to produce larger frequency parameter values than the C-F-SS-F edge boundary, however as the flow rate increases these values begin to converge suggesting that they may become equal in magnitude if the flow rate, or applied membrane pressures, are increased sufficiently. The relationship between frequency parameter and flow velocity is nonlinear for all cases, however, through observation of the data presented in Table 6-3 and Table 6-4 the frequency parameter and applied loads are nearly linear suggesting that the a relationship between frequency parameter and flow rate may be $\Delta \tilde{\propto} U_i^2$, or the frequency parameter is approximately proportional to the square of the inlet velocity.

6.3.2 Relations with Static Buckling

The critical velocity predicted by Miller for C-F-C-F and C-F-SS-F edge boundaries given this study's geometry is 159.395 and 158.2083 m/s, respectively (Table 4-2). Recall that a relation between pressure and velocity were created by Miller

$$P_{cr} = 2\rho V_{cr}^2 \frac{\Delta S}{S_0}. \tag{2-2}$$

The critical pressure necessary for buckling a cylindrical plate may then be evaluated using (2-2) where the critical pressure for C-F-C-F edge boundaries is 0.5179 MPa and for C-F-SS-F edge boundaries is 0.5103 MPa. These pressures are representative of P_r accounted for in the flow module; however, because inlet form losses are considered, a flow bias in one subchannel is considered in this study while it is not considered as a part of Miller's method. Based on this study's flow geometry, channel two observes higher superficial velocities than that in channel one. Figure 6-18 presents each channel's coolant velocity plotted against the inlet coolant velocity. Notice that for an inlet flow velocity of 70 m/s channel two's flow velocity reaches the critical velocity of ~160 m/s predicted by Miller, both of which are significantly larger than that observed in the ATR. The difference in coolant velocities between channel one and two is directly proportional to the relative difference in pressure drop along the length of each subchannel as discussed earlier in the flow module development section.

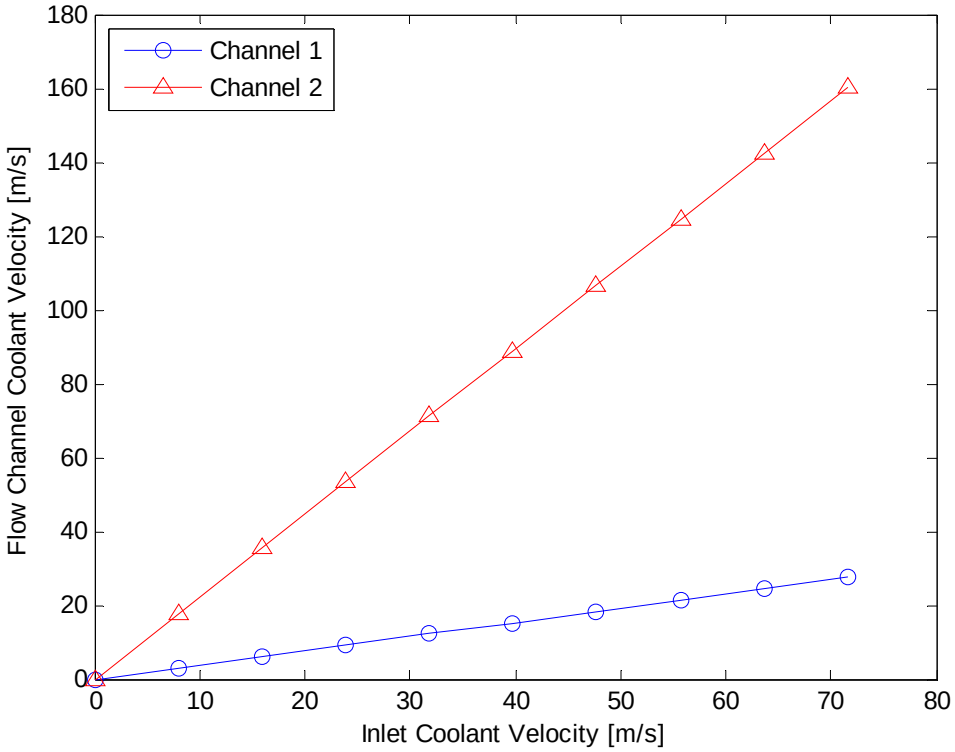

Figure 6-18: Coolant channel velocity versus inlet coolant velocity

Consider the relationship between the coolant velocity in channel two and the radial membrane pressure applied to the plate. Figure 6-19 provides a visual representation of the radial pressure over a range of coolant velocities associated with channel two. Notice from Figure 6-19 that this study's evaluated radial pressure is approximately 14 times larger than that predicted by Miller's, corresponding to the critical velocity of ~160 m/s. It may be qualitatively concluded from Figure 6-19 that for membrane pressure's greater than that predicted by Miller's method the plate of interest will fail through static instability (buckle) regardless of its previous state, as this has been demonstrated through previous studies [33]. Thus the region above "Miller's P_r" in Figure 6-19 need not be evaluated for dynamic instability as the plate is assumed to already have mechanically failed. In contrast the region below "Miller's P_r" is assumed not to have mechanically failed through static instability and is therefore susceptible to dynamic instability.

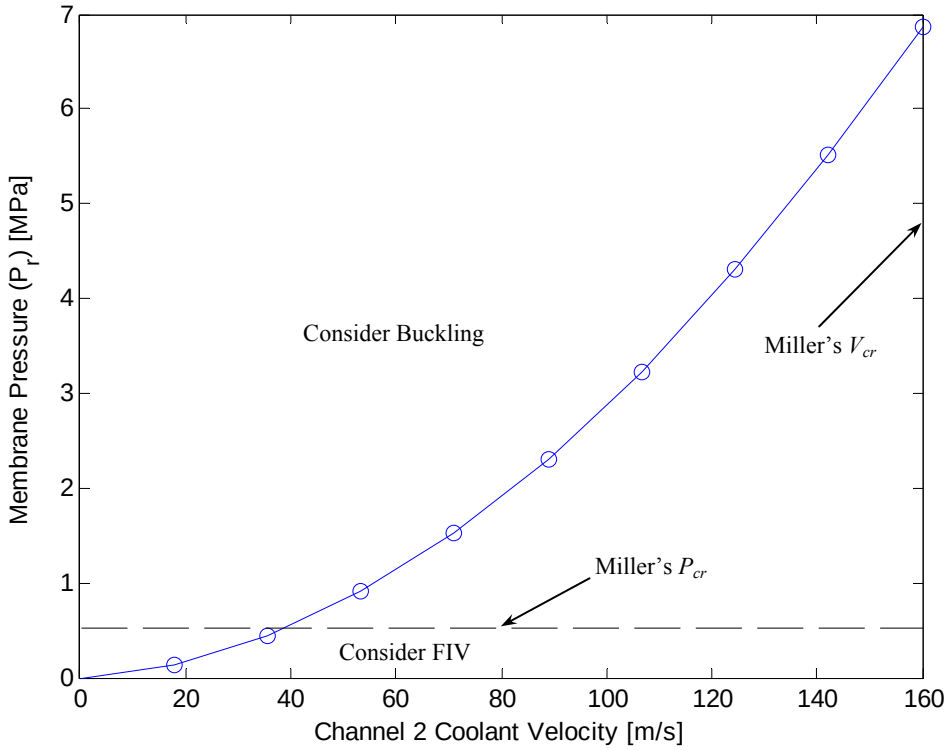

Figure 6-19: Radial membrane pressure versus coolant channel two velocity

The reason that Miller's critical velocity and pressure are different than that acquired during this study is a direct result from the use of Bernoulli's effect employed during Miller's study. It was assumed in Millers study that the flow velocity in both channels adjacent to the central plate are of equal velocity until a small perturbation in the flow area causes plate failure, while it was found in this study that for the flow geometry under discussion, the flow velocities are in fact unequal in adjacent flow channels. As a result of the observations made from Figure 6-19 a relationship between radial pressure imposed on the plate of interest and the NF of the plate up to the coolant velocity which produced a radial pressure equivalent to that predicted by Miller may be made. Because the frequency parameter associated with n = 1 in Table 6-3 and Table 6-4 is the lower than n = 2 and 3 through the entire flow regime considered, the plate is most likely to dynamically fail through n = 1 modal shape. Figure 6-20 presents the NF of the plate as a function of flow rate, or applied radial pressure load. Notice the linear relation between

NF and applied load in the positive (radially outward) direction indicating that, hydraulic loading a cylindrical plate increases the mechanical stiffness of the plate.

A fluid's resonant frequency (f_R) may be estimated through the use of [78, 79],

$$f_R = \frac{c}{2}\left[\left(\frac{1}{L}\right)^2 + \left(\frac{1}{h}\right)^2\right]^{\frac{1}{2}} \tag{6-4}$$

where c is the speed of sound in the fluid under consideration. Considering this study's geometric parameters (Table 4-1) and if the speed of sounds in water is approximated to be 1,500 m/s, the resonant frequency for the fluid is 3787 Hz. In order for convective instability, that is forced instability of the plate under discussion to occur the fluid resonant frequency and the plate's natural frequency must align. Visual examination of Figure 6-20 demonstrates that of the two boundary condition sets considered herein, the case of C-F-SS-F produces the lowest natural frequency at a flow rate of 0 m/s of approximately 4379 Hz. From this relation, and for the case considered, the fluid NF will never reach the plate's NF, thus plate dynamic instability for an ATR element is highly unlikely.

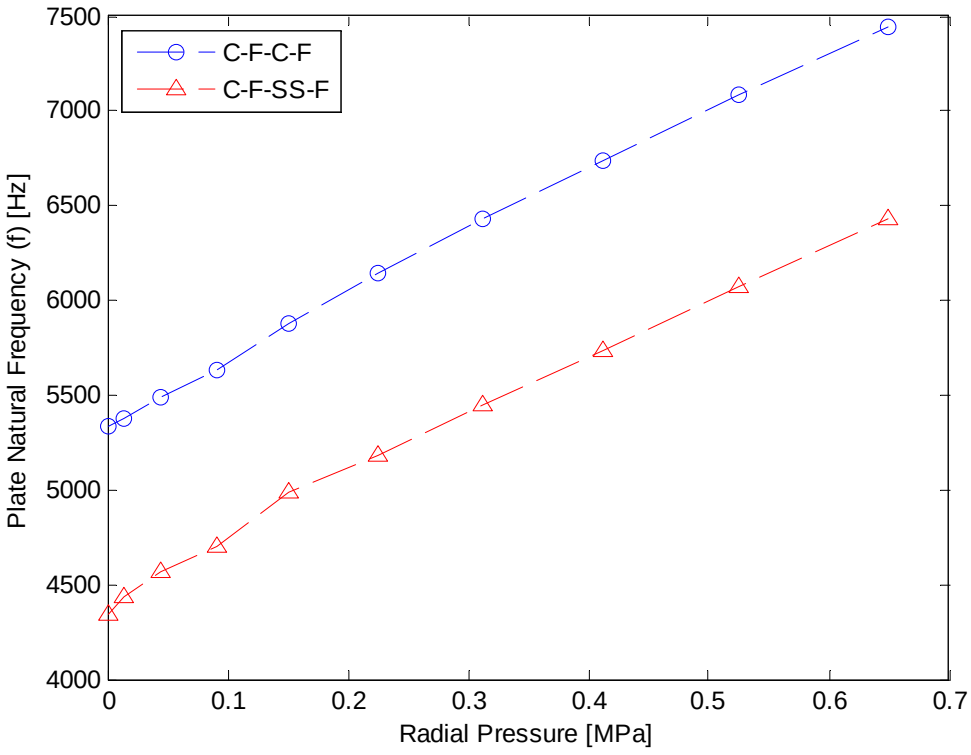

Figure 6-20: Plate natural frequency versus applied radial pressure load

7 CONCLUSIONS

This investigation leads to the first implementation of a simulated dynamic model for assessing mechanical instability of cylindrical plate-type geometry under axial flow conditions. Although much research has been conducted in the area of mechanical instability cause by the hydro-elasticity between a fluid and solid surface, current safety analysis methods for the high flux research reactors employ the oldest “static deformation” model developed by Daniel Miller in 1958.

As the U.S. HPRRs begin to convert their cores and update their safety analyses, it is crucial to update methods used to calculate key parameters. By employing this new model, predictive uncertainty will be reduced regarding flow induced mechanical instability safety. This, in turn, leads to higher confidence in life-cycle fuel performance and potentially greater safety margins or higher performance because we understand the margins better. Incidentally, this also leads to better insight into other key performance characteristics we thought were “good” but now we have concerns.

7.1 Observations

An extensive review of the published work related to mechanical instability of flat and cylindrical plates with emphasis on numerical methods previously employed was conducted. The open literature contains broad descriptions of numerical models developed and their relation to cylindrical plate type geometry. Very little detail was found describing the development of dynamic instability models which apply to cylindrical plate type elements, likely due to the fact that the application of instability models one developed herein are developed for the purpose of safety analyses in reactor specific applications. There were four objectives that governed the model development

1. Compare plastic plate deformation prediction methods of cylindrical plate type geometry (of ATR element geometry) using current safety analysis methods.

2. Develop a three dimensional FIV model for axial flow over a cylindrical plate based on ATR type fuel element geometry.

3. Employ the developed vibration model and compare the criticality of plastic plate deflection safety criteria used in current safety analyses to the fatigue of a cylindrical fuel plate over a fuel element life cycle. This fatigue information will be explicitly calculated using the natural frequencies (eigenvalues) and modal shapes (eigenfunctions) produced from the FIV model.

4. Assess the pressure fields which are most likely to cause FIV in geometry representative of an ATR element and provide a relation between plate dimensional characteristics and the onset of mechanical instability for range of pressure values along the axial and radial direction of the plate.

All four objectives were met. The plate stability module was found to adequately predict the NF of a cylindrical plate under test case conditions when compared against other published results. Although the test case is not representative of the two boundary condition sets considered during this study no analytical adjustment of the model was required when considering the test case, but rather the employment of two alternative edge boundary conditions used adding credibility to the derived model's capability. The NF trended toward the value of a flat plate with an increase in radius, as expected, however, did not fully collapse on the solution of a flat plate due to the flexural terms left in the equations of motion for a cylindrical plate relative to that of a flat plate.

A relationship between the pressure fields associated with an ATR type element and its NF was created along with a general relationship for the NF of a plate given C-F-C-F and C-F-SS-F edge boundaries as a function of plate aspect ratio. An assessment of the pressure fields and natural frequencies demonstrates that an ATR type fuel plate mechanically stiffness with an increase in load rendering it advantageous by design and the fluid NF will not reach that of the plate demonstrating that dynamic instability is unlikely under the conditions considered during this study.

7.2 Relevance of Work

The FIV model developed herein represents a first step toward improving the capabilities of predicting complex failure mechanisms associated with plate type fuel. The addition of this model provides an alternative method through the use of semi-numerical techniques to produce a relationship between cylindrical plate type geometry and its NF as opposed to finite element codes which are widely used. This study lastly objectively demonstrates that an ATR element is mechanical stable by design and is most likely to fail through buckling rather than flutter.

7.3 Assumptions and Limitations

Although this rigorous study on cylindrical plate instability caused by hydraulic characteristics attempts to capture all important physics that are associated with this phenomenon, it inherently requires the assistance of numerous assumptions. These assumptions innately affect the limitations of the study at hand and the model developed for the application and use in identifying conditions susceptible to vibration caused under axial flow conditions.

7.3.1 Plate Module

The most fundamental assumption included into the plate instability model is that associated with the modal response of the plate itself. Hypotheses associated with plate vibration in cylindrical form acknowledge the likelihood that cylindrical plates do not undergo single mode vibration under any conditions, but rather deflect in multiple modes which both constructively and destructively interfere with each other [63]. This study assumes that a single mode of vibration occurs independent of all other modes for a given boundary value case.

The plate geometry considered during this study assumes homogeneity throughout the entire plate material in contrast to that which is representative of actual fuel plate geometry (Figure 1-3). HPRR type fuel plates are of the laminate type with three distinct layers. The outer two layers are comprised of an aluminum shell while the inner is of a uranium molybdenum alloy which has much different characteristic properties to that of

the aluminum. This assumption alters the numerical eigenvalue solution by an unknown amount relative to that of a physical HPRR plate.

A simplification to the exact set of plate equations was performed with the removal of deflection (u) as it was necessary to reduce the order of equations in the axial direction (x) from nine to eight such that both the x and ϕ coordinate directions matched in order. As a result of eliminating u it was also necessary to remove the bending term $[k]\partial^3 w/\partial x^3$ to preserve symmetry in the system.

Kantrovich's reduction limits the calculation to be projected in a single coordinate direction while the perpendicular coordinate direction solution is iterated upon. During this study it was chosen to assume a modal shape along the axial length (x) of the plate and iterate upon the azimuthal (ϕ) direction. This assumption was chosen because previous studies employing the Rayleigh-Ritz method, which depends solely on eigenfunctions, has shown that an acceptable solution may be produced given an assumed modal shape for a straight beam [75]. The axial direction of the plate is associated to the 'straight beam' during this study. Furthermore it has been shown that the modified matrix method produces reliable, accurate, and stable solutions when applied to complex geometries [86] justifying its implementation in and the iteration on the azimuthal direction rather than the axial direction.

The model under discussion assumes that the plate (prior to vibration) is a 'perfect cylindrical plate'. It assumes that the surface is 'smooth' and that there are no geometric abnormalities to the plate geometry. Previous studies have addressed the effect of imperfections of geometries and their association with the mechanical instability of flat plate type elements [39], however, these considerations were neglected as a part of this study's model development process.

The study presented herein focuses on the analysis of a single cylindrical plate under vibrational conditions, however, a truly representative FIV model which reflects ATR

type fuel element geometry must include all plates and characteristic flow through concurrent subchannels. This oversight in the model development has an unknown impact on the results of the model relative to that compared against the actual vibrational characteristics of a complete ATR element. Kim and Davis [30] found that the added mass of fluid and affect of adjacent plates in flat plate type geometry significantly alters the NF for a single plate under axial flow conditions.

This study is limited to digits of precision available in 32 bit computer software. Matlab® was employed during this study and was installed on a 32 bit desktop work station. As has been previously discussed, the use of sufficient significant digits is paramount to success for numerical studies regarding plate stability, in particular those associated with complex mode shapes and complex geometries (both characteristic of this study). During the use of the modified matrix progression method coefficients of the forcing function compound over each iteration resulting in potentially large deviations from the correct solution even if the solution has converged if a sufficient number of significant digits are not considered during the calculation.

The data available for coefficients of the eigenfunction (λ_m and σ_m) chosen to be used during this study, presented in (5-57), are limited to a select number of references. As discussed in Chapter 4, previous studies have demonstrated that even changes of the order 10^{-6} to these coefficients may significantly alter the modal shape in higher order modes. It is for this reason that the use of as many available significant digits of these eigenfunction coefficients is paramount to the accuracy of the solution. Data from Blevins [75] was chosen for use here as it is the most recently published available data.

7.3.2 Flow Module

The fluid module is steady. That is, no temporal response of the fluid is considered as a part of the flow module. It is assumed that the flow conditions are incremented at infinitely small increments until they induce plate instability. This may be an accurate assumption for eigenvalues which are located near the steady state operating conditions

of the ATR, however, they do not reflect the correct NF that a plate may undergo as it observes transient flow conditions.

The membrane pressures applied to the plate stability module are produced through the application flow module. It is assumed that the fluid passing through each of the flow channels is fully developed through the channels' entire length. This significantly alters the physics associated with flow redistribution. By assuming the flow field is turbulent through the entire element length both P_x and P_r values may be significantly altered in contrast to a model which includes a flow field region with developing turbulent flow.

It was assumed that the plate deformation is insignificant to the alteration of the flow field. That is that the pressure losses due to acceleration along the channel caused by the plate's deformation is negligibly small relative to the other forces. Although this was qualitatively justified for the study herein, it may be applicable for alternative geometry and flow conditions to include these phenomena into the model.

The radial pressure is assumed to be uniformly applied along the entire axial length of the plate, however, this is not representative of the physical system. Because the radial pressure is a function of the pressure in each channel and the pressure acquired for a given channel is dependent upon the friction losses in that channel, a net pressure gradient along the stream wise direction is bound to occur.

7.4 Future Work

The study presented herein supports the ongoing work in the field of FIV and demonstrates a feasible method for computing and identifying this phenomenon using a semi-numerical method. This study is intended to be the first step in a continuing effort to create a representative FIV model developed around ATR type element geometry which may be employed during the process of core conversion from HEU to LEU fuel. A number of necessary assumptions made in the development of this FIV model may be addressed during these future studies.

The addition of multiple plates in previous studies have shown to produce a significant impact on the converged NF solution produced using semi-numerical methods and applied to flat plate type geometries submerged in liquids. This consideration as a part of the model development will provide an objective evaluation as to whether this phenomenon is observed for cylindrical plate type geometry as well and add credibility to the development of the current work under discussion.

All phenomena considered during this study were that of the mesa-scale order, however, the influence of many micro-scale phenomena including surface roughness and oxide layer growth have been experimentally shown to influence flow characteristics of large aspect ratio geometries like that considered herein, thus influencing the vibrational conditions necessary to a induce NF of various modes.

Additional work with the focus of laminate plate type geometry relative to that of the homogeneous type considered here will provide a more representative eigenvalue to that of the physical HPRR type plate. Flügge [94] presents the following set of relations, which in future studies may replace the relations (5-15) through (5-22) considered during this study

$$N_\phi = \frac{D_\phi}{R}\left(\frac{\partial v}{\partial \phi} + w\right) + \frac{D_v}{R}\left(\frac{\partial u}{\partial x}\right) + \frac{K_\phi}{R^3}\left(w + \frac{\partial^2 w}{\partial \phi^2}\right) \tag{7-1}$$

where D_ϕ, D_v, and K_ϕ are directionally dependant characteristic parameters and are defined as, $D_\phi = E_2 h_1 + 2E_1 h_2$, $D_v = E_v h$, and $K_\phi = E_1/12\left(h^3 - h_1^3\right) + E_2/12\left(h_1^3\right)$, respectively. Note that subscript 1 represents the inner core parameter, and subscript 2 represents characteristics of the outer layers (assuming both outer layers are similar in geometry and material).

$$N_x = \frac{D_x}{R}\left(\frac{\partial u}{\partial x}\right) + \frac{D_v}{R}\left(\frac{\partial v}{\partial \phi} + w\right) + \frac{K_x}{R^3}\left(\frac{\partial^2 w}{\partial x^2}\right), \tag{7-2}$$

where $D_x = E_1 h_1 + 2E_2 h_2$ and $K_x = E_2/12\left(h^3 - h_1^3\right) + E_1/12\left(h_1^3\right)$;

$$N_{\phi x} = \frac{D_{x\phi}}{R}\left(\frac{\partial u}{\partial \phi} + \frac{\partial v}{\partial x}\right) + \frac{K_{x\phi}}{R^3}\left(\frac{\partial u}{\partial \phi} + \frac{\partial w}{\partial x}\frac{\partial w}{\partial \phi}\right), \tag{7-3}$$

where $D_{x\phi} = Gh$, $K_{x\phi} = 1/\left(12Gh^3\right)$, and G is the shear modulus of the plate;

$$N_{x\phi} = \frac{D_{x\phi}}{R}\left(\frac{\partial u}{\partial \phi} + \frac{\partial v}{\partial x}\right) + \frac{K_{x\phi}}{R^3}\left(\frac{\partial v}{\partial x} - \frac{\partial w}{\partial x}\frac{\partial w}{\partial \phi}\right), \tag{7-4}$$

$$M_{\phi} = \frac{K_{\phi}}{R^2}\left(w + \frac{\partial^2 w}{\partial \phi^2}\right) + \frac{K_{v}}{R^2}\left(\frac{\partial^2 w}{\partial x^2}\right), \tag{7-5}$$

where $K_{v} = 1/12\left(E_{v}h^3\right)$;

$$M_{x} = \frac{K_{x}}{R^2}\left(\frac{\partial^2 w}{\partial x^2} - \frac{\partial u}{\partial x}\right) + \frac{K_{v}}{R^2}\left(\frac{\partial^2 w}{\partial \phi^2} - \frac{\partial v}{\partial \phi}\right), \tag{7-6}$$

$$M_{\phi x} = \frac{K_{x\phi}}{R^2}\left(2\frac{\partial w}{\partial x}\frac{\partial w}{\partial \phi} + \frac{\partial u}{\partial \phi} - \frac{\partial v}{\partial x}\right), \tag{7-7}$$

and

$$M_{x\phi} = \frac{2K_{x\phi}}{R^2}\left(\frac{\partial w}{\partial x}\frac{\partial w}{\partial \phi} - \frac{\partial v}{\partial x}\right) \tag{7-8}$$

A comparison to this study's solutions by that produced by experimental work will further expand upon the credibility for the model discussed herein. OSU and INL are currently collaborating on a test program which will conduct hydro-mechanical testing of a generic plate type fuel element, or standard fuel element (SFE), for the purpose of qualitatively demonstrating an increase in mechanical integrity of U-Mo alloy monolithic plates as compared to that of uranium aluminum, and aluminum fuel plates due to hydraulic forces. This test program supports ongoing work conducted for/by the fuel development program and will take place at OSU in the Hydro-Mechanical Fuel Test Facility (HMFTF). Once all SFE tests have concluded it is incumbent upon OSU to employ the HMFTF in the experimental examination of vibration and plate deformation under flow conditions with fuel plate geometries representative of that in the ATR.

8 BIBLIOGRAPHY

1. Leventhal, P. and A. Kuperman (1995) *RERTR At The Crossroads: Success or Demise*. Nuclear Control Institute **1**.

2. Argonne National Laboratory, *Reduced Enrichment for Research and Test Reactors*. 2007, Nuclear Engineering Division at Argonne.

3. Staples, P., *Request For Information - NNSA Fuel Fabrication Capability Project*, Department of Energy, Editor. 2008, IIPS. p. 1-5.

4. Lemoine, P. and D. Wachs, *High Density Fuel Development for Research Reactors*, in *2007 Reduced Enrichment for Research and Test Reactors Meeting*. 2007: Prague, Czech Republic. p. 1-15.

5. Wachs, D.M., C.R. Clark, and R.J. Dunavant, *Conceptual Process Description for the Manufacture of Low-Enriched Uranium-Molybdenum Fuel*, Department of Energy, Editor. 2008, Idaho National Laboratory: Idaho Falls. p. 1-29.

6. Robinson, A.B., D.E. Burkes, and D.M. Wachs, *Post Irradiation Examination of Modified Interface High Density Monolithic Fuel*, in *2008 International RERTR Meeting*. 2008, Idaho National Laboratory: Washington DC, USA.

7. Miller, B.D., et al., *Radiation Effects on the Microstructure Stability of RERTR Fuels*, in *RERTR 2008*. 2008, Idaho National Laboratory: Washington DC, USA.

8. Burkes, D.E., et al., *Dilatometry and Thermal Diffusivity Measurements of DU-xMo Alloys with x = 7, 10, and 12 wt%.* Journal of Nuclear Materials, 2009: p. 38.

9. Burkes, D.E., et al., *Effects of Applied Load on 6061-T6 Aluminum Joined Employing a Novel Friction Bonding Process.* Metallurgical and Materials Transactions A, 2008. **39A**: p. 10.

10. Burkes, D.E., et al., *Fresh Fuel Characterization of U-Mo Alloys*, in *RERTR 2008*. 2008, Idaho National Laboratory: Washington DC, USA.

11. Burkes, D.E., et al., *Mechanical Properties of DU-xMo Alloys with x = 7-12 wt%.* Matallurgical and Materials Transactions A, 2008: p. 34.

12. Burkes, D.E., et al., *Microstructural Characteristics of DU-xMo Alloys with x=7 to 12 wt%.* Journal of Alloys and Compounds, 2009: p. 29.

13. Burkes, D.E., et al., *Properties of DU-10wt%Mo Alloys Subjected to Various Post-Rolling Heat Treatments.* Nuclear Engineering and Design, 2009: p. 23.

14. Wachs, D., *Status of GTRI Fuel Development Program*, in *2008 International RERTR Meeting*. 2008, Idaho National Laboratory: Washington DC.

15. Marcum, W.R., B.G. Woods, and D.M. Wachs, *High Performance Research Reactor Fuel Development Hydraulic Test Loop*, in *RERTR 2008*. 2008, Oregon State University: Washington DC, USA.

16. Wachs, D.M., *RERTR Fuel Development and Qualification Plan*, Department of Energy, Editor. 2007, Idaho National Laboratory: Idaho Falls.

17. Ferris, H.D. and G.A. Jahren, *Advanced Test Reactor Fuel Plate Pressure Deflection Tests*, A.E. Commission, Editor. 1963, The Babcock & Wilcox Company. p. 1-188.

18. Deville, R.E., *Differential Thermal Expansion Tests on Advanced Test Reactor Fuel Plates*. October 1963, Babcock & Wilcox Co. p. 1-117.

19. Francis, W.C., et al., *Quarterly Report: Status of Test Reactor Fuel Element Activities*. January 1967, Idaho Nuclear Corporation.: Idaho Falls.

20. Laboratory, I.N., *Upgraded Final Safety Analysis Report for the Advanced Test Reactor*. 2003, Idaho National Laboratory.

21. deBoisblanc, D.R. and S. Cohen, *Safety Analysis Report: Advanced Test Reactor - Volume 1 of 2*, A.E. Commission, Editor. 1965, Phillips Petroleum Company. p. 1-332.

22. Gribenow, M.L., *Isothermal Hydraulic Measurements In Fuel Elements in ATR Core*. September 1968, Idaho Nuclear Corporation: Idaho Falls.

23. Croft, M.W., *Advanced Test Reactor Burnout Heat Transfer Tests*, A.E. Division, Editor. 1984, The Babcock & Wilcox Company: Lynchburg Verginia. p. 1-58.

24. Griess, J.C., et al., *Effect of Heat Flux on the Corrosion of Aluminum by Water, Part I, Experimental Equipment and Preliminary Test Results*, Department of Energy, Editor. 1960, Oak Ridge National Laboratory: Oak Ridge Tennessee.

25. Griess, J.C., et al., *Effect of Heat Flux on the Corrosion of Aluminum by Water, Part II, Influence of Water Temperature, Velocity, and pH on Corrosion Product Formation*, Department of Energy, Editor. 1961, Oak Ridge National Laboratory: Oak Ridge Tennessee.

26. Griess, J.C., et al., *Effect of Heat Flux on the Corrosion of Aluminum by Water, Part III, Final Report of Tests Relative to the High Flux Isotope Research Reactor*, Department of Energy, Editor. 1961, ORNL-3230: Oak Ridge Tennessee.

27. Griess, J.C., H.C. Savage, and J.L. English, *Effect of Heat Flux on the Corrosion of Aluminum by Water, Part IV, Tests Relative to the Advanced Test Reactor and Correlation with Previous Results*, Department of Energy, Editor. 1964, Oak Ridge National Laboratory: Oak Ridge Tennessee.

28. Atkinson, S.A., *A Study of the Onset of Flow Instability in ATR Fuel Channels*, E. Devision, Editor. 1975, Aeroject Nuclear Company. p. 1-42.

29. Welsh, M.C., et al., *Sources of Flow Induced Vibration*, in *Workshop on Industrial Fluid Dynamics, Heat Transfer and Wind Engineering*. 1990: Victoria Australia. p. 16-17.

30. Kim, G. and D.C. Davis, *Hydrodynamic Instabilities in Flat-Plate-Type Fuel Assemblies.* Nuclear Engineering and Design, 1995. **158**: p. 17.

31. Stromquist, W.K. and O. Sisman, *High Flux Reactor Fuel Assemblies Vibration and Water Flow.*, National Defense of the United States, Editor. June 1948, Oak Ridge National Laboratory.

32. Doan, R.L., *The Engineering Test Reactor - A Status Report.* Nucleonics, 1958. **16**: p. 102-105.

33. Miller, D.R., *Critical Flow Velocities for Collapes of Reactor Parallel-Plate Fuel Assemblies*. 1958, General Electric Company; Knolls Atomic Power Laboratory: Schenectady, New York. p. 24.

34. Davis, D.C. and G. Kim, *Design Against Hydrodynamic Instabilities in Flat-Plate Type Fuel Element Assemblies*, in *International Conference on Structural Mechanics in Reactor Technology*. 1991: Tokyo Japan.

35. Zabriskie, W.L., *An Experimental Evaluation of Critical Flow Velocity Formulas for Parallel Plate Assemblies*. October 31, 1958, General Electric Co.

36. Zabriskie, W.L., *An Experimental Evaluation of the Effect of Length-to-Width Ratio on the Critical Flow Velocity of Single Plate Assemblies*. September 1, 1959, General Electric Co.

37. Johansson, R.B., *Hydraulic Instability of Reactor Parallel Plate Fuel Assemblies*, in *Nuclear Engineering Science Conference*. 1960. p. Paper No. 57.

38. Rosenberg, G.S. and C.K. Yougdahl, *A Simplified Dynamic Model for the Vibration Frequencies and Critical Coolant Flow Velocities for Reactor Parallel Plate Fuel Assemblies.* Nuclear Science and Engineering, 1962. **13**: p. 91-102.

39. Kane, J.J., *The Effect of Inlet Spacing Deviations on the Flow-Induced Deflections of Parallel Plates.* Nuclear Science and Engineering, 1963. **15**(3): p. 305-308.

40. Groninger, R.D. and J.J. Kane, *Flow Induced Deflections of Parallel Flat Plates.* Nuclear Science and Engineering, 1963. **16**: p. 218-226.

41. Dowell, E., *General Aerodynamic Forces on an Oscillating Cylindrical Shell: Subsonic and Supersonic Flow.* AIAA Journal, 1967. **4**: p. 607-610.

42. Dowell, E.H., *Nonlinear Oscillations of a Fluttering Plate II.* AIAA Journal, 1967. **5**(10): p. 1856-1862.

43. Scavuzzo, R.J., *Hydraulic Instability of Flat Parallel-Plate Assemblies.* Nuclear Science and Engineering, 1965. **21**: p. 463-472.

44. Wambsganss, M.W., *Second-Order Effects as Related to Critical Coolant Flow Velocities in Reactor Parallel Plate Fuel Assemblies.* Nuclear Engineering and Design, 1967. **5**: p. 268-276.

45. Smissaert, G.E., *Static and Dynamic Hydroelastic Instabilities in MTR-Type Fuel Elements Part I. Introduction and Experimental Investigation.* Nuclear Science and Engineering, 1968. **7**: p. 11.

46. Smissaert, G.E., *Static and Dynamic Hydroelastic Instabilities in MTR-Type Fuel Elements Part II. Theoretical Investigation and Discussion.* Nuclear Science and Engineering, 1969. **9**: p. 17.

47. Smith, R.L., *Dynamic Pressure Limits for Flat Plates as Related to Nuclear Fuel Elements*, Department of Energy, Editor. 1968, National Aeronautics and Space Administration: Washington DC. p. 27.

48. Weaver, D.S. and T.E. Unny, *The Hydroelastic Stability of a Flat Plate.* Journal of Applied Mechanics, 1970. **37**(3): p. 823-827.

49. Leissa, A.W., *The Free Vibration of Rectangular Plates.* Journal of Sound and Vibration, 1973. **31**(3): p. 257-293.

50. Kornecki, A., E.H. Dowell, and J. O'Brien, *On the Aeroelastic Instbility of Two-Dimensional Panels in Uniform Incompressible Flow.* Journal of Sound and Vibration, 1976. **47**(2): p. 163-178.

51. Holmes, P.J., *Bifurcations to Divergence and Flutter in Flow Induced Oscillations: A Finite Dimensional Analysis.* Journal of Sound and Vibration, 1977. **53**(4): p. 471-503.

52. Ramm, E. and H. Stegmuller, *The Displacement Finite Element Method in Nonlinear Buckling Analysis of Shells*. Buckling of Shells, ed. E. Ramm. 1982, Berlin: Springer-Verlag.

53. Pica, A., R.D. Wood, and E. Hinton, *Finite Element Analysis of Geometrically Nonlinear Plate Behaviour Using a Mindlin Formulation.* Computers & Structures, 1980. **11**: p. 203-215.

54. Gallagher, R.H., *Finite Element Method for Instability Analysis*. Handbook of Finite Elements, ed. H. Kardestuncer. 1987, New York: McGraw-Hill.

55. Zhongnian, X., *A Simple and Efficient Triangle Finite Element for Plate Bending.* Acta Mechanica Sinica, 1986. **2**(2): p. 185-192.

56. Guo, A.C.Q., R.H. Peng, and D.L. Sun, *A Dynamic Model for Flow-Induced Vibration of Parallel-Plates*, in *International Conference on Structural Mechanics in Reactor Technology*, K. Kussmaul, Editor. 1993. p. 4.

57. Miklavcic, M., M. Williams, and D.D. Joseph, *Stability of Mean Flows over an Infinite Flat Plate.* Archive for Rational Mechanics and Analysis, 1982. **80**(1): p. 13.

58. Lucey, A.D., *The excitation of waves on a flexible panel in a uniform flow.* Phil. Trans. R. Soc. Lond., 1996. **356**: p. 40.

59. Wang, J., et al., *Experimental Study of Flow Induced Vibration of the Planar Fuel Assembly*, in *International Conference on Structural Mechanics in Reactor Technology*. 2005: Beijing China. p. 9.

60. Hu, M.-y. and A.-w. Wang, *Free Vibration and Transverse Stresses of Viscoelastic Laminated Plates.* Applied Mathematics and Mechanics, 2008. **30**(1): p. 8.

61. Hinton, E., M. Ozakca, and N.V. Rao, *Free Vibration Analysis and Shape Optimization of Variable Thickness Plates, Prismatic Folded Plates and Curved Shells, Part 2: Shape Optimization.* Journal of Sound and Vibration, 1995. **181**(4): p. 18.

62. Morris, I.R. and D.J. Dawe, *Free Vibration of Curved-Plate Assemblies With Diaphragm Ends.* Journal of Sound and Vibration, 1980. **73**(1): p. 17.

63. Dawe, D.J. and I.R. Morris, *Vibration of Curved Plate Assemblies Subjected to Membrane Stresses.* Journal of Sound and Vibration, 1982. **81**(2): p. 18.

64. Banerjee, M.M. and G.A. Rogerson, *On the Application of the Constant Deflection-Contour Method in Nonlinear Vibrations of Elastic Plates.* Archive of Applied Mechanics, 2002. **72**: p. 13.

65. Shintani, M. and M. Hamai, *Study on Analytical Model of Nonlinear Vibration for Elastic Plates With Gaps Under Random Waves.* Transactions of the ASME, 2004. **126**: p. 6.

66. Sen'kovskawa, S.M. and A.L. Shleykel', *Effects of High-Frequency Vibration on the Onset of Convection in a Horizontal Fluid Layer.* Doklady Physics, 2002. **47**(2): p. 4.

67. Biswas, P., *Critical Analysis and Overview of the Nonlinear Deformations, Buckling and Vibrations of Thermally-Stressed Plate and Shell Structures of Regular and Irregular Geometric Shapes*, in *International Conference on Structural Mechanics in Reactor Technology*. 1997: Lyon France. p. 18.

68. Yang, Y.R. and J.Y. Zhang, *Frequency Analysis of a Parallel Flat Plate-Type Structure in Still Water, Part I: A Multi-Span Beam.* Journal of Sound and Vibration, 1997. **203**: p. 795-804.

69. Yang, Y.R. and J.Y. Zhang, *Frequency Analysis of a Parallel Flat Plate-Type Structure in Still Water, Part II: A Complex Structure.* Journal of Alloys and Compounds, 1997. **203**(805-814).

70. Guo, C.Q. and M.P. Paidoussis, *Analysis of Hydroelastic Instabilities of Rectangular Parallel-Plate Assemblies.* Journal of Pressure Vessel Technology, 2000. **122**: p. 171-176.

71. Guo, C.Q. and M.P. Paidoussis, *Stability of Rectangular Plates With Free Side-Edges in Two-Dimensional Inviscid Channel Flow.* Journal of Applied Mechanics, 2000. **67**: p. 6.

72. Ugural, A.C. and S.K. Fenster, *Advanced Strength and Applied Elasticity*. Fourth ed. 2003, Upper Saddle River: Pearson Education Inc.

73. Ho, M., G. Hong, and A.N.F. Mack. *Experimental Investigation of Flow-Induced Vibration in a Parallel Plate Reactor Fuel Assembly*. in *Australian Fluid Mechanics Conference*. 2004. The University of Sydney, Sydney, Australia.

74. Shufrin, I., O. Rabinovitch, and M. Eisenberger, *Elastic Nonlinear Stability Analysis of Thin Rectangular Plates Through a Semi-Analytical Approach.* International Journal of Solids and Structures, 2009. **46**: p. 2075-2092.

75. Blevins, R.D., *Formulas for Natural Frequency and Mode Shape*. 2001: Krieger Publishing Company. 492.

76. Yu, Y., *Vibrations of Elastic Plates*. 1995, Verlag: Springer. 228.

77. Qatu, M.S., *Vibration of Laminated Shells and Plates*. 2004, Kidlington: Elsevier Limited. 409.

78. Blevins, R.D., *Flow Induced Vibration*. 1977, New York: Van Nostrand Reinhold Company. 363.

79. Naudascher, E. and D. Rockwell, *Flow Induced Vibration - An Engineering Guide*. 2005, Mineola: Dover Publications, Inc. 414.

80. Kaneko, S., et al., *Flow-Induced Vibrations Classifications and Leassons from Practical Experiences*. 2008, Kidlington: Elsevier Limited. 284.

81. Sanders, J.L., *An Improved First-Approximation Theory for Thin Shells*, N.A.a.S. Administration, Editor. 1959, Langly Research Center: Langly Field, VA. p. 1-11.

82. Ferris, H.D. and J.C. Moyers, *Advanced Test Reactor Hydraulic Buckling Tests*, A.E. Commission, Editor. 1963, The Babcock & Wilcox Company. p. 1-188.

83. Sewall, J.L., R.R. Clary, and S.A. Leadbetter, *An Experimental and Analytical Vibration Study of a Ring-Stiffened Cylindrical Shell Structure with Various Support Conditions*, NASA, Editor. 1964, Langly Research Center, NASA TN D-2398: Washington DC.

84. Sewall, J.L., *Vibration Analysis of Cylindrically Curved Panels with Simply Supported or Clamped Edges and Comparison with Some Experiments*, NASA, Editor. 1967, Langly Research Center, NASA TN D-3791: Washington DC.

85. Petyt, M. and J.M. DebNath, *Vibration Analysis of Sinlgy Curved Rectangular Plates.* Journal of Sound and Vibration, 1971. **13**(4): p. 485-597.

86. DebNath, J.M., *Dynamics of Rectangular Curved Plates*. 1969, University of Southampton: Southampton.

87. Tottenham, H., *The Matrix Progression Method in Structural Analysis*, in *Introduction to Structural Problems in Nuclear Reactor Engineering*, J.R. Rydzewski, Editor. 1982, The Macmillan Company: New York.

88. Swinson, W.F. and G.T. Yahr. *Dynamic Pressure Approach to Analysis of Reactor Fuel Plate Stability*. in *American Nuclear Society Annual Meeting*. 1990.

89. Swinson, W.F., et al., *Follow-Up Fuel Plate Stability Experiments and Analyses for the Advanced Neutron Source*, U.S. Department of Energy, Editor. 1993, Oak Ridge National Laboratory: Oak Ridge Tennessee. p. 1-64.

90. Sartory, W.K., *Nonlinear Analysis of Hydraulic Buckling Instability of ANS Involute Fuel Plates*, U.S. Department of Energy, Editor. 1993, Oak Ridge National Laboratory: Oak Ridge Tennessee. p. 1-30.

91. Luttrell, C.R., *Finite Element Analysis of Advanced Neutron Source Fuel Plates*, U.S. Department of Energy, Editor. 1995, Oak Ridge National Laboratory: Oak Ridge Tennessee. p. 1-23.

92. Bedford, A. and I.M. Liechti, *Mechanics of Materials*. 2000, Upper Saddle River: Prentice Hall.

93. Kerboua, Y. and A.A. Lakis, *Dynamic Behaviour of Plates Subjected to a Flowing Fluid.* WSEAS Transactions on Fluid Mechanics, 2008. **3**(2): p. 101-115.

94. Flugge, W., *Stresses in Shells*. Second Print. 1962, Berlin/Gottingen, Heidelberg: Pringer-Verlag.

95. Kantorovich, L.V. and V.I. Krylov, *Approximate Methods of Higher Analysis.*, New York: Interscience Publishers Inc.

96. Chang, T.C. and R.R. Craig, *Normal Modes of Uniform Beams.* Journal of Engineering Mechanics Division, American Society of Civil Engineers, 1969. **95**: p. 1027-1031.

97. Kreyszig, E., *Advanced Engineering Mathematics*. 8th ed, ed. B. Holland. 1999, New York: Peter Janzow. 1156.

98. White, F., *Fluid Mechanics*. Fifth ed. 2003: McGraw-Hill Higher Education.

99. White, F.M., *Viscous Fluid Flow*. 1974, New York: McGraw-Hill Book Company.

100. Haaland, S.E., *Simple and Explicit Formulas for the Friction Factor in Turbulent Flow.* Journal of Fluids Engineering (ASME), 1983. **103**(5): p. 89-90.

101. Churchill, S.W., *Frictional Equation Spans All Fluid Flow Regimes.* Chemical Engineering, 1977. **84**: p. 91-92.

102. Moody, L.F., *Friction Factors for Pipe Flow.* Transactions of the American Society of Mechanical Engienering, 1944. **66**(8): p. 671-684.

103. Drew, T.B., R.C. Koo, and W.H. McAdams, *The Friction Factor for Clean Round Pipes.* Trans. AIChE, 1932. **28**(53).

104. Abdelall, F.F., et al., *Pressure Drop Caused by Abrupt Flow Area Changes in Small Channels.* Experimental Thermal and Fluid Science, 2005. **29**: p. 425-434.

105. Jeong, K.-H., *Hydroelastic Vibration of Two Annular Plates Coupled with a Bounded Compressible Fluid.* Journal of Fluids and Structures, 2006. **22**: p. 1079-1096.

106. Team, R.-D.C., *Volume IV: Models and Correlations*, in *Code Manual*, R.-D.C. Team, Editor. 2004, Idaho National Laboratory: Idaho Falls, Idaho.

107. Team, R.-D.C.D., *Volume I: code structure, system models, and solution methods*, in *RELAP5-3D code manual*. 2005, Idaho National Laboratory: Idaho Falls, Idaho. p. 600.

108. Zigrang, D.J. and N.D. Sylvester, *A Review of Explicit Friction Factor Equations.* Journal of Energy Resources Technology, 1985. **107**: p. 280-283.

109. Colebrook, C.F., *Turbulent Flow in Pipes with Particular Reference to the Transition Region Between Smoth and Rough Pipe Laws.* Journal of Institute of Civil Engineers, 1939. **11**: p. 133-156.

9 NOMENCLATURE

Symbols

a	Plate thickness
b	Plate width
f_1	Spatial function in *u* direction dependant only on x
f_2	Spatial function in *v* direction dependant only on x
f_3	Spatial function in *w* direction dependant only on x
g	Gravitational acceleration
g_1	Spatial function in *u* direction dependant only on ϕ
g_2	Spatial function in *v* direction dependant only on ϕ
g_3	Spatial function in *w* direction dependant only on ϕ
h	Flow channel height
h_1	Flow channel height of channel one
h_2	Flow channel height of channel two
k	Bending stiffness
k_i	Flow channel inlet form loss
k_e	Flow channel exit form loss
l	Effective plate length
m	Plate mass per unit area, mode number in axial direction
$\overline{\mathrm{n}}$	Normal vector directional pointed outward from control surface
n	Mode number in span-wise direction, number of discrete nodes in $\phi \in [0, \theta]$
q_ϕ	$P_r R / D$

q_x	P_x/D
q_z	$N_{x\phi}/D$
r	Directional component positively pointing outward
t	Time
u	Local plate position in axial direction
u_i	Average fluid velocity at inlet of control surface
u_o	Average fluid velocity at outlet of control surface
u_r	Radial component of instantaneous fluid velocity
u_ϕ	Azimuthal component of instantaneous fluid velocity
u_x	Axial component of instantaneous fluid velocity
$\overline{u}_r$	Radial component of mean fluid velocity
$\overline{u}_\phi$	Azimuthal component of mean fluid velocity
$\overline{u}_x$	Axial component of mean fluid velocity
u'_r	Radial component of fluctuating fluid velocity
u'_ϕ	Azimuthal component of fluctuating fluid velocity
u'_x	Axial component of fluctuating fluid velocity
v	Local plate position in traverse direction
$\overline{\mathrm{v}}$	Mean flow vector
w	Local lateral plate deflection
w_o	Normalized lateral local plate deflection relative
$\overline{x}$	Dimensionless plate length scale, (L/R)
x	Spatial coordinate in axial flow direction
x_i	Axial location at inlet of control surface

x_o	Axial location at outlet of control surface
y	Spatial coordinate in span-wise direction
z	Spatial coordinate in traverse direction
A	Coefficient matrix of first order differential equations of motion (8 x 8)
$\tilde{A}$	Plate cross sectional area per unit width
C	Defined in (4-13)
D	Plate extensional rigidity
D_h	Flow channel hydraulic diameter
$D_{h,1}$	Hydraulic diameter of channel one
$D_{h,2}$	Hydraulic diameter of channel two
$D_{h,i}$	Hydraulic diameter at inlet of form loss junction
$D_{h,o}$	Hydraulic diameter at outlet of form loss junction
E	Modulus of elasticity
F	Product of H and J_0
F^*	Rows 1 through 4 of F
F^{**}	Rows 5 through 8 of F
F_m	m^{th} eigenfunction of a straight beam
G	Displacement matrix $[g_1, g_2, ...g_8]$
G^*	Rows 1 through 4 of G
G^{**}	Rows 5 through 8 of G
G	Parameter defined by (2-5)

H	Exponential of $[\mathrm{A}]\phi$
I	Area moment of inertia of plate
I_m	Area moment of inertia of a beam per unit width
J_0	Boundary condition matrix acting on G at $\phi = 0$
K_θ	Boundary condition matrix acting on G at $\phi = \theta$
K	Flexural rigidity of plate, form loss coefficient
$K_{1,i}$	Form loss coefficient resulting from sudden contraction from common flow channel to subchannel one
$K_{1,o}$	Form loss coefficient resulting from sudden expansion from subchannel one to common flow channel
$K_{2,i}$	Form loss coefficient resulting from sudden contraction from common flow channel to subchannel two
$K_{2,o}$	Form loss coefficient resulting from sudden expansion from subchannel two to common flow channel
K_{SC}	Sudden contraction form loss coefficient
K_{SE}	Sudden expansion form loss coefficient
L	Plate length in x direction
L_{a1}	Partial differential operator acting on the x directional equation of motion with constant coefficients
L_{a2}	Partial differential operator acting on the ϕ directional equation of motion with constant coefficients
L_{a3}	Partial differential operator acting on the r directional equation of motion with constant coefficients
L_1	Partial differential operator acting on the x directional equation of motion
L_2	Partial differential operator acting on the ϕ directional equation of motion
L_3	Partial differential operator acting on the r directional equation of motion

M_{ϕ}	ϕ directional bending moment on plate x
$M_{\phi x}$	ϕ directional bending moment on plate crossed by x
M_{x}	x directional bending moment on plate
$M_{x\phi}$	x directional bending moment on plate crossed by ϕ
M	Mach Number
N_{ϕ}	ϕ directional normal stress resultant component
$N_{\phi x}$	ϕ directional normal stress resultant component crossed by x
N_{x}	x directional normal stress resultant component
$N_{x\phi}$	x directional normal stress resultant component crossed by ϕ
P	Pressure imposed on exposed plate surface, local instantaneous pressure of fluid
$\overline{P}$	Local mean pressure of fluid
P'	Local fluctuating pressure of fluid
$P_{1,i}$	Inlet pressure of subchannel one
$P_{1,i}$	Outlet pressure of subchannel one
$P_{2,i}$	Inlet pressure of subchannel two
$P_{2,i}$	Outlet pressure of subchannel two
P_{BC}	Inlet boundary condition pressure
P_{cr}	Critical dynamic pressure
P_{i}	Fluid pressure at inlet control surface, fluid pressure in common flow channel of inlet flow geometry region
P_{o}	Fluid pressure at outlet control surface, fluid pressure in common flow channel of outlet flow geometry region
P_{r}	Membrane pressure imposed on plate in radial direction

P_w	Wetted perimeter or flow channel
P_x	Membrane pressure imposed on plate in axial direction
Q_ϕ	ϕ directional shear stress resultant component
Q_x	x directional shear stress resultant component
$R,\ R_{cl}$	Mean radius of plate curvature
$R_{1,i}$	Inner radius of subchannel one
$R_{1,o}$	Outer radius of subchannel one
$R_{2,i}$	Inner radius of subchannel two
$R_{2,o}$	Outer radius of subchannel two
R_i	Inner radius of flow channel
R_h	Hydraulic radius, $\left(A/P_w\right)$
R_{h_1}	Hydraulic radius of subchannel one
R_{h_2}	Hydraulic radius of subchannel two
R_m	Mean radius corresponding to radial location where maximum velocity in annulus occurs
R_o	Outer radius of flow channel
Re	Reynolds number
S_0	Cross sectional area of flow channel prior to deformation
S_1	Cross sectional flow area of channel one
S_2	Cross sectional flow area of channel two
S_i	Generic cross sectional flow area at control volume inlet
S_o	Generic cross sectional flow area at control volume outlet
U	Superficial fluid velocity

U_1	Superficial fluid velocity in channel one
U_2	Superficial fluid velocity in channel two
U_i	Superficial fluid velocity at inlet control surface
U_o	Superficial fluid velocity at outlet control surface
V_{cr}	Critical velocity
VR_1	Critical velocity ratio, a cylindrical plate with C-F-C-F edge boundaries to a cylindrical plate with C-F-SS-F edge boundaries
VR_2	Critical velocity ratio, a cylindrical plate with C-F-C-F edge boundaries to a cylindrical plate with SS-F-SS-F edge boundaries
VR_3	Critical velocity ratio, a cylindrical plate with C-F-C-F edge boundaries to a flat plate with C-F-C-F edge boundaries
VR_4	Critical velocity ratio, a cylindrical plate with C-F-SS-F edge boundaries to a flat plate with C-F-SS-F edge boundaries
VR_5	Critical velocity ratio, Miller's critical velocity for a flat plate with C-F-C-F edge boundaries to Smith's critical velocity for a flat plate with C-F-C-F edge boundaries
W	Lateral plate displacement
2α	Curved-plate arc between two supports
β	Parameter defined by (2-13)
χ	Coefficient(s) of first order differential equations of motion
δ_{CR}	Critical plate deflection
$\delta\theta$	Discrete interval of ϕ between 0 and θ
ε	Normal component of strain in plate
ε_ϕ	Plate normal strain in ϕ direction
ε_x	Plate normal strain in x direction

γ	Shear Component of strain in plate
$\gamma_{x\phi}$	Plate shear strain in x,ϕ direction
ℓ_1	Axial distance from subchannel inlet to start of plate deflection
ℓ_2	Axial length of deflected plate region
ℓ_i	Axial length of common flow channel at inlet of flow geometry
ℓ_o	Axial length of common flow channel at outlet of flow geometry
λ	Frequency parameter
λ_m	Modal dependant eigenfunction coefficient, (5-55)
μ	Fluid dynamic viscosity
υ	Poisson's ratio
ω	Circular frequency of vibration
$\mathcal{O}$	Order of magnitude
ϕ	Mode dependent constant
ψ	Coefficient(s) of first order differential equations of motion
ρ	Fluid density
ρ_1	Fluid density in channel two
ρ_2	Fluid density in channel one
ρ_i	Fluid density at inlet of control surface
ρ_o	Fluid density at outlet of control surface
σ_m	Defined in (5-56)
σ_ϕ	Plate normal stress in ϕ direction
σ_x	Plate normal stress in x direction
$\tau_{\phi x}$	Plate shear stress in ϕ, x direction

τ_t Turbulent shear stress

$\tau_{x\phi}$ Plate shear stress in x, ϕ direction

τ_w Wall shear stress

θ Mode dependent constant, curved-plate arc angle between two supports

ϖ Friction factor

ϖ_1 Friction factor representative of flow in subchannel one

ϖ_2 Friction factor representative of flow in subchannel two

ϑ Specific energy of fluid, $\left(\varsigma + \overline{u}^2/2 + gz\right)$

ξ Coefficient(s) of first order differential equations of motion

Φ Corrective parameter for axial bending stiffness

Δ Frequency parameter, $\left(R^2\omega^2\rho a/Dg\right)$

ΔP Pressure difference along a discrete length

ΔP_i Average inlet pressure drop due to form losses

$\Delta P_{K_{1,i}}$ Pressure difference caused by sudden contraction from inlet flow channel to subchannel one

$\Delta P_{K_{1,o}}$ Pressure difference caused by sudden expansion from subchannel one to outlet flow channel

$\Delta P_{K_{2,i}}$ Pressure difference caused by sudden contraction from inlet flow channel to subchannel two

$\Delta P_{K_{2,o}}$ Pressure difference caused by sudden expansion from subchannel two to outlet flow channel

ΔP_L Average pressure drop due to friction and body forces in channels one and two along length L

ΔP_{L_1} Pressure drop due to friction and body forces in subchannel one along length L

$\Delta\overline{P}_{L_1}$	Average pressure drop due to friction and body forces in subchannel one in the interval $x \in [0, L]$
ΔP_{L_2}	Pressure drop due to friction and body forces in subchannel two along length L
$\Delta\overline{P}_{L_2}$	Average pressure drop due to friction and body forces in subchannel two in the interval $x \in [0, L]$
ΔP_o	Average outlet pressure drop due to form losses
ΔS	Change in flow channel area due to plate deformation
Δt	Discrete differential time interval
Γ_x	Body forces acting on fluid in the axial direction
Λ	Kinetic potential
$\boldsymbol{\mathcal{L}}$	Linear operator representing the load-deflection relation of a plate
Υ	Defined in (4-12)

Acronyms

ANS	Advanced Neutron Source
ATR	Advanced Test Reactor
C	Clamped Edge
DoE	Department of Energy
ETR	Engineering Test Reactor
F	Free Edge
FEA	Finite element analysis
FIV	Flow induced Vibration

GTRI	Global Threat Reduction Initiative
HEU	Highly Enriched Uranium
HFIR	High Flux Isotope Reactor
HFR	High Flux Reactor
HPRR	High Performance Research Reactor
INL	Idaho National Laboratory
LEU	Low Enriched Uranium
LWR	Light Water Reactor
MIT	Massachusetts Institute of Technology
MITR	Massachusetts Institute of Technology Reactor
MTEKM	Multi-term extended Kantorovich Method
MTR	Materials Test Reactor
MMM	Modified Matrix Method
MMP	Modified Matrix Progression
MURR	Missouri University Research Reactor
NASA	National Aeronautics and Space Administration
NBSR	National Bureau of Standards Reactor
NF	Natural Frequency
NIST	National Institute of Standards and Technology
NNSA	National Nuclear Security Administration
NS	Navier Stokes
PCP	Primary Coolant Pump
PCS	Primary Coolant System

QAP	Quality Assurance Plan
RERTR	Reduced Enrichment for Research and Test Reactors
RTR	Research and Test Reactor
SS	Simply Supported Edge
UFSAR	Upgraded Final Safety Analysis Report
U-Mo	Uranium-Molybdenum

10 APPENDIX A (Classical Plate Equation)

The classical plate equation arises from a combination of four distinct subsets of plate theory: the kinematic, constitutive, force resultant, and equilibrium equations. The explanation presented is expanded upon based on that presented in Ugural and Fenster [72].

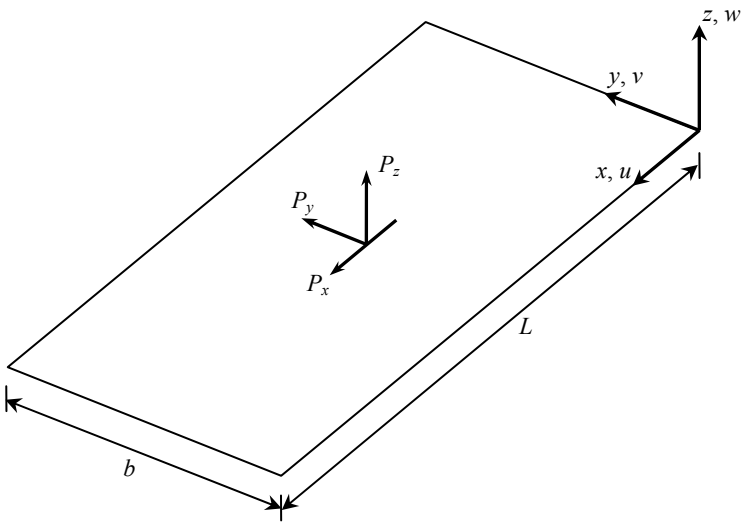

Figure A-1: Geometry of a flat rectangular plate

The coordinate system for flat plate type geometry discussed in this chapter is presented in Figure A-1. Several similarities can be observed between the coordinate system in Figure A-1 and that of a cylindrical plate (Figure 5-1); the primary difference between the two systems is found in the arc length of the plate in the span wise direction where b may be evaluated as $b = R\sin(\theta)$ for a cylindrical plate and is simply the length in the y direction for a flat plate.

Figure A-2 displays the shell element of differential length ∂y along the span wise direction and ∂x along the axial direction based on the coordinate system of choice presented in Figure A-1. Figure A-2(a) contains all external and internal forces acting on the element and Figure A-2(b) contains the moments.

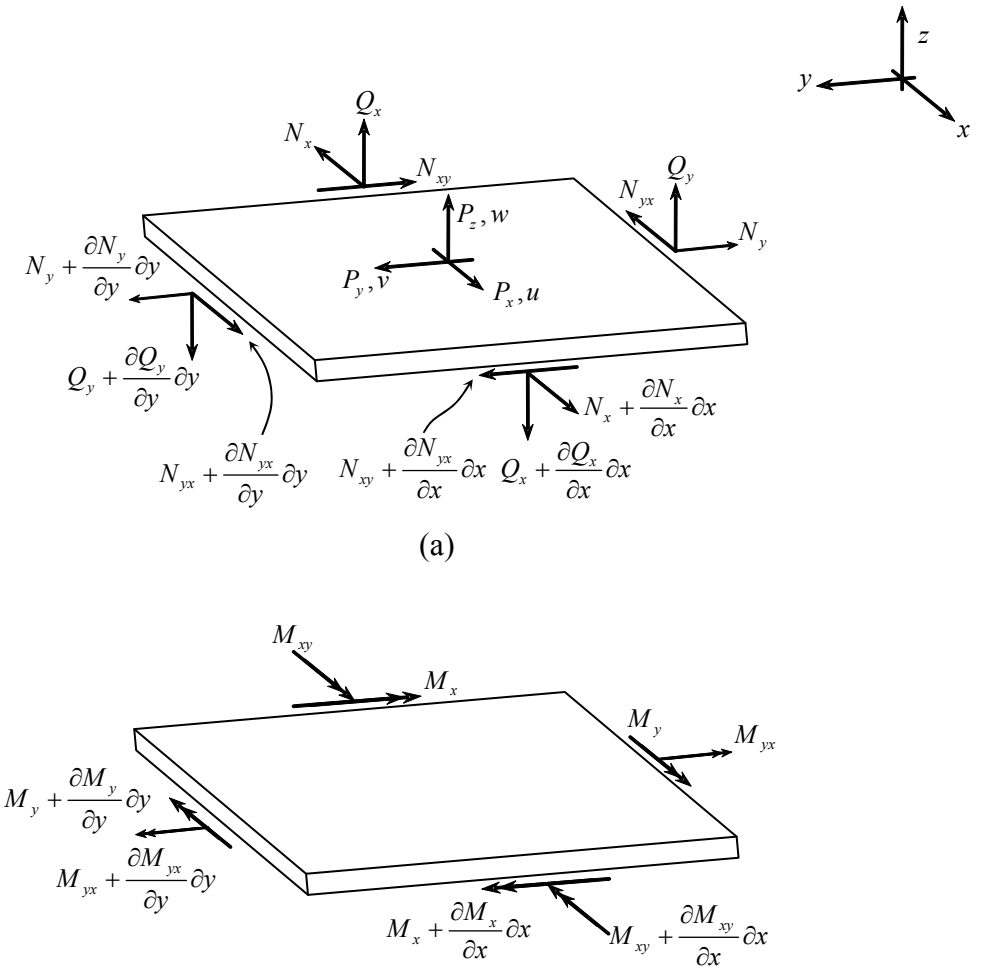

Figure A-2: An element of flat shell geometry (a) forces and (b) moments

10.1 The Kinematic Equation

Kinematics describes how the plate's displacement and strains relate:

$$\varepsilon_x = \frac{\partial u}{\partial x}, \tag{A-1}$$

$$\varepsilon_y = \frac{\partial v}{\partial y}, \tag{A-2}$$

$$\varepsilon_z = \frac{\partial w}{\partial z}, \tag{A-3}$$

$$\gamma_{xy} = \frac{\partial v}{\partial x} + \frac{\partial u}{\partial y}, \tag{A-4}$$

$$\gamma_{zx} = \frac{\partial u}{\partial z} + \frac{\partial w}{\partial x}, \tag{A-5}$$

and

$$\gamma_{yz} = \frac{\partial w}{\partial y} + \frac{\partial v}{\partial z}, \tag{A-6}$$

where u, v, and w are the displacement in x, y, and z direction, respectively. This system of equations does not tend to be useful in applications. In order to acquire the correct form of the kinematic equations for this study, Kirchhoff's assumptions must be made: (a) normal resultants remain straight, (b) normal resultants remain un-stretched, (c) normal resultants remain normal. Based on these assumptions, the displacement field can be expressed in terms of the distances by which the plate's middle plane movies from its resting (unloaded position), u_o, v_o, w_o. With the normal resultants straight and unstretched, the shear strain in the z direction and be assumed negligible and therefore:

$$\gamma_{yz} = \frac{\partial w}{\partial y} + \frac{\partial v}{\partial z} \approx 0 \quad \Rightarrow \quad \frac{\partial v}{\partial z} \approx -\frac{\partial w}{\partial y} \tag{A-7}$$

and

$$\gamma_{xz} = \frac{\partial w}{\partial x} + \frac{\partial u}{\partial z} \approx 0 \quad \Rightarrow \quad \frac{\partial u}{\partial z} \approx -\frac{\partial w}{\partial x}. \tag{A-8}$$

Employing the assumption that the normal resultants remain normal to the mid-plane, the x, y dependence can be made explicit via a simple geometric expression,

$$u = u_o + z\frac{\partial u_o}{\partial z} + \mathcal{O}(2) \quad \Rightarrow \; u_o - z\frac{\partial w_o}{\partial x} \tag{A-9}$$

and

$$v = v_o + z\frac{\partial v_o}{\partial z} + \mathcal{O}(2) \quad \Rightarrow \; v_o - z\frac{\partial w_o}{\partial y}. \tag{A-10}$$

The kinematic equations therefore become

$$\varepsilon_x = \frac{\partial u_o}{\partial x} - z\frac{\partial^2 w_o}{\partial x^2}, \tag{A-11}$$

$$\varepsilon_y = \frac{\partial v_o}{\partial y} - z\frac{\partial^2 w_o}{\partial y^2}, \tag{A-12}$$

and

$$\gamma_{xy} = \frac{\partial v_o}{\partial x} + \frac{\partial y_o}{\partial y}. \tag{A-13}$$

The above system of equations can be further simplified by noting that if there are no in-plane resultants, all strains at the middle plane are zero, yielding

$$\varepsilon_x = -z\frac{\partial^2 w_o}{\partial x^2}, \tag{A-14}$$

$$\varepsilon_y = -z\frac{\partial^2 w_o}{\partial y^2}, \tag{A-15}$$

and

$$\gamma_{xy} = -2z\frac{\partial^2 w_o}{\partial x \partial y}. \tag{A-16}$$

10.2 The Constitutive Equation

The constitutive equation describes how the stresses and strains are related within a plate (i.e. Hooke's Law). In linear elasticity, the most generalized Hooke's Law contains six components of stress that are linearly related to six components of strain as follows

$$\begin{bmatrix} \varepsilon_{xx} \\ \varepsilon_{yy} \\ \varepsilon_{zz} \\ \varepsilon_{yz} \\ \varepsilon_{zx} \\ \varepsilon_{xy} \end{bmatrix} = \frac{1}{E}\begin{bmatrix} 1 & -\upsilon & -\upsilon & 0 & 0 & 0 \\ -\upsilon & 1 & -\upsilon & 0 & 0 & 0 \\ -\upsilon & -\upsilon & 1 & 0 & 0 & 0 \\ 0 & 0 & 0 & 1+\upsilon & 0 & 0 \\ 0 & 0 & 0 & 0 & 1+\upsilon & 0 \\ 0 & 0 & 0 & 0 & 0 & 1+\upsilon \end{bmatrix}\begin{bmatrix} \sigma_{xx} \\ \sigma_{yy} \\ \sigma_{zz} \\ \sigma_{yz} \\ \sigma_{zx} \\ \sigma_{xy} \end{bmatrix}. \tag{A-17}$$

This can be rearranged into the stiffness (strain to stress) form

$$\begin{bmatrix} \varepsilon_{xx} \\ \varepsilon_{yy} \\ \varepsilon_{zz} \\ \varepsilon_{yz} \\ \varepsilon_{zx} \\ \varepsilon_{xy} \end{bmatrix} = \frac{E}{(1+\upsilon)(1-2\upsilon)}\begin{bmatrix} 1-\upsilon & \upsilon & \upsilon & 0 & 0 & 0 \\ \upsilon & 1-\upsilon & \upsilon & 0 & 0 & 0 \\ \upsilon & \upsilon & 1-\upsilon & 0 & 0 & 0 \\ 0 & 0 & 0 & 1-2\upsilon & 0 & 0 \\ 0 & 0 & 0 & 0 & 1-2\upsilon & 0 \\ 0 & 0 & 0 & 0 & 0 & 1-2\upsilon \end{bmatrix}\begin{bmatrix} \sigma_{xx} \\ \sigma_{yy} \\ \sigma_{zz} \\ \sigma_{yz} \\ \sigma_{zx} \\ \sigma_{xy} \end{bmatrix}. \tag{A-18}$$

Employing the same assumptions (Kirchhoff's assumptions) used in the previous section to apply to plates, the stress-strain relations can be simplified to

$$\begin{bmatrix} \sigma_x \\ \sigma_y \\ \sigma_{xy} \end{bmatrix} = \frac{E}{1-\upsilon^2}\begin{bmatrix} 1 & \upsilon & 0 \\ \upsilon & 1 & 0 \\ 0 & 0 & \dfrac{1-\upsilon}{2} \end{bmatrix}\begin{bmatrix} \varepsilon_x \\ \varepsilon_y \\ \gamma_{xy} \end{bmatrix}, \tag{A-19}$$

where $\sigma_z \approx 0,\ \sigma_{xy} \approx 0,$ and $\sigma_{yz} \approx 0$ which yields the following constitutive equations in for plates;

$$\varepsilon_z = -\frac{\upsilon}{E}\left(\sigma_x + \sigma_y\right), \tag{A-20}$$

$$\gamma_{xz} = 0\,, \tag{A-21}$$

and

$$\gamma_{yz} = 0\,. \tag{A-22}$$

10.3 The Force Resultants Equation

Force and momentum resultants are quantities used to track the important stresses in plates. They are analogous to the moments and forces in statics theories, in that their influence is felt throughout the plate. Recall that the stress tensor has nine components at any given point. Each portion of the direct stress acting on the cross section creates a moment about the neutral plane ($z = 0$). Summing these individual moments over the area of the cross section is the definition of the moment resultants M_x, M_y, M_{xy}, and M_{yx}, where

$$M_x = \int_{-a/2}^{a/2} z\sigma_{xx}dz\,, \tag{A-23}$$

$$M_y = \int_{-a/2}^{a/2} z\sigma_{yy}dz\,, \tag{A-24}$$

$$M_{xy} = \int_{-a/2}^{a/2} z\sigma_{xy}dz\,, \tag{A-25}$$

and

$$M_{yx} = \int_{-a/2}^{a/2} z\sigma_{yx}dz\,, \tag{A-26}$$

where z is the coordinate pointing in the direction normal to the plate's primary surface(s). Summing the shear forces on the cross-section is the definition of the transverse shear resultants Q_x and Q_y,

$$Q_{xz} = \int_{-a/2}^{a/2} z\sigma_{xz}dz \tag{A-27}$$

and

$$Q_{yz} = \int_{-a/2}^{a/2} \sigma_{yz} dz \,. \tag{A-28}$$

The last set of resultants is the sum of all direct forces acting on the cross-section, these are known as N_x, N_y, and N_{xy}, where

$$N_x = \int_{-a/2}^{a/2} \sigma_{xx} dz \,, \tag{A-29}$$

$$N_y = \int_{-a/2}^{a/2} \sigma_{yy} dz \,, \tag{A-30}$$

$$N_{xy} = \int_{-a/2}^{a/2} \sigma_{xx} dz \,, \tag{A-31}$$

and

$$N_{yx} = \int_{-a/2}^{a/2} \sigma_{yx} dz \,. \tag{A-32}$$

10.4 The Equilibrium Equation

The equilibrium equations describe how the plate carries external pressure loads with its internal stresses. There are six equilibrium equations, three for the forces and three for the moments that need to be satisfied. The equations of force equilibrium are

$$\frac{\partial N_x}{\partial x} + \frac{\partial N_{yx}}{\partial y} + P_x = 0 \,, \tag{A-33}$$

$$\frac{\partial N_{xy}}{\partial x} + \frac{\partial N_y}{\partial y} + P_y = 0 \,, \tag{A-34}$$

and

$$\frac{\partial Q_{xz}}{\partial x} + \frac{\partial Q_{yz}}{\partial y} + P_z = 0 \,, \tag{A-35}$$

where N_x, N_y, N_{xy}, Q_{xz}, and Q_{yz} are the corresponding force resultants described in the previous section; P_x, P_y, and P_z are distributed external forces applied on the plate. The equations of moment equilibrium are

$$-\frac{\partial M_{xy}}{\partial x} - \frac{\partial M_y}{\partial y} + Q_{yz} = 0 \,, \tag{A-36}$$

$$\frac{\partial M_x}{\partial x} + \frac{\partial M_{yx}}{\partial y} - Q_{yz} = 0 \,, \tag{A-37}$$

and

$$N_{xy} - N_{yx} = 0\,, \tag{A-38}$$

where M_x, M_y, M_{xy}, M_{yx}, N_{xy}, and N_{yx} are moment resultants. The above equations assume that all second and higher order terms are negligible. To further simplify the problem, consider a plate subjected to transverse loads (P_z is the non-zero external force). All forces and moments in other directions are zero. The above six equations then become

$$\frac{\partial N_x}{\partial x} + \frac{\partial N_{yx}}{\partial y} = 0\,, \tag{A-39}$$

$$\frac{\partial M_{xy}}{\partial x} + \frac{\partial M_y}{\partial y} = Q_{yz}\,, \tag{A-40}$$

$$\frac{\partial N_{xy}}{\partial x} + \frac{\partial N_y}{\partial y} = 0\,, \tag{A-41}$$

$$\frac{\partial M_x}{\partial x} + \frac{\partial M_{yx}}{\partial y} = Q_{yz}\,, \tag{A-42}$$

$$\frac{\partial Q_{xz}}{\partial x} + \frac{\partial Q_{yz}}{\partial y} = -P_z\,, \tag{A-43}$$

and

$$N_{xy} = N_{yx}\,. \tag{A-44}$$

Due to the lack of external force components other than P_z the shear stresses at any given point are paired with their symmetric partners to yield

$$N_{xy} = N_{yx} \tag{A-44}$$

and

$$M_{xy} = M_{yx}\,. \tag{A-45}$$

10.5 Acquiring the Classical Plate Equation

The four equations presented above are combined using the following method to acquire the plate equation. By first combining the three equilibrium equations, Q_{xy}, and Q_{yz} can be eliminated to give

$$\frac{\partial^2 M_x}{\partial x^2} + 2\frac{\partial^2 M_{xy}}{\partial x \partial y} + \frac{\partial^2 M_y}{\partial y^2} = -P_z\,. \tag{A-46}$$

Secondly, the moment resultants in (A-23) can be replaced with the true definition of terms of the direct stresses to give

$$\int_{-a/2}^{a/2} z\left(\frac{\partial^2\sigma_x}{\partial x^2}+2\frac{\partial^2\sigma_{xy}}{\partial x\partial y}+\frac{\partial^2\sigma_y}{\partial y^2}\right)dz=-P_z\,. \tag{A-47}$$

Using the constitutive relation in (A-19) and then using the kinematics equation to replace strain in favor of the normal displacement w_o yields

$$\begin{bmatrix}\sigma_x\\ \sigma_y\\ \sigma_{xy}\end{bmatrix}=\frac{E}{1-\upsilon^2}\begin{bmatrix}1 & \upsilon & 0\\ \upsilon & 1 & 0\\ 0 & 0 & 1-\upsilon\end{bmatrix}\begin{bmatrix}\dfrac{\partial^2 w_o}{\partial x^2}\\ \dfrac{\partial^2 w_o}{\partial y^2}\\ \dfrac{\partial^2 w_o}{\partial x\partial y}\end{bmatrix}. \tag{A-48}$$

The equilibrium equation can then be expressed in terms of the normal displacement w_o

$$\int_{-a/2}^{a/2}\frac{Ez^2}{1-\upsilon^2}\left(\left(\frac{\partial^4 w_o}{\partial x^4}+\upsilon\frac{\partial^4 w_o}{\partial x^2\partial y^2}\right)+2(1-\upsilon)\frac{\partial^4 w_o}{\partial x^2\partial y^2}+\left(\frac{\partial^4 w_o}{\partial y^4}+\upsilon\frac{\partial^4 w_o}{\partial x^2\partial y^2}\right)\right)dz=P_z\,, \tag{A-49}$$

which can be simplified to

$$\int_{-a/2}^{a/2}\frac{Ez^2}{1-\upsilon^2}dz\left(\frac{\partial^4 w_o}{\partial x^4}+2\frac{\partial^4 w_o}{\partial x^2\partial y^2}+\frac{\partial^4 w_o}{\partial y^4}\right)=P_z\,. \tag{A-50}$$

As a final step, assuming homogeneous material along the thickness of the plate, the flexural rigidity of the plate can be written as

$$K=\int_{-a/2}^{a/2}\frac{E}{1-\upsilon^2}z^2dz=\frac{Ea^3}{12\left(1-\upsilon^2\right)}\,. \tag{A-51}$$

Then the classical plate equation can be written in the form

$$K\left(\frac{\partial^4}{\partial x^4}+2\frac{\partial^4}{\partial x^2\partial y^2}+\frac{\partial^4}{\partial y^4}\right)w_o=\mathcal{L}[W]=P_z\,. \tag{A-52}$$

11 APPENDIX B (Reduced Plate Equations)

11.1 Integrating Equations of Motion (Reduction to One Dimension)

11.1.1 Axial Coordinate

The integration of (5-48) expanded in the form of (5-30) is presented here:

$$\int_{x=0}^{\bar{x}} \left[L_1\left(f_1 g_1, f_2 g_2, f_3 g_3\right) + \Delta f_1 g_1 \right] f_1 dx = 0 \tag{5-48}$$

Note that from (5-42), $L_1(u,v,w) = \left(R^2 \rho a / Dg\right) \partial^2 u / \partial t^2$, then if the acceleration term (right side of the equation) is inserted into (5-30) the equation of motion in the *u* direction becomes

$$\begin{aligned} L_1(u,v,w) = {} & (1+q_x)\frac{\partial^2 u}{\partial x^2} + \left(\frac{(1-\upsilon)(1+k)}{2} + q_\phi\right)\frac{\partial^2 u}{\partial \phi^2} \\ & + (\upsilon - q_\phi)\frac{\partial w}{\partial x} - (k)\frac{\partial^3 w}{\partial x^3} + \left(\frac{1+\upsilon}{2}\right)\frac{\partial v}{\partial x}\frac{\partial v}{\partial \phi} + \frac{k(1-\upsilon)}{2}\frac{\partial w}{\partial x}\frac{\partial^2 w}{\partial \phi^2} \end{aligned} . \tag{B-1}$$

Inserting (5-30) into the integral (5-48) gives

$$\int_{x=0}^{\bar{x}} \left[\begin{aligned} & (1+q_x)\frac{\partial^2 f_1}{\partial x^2} + \left(\frac{(1-\upsilon)(1+k)}{2} + q_\phi\right)\frac{\partial^2 f_1}{\partial \phi^2} + (\upsilon - q_\phi)\frac{\partial f_3}{\partial x} \\ & -k\frac{\partial^3 f_3}{\partial x^3} + \left(\frac{1+\upsilon}{2}\right)\frac{\partial f_2}{\partial x}\frac{\partial g_2}{\partial \phi} + \frac{k(1-\upsilon)}{2}\frac{\partial f_3}{\partial x}\frac{\partial^2 g_3}{\partial \phi^2} + \Delta f_1 g_1 \end{aligned} \right] f_1 dx = 0 . \tag{B-2}$$

If f_1 is factored through all the terms inside the integral then (B-2) further expands to

$$\begin{aligned} & \underbrace{(1+q_x)\int_{x=0}^{\bar{x}} \frac{\partial^2 f_1}{\partial x^2} f_1 dx}_{\xi_{11}} g_1 + \underbrace{\left(\frac{(1-\upsilon)(1+k)}{2} + q_\phi\right)\int_{x=0}^{\bar{x}} f_1 f_1 dx}_{\xi_{12}} \frac{\partial^2 g_1}{\partial \phi^2} \\ & + \underbrace{\left(\frac{1+\upsilon}{2}\right)\int_{x=0}^{\bar{x}} \frac{\partial f_2}{\partial x} f_1 dx}_{\xi_{13}} \frac{\partial g_2}{\partial \phi} + \underbrace{(\upsilon - q_\phi)\int_{x=0}^{\bar{x}} \frac{\partial f_3}{\partial x} f_1 dx}_{\xi_{14}} g_3 \\ & \underbrace{-k\int_{x=0}^{\bar{x}} \frac{\partial^3 f_3}{\partial x^3} f_1 dx}_{\xi_{15}} g_3 + \underbrace{\frac{k(1-\upsilon)}{2}\int_{x=0}^{\bar{x}} \frac{\partial f_3}{\partial x} f_1 dx}_{\xi_{16}} \frac{\partial^2 g_3}{\partial \phi^2} + \underbrace{\Delta \int_{x=0}^{\bar{x}} f_1 f_1 dx}_{\xi_{17}} g_1 = 0 \end{aligned} . \tag{B-3}$$

Reducing (B-3) based on the defined values presented below each term yields

$$\xi_{11} g_1 + \xi_{12}\frac{\partial^2 g_1}{\partial \phi^2} + \xi_{13}\frac{\partial g_2}{\partial \phi} + \xi_{14} g_3 - \xi_{15} g_3 + \xi_{16}\frac{\partial^2 g_3}{\partial \phi^2} + \xi_{17} g_1 = 0 . \tag{B-4}$$

Combining all common terms dependant on ϕ

$$\left(\xi_{11}+\xi_{17}\right)g_1+\xi_{12}\frac{\partial^2 g_1}{\partial\phi^2}+\xi_{13}\frac{\partial g_2}{\partial\phi}+\left(\xi_{14}-\xi_{15}\right)g_3+\xi_{16}\frac{\partial^2 g_3}{\partial\phi^2}=0\,, \tag{B-5}$$

or

$$\psi_{11}g_1+\xi_{12}\frac{\partial^2 g_1}{\partial\phi^2}+\xi_{13}\frac{\partial g_2}{\partial\phi}+\psi_{12}g_3+\xi_{16}\frac{\partial^2 g_3}{\partial\phi^2}=0\,. \tag{5-69}$$

11.1.2 Azimuthal Coordinate

The integration of (5-49) expanded in the form of (5-31) is presented here:

$$\int_{x=0}^{\bar{x}}\left[L_2\left(f_1g_1,f_2g_2,f_3g_3\right)+\Delta f_2g_2\right]f_2dx=0 \tag{5-49}$$

Note that from (5-43), $L_2\left(u,v,w\right)=\left(R^2\rho a/Dg\right)\partial^2 v/\partial t^2$, then if the acceleration term (right side of the equation) is inserted into (5-31) the equation of motion in the v direction becomes

$$\begin{aligned}L_2=&\left(\frac{1+\upsilon}{2}\right)\frac{\partial f_1}{\partial x}\frac{\partial g_1}{\partial\phi}+\left(1+q_\phi\right)\frac{\partial^2 g_2}{\partial\phi^2}\\&+\left(\frac{\left(1-\upsilon\right)\left(1+3k\right)}{2}+q_x\right)\frac{\partial^2 f_2}{\partial x^2}+\left(1+q_\phi\right)\frac{\partial g_3}{\partial\phi}-\left(\frac{k\left(3-\upsilon\right)}{2}\right)\frac{\partial^2 f_3}{\partial x^2}\frac{\partial g_3}{\partial\phi}\end{aligned}\,. \tag{B-6}$$

Inserting (5-31) into the integral (5-49) gives

$$\int_{x=0}^{\bar{x}}\left[\begin{aligned}&\left(\frac{1+\upsilon}{2}\right)\frac{\partial f_1}{\partial x}\frac{\partial g_1}{\partial\phi}+\left(1+q_\phi\right)\frac{\partial^2 g_2}{\partial\phi^2}+\left(\frac{\left(1-\upsilon\right)\left(1+3k\right)}{2}+q_x\right)\frac{\partial^2 f_2}{\partial x^2}\\&+\left(1+q_\phi\right)\frac{\partial g_3}{\partial\phi}-\left(\frac{k\left(3-\upsilon\right)}{2}\right)\frac{\partial^2 f_3}{\partial x^2}\frac{\partial g_3}{\partial\phi}+\Delta f_2g_2\end{aligned}\right]f_2dx=0\,. \tag{B-7}$$

If f_2 is factored through all the terms inside the integral then (B-7) further expands to

$$\begin{aligned}&\underbrace{\left(\frac{1+\upsilon}{2}\right)\int_{x=0}^{\bar{x}}\frac{\partial f_1}{\partial x}f_2dx}_{\xi_{21}}\frac{\partial g_1}{\partial\phi}+\underbrace{\left(1+q_\phi\right)\int_{x=0}^{\bar{x}}f_2f_2dx}_{\xi_{22}}\frac{\partial^2 g_2}{\partial\phi^2}\\&+\underbrace{\left(\frac{\left(1-\upsilon\right)\left(1+3k\right)}{2}+q_x\right)\int_{x=0}^{\bar{x}}\frac{\partial^2 f_2}{\partial x^2}f_2dx}_{\xi_{23}}g_2+\underbrace{\left(1+q_\phi\right)\int_{x=0}^{\bar{x}}f_3f_2dx}_{\xi_{24}}\frac{\partial g_3}{\partial\phi}\\&-\underbrace{\left(\frac{k\left(3-\upsilon\right)}{2}\right)\int_{x=0}^{\bar{x}}\frac{\partial^2 f_3}{\partial x^2}f_2dx}_{\xi_{25}}\frac{\partial g_3}{\partial\phi}+\underbrace{\int_{x=0}^{\bar{x}}\Delta f_2f_2dx}_{\xi_{26}}g_2=0\end{aligned}\,. \tag{B-8}$$

Reducing (B-8) based on the defined values presented below each term yields

$$\xi_{21}\frac{\partial g_1}{\partial\phi}+\xi_{22}\frac{\partial^2 g_2}{\partial\phi^2}+\xi_{23}g_2+\xi_{24}\frac{\partial g_3}{\partial\phi}-\xi_{25}\frac{\partial g_3}{\partial\phi}+\xi_{26}g_2=0\,. \tag{B-9}$$

Combining all common terms dependant on ϕ

$$\xi_{21}\frac{\partial g_1}{\partial \phi}+\xi_{22}\frac{\partial^2 g_2}{\partial \phi^2}+\left(\xi_{23}+\xi_{26}\right)g_2+\left(\xi_{24}-\xi_{25}\right)\frac{\partial g_3}{\partial \phi}=0\,, \tag{B-10}$$

or

$$\xi_{21}\frac{\partial g_1}{\partial \phi}+\xi_{22}\frac{\partial^2 g_2}{\partial \phi^2}+\psi_{21}g_2+\psi_{22}\frac{\partial g_3}{\partial \phi}=0\,. \tag{5-70}$$

11.1.3 Radial Coordinate

The integration of (5-50) expanded in the form of (5-32) is presented here:

$$\int_{x=0}^{\bar{x}}\left[L_3\left(f_1g_1,f_2g_2,f_3g_3\right)-\Delta f_3g_3\right]f_3dx=0 \tag{5-50}$$

Note that from (5-44), $L_3(u,v,w)=-\left(R^2\rho a/Dg\right)\partial^2 w/\partial t^2$, then if the acceleration term (right side of the equation) is inserted into (5-32) the equation of motion in the *w* direction becomes

$$\begin{aligned}L_2=&\left(\frac{1+\upsilon}{2}\right)\frac{\partial f_1}{\partial x}\frac{\partial g_1}{\partial \phi}+\left(1+q_\phi\right)\frac{\partial^2 g_2}{\partial \phi^2}\\&+\left(\frac{(1-\upsilon)(1+3k)}{2}+q_x\right)\frac{\partial^2 f_2}{\partial x^2}+\left(1+q_\phi\right)\frac{\partial g_3}{\partial \phi}-\left(\frac{k(3-\upsilon)}{2}\right)\frac{\partial^2 f_3}{\partial x^2}\frac{\partial g_3}{\partial \phi}\end{aligned}\,. \tag{B-11}$$

Inserting (5-32) into the integral (5-50) gives

$$\int_{x=0}^{\bar{x}}\left[\begin{aligned}&\left(\upsilon-q_\phi\right)\frac{\partial f_1}{\partial x}+\left(\frac{k(1-\upsilon)}{w}\right)\frac{\partial f_1}{\partial x}\frac{\partial^2 g_2}{\partial \phi^2}-k\frac{\partial^3 f_1}{\partial x^3}+\left(1+q_\phi\right)\frac{\partial g_2}{\partial \phi}\\&-\left(\frac{k(3-\upsilon)}{2}\right)\frac{\partial^2 f_2}{\partial x^2}\frac{\partial g_2}{\partial \phi}+(1+k)g_3+k\frac{\partial^4 f_3}{\partial x^4}\\&+2k\frac{\partial^2 f_3}{\partial x^2}\frac{\partial^2 g_3}{\partial \phi^2}+k\frac{\partial^4 g_3}{\partial \phi^4}+\left(2k-q_\phi\right)\frac{\partial^2 g_3}{\partial \phi^2}-q_x\frac{\partial^2 f_3}{\partial x^2}-\Delta f_3g_3\end{aligned}\right]f_3dx=0\,. \tag{B-12}$$

If f_3 is factored through all the terms inside the integral then (B-12) further expands to

$$\underbrace{\left(\upsilon - q_\phi\right)\int_{x=0}^{\bar{x}} \frac{\partial f_1}{\partial x} f_3 dx}_{\xi_{31}} g_1 + \underbrace{\left(1+q_\phi\right)\int_{x=0}^{\bar{x}} f_2 f_3 dx}_{\xi_{32}} \frac{\partial g_2}{\partial \phi} + \underbrace{\left(1+k\right)\int_{x=0}^{\bar{x}} f_3 f_3 dx}_{\xi_{33}} g_3$$
$$+ \underbrace{\left(\frac{k\left(1-\upsilon\right)}{2}\right)\int_{x=0}^{\bar{x}} \frac{\partial f_1}{\partial x} f_3 dx}_{\xi_{34}} \frac{\partial^2 g_1}{\partial \phi^2} - \underbrace{k\int_{x=0}^{\bar{x}} \frac{\partial^3 f_1}{\partial x^3} f_3 dx}_{\xi_{35}} g_1 - \underbrace{\left(\frac{k\left(3-\upsilon\right)}{2}\right)\int_{x=0}^{\bar{x}} \frac{\partial^2 f_2}{\partial x^2} f_3 dx}_{\xi_{36}} \frac{\partial g_2}{\partial \phi}$$
$$+ \underbrace{k\int_{x=0}^{\bar{x}} \frac{\partial^4 f_3}{\partial x^4} f_3 dx}_{\xi_{37}} g_3 + \underbrace{2k\int_{x=0}^{\bar{x}} \frac{\partial^2 f_3}{\partial x^2} f_3 dx}_{\xi_{38}} \frac{\partial^2 g_3}{\partial \phi^2} + \underbrace{k\int_{x=0}^{\bar{x}} f_3 f_3 dx}_{\xi_{39}} \frac{\partial^4 g_3}{\partial \phi^4}$$
$$+ \underbrace{\left(2k - q_\phi\right)\int_{x=0}^{\bar{x}} f_3 f_3 dx}_{\xi_{40}} \frac{\partial^2 g_3}{\partial \phi^2} - \underbrace{\Delta\int_{x=0}^{\bar{x}} f_3 f_3 dx}_{\xi_{41}} g_3 - \underbrace{q_x\int_{x=0}^{\bar{x}} f_3'' f_3 dx}_{\xi_{42}} g_3 = 0 \quad . \tag{B-13}$$

Reducing (B-13) based on the defined values presented below each term yields

$$\xi_{31} g_1 + \xi_{32}\frac{\partial g_2}{\partial \phi} + \xi_{33} g_3 + \xi_{34}\frac{\partial^2 g_1}{\partial \phi^2} - \xi_{35} g_1 - \xi_{36}\frac{\partial g_2}{\partial \phi}$$
$$+ \xi_{37} g_3 + \xi_{38}\frac{\partial^2 g_3}{\partial \phi^2} + \xi_{39}\frac{\partial^4 g_3}{\partial \phi^4} + \xi_{40}\frac{\partial^2 g_3}{\partial \phi^2} - \xi_{41} g_3 - \xi_{42} g_3 = 0 \tag{B-14}$$

combining all common terms dependant on ϕ

$$\left(\xi_{31} - \xi_{35}\right) g_1 + \xi_{34}\frac{\partial^2 g_1}{\partial \phi^2} + \left(\xi_{32} - \xi_{36}\right)\frac{\partial g_2}{\partial \phi}$$
$$+ \left(\xi_{33} + \xi_{37} - \xi_{41} - \xi_{42}\right) g_3 + \left(\xi_{38} + \xi_{40}\right)\frac{\partial^2 g_3}{\partial \phi^2} + \xi_{39}\frac{\partial^4 g_3}{\partial \phi^4} = 0 \tag{B-15}$$

or

$$\psi_{31} g_1 + \xi_{34}\frac{\partial^2 g_1}{\partial \phi^2} + \psi_{33}\frac{\partial g_2}{\partial \phi} + \psi_{32} g_3 + \psi_{34}\frac{\partial^2 g_3}{\partial \phi^2} + \xi_{39}\frac{\partial^4 g_3}{\partial \phi^4} = 0 \tag{5-71}$$

11.2 Reduced Equations and Coefficients

The reduced equations (5-69) through (5-71) and their coefficients are given below.

$$\psi_{11} g_1 + \xi_{12}\frac{\partial^2 g_1}{\partial \phi^2} + \xi_{13}\frac{\partial g_2}{\partial \phi} + \psi_{12} g_3 + \xi_{16}\frac{\partial^2 g_3}{\partial \phi^2} = 0 \tag{5-69}$$

$$\xi_{21}\frac{\partial g_1}{\partial \phi} + \xi_{22}\frac{\partial^2 g_2}{\partial \phi^2} + \psi_{21} g_2 + \psi_{22}\frac{\partial g_3}{\partial \phi} = 0 \tag{5-70}$$

$$\psi_{31} g_1 + \xi_{34}\frac{\partial^2 g_1}{\partial \phi^2} + \psi_{33}\frac{\partial g_2}{\partial \phi} + \psi_{32} g_3 + \psi_{34}\frac{\partial^2 g_3}{\partial \phi^2} + \xi_{39}\frac{\partial^4 g_3}{\partial \phi^4} = 0 \tag{5-71}$$

In an attempt to be explicit in the methodology used and parameters employed in the model, the compressed form of coefficients ξ_{11}, through ψ_{34} are presented below such that

any prescribed function f_1, f_2, and f_3, may be inserted for future application, each coefficient is also presented with the eigenfunction (or its applicable derivative) employed in the x direction throughout this study and lastly the integrations for each coefficient have been performed and are displayed as well. Note that after performing the integrations a number of the coefficients contain no dependencies in on the eigenvalue of eigenfunction in the axial direction, that is no $\bar{x}$ terms appear in their value. This can be directly related back to the stress resultants shown in Figure 5-2 where both normal and bending stress resultants N and M, where there is no x dependence in their form.

Recall from (B-3) that ξ_{11} is defined as that presented below in (B-16). In chapter 4 a discussion of the eigenfunctions (f_i) and their respective derivatives $\left(\partial^j f_i/\partial x^j\right)$ are presented for the case of a straight beam with both ends free.

$$\xi_{11} = (1+q_x)\int_{x=0}^{\bar{x}} \frac{\partial^2 f_1}{\partial x^2} f_1 dx \tag{B-16}$$

Considering (B-16), inserting (5-62) and (5-59), then integrating $x \in [0,\bar{x}]$ yields (B-17). ξ_{11} is then combined with ξ_{17} in (B-28) to form ψ_{11}.

$$\xi_{11} = \frac{-\lambda_m(1+q_x)}{4\bar{x}}\left[\begin{array}{l} 4\lambda_m - 2\sigma_m\cos(2\lambda_m) + 2\sigma_m\cosh(2\lambda_m) \\ +\left(\sigma_m^2-1\right)\sin(2\lambda_m) - \left(1+\sigma_m^2\right)\sinh(2\lambda_m) \end{array}\right] \tag{B-17}$$

From (B-3), ξ_{12} is defined as

$$\xi_{12} = \left[\frac{(1-\upsilon)(1+k)}{2} + q_\phi\right]\int_{x=0}^{\bar{x}} f_1 f_1 dx\,. \tag{B-18}$$

Inserting (5-59) into (B-18) and integrating $x \in [0,\bar{x}]$ gives

$$\xi_{12} = \frac{\bar{x}\left(1+k+2q_\phi-\upsilon-k\upsilon\right)}{8\lambda_m}\left[\begin{array}{l} 12\sigma_m + 4\lambda_m\sigma_m^2 - 2\sigma_m\cos(2\lambda_m) - 2\sigma_m\cosh(2\lambda_m) \\ +4\cosh(\lambda_m)\left(-2\sigma_m\cos(\lambda_m) + \left(\sigma_m^2-1\right)\sin(\lambda_m)\right) \\ +\left(\sigma_m^2-1\right)\sin(2\lambda_m) \\ +2\left(1+\sigma_m^2\right)\left(2\cos(\lambda_m)+\cosh(\lambda_m)\right)\sinh(\lambda_m) \end{array}\right], \tag{B-19}$$

which is then input into (5-69) to form the second term in (5-69). From (B-3), ξ_{13} is defined as

$$\xi_{13} = \frac{(1+\upsilon)}{2}\int_{x=0}^{\bar{x}} \frac{\partial f_2}{\partial x} f_1 dx\,. \tag{B-20}$$

Inserting (5-65) and (5-59) into (B-20) and integrating $x \in [0, \bar{x}]$ gives

$$\xi_{13} = \frac{(1+\upsilon)}{8}\begin{bmatrix} 12\sigma_m + 4\lambda_m\sigma_m^2 - 2\sigma_m\cos(2\lambda_m) - 2\sigma_m\cosh(2\lambda_m) \\ +4\cosh(\lambda_m)\left(-2\sigma_m\cos(\lambda_m) + (\sigma_m^2 - 1)\sin(\lambda_m)\right) \\ +(\sigma_m^2 - 1)\sin(2\lambda_m) + 2(1+\sigma_m^2)(2\cos(\lambda_m) + \cosh(\lambda_m))\sinh(\lambda_m) \end{bmatrix}, \quad \text{(B-21)}$$

which is then input into (5-69) to form the third term in (5-69). From (B-3), ξ_{14} is defined as

$$\xi_{14} = (\upsilon - q_\phi)\int_{x=0}^{\bar{x}} \frac{\partial f_3}{\partial x} f_1 dx \,. \quad \text{(B-22)}$$

Inserting (5-65) and (5-59) into (B-22) and integrating $x \in [0, \bar{x}]$ gives

$$\xi_{14} = \frac{(\upsilon - q_\phi)}{4}\begin{bmatrix} 12\sigma_m + 4\lambda_m\sigma_m^2 - 2\sigma_m\cos(2\lambda_m) - 2\sigma_m\cosh(2\lambda_m) \\ +4\cosh(\lambda_m)\left(-2\sigma_m\cos(\lambda_m) + (\sigma_m^2 - 1)\sin(\lambda_m)\right) \\ +(\sigma_m^2 - 1)\sin(2\lambda_m) + 2(1+\sigma_m^2)(2\cos(\lambda_m) + \cosh(\lambda_m))\sinh(\lambda_m) \end{bmatrix}, \quad \text{(B-23)}$$

which is then input combined with ξ_{15} in (B-67) to produce ψ_{12} and inserted into the x directional equation of motion to form the fourth term in (5-69). From (B-3), ξ_{15} is defined as

$$\xi_{15} = k\int_{x=0}^{\bar{x}} \frac{\partial^3 f_3}{\partial x^3} f_1 dx \,. \quad \text{(B-24)}$$

Inserting (5-67) and (5-59) into (B-24) and integrating $x \in [0, \bar{x}]$ gives

$$\xi_{15} = \frac{k\lambda_m^2}{4\bar{x}^2}\begin{bmatrix} -4\lambda_m + 2\sigma_m\cos(2\lambda_m) - 2\sigma_m\cosh(2\lambda_m) \\ +\sin(2\lambda_m) - \sigma_m^2\sin(2\lambda_m) + (1+\sigma_m^2)\sinh(2\lambda_m) \end{bmatrix}, \quad \text{(B-25)}$$

which is then combined with ξ_{14} in (B-67) to produce ψ_{12} and inserted into the x directional equation of motion to form the fourth term in (5-69). From (B-3), ξ_{16} is defined as

$$\xi_{16} = \frac{k(1-\upsilon)}{2}\int_{x=0}^{\bar{x}} \frac{\partial f_3}{\partial x} f_1 dx \,. \quad \text{(B-26)}$$

Inserting (5-65) and (5-59) into (B-26) and integrating $x \in [0, \bar{x}]$ gives

$$\xi_{16} = \frac{k(1-\upsilon)}{8}\begin{bmatrix} 12\sigma_m + 4\lambda_m\sigma_m^2 - 2\sigma_m\cos(2\lambda_m) - 2\sigma_m\cosh(2\lambda_m) \\ +4\cosh(\lambda_m)\left(-2\sigma_m\cos(\lambda_m) + (\sigma_m^2 - 1)\sin(\lambda_m)\right) \\ +(\sigma_m^2 - 1)\sin(2\lambda_m) + 2(1+\sigma_m^2)(2\cos(\lambda_m) + \cosh(\lambda_m))\sinh(\lambda_m) \end{bmatrix}, \quad \text{(B-27)}$$

which is then inserted into the x directional equation of motion to form the fifth term in (5-69). From (B-3), ξ_{17} is defined as

$$\xi_{17} = \Delta \int_{x=0}^{\bar{x}} f_1 f_1 dx \,. \tag{B-28}$$

Inserting (5-59) into (B-28) and integrating $x \in [0, \bar{x}]$ gives

$$\xi_{17} = \frac{\bar{x}\Delta}{4\lambda_m}\begin{bmatrix} 12\sigma_m + 4\lambda_m\sigma_m^2 - 2\sigma_m\cos(2\lambda_m) - 2\sigma_m\cosh(2\lambda_m) \\ +4\cosh(\lambda_m)\left(-2\sigma_m\cos(\lambda_m) + (\sigma_m^2 - 1)\sin(\lambda_m)\right) \\ +(\sigma_m^2 - 1)\sin(2\lambda_m) + 2(1+\sigma_m^2)\left(2\cos(\lambda_m) + \cosh(\lambda_m)\right)\sinh(\lambda_m) \end{bmatrix}. \tag{B-29}$$

Equation (B-29) is then combined with ξ_{11} in (B-66) to produce ψ_{11} and inserted into the x directional equation of motion to form the first term in (5-69).

The second equation of motion, (5-70), contains the coefficient ξ_{21} as seen in (B-30)

$$\xi_{21} = \frac{(1+\upsilon)}{2}\int_{x=0}^{\bar{x}} \frac{\partial f_1}{\partial x} f_2 dx \,. \tag{B-30}$$

Inserting (5-61) and (5-60) into (B-30) and integrating $x \in [0, \bar{x}]$ gives

$$\xi_{21} = \frac{(1+\upsilon)}{8}\begin{bmatrix} -2\sigma_m\left(-2 + 2\lambda_m\sigma_m + \cos(2\lambda_m)\right) \\ -2\sigma_m\cosh(2\lambda_m) + (\sigma_m^2 - 1)\sin(2\lambda_m) + (1+\sigma_m^2)\sinh(2\lambda_m) \end{bmatrix}, \tag{B-31}$$

which is then input into the ϕ directional equation of motion to form the first term in (5-70). From (B-8), ξ_{22} is defined as

$$\xi_{22} = (1+q_\phi)\int_{x=0}^{\bar{x}} f_2 f_2 dx \,. \tag{B-32}$$

Inserting (5-60) into (B-32) and integrating $x \in [0, \bar{x}]$ gives

$$\xi_{22} = \frac{\bar{x}(1+q_\phi)}{4\lambda_m}\begin{bmatrix} 4\lambda + 2\sigma_m\cos(2\lambda_m) - 2\sigma_m\cosh(2\lambda_m) - (\sigma_m^2 - 1)\sin(2\lambda_m) \\ +4\sin(\lambda_m)\left((1+\sigma_m^2)\cosh(\lambda_m) - 2\sigma_m\sinh(\lambda_m)\right) \\ +\sinh(2\lambda_m) - 4(\sigma_m^2 - 1)\cos(\lambda_m)\sinh(\lambda_m) + \sigma_m^2\sinh(2\lambda_m) \end{bmatrix}, \tag{B-33}$$

which is then inserted into the ϕ directional equation of motion to form the second term in (5-70). From (B-8), ξ_{23} is defined as

$$\xi_{23} = \left[\frac{(1-\upsilon)(1+3k)}{2} + q_x\right]\int_{x=0}^{\bar{x}} \frac{\partial^2 f_2}{\partial x^2} f_2 dx \,. \tag{B-34}$$

Inserting (5-66) and (5-60) into (B-34) and integrating $x \in [0, \bar{x}]$ gives

$$\xi_{23} = \frac{\lambda_m \left(3k(\upsilon-1)+\upsilon-1-2q_x\right)}{8\bar{x}} \begin{bmatrix} 2\sigma_m\left(-2+2\lambda_m\sigma_m+\cos(2\lambda_m)\right)+2\sigma_m\cosh(2\lambda_m) \\ -\left(\sigma_m^2-1\right)\sin(2\lambda_m)-\left(1+\sigma_m^2\right)\sinh(2\lambda_m) \end{bmatrix}. \quad \text{(B-35)}$$

Equation (B-35) is then combined with ξ_{26} in (B-68) to produce ψ_{21} and inserted into the ϕ directional equation of motion to form the third term in (5-70). From (B-8), ξ_{24} is defined as

$$\xi_{24} = \left(1+q_\phi\right) \int_{x=0}^{\bar{x}} f_3 f_2 dx. \quad \text{(B-36)}$$

Inserting (5-60) into (B-32) and integrating $x \in [0, \bar{x}]$ gives

$$\xi_{24} = \frac{\bar{x}\left(1+q_\phi\right)}{4\lambda_m} \begin{bmatrix} 4\lambda_m+2\sigma_m\cos(2\lambda_m)-2\sigma_m\cosh(2\lambda_m)-\left(\sigma_m^2-1\right)\sin(2\lambda_m) \\ +4\sin(\lambda_m)\left(\left(1+\sigma_m^2\right)\cosh(\lambda_m)-2\sigma_m\sinh(\lambda_m)\right) \\ +\sinh(2\lambda_m)-4\left(\sigma_m^2-1\right)\cos(\lambda_m)\sinh(\lambda_m)+\sigma_m^2\sinh(2\lambda_m) \end{bmatrix} \quad \text{(B-37)}$$

which is then combined with ξ_{25} in (B-69) to produce ψ_{22} and inserted into the ϕ directional equation of motion to form the fourth term in (5-70). From (B-8), ξ_{25} is defined as

$$\xi_{25} = \frac{k(3-\upsilon)}{2} \int_{x=0}^{\bar{x}} \frac{\partial^2 f_3}{\partial x^2} f_2 dx \quad \text{(B-38)}$$

Inserting (5-66) and (5-60) into (B-38) and integrating $x \in [0, \bar{x}]$ gives

$$\xi_{25} = \frac{\lambda_m k(\upsilon-3)}{8\bar{x}} \begin{bmatrix} 2\sigma_m\left(-2+2\lambda_m\sigma_m+\cos(2\lambda_m)\right)+2\sigma_m\cosh(2\lambda_m) \\ -\left(\sigma_m^2-1\right)\sin(2\lambda_m)-\left(1+\sigma_m^2\right)\sinh(2\lambda_m) \end{bmatrix}. \quad \text{(B-39)}$$

which is then combined with ξ_{24} in (B-69) to produce ψ_{22} and inserted into the ϕ directional equation of motion to form the fourth term in (5-70). From (B-8), ξ_{26} is defined as

$$\xi_{26} = \Delta \int_{x=0}^{\bar{x}} f_2 f_2 dx. \quad \text{(B-40)}$$

Inserting (5-60) into (B-40) and integrating $x \in [0, \bar{x}]$ gives

$$\xi_{26} = \frac{\Delta\bar{x}}{4\lambda_m} \begin{bmatrix} 4\lambda_m+2\sigma_m\cos(2\lambda_m)-2\sigma_m\cosh(2\lambda_m)-\left(\sigma_m^2-1\right)\sin(2\lambda_m) \\ +4\sin(\lambda_m)\left(\left(1+\sigma_m^2\right)\cosh(\lambda_m)-2\sigma_m\sinh(\lambda_m)\right) \\ +\sinh(2\lambda_m)-4\left(\sigma_m^2-1\right)\cos(\lambda_m)\sinh(\lambda_m)+\sigma_m^2\sinh(2\lambda_m) \end{bmatrix}. \quad \text{(B-41)}$$

Equation (B-41) is then combined with ξ_{23} in (B-68) to produce ψ_{21} and inserted into the ϕ directional equation of motion to form the third term in (5-70).

The third equation of motion, (5-71), contains the coefficient (B-42) as seen in (B-42),

$$\xi_{31} = \left(\upsilon - q_\phi\right) \int_{x=0}^{\bar{x}} \frac{\partial f_1}{\partial x} f_3 dx \,. \tag{B-42}$$

Inserting (5-61) and (5-60) into (B-42) and integrating $x \in [0, \bar{x}]$ gives

$$\xi_{31} = \frac{\left(\upsilon - q_\phi\right)}{4} \begin{bmatrix} -2\sigma_m\left(-2 + 2\lambda_m\sigma_m + \cos\left(2\lambda_m\right)\right) - 2\sigma_m \cosh\left(2\lambda_m\right) \\ +\left(\sigma_m^2 - 1\right)\sin\left(2\lambda_m\right) + \left(1 + \sigma_m^2\right)\sinh\left(2\lambda_m\right) \end{bmatrix}, \tag{B-43}$$

which is then combined with ξ_{35} in (B-70) to produce ψ_{31} and inserted into the z directional equation of motion to form the first term in (5-71). From (B-13), ξ_{32} is defined as

$$\xi_{32} = \left(1 + q_\phi\right) \int_{x=0}^{\bar{x}} f_2 f_3 dx \,. \tag{B-44}$$

Inserting (5-60) into (B-44) and integrating $x \in [0, \bar{x}]$ gives

$$\xi_{32} = \frac{\bar{x}\left(1 + q_\phi\right)}{4\lambda_m} \begin{bmatrix} 4\lambda_m + 2\sigma_m \cos\left(2\lambda_m\right) - 2\sigma_m \cosh\left(2\lambda_m\right) - \left(\sigma_m^2 - 1\right)\sin\left(2\lambda_m\right) \\ +4\sin\left(\lambda_m\right)\left(\left(1 + \sigma_m^2\right)\cosh\left(\lambda_m\right) - 2\sigma_m \sinh\left(\lambda_m\right)\right) \\ +\sinh\left(2\lambda_m\right) - 4\left(\sigma_m^2 - 1\right)\cos\left(\lambda_m\right)\sinh\left(\lambda_m\right) + \sigma_m^2 \sinh\left(2\lambda_m\right) \end{bmatrix}. \tag{B-45}$$

The resolved form of ξ_{32} presented in (B-45) is then combined with ξ_{36} in (B-72) to produce ψ_{33} and inserted into the z directional equation of motion to form the third term in (5-71). From (B-13), ξ_{33} is defined as

$$\xi_{33} = \left(1 + k\right) \int_{x=0}^{\bar{x}} f_3 f_3 dx \,. \tag{B-46}$$

Inserting (5-60) into (B-46) and integrating $x \in [0, \bar{x}]$ gives

$$\xi_{33} = \frac{\bar{x}\left(1 + k\right)}{4\lambda_m} \begin{bmatrix} 4\lambda_m + 2\sigma_m \cos\left(2\lambda_m\right) - 2\sigma_m \cosh\left(2\lambda_m\right) - \left(\sigma_m^2 - 1\right)\sin\left(2\lambda_m\right) \\ +4\sin\left(\lambda_m\right)\left(\left(1 + \sigma_m^2\right)\cosh\left(\lambda_m\right) - 2\sigma_m \sinh\left(\lambda_m\right)\right) \\ +\sinh\left(2\lambda_m\right) - 4\left(\sigma_m^2 - 1\right)\cos\left(\lambda_m\right)\sinh\left(\lambda_m\right) + \sigma_m^2 \sinh\left(2\lambda_m\right) \end{bmatrix}, \tag{B-47}$$

which is then combined with ξ_{37}, ξ_{41}, and ξ_{42} in (B-71) to form ψ_{32} and is inserted into the *z* directional equation of motion to form the fourth term in (5-71). From (B-13), ξ_{34} is defined as

$$\xi_{34} = \frac{k(1-\upsilon)}{2}\int_{x=0}^{\bar{x}} \frac{\partial f_1}{\partial x} f_3 dx . \tag{B-48}$$

Inserting (5-61) and (5-60) into (B-48) and integrating $x \in [0,\bar{x}]$ gives

$$\xi_{34} = \frac{k(1-\upsilon)}{8}\begin{bmatrix} -2\sigma_m\left(-2+2\lambda_m\sigma_m+\cos(2\lambda_m)\right)-2\sigma_m\cosh(2\lambda_m) \\ +\left(\sigma_m^2-1\right)\sin(2\lambda_m)+\left(1+\sigma_m^2\right)\sinh(2\lambda_m) \end{bmatrix}, \tag{B-49}$$

which is input into the *z* directional equation of motion to form the second term in (5-71). From (B-13), ξ_{35} is defined as

$$\xi_{35} = k\int_{x=0}^{\bar{x}} \frac{\partial^3 f_1}{\partial x^3} f_3 dx . \tag{B-50}$$

Inserting (5-63) and (5-60) into (B-50) and integrating $x \in [0,\bar{x}]$ gives

$$\xi_{35} = \frac{k\lambda_m^2}{4\bar{x}^2}\begin{bmatrix} 4\lambda_m+2\sigma_m\cos(2\lambda_m)-2\sigma_m\cosh(2\lambda_m) \\ -\left(\sigma_m^2-1\right)\sin(2\lambda_m)-4\left(\sigma_m^2-1\right)\cos(\lambda_m)\sinh(\lambda_m) \\ +4\sin(\lambda_m)\left(\left(1+\sigma_m^2\right)\cosh(\lambda_m)-2\sigma_m\sinh(\lambda_m)\right)+\left(1+\sigma_m^2\right)\sinh(2\lambda_m) \end{bmatrix}, \tag{B-51}$$

which is then combined with ξ_{31} in (B-70) to produce ψ_{31} and inserted into the *z* directional equation of motion to form the first term in (5-71). From (B-13), ξ_{36} is defined as

$$\xi_{36} = \frac{k(3-\upsilon)}{2}\int_{x=0}^{\bar{x}} \frac{\partial^2 f_3}{\partial x^2} f_3 dx . \tag{B-52}$$

Inserting (5-66) and (5-60) into (B-52) and integrating $x \in [0,\bar{x}]$ gives

$$\xi_{36} = \frac{k\lambda_m(3-\upsilon)}{8\bar{x}}\begin{bmatrix} 2\sigma_m\left(-2+2\lambda_m\sigma_m+\cos(2\lambda_m)\right)+2\sigma_m\cosh(2\lambda_m) \\ -\left(\sigma_m^2-1\right)\sin(2\lambda_m)-\left(1+\sigma_m^2\right)\sinh(2\lambda_m) \end{bmatrix}. \tag{B-53}$$

The resolved form of ξ_{36} presented in (B-53) is then combined with ξ_{32} in (B-72) to produce ψ_{33} and is inserted into the *z* directional equation of motion to form the third term in (5-71). From (B-13), ξ_{37} is defined as

$$\xi_{37} = k\int_{x=0}^{\bar{x}} \frac{\partial^4 f_3}{\partial x^4} f_3 dx . \tag{B-54}$$

Inserting (5-68) and (5-60) into (B-54) and integrating $x \in [0, \bar{x}]$ gives

$$\xi_{37} = \frac{k\lambda_m^3}{4\bar{x}^3}\begin{bmatrix} 4\lambda_m + 2\sigma_m \cos(2\lambda_m) - 2\sigma_m \cosh(2\lambda_m) \\ -(\sigma_m^2 - 1)\sin(2\lambda_m) - 4(\sigma_m^2 - 1)\cos(\lambda_m)\sinh(\lambda_m) \\ +4\sin(\lambda_m)\left((1+\sigma_m^2)\cosh(\lambda_m) - 2\sigma_m \sinh(\lambda_m)\right) + (1+\sigma_m^2)\sinh(2\lambda_m) \end{bmatrix}, \quad \text{(B-55)}$$

which is then combined with ξ_{33}, ξ_{41}, and ξ_{42} in (B-71) to form ψ_{32} and inserted into the z directional equation of motion to form the fourth term in (5-71). From (B-13), ξ_{38} is defined as

$$\xi_{38} = 2k \int_{x=0}^{\bar{x}} \frac{\partial^2 f_3}{\partial x^2} f_3 dx \,. \quad \text{(B-56)}$$

Inserting (5-66) and (5-60) into (B-56) and integrating $x \in [0, \bar{x}]$ gives

$$\xi_{38} = \frac{k\lambda_m}{2\bar{x}}\begin{bmatrix} -2\sigma_m\left(-2 + 2\lambda_m\sigma_m + \cos(2\lambda_m)\right) - 2\sigma_m \cosh(2\lambda_m) \\ +(\sigma_m^2 - 1)\sin(2\lambda_m) + (1+\sigma_m^2)\sinh(2\lambda_m) \end{bmatrix}. \quad \text{(B-57)}$$

The resolved form of ξ_{38} presented in (B-57) is then combined with ξ_{40} in (B-73) to produce ψ_{34} and is inserted into the z directional equation of motion to form the fifth term in (5-71). From (B-13), ξ_{39} is defined as

$$\xi_{39} = k \int_{x=0}^{\bar{x}} f_3 f_3 dx \quad \text{(B-58)}$$

Inserting (5-60) into (B-58) and integrating $x \in [0, \bar{x}]$ gives

$$\xi_{39} = \frac{k\bar{x}}{4\lambda_m}\begin{bmatrix} 4\lambda_m + 2\sigma_m \cos(2\lambda_m) - 2\sigma_m \cosh(2\lambda_m) - (\sigma_m^2 - 1)\sin(2\lambda_m) \\ +4\sin(\lambda_m)\left((1+\sigma_m^2)\cosh(\lambda_m) - 2\sigma_m \sinh(\lambda_m)\right) \\ +\sinh(2\lambda_m) - 4(\sigma_m^2 - 1)\cos(\lambda_m)\sinh(\lambda_m) + \sigma_m^2 \sinh(2\lambda_m) \end{bmatrix} \quad \text{(B-59)}$$

Equation (B-59) is input into the z directional equation of motion to form the last term in (5-71). From (B-13), ξ_{40} is defined as

$$\xi_{40} = (2k - q_\phi) \int_{x=0}^{\bar{x}} f_3 f_3 dx \quad \text{(B-60)}$$

Inserting (5-60) into (B-60) and integrating $x \in [0, \bar{x}]$ gives

$$\xi_{40} = \frac{\bar{x}(2k - q_\phi)}{4\lambda_m}\begin{bmatrix} 4\lambda_m + 2\sigma_m \cos(2\lambda_m) - 2\sigma_m \cosh(2\lambda_m) - (\sigma_m^2 - 1)\sin(2\lambda_m) \\ +4\sin(\lambda_m)\left((1+\sigma_m^2)\cosh(\lambda_m) - 2\sigma_m \sinh(\lambda_m)\right) \\ +\sinh(2\lambda_m) - 4(\sigma_m^2 - 1)\cos(\lambda_m)\sinh(\lambda_m) + \sigma_m^2 \sinh(2\lambda_m) \end{bmatrix} \quad \text{(B-61)}$$

which is then combined with ξ_{38} in (B-73) to produce ψ_{34} and is inserted into the z directional equation of motion to form the fifth term in (5-71). From (B-13), ξ_{41} is defined as

$$\xi_{41} = \Delta \int_{x=0}^{\bar{x}} f_3 f_3 dx \tag{B-62}$$

Inserting (5-60) into (B-62) and integrating $x \in [0, \bar{x}]$ gives

$$\xi_{41} = \frac{\Delta \bar{x}}{4\lambda_m} \begin{bmatrix} 4\lambda_m + 2\sigma_m \cos(2\lambda_m) - 2\sigma_m \cosh(2\lambda_m) - (\sigma_m^2 - 1)\sin(2\lambda_m) \\ +4\sin(\lambda_m)\left((1+\sigma_m^2)\cosh(\lambda_m) - 2\sigma_m \sinh(\lambda_m)\right) \\ +\sinh(2\lambda_m) - 4(\sigma_m^2 - 1)\cos(\lambda_m)\sinh(\lambda_m) + \sigma_m^2 \sinh(2\lambda_m) \end{bmatrix} \tag{B-63}$$

The resolved form of ξ_{41} presented in (B-63) is then combined with ξ_{33}, ξ_{37}, and ξ_{42} in (B-71) to form ψ_{32} and inserted into the z directional equation of motion to form the fourth term in (5-71). From (B-13), ξ_{42} is defined as

$$\xi_{42} = q_x \int_{x=0}^{\bar{x}} \frac{\partial^2 f_3}{\partial x^2} f_3 dx \tag{B-64}$$

Inserting (5-66) and (5-60) into (B-64) and integrating $x \in [0, \bar{x}]$ gives

$$\xi_{42} = \frac{q_x \lambda_m}{4\bar{x}} \begin{bmatrix} 4\sigma_m \left(\sin(\lambda_m)^2 - \lambda_m \sigma_m\right) + (\sigma_m^2 - 1)\sin(2\lambda_m) \\ -4\sigma_m \sinh(\lambda_m) + (\sigma_m^2 + 1)\sinh(2\lambda_m) \end{bmatrix} \tag{B-65}$$

Which is then combined with ξ_{33}, ξ_{37}, and ξ_{41} in (B-71) to form ψ_{32} and inserted into the z directional equation of motion to form the fourth term in (5-71). In an attempt to simplify the three equations of motion; (5-69), (5-70), and (5-71), the coefficients of like terms were combined as a part of the linearization process. These coefficients are as follows:

$$\psi_{11} = \xi_{11} + \xi_{17}, \tag{B-66}$$

$$\psi_{12} = \xi_{14} - \xi_{15}, \tag{B-67}$$

$$\psi_{21} = \xi_{23} + \xi_{26}, \tag{B-68}$$

$$\psi_{22} = \xi_{24} - \xi_{25}, \tag{B-69}$$

$$\psi_{31} = \xi_{31} - \xi_{35}, \tag{B-70}$$

$$\psi_{32} = \xi_{33} + \xi_{37} - \xi_{41} - \xi_{42}, \tag{B-71}$$

$$\psi_{33} = \xi_{32} - \xi_{36}, \tag{B-72}$$

and

$$\psi_{34} = \xi_{38} + \xi_{40}. \tag{B-73}$$

12 APPENDIX C (Stability Module Test Case)

It is necessary to compare a solution set produced by the plate stability module to values acquired in previous works in an attempt to credibly justify the solutions produced for this study. No known available literature was found to include natural frequency values for a cylindrical plate with C-F-C-F or C-F-SS-F boundary conditions, respectively. However, a set of cases were published by Sewall [83, 84], Blevins [75], and Deb Nath and Petyt [85] for a cylindrical square plate $(\overline{x}=1)$. These cases will be used for comparison against the solution produced by the plate stability module, presented in Section 5.1.

12.1 Definition of Coefficients

Using the same methodology presented in Appendix B, a set of coefficients were derived while applying the boundary condition (5-36).

$$\xi_{12}=\frac{(1-\upsilon)(1+k)}{2}\left(\sigma_m^2-\frac{2\sigma_m}{\lambda_m}\right)\overline{x} \tag{C-1}$$

$$\xi_{13}=\frac{\lambda_m(1-\upsilon)}{2}\left(\sigma_m^2-\frac{2\sigma_m}{\lambda_m}\right) \tag{C-2}$$

$$\xi_{16}=k\xi_{13} \tag{C-3}$$

$$\xi_{21}=-\xi_{13} \tag{C-4}$$

$$\xi_{22}=\overline{x} \tag{C-5}$$

$$\xi_{34}=-\xi_{16} \tag{C-6}$$

$$\xi_{39}=k\xi_{22} \tag{C-7}$$

$$\psi_{11}=-\frac{\lambda_m^2}{\overline{x}}+\Delta\left(\sigma_m^2-\frac{2\sigma_m}{\lambda_m}\right)\overline{x}\,, \tag{C-8}$$

$$\psi_{12}=\sigma_m\upsilon\left(\lambda_m\sigma_m-2\right)+\frac{k\lambda_m^3}{\overline{x}^2}, \tag{C-9}$$

$$\psi_{21}=-\frac{\lambda_m^2(1-\upsilon)(1+3k)}{2\overline{x}}\left(\sigma_m^2-\frac{2\sigma_m}{\lambda_m}\right)+\Delta\overline{x}\,, \tag{C-10}$$

$$\psi_{22}=\overline{x}+\frac{\lambda_m^2k(3-\upsilon)}{2\overline{x}}\left(\sigma_m^2-\frac{2\sigma_m}{\lambda_m}\right), \tag{C-11}$$

$$\psi_{31}=-\upsilon\lambda_m\left(\sigma_m^2-\frac{2\sigma_m}{\lambda_m}\right)-\frac{k\lambda_m^3}{\overline{x}^2}\,, \tag{C-12}$$

$$\psi_{32} = (1+k)\bar{x} + k\frac{\lambda_m^4}{\bar{x}^3} - \Delta\bar{x}\,, \tag{C-13}$$

$$\psi_{33} = \bar{x} + \frac{(3-\upsilon)k\lambda_m^2}{2\bar{x}}\left(\sigma_m^2 - \frac{2\sigma_m}{\lambda_m}\right), \tag{C-14}$$

$$\psi_{34} = -4k^2\lambda_m^2\left(\sigma_m^2 - \frac{2\sigma_m}{\lambda_m}\right). \tag{C-15}$$

The coefficients for this test case were developed using the same method presented in Appendix B, however, the pressure terms (P_x and P_r) in the equations of motion were set to zero. This was done because all previous studies considered curved plates under "free vibration" with no externally applied membrane forces. The newly defined coefficients above were then inserted into the coefficient matrix, (5-89), and frequency parameter (Δ) was solved for by employing the algorithm shown in Figure 5-6.

12.2 Test Case Results

A common set of material properties were considered when producing all solution for the test case, these properties are presented in Table C-1.

Table C-1: Test case material properties

Parameter	Value
Density [kg/m^3] (psi)	2700 (0.098)
Modulus of Elasticity [MPa] (psi)	68947.57 (10×10^6)
Poisson's Ratio	0.33

The circular frequency $(\omega = 2\pi f)$ of cylindrical square plates with all edges clamped was found for in available literature for two different radii, and three plate thicknesses. A number of different studies either experimentally or theoretically found the circular frequency for various modal combinations. In all cases the modal number along the axial length of the plate (m) was held to one, while the free vibration solution in the azimuthal direction was determined for several modal numbers (n). Table C-2 summarizes these results. Columns 4 and 5 in Table C-2 show the theoretical solution produced during previous studies using the Rayleigh [75] and Rayleigh-Ritz [85] solution, respectively. Column 6 in Table C-2 is the experimentally acquired eigenvalues for a number for

various modal combinations. Column 7 in Table C-2 presents the circular frequency predicted by this study's model while imposing similar geometric boundary conditions and material properties as employed in the previous studies. Of the three independent methods compared against, the circular frequencies predicted by the Rayleigh-Ritz method compare the best with the work presented here deviating between 0.13 and 11.87 in percent difference, while those predicted using the fundamental Rayleigh method

Table C-2: Circular frequencies (ω) and percent error relative to this study

R [m] (in)	a [m] (in)	m, n	Rayleigh [75]	Rayleigh-Ritz [85]	Experimental [83, 84]	MMP (this study)
2.44 (96)	0.0007 (0.02)	1,3	1420.00 (100.35)	704.97 (0.53)	534.07 (24.65)	708.74
		1,4	1460.84 (84.52)	-	810.53 (2.38)	791.68
		1,5	1678.87 (30.79)	-	1193.81 (7.00)	1283.65
	0.0008 (0.032)	1,2	1595.93 (61.79)	-	735.13 (25.81)	990.86
		1,3	1583.36 (65.79)	942.48 (1.31)	785.40 (17.76)	955.04
		1,4	1840.97 (19.06)	-	1438.85 (6.95)	1546.29
	0.0010 (0.04)	1,2	1636.77 (51.54)	1036.73 (4.01)	772.83 (28.45)	1080.08
		1,3	1718.45 (52.54)	-	1237.79 (9.87)	1126.58
1.22 (48)	0.0007 (0.02)	1,3	2662.81 (157.63)	-	540.35 (47.72)	1033.58
		1,4	2474.32 (148.93)	992.74 (0.13)	929.91 (6.45)	994.00
		1,5	2469.29 (71.84)	-	1514.25 (5.38)	1436.96
	0.0008 (0.032)	1,3	2726.90 (115.49)	1275.49 (0.79)	904.78 (28.5)	1265.43
		1,4	2714.34 (100.46)	-	1696.46 (25.29)	1354.03
	0.0010 (0.04)	1,3	2833.72 (76.65)	1413.72 (11.87)	1130.97 (29.49)	1604.10
		1,4	3550.00 (125.37)	-	1815.84 (15.28)	1575.19
		1,5	3355.22 (30.82)	-	2500.71 (2.50)	2565.89

compare the most poorly to that predicted circular frequencies found in this study. This observation is expected as it has been demonstrated by Blevins [75] that because the Rayleigh method requires an analytical modal shape for the determination of a given eigenvalue, it does not approximate well for high number modal values and curved surfaces (i.e. cylindrical plates).

Considering that the iterative parameter used for this study was selected to be the "frequency parameter", $\Delta = R_{cl}^2 \rho \omega^2 (1-\upsilon^2)/Eg$, the results presented have been reformulated in the form of the frequency parameter and are presented in Figure C-1. The horizontal axis represents the frequency parameter predicted during this study while the vertical axis represents the frequency parameter produced using methods produced in previous studies. The trend in the figure demonstrates that both experimental results and Rayleigh-Ritz solutions compare well against that produced herein, while the Rayleigh method predicts frequency parameters which are approximately proportional to that predicted by herein, but are much larger in magnitude for a prescribed set of boundary conditions. The error bars associated with experimental results reflect 95% confidence [83, 84].

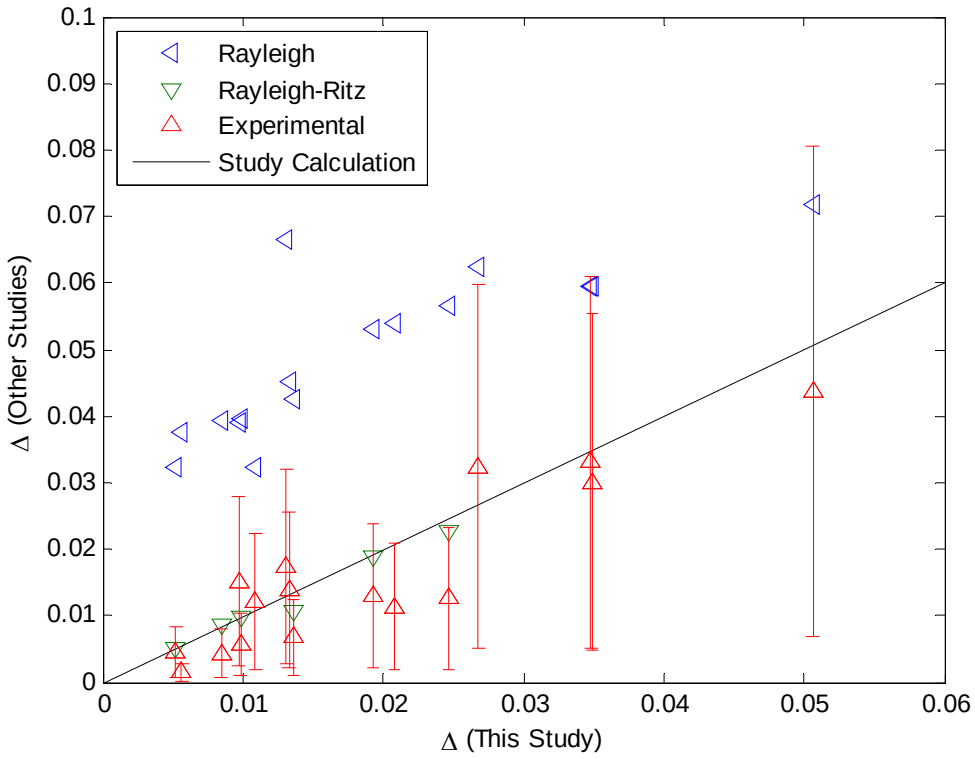

Figure C-1: Comparison of frequency parameters for test case

13 APPENDIX D (Contour Plots)

The relations f_1, f_2, and f_3 describe the eigenfunction shape, and do not account for amplitude (true displacement), it is for this reason that the figures in this appendix are presented in the form of normalized displacement such that the absolute maximum displacement (red or blue) coincides with an absolute amplitude of one.

13.1 C-F-C-F Boundary Condition

The displacement contours representing C-F-C-F boundaries show that for all modal combinations, m, n, the plate displacement is either reflective for even modes of m or truly symmetric for odd modes of m, about $x = L/2$. Similarly for even modes of n the plate is reflective and for odd modes of n the plate is truly symmetric about $\phi = \theta/2$.

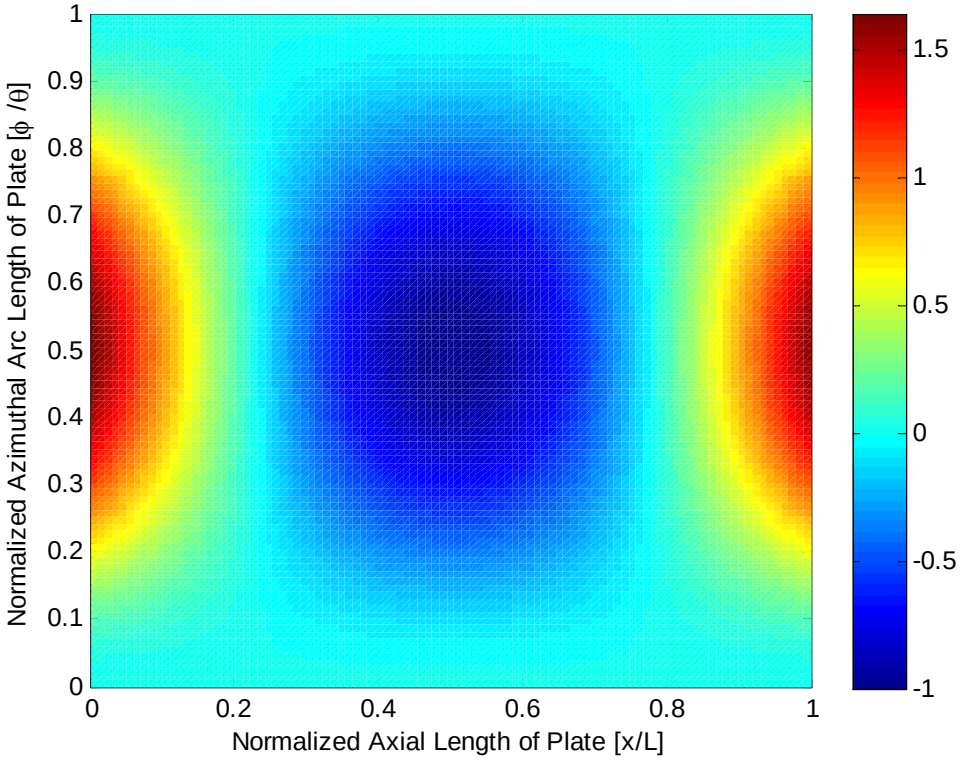

Figure D-1: Displacement view graph of C-F-C-F plate modal shape (m = 1, n = 1)

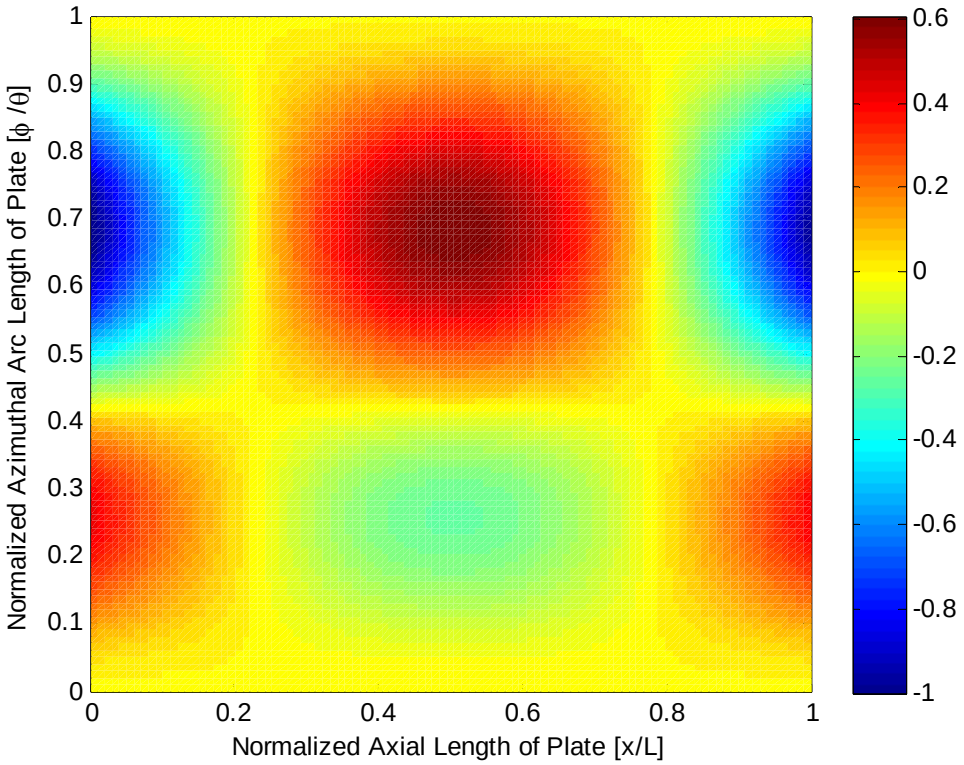

Figure D-2: Displacement view graph of C-F-C-F plate modal shape ($m = 1$, $n = 2$)

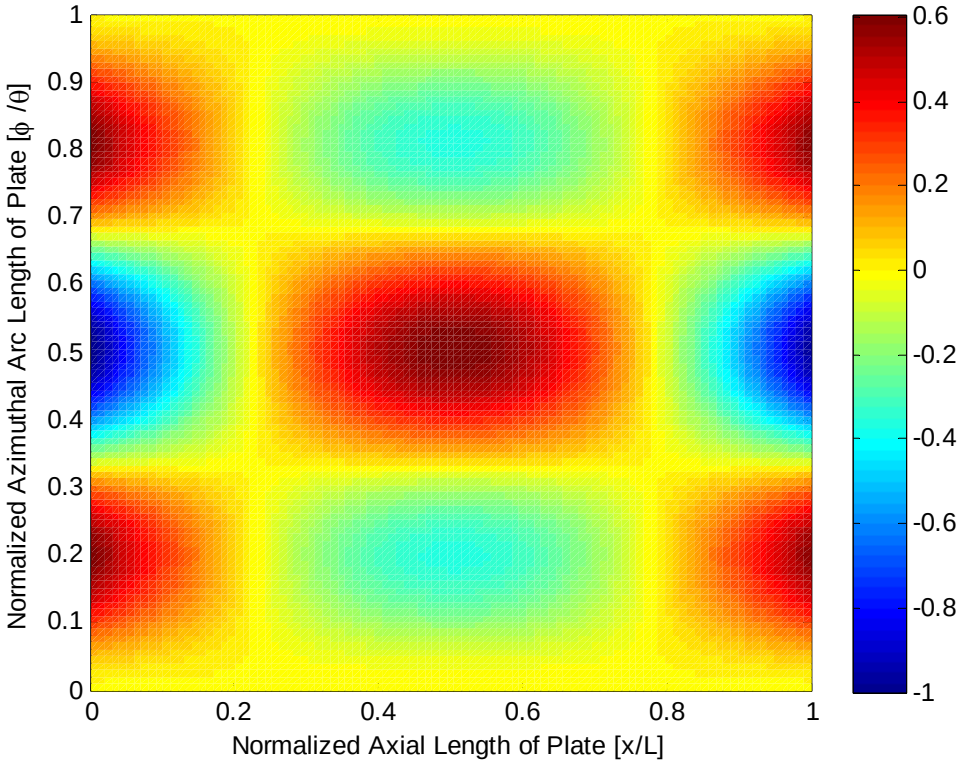

Figure D-3: Displacement view graph of C-F-C-F plate modal shape ($m = 1$, $n = 3$)

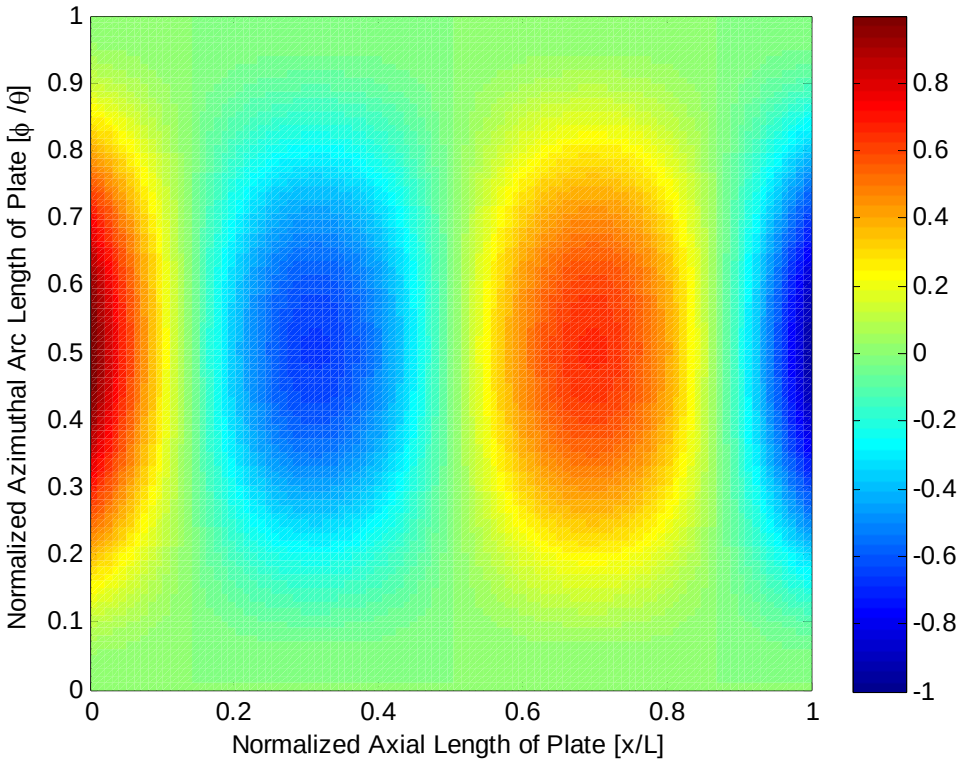

Figure D-4: Displacement view graph of C-F-C-F plate modal shape ($m = 2$, $n = 1$)

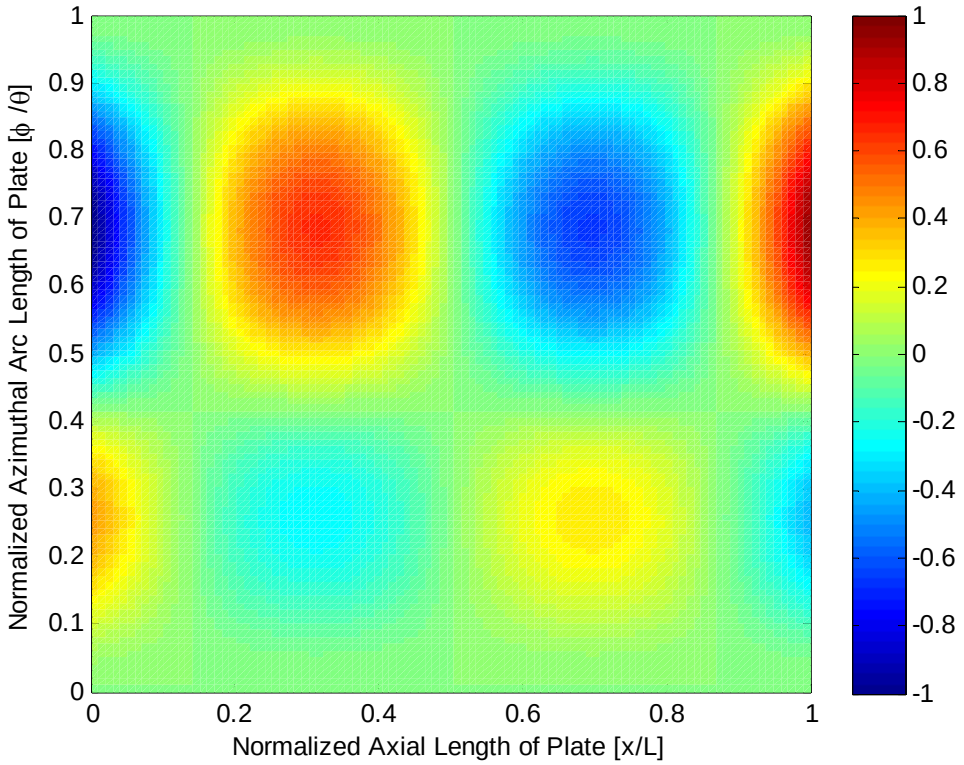

Figure D-5: Displacement view graph of C-F-C-F plate modal shape ($m = 2$, $n = 2$)

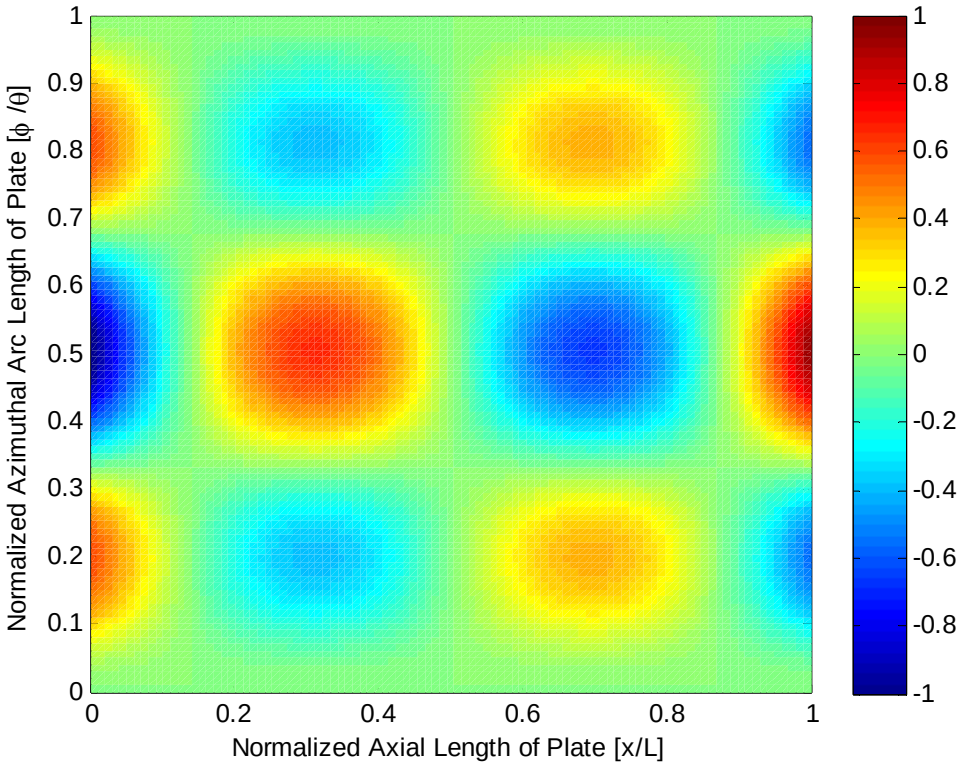

Figure D-6: Displacement view graph of C-F-C-F plate modal shape ($m = 2$, $n = 3$)

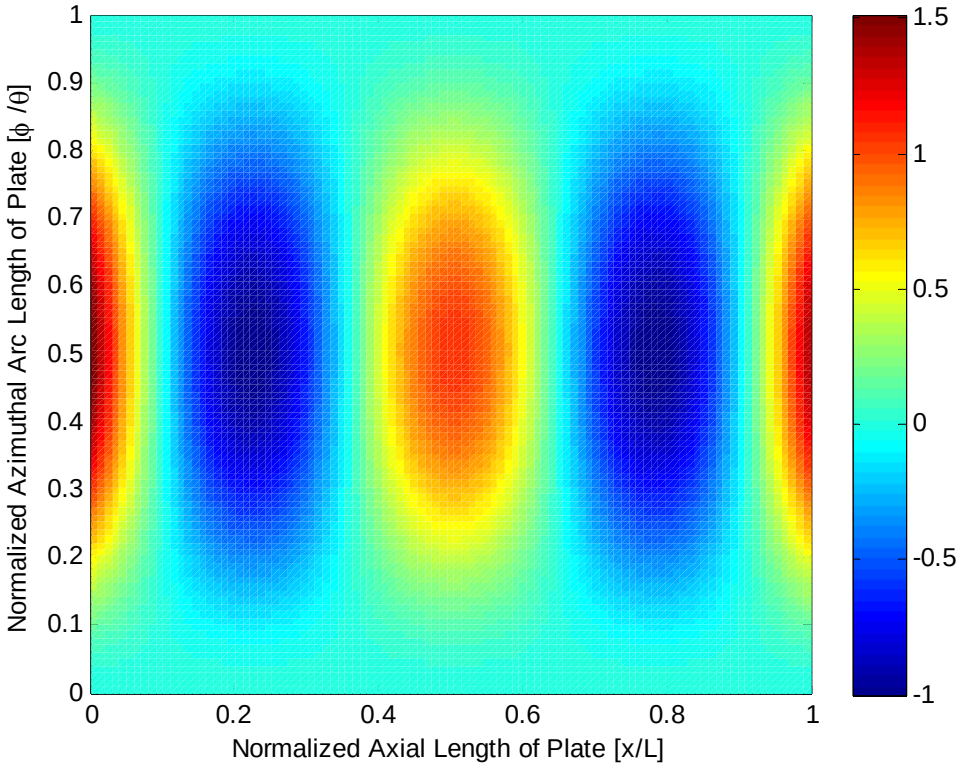

Figure D-7: Displacement view graph of C-F-C-F plate modal shape ($m = 3$, $n = 1$)

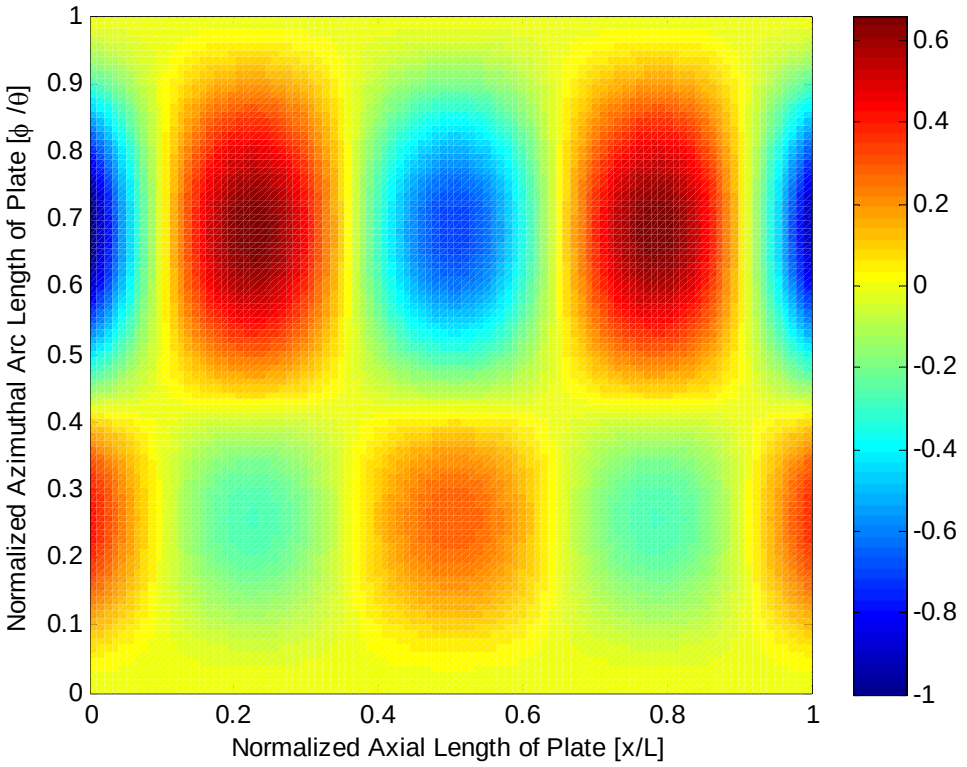

Figure D-8: Displacement view graph of C-F-C-F plate modal shape ($m = 3$, $n = 2$)

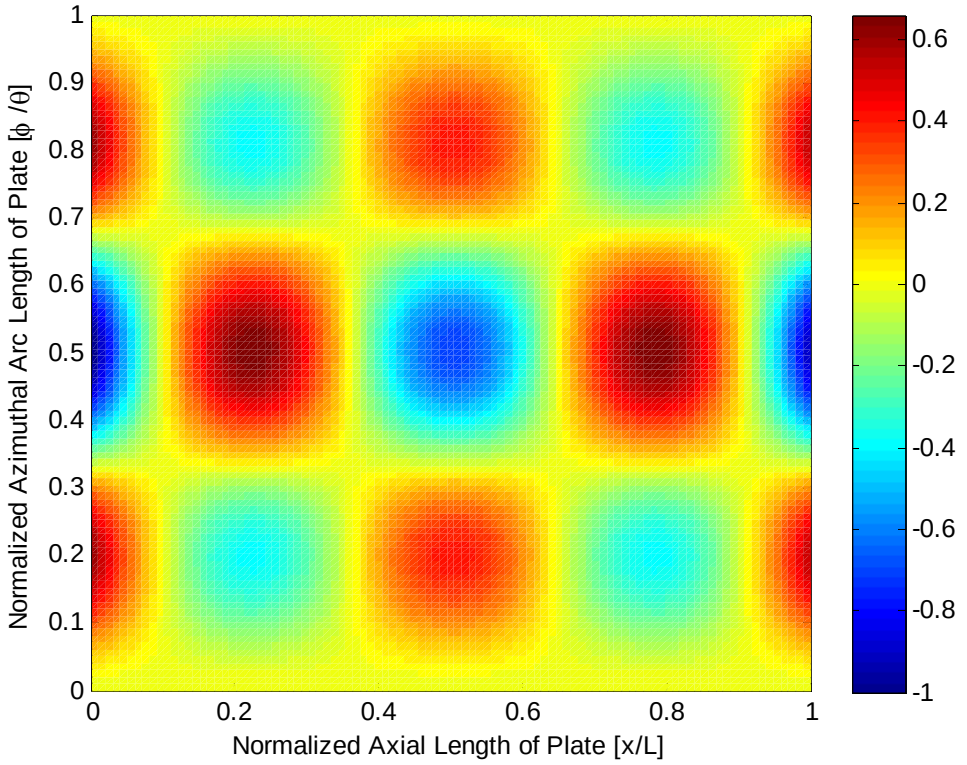

Figure D-9: Displacement view graph of C-F-C-F plate modal shape ($m = 3$, $n = 3$)

13.2 C-F-SS-F Boundary Condition

The displacement representing C-F-SS-F boundaries show that for all modal combinations, *m*, *n*, the plate displacements are identical in shape to those with C-F-C-F edge boundaries along the *x* direction. This is expected as the boundary conditions for *x* = constant do not change during the study. However, not modal shape along the ϕ direction is symmetric or reflective about $\phi = \theta/2$ as a result of the miss-match in boundary conditions at ϕ = constant.

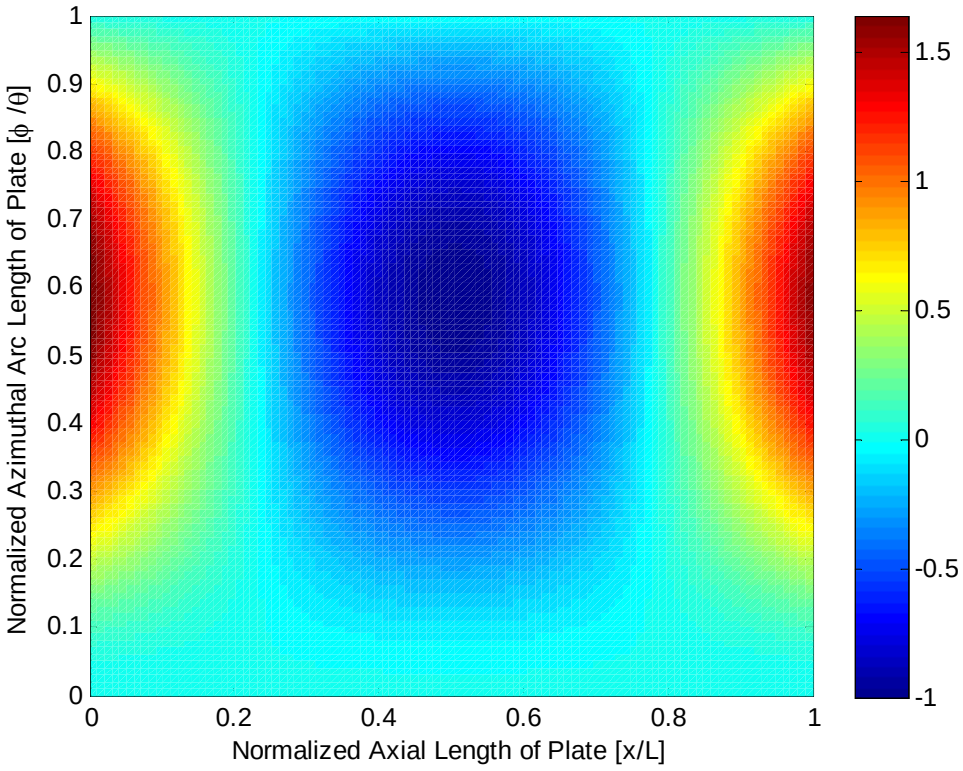

Figure D-10: Displacement view graph of C-F-SS-F plate modal shape (*m* = 1, *n* = 1)

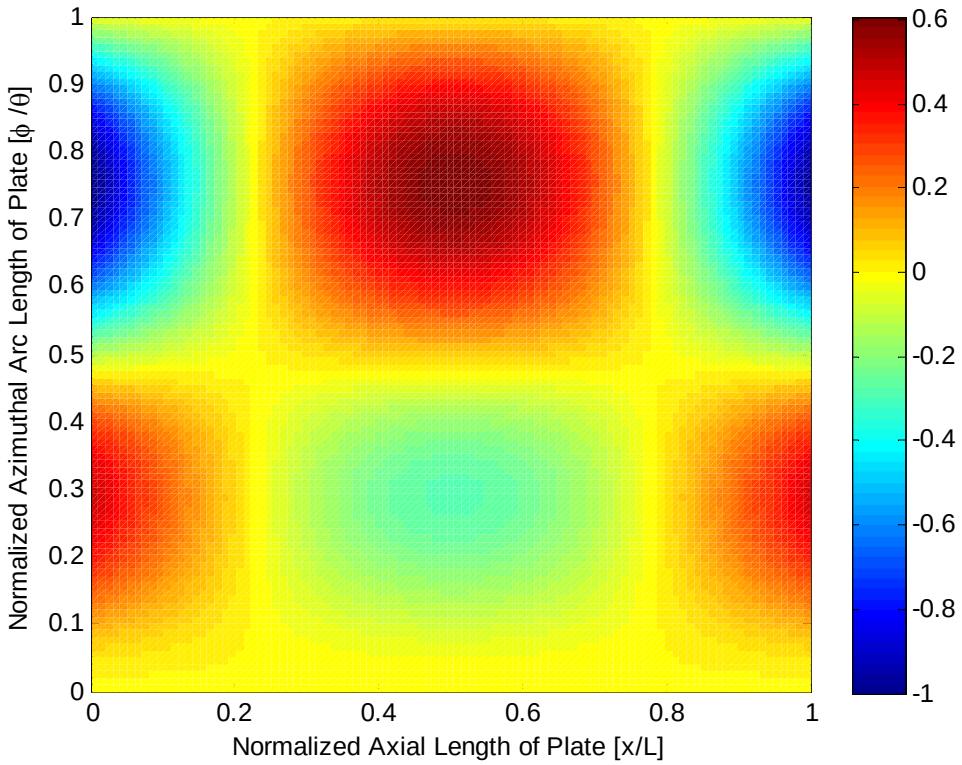

Figure D-11: Displacement view graph of C-F-SS-F plate modal shape ($m = 1$, $n = 2$)

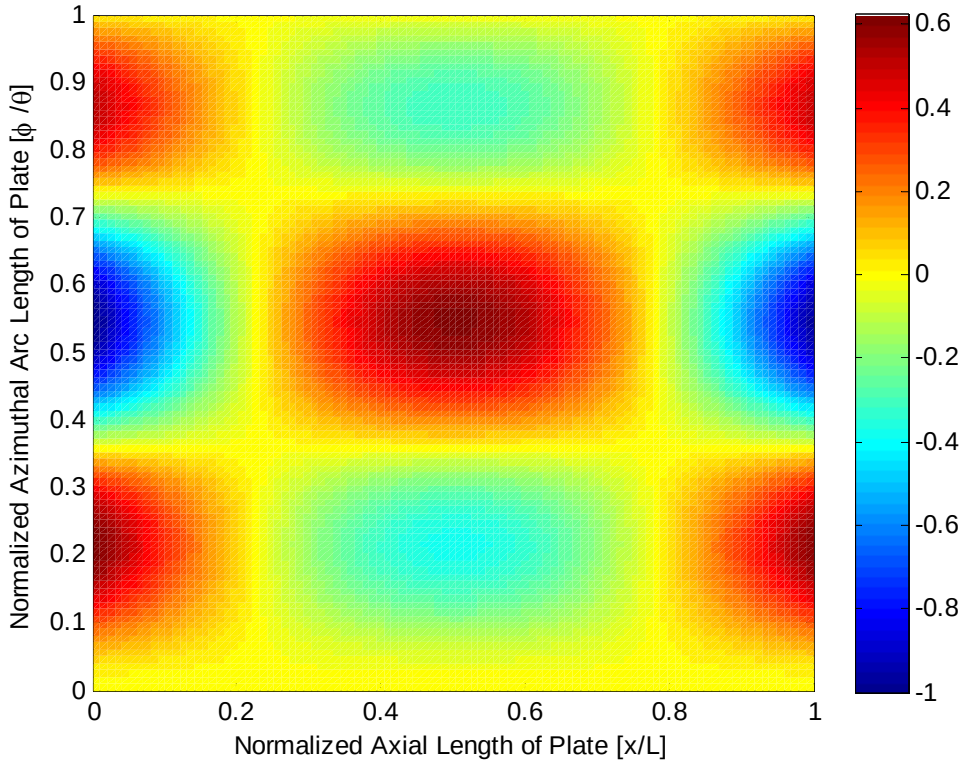

Figure D-12: Displacement view graph of C-F-SS-F plate modal shape ($m = 1$, $n = 3$)

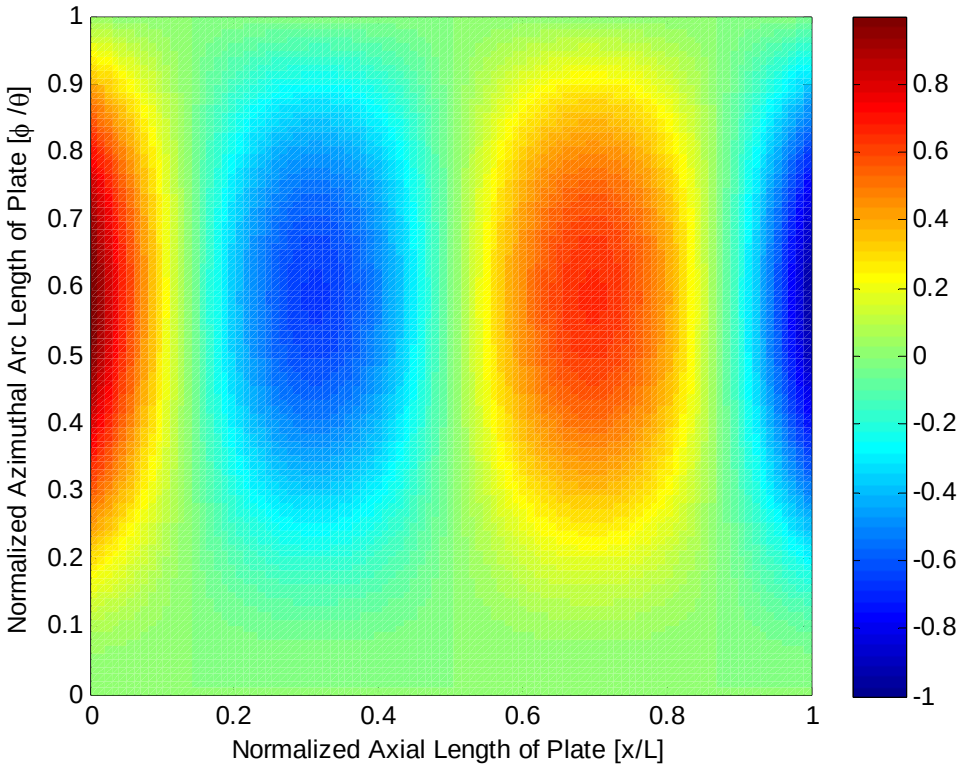

Figure D-13: Displacement view graph of C-F-SS-F plate modal shape ($m = 2$, $n = 1$)

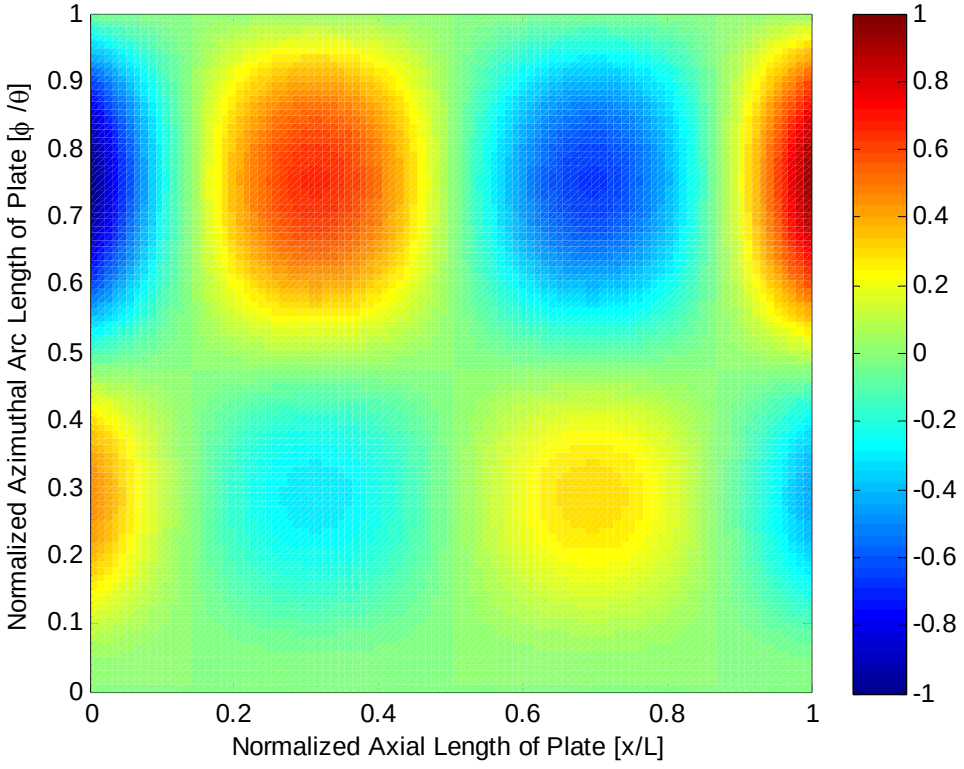

Figure D-14: Displacement view graph of C-F-SS-F plate modal shape ($m = 2$, $n = 2$)

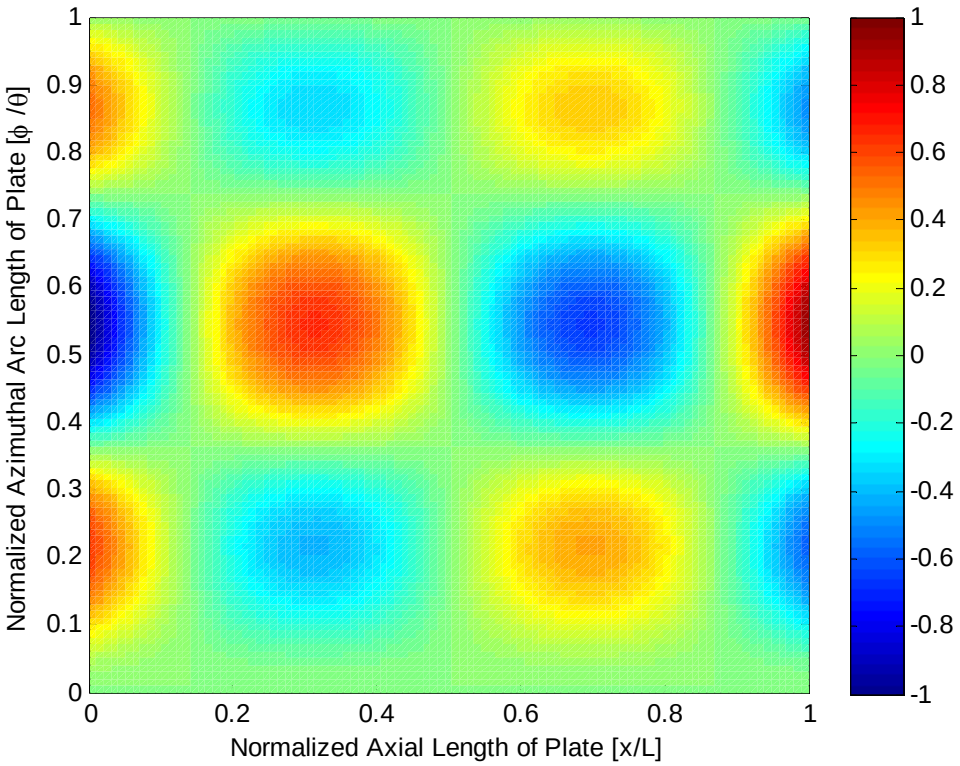

Figure D-15: Displacement view graph of C-F-SS-F plate modal shape ($m = 2$, $n = 3$)

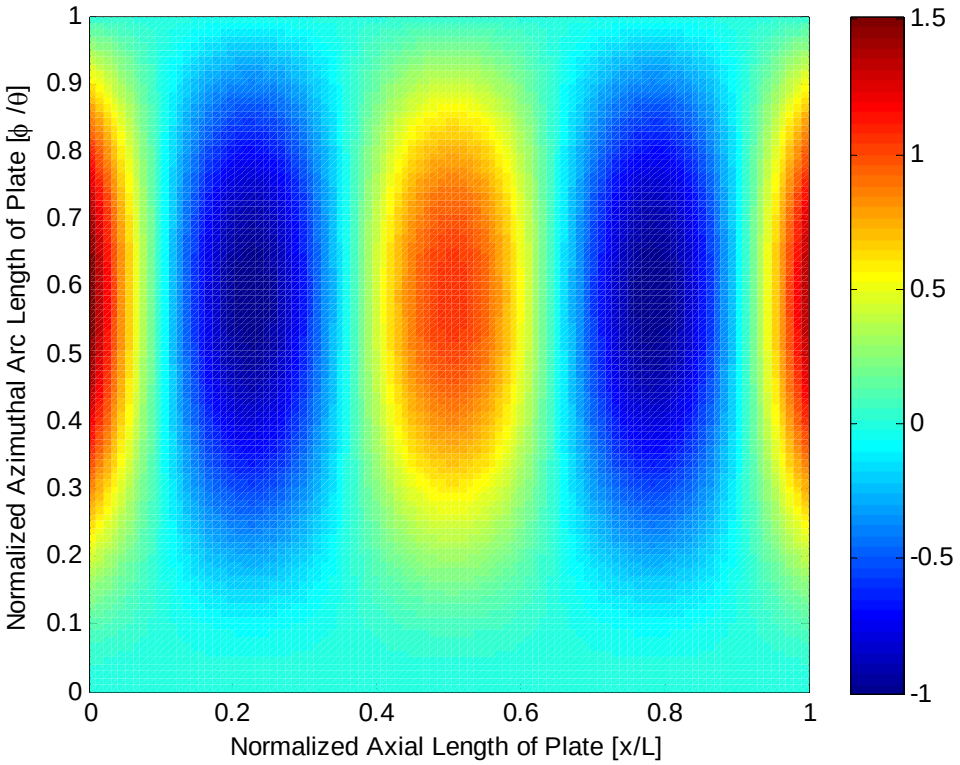

Figure D-16: Displacement view graph of C-F-SS-F plate modal shape ($m = 3$, $n = 1$)

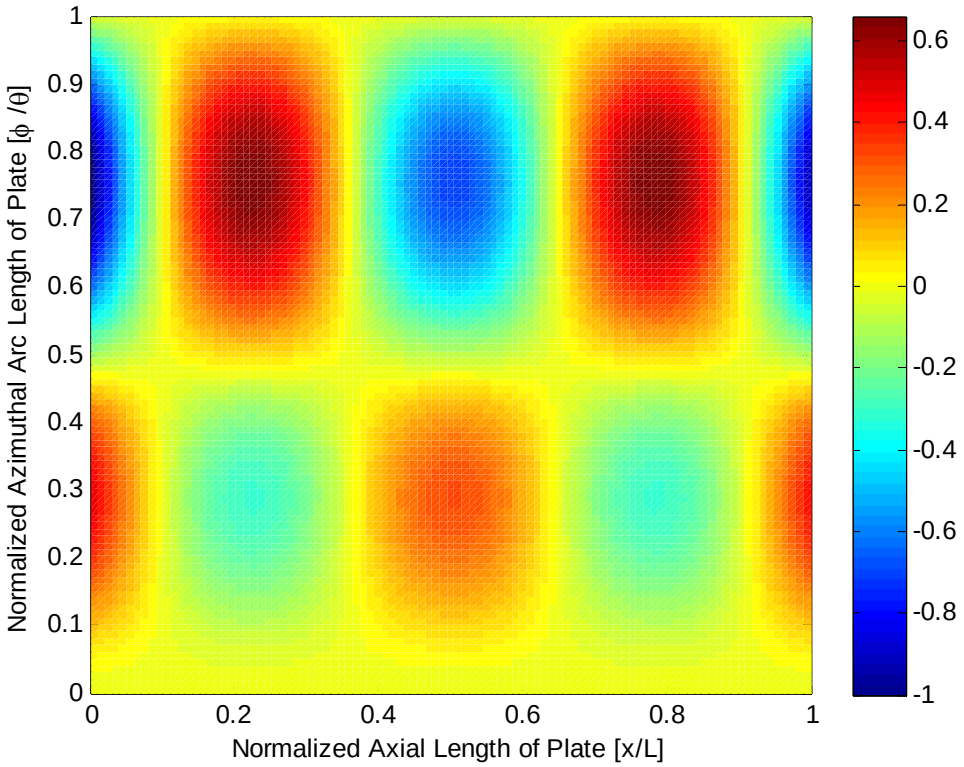

Figure D-17: Displacement view graph of C-F-SS-F plate modal shape ($m = 3$, $n = 2$)

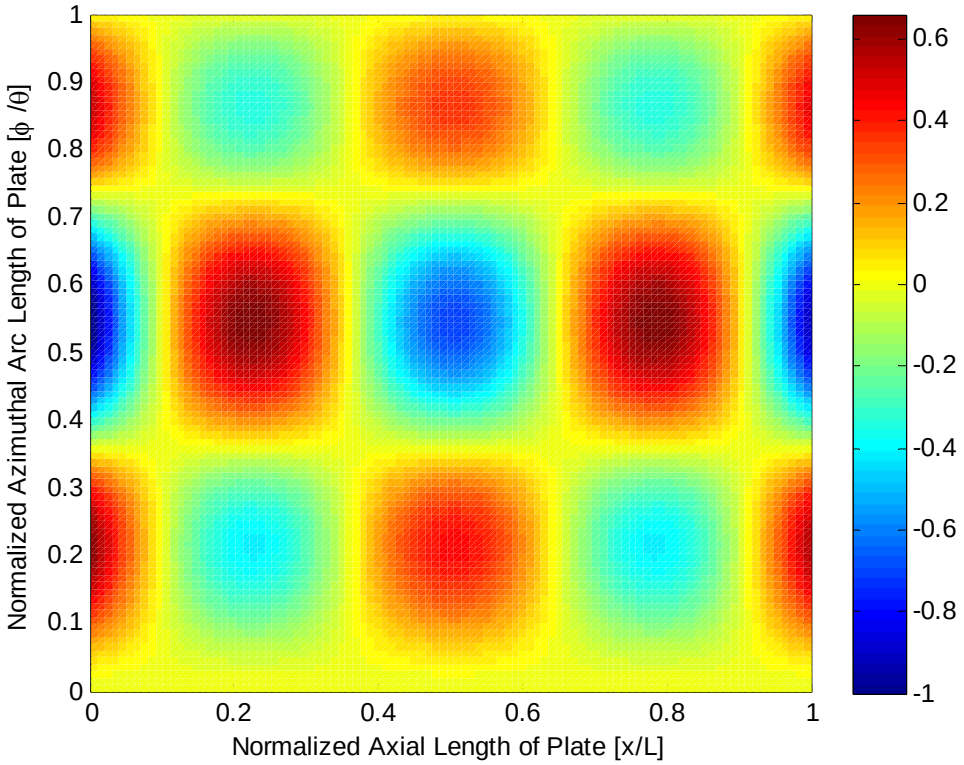

Figure D-18: Displacement view graph of C-F-SS-F plate modal shape ($m = 3$, $n = 3$)

14 APPENDIX E (Flow Module Test Case)

In order to provide a credible basis for the predictive capability of the flow module, a of test case have been compared between the flow module and an industry standard lumped parameter code.

14.1 RELAP5-3D Model

RELAP5-3D version 2.4.2 is the lumped parameter code used for all comparative results in this test case [106, 107]. A lumped parameter code is a simplified mathematical model where variables that are spatially distributed are represented as single scalars rather than vectors. As a result, the spatial resolution of a lumped parameter code is limited; however, it is assumed that RELAP5-3D can sufficiently model the hydraulic characteristics of the study geometric conditions (Table 4-1).

The RELAP5-3D model consists of six volumes as seen in Figure E-1. The coolant source (volume 201) contains the model's inlet boundary conditions including a fluid temperature of 20 °C and pressure of 4.13685 MPa. The inlet region of the study geometry is represented by volume 202. At this location the flow field enters with the total effective hydraulic diameter and contains a length of 0.1524 m. The outlet of volume 202 splits into subchannel one and two with hydraulic diameters of 0.003886 m and 0.003887 m, respectively. Form losses in the inlet regions are manually inserted in to the RELAP5-3D model as were calculated for the flow module in order to provide as much of a representative comparison as possible. The inlet form loss coefficient for subchannel one is 0.356165 and for subchannel two is 0.356049.

Each of the subchannels (volumes 101 and 102) contain two axial nodes and have a total length of 1.2573 m. The subchannels merge back into a common flow volume at the outlet region (volume 203). The outlet region accounts for the form losses associated with the sudden expansion of flow from each subchannel passing into the common flow channel. As previously done, the sudden expansion form loss coefficients were manually inserted into volume 203; for channel one the form loss coefficient is 0.7188879 and for

channel two the form loss coefficient is 0.71865541. Lastly, volume 203 is connected to the coolant sink (volume 204) which provides a location for the outlet boundary conditions.

RELAP5-3D only permits the use of one advective boundary conditions type, pressure. Due to this limitation, an inlet pressure of 4.13685 MPa was held constant and the outlet pressure was varied for different calculations. A corresponding flow rate and pressure field was then calculated by RELAP5-3D for each pressure driven simulation.

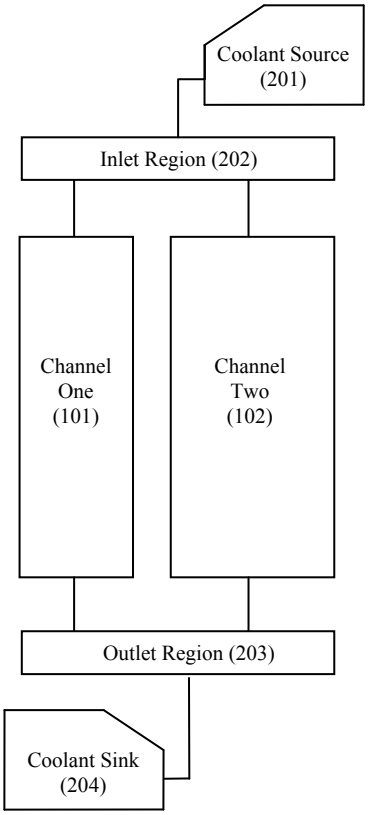

Figure E-1: RELAP5-3D model configuration

Inserting an inlet flow velocity boundary condition of 10 m/s into the flow module results in a total pressure drop of 0.2998 MPa. After inserting a total pressure loss boundary condition of 0.4078 MPa results, RELAP5-3D calculated an inlet flow velocity of 10.003 m/s. The pressure profiles for these two simulations are presented in Figure E-2. Note that the total pressure drop values between the two codes differ by approximately 30%.

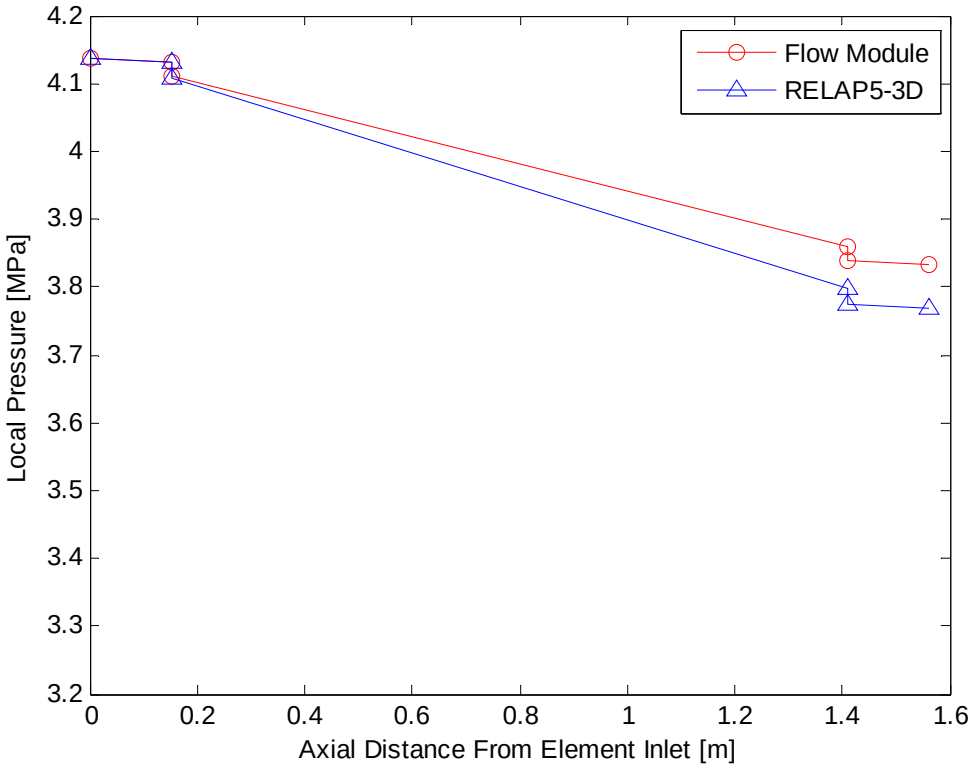

Figure E-2: Comparison of local pressure values pre-modification

From Figure E-2, a significant contribution to the difference in pressure drop values between the two codes is due to the pressure drop along the length of each subchannel, attributing the difference between the pressure drop values to frictional losses. A literature review on the method that RELAP5-3D employs to calculate the pressure losses in a pipe for single phase flow concludes with the developers use of the Zigrang-Sylvester approximation [108] to the Colebrook-White correlation [109];

$$\frac{1}{\varpi^{\frac{1}{2}}} = -2\log\left[\frac{\varepsilon}{3.7D_h} + \frac{2.51}{\mathrm{Re}}\left(1.14 - 2\log\left(\frac{\varepsilon}{D_h} + \frac{21.25}{\mathrm{Re}^{0.9}}\right)\right)\right] \tag{E-1}$$

where ε is the surface roughness and is assumed to be equal to 0.0000021336 meters as acknowledged in the ATR Upgraded Final Safety Analysis Report [20]. A more representative comparison of the two codes' capabilities may be conducted by employing (E-1) into the flow module rather than the use of (5-131) which was solely acquire for the ATR [20]. This is explicitly handled by inserting the Re for each subchannel into (E-1),

$$\frac{1}{\varpi_1^{\frac{1}{2}}} = -2\log\left[\frac{\varepsilon}{3.7D_{h,1}} + \frac{2.51}{\left(\frac{U_1\rho D_{h,1}}{\mu}\right)}\left(1.14 - 2\log\left(\frac{\varepsilon}{D_{h,1}} + \frac{21.25}{\left(\frac{U_1\rho D_{h,1}}{\mu}\right)^{0.9}}\right)\right)\right] \tag{E-2}$$

and

$$\frac{1}{\varpi_2^{\frac{1}{2}}} = -2\log\left[\frac{\varepsilon}{3.7D_{h,2}} + \frac{2.51}{\left(\frac{\left(U_iS_i - U_1S_1\right)\rho D_{h,2}}{S_2\mu}\right)} \cdot \left(1.14 - 2\log\left(\frac{\varepsilon}{D_{h,2}} + \frac{21.25}{\left(\frac{\left(U_iS_i - U_1S_1\right)\rho D_{h,2}}{S_2\mu}\right)^{0.9}}\right)\right)\right]. \tag{E-3}$$

Replacing (5-159) and (5-161) with (E-2) and (E-3), respectively, allows for the closure of the needed equations while utilizing the newly considered friction factor correlation. Figure E-3 presents the newly developed pressure profile calculated from the flow module against that calculated by RELAP5-3D. In this case the pressure losses are nearly identical, a total pressure loss of 0.3774 MPa is calculated from the flow module while RELAP5-3D has the same 0.4078 MPa loss necessary to drive a 10.003 m/s inlet velocity. Note that the total pressure drop values between the two codes differ by approximately 7.7%. Due to the simplified method for handling complex flow fields using bulk fluid characterization methods, this a difference of less than 10% is qualitatively considered acceptable for this study.

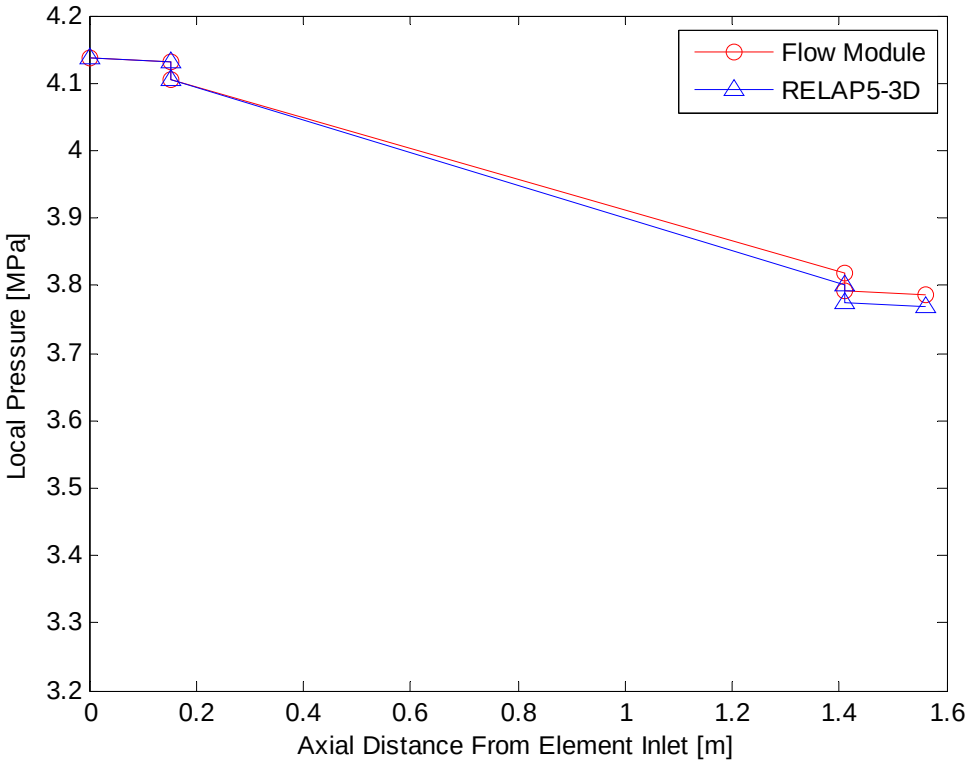

Figure E-3: Comparison of local pressure values post-modification

A comparison of the velocity of each subchannel channel as a function of the inlet flow velocity is presented in Figure E-4 calculated from both the flow module and RELAP5-3D. As seen in Figure E-4 velocity trends for the flow module and RELAP5-3D are nearly analogous to one another providing a basis for the qualitative conclusion that the flow module performs sufficiently well to capture bulk coolant characteristics of the study geometry relative to that of an industry standard computational tool.

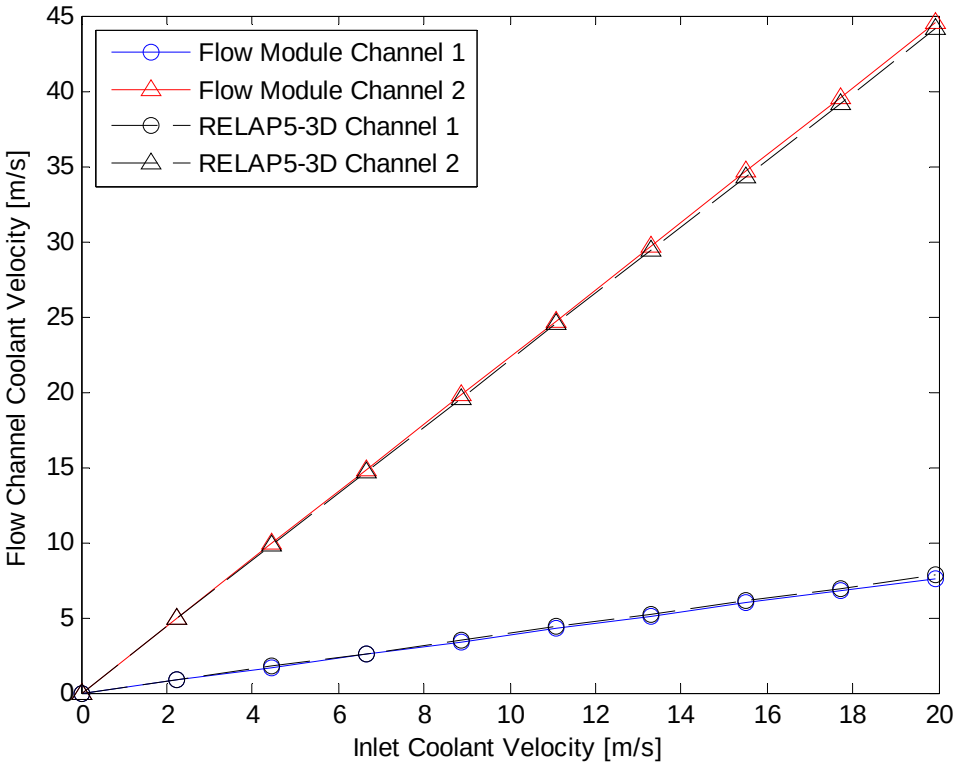

Figure E-4: Comparison of flow distribution in channel one and channel two